**Scuola Normale Superiore di Pisa**

Ph.D. Thesis

# Band Structure Engineering of Ge-rich SiGe Nanostructures for Photonics Applications

Giovanni Pizzi

Advisor
**Prof. Giuseppe Grosso**

# Contents

# Introduction

Information and Communication Technology (ICT) is currently dominated by silicon, because of its advantageous physical and electronic properties, and also due to its large availability. However, the required data transfer rates of modern electronic chips increase very rapidly and are going beyond the switching speeds provided by current state-of-the-art electronics.

Electronic–Photonic Integrated Circuits (EPIC) on Si are probably the most promising answer to this challenge. A laser compatible with the current processing of electronic chips for integrated circuits, based on group-IV materials, is extremely desirable to monolithically integrate electronics and photonics.

Indeed, in the recent years, there has been a renewed interest for Si and Ge as materials for photonics devices [1–3], also thanks to the developments of the their growth technique and to the first demonstration at MIT of a CMOS-compatible optically pumped Ge-on-Si laser [4].

In this Thesis I study bulk and multilayered heterostructures composed of Si, Ge and their alloys with particular attention to Ge-rich systems, with the aim of realizing optical sources in different regions of the electromagnetic spectrum. In particular, the systems investigated are thin layers, superlattices, multiple quantum well (MQW) heterostructures or quantum cascade structures with alternating $Si_{1-x}Ge_x$ layers of different composition $x$, coherently grown along the [001] direction on relaxed virtual substrates.

The Thesis is divided in two main Parts. Part I is devoted to the description of the methods that are at the basis of the calculations carried out in the second Part. In particular, in Chap. 1 I describe the models that are used for the evaluation of the electronic states of the studied systems. The two models here adopted are the tight-binding (Sec. 1.2) and the $\mathbf{k} \cdot \mathbf{p}$ method (Sec. 1.6). In both cases, the discussion starts from the application of the model to Si or Ge bulk systems, and it is then generalized to the case of multilayer heterostructures. Moreover, I discuss how strain (Sec. 1.3) and alloying (Sec. 1.4) can be taken into account in the calculations, due to the high relevance of these effects in Si/Ge heterostructures. The last Sections of Chap. 1 are devoted to the description of further theoretical models that are adopted in the second Part of the Thesis, such as for instance the solution of the coupled Schrödinger–Poisson equations that must be solved to take into account self-consistent charge distribution effects (Sec. 1.9), the evaluation of the intersubband phonon scattering lifetimes (Sec. 1.10), or the simulation of the interdiffusion process due to a thermal

annealing of a MQW system (Sec. 1.11).

Chap. 2 is instead dedicated to the theory of the optical properties of bulk and heterostructured semiconductors. In particular, the general definition of the absorption and gain spectra is presented in Sec. 2.1, and then in Sec. 2.2 I discuss how to calculate these spectra both in the tight-binding framework and in the $\mathbf{k} \cdot \mathbf{p}$ effective-mass framework. In Sec. 2.3 the photoluminescence spectra due to the spontaneous recombination in optically-pumped bulk Ge systems is addressed. In Sec. 2.4, 2D excitonic effects on the evaluated absorption spectra are included, and the absorption coefficient in the case of intersubband transitions is addressed in Sec. 2.5.

The models and techniques discussed in Part I are then exploited in Part II which is instead dedicated to several applications, i.e. to the identification and study of different systems that are potential candidates as Si-based light sources.

In particular, this second Part is divided in two Chapters, focusing on two kind of problems which are different both from the point of view of the underlying physics (intersubband vs. interband transitions) and from the point of view of the applications, since the emission frequency is in the far-infrared or in the near-infrared regions, respectively. Consequently, especially for what concerns the applications, the problems addressed in the two Chapters are for many aspects independent. For this reason, a more detailed discussion of the motivations of the investigations of the topics presented in this Thesis can be found in the Introductions of the respective Chapters.

In Chapter 3 I address the use of intersubband transitions in the conduction band of Ge/SiGe MQWs and quantum cascade structures with the final objective of realizing an emitter in the THz region of the electromagnetic spectrum. I start from the study of the absorption due to the intersubband transitions in the conduction band (at the L point) of Ge/SiGe MQW systems (Sec. 3.2). This study is indeed preliminary to the observation of light emission. However, beside the demonstration of intersubband absorption, it is important to study also the non-radiative channels through which the electrons can relax without emission of photons: Sec. 3.3 is devoted to this aim. We then propose a few different designs of THz electroluminescent emitters, based on Ge/SiGe (Sec. 3.4) or on Si/SiGe quantum cascade structures (Sec. 3.5).

In Chapter 4 I focus instead on interband transitions in SiGe systems (thin layers, MQWs and superlattices) with the aim of obtaining a laser emitting in the near-infrared, which could be employed for instance as a source for the optical fiber interconnects used in long-range telecommunications. In particular, in Sec. 4.2 the interband absorption spectrum of a Ge/SiGe MQW system is studied and from comparison with the experimental measures the different involved transitions are identified. In Sec. 4.3 I study the possibility of reaching a direct gap in Ge/SiGe MQW systems by means of a large applied tensile strain, thanks to the different shifts of the conduction Γ and L valleys under biaxial strain. Then, the possibility of reaching positive gain by means of a smaller tensile strain in a strongly $n-$doped Ge system is analyzed with reference to recent literature results (Sec. 4.4), motivating the development of a code to evaluate the photoluminescence spectrum of bulk-like

strained and doped Ge systems; the results obtained with this code are presented and discussed in Sec. 4.5. Furthermore, due to the relevant role of the tensile strain in the relative positioning of the different states in Ge systems, several strategies have been addressed to increase the magnitude of the strain: in particular, in Sec. 4.6 I discuss the effects of thermal annealing on a Ge/SiGe MQW system, focusing on the competitiveness between the redshift of the lowest-energy transitions due to the increase of the biaxial tensile strain, and their blueshift caused by the interdiffusion of the Si atoms in the Ge wells. Eventually, I present a different strategy to obtain a direct-gap structure based on the adoption of short-period Si/Ge superlattices: in Sec. 4.7 I discuss how in this kind of heterostructures the band folding and the reduced symmetry may be able to produce a direct gap, and I then show that in selected superlattices a positive gain can be expected.

Finally, in Appendix A I briefly describe a few further topics that I have addressed: Si/Ge nanotubes, porous silicon and intersubband polaritons. Even if the first two topics are not planar multilayer heterostructures, they show the potential and the peculiar properties of SiGe materials. In the study of the intersubband polaritons, I addressed the specific role of the non-parabolicity of the confined bands and their interactions with cavity modes: the adopted methodology will be further developed for the analysis of intersubband polaritons in SiGe systems.

# Part I

# Methods

# Chapter 1

# Adopted models and methods for the electronic states

Many of the electronic and optical properties reported in this Thesis are calculated by means of a first-neighbor tight binding (TB) Hamiltonian with $sp^3d^5s^*$ orbitals and including spin-orbit interaction. The advantage of this atomistic approach is that it allows us to take into account the geometric details of the whole structure, the chemical composition of the deposited materials and the strain within each layer. The method provides the electronic band structure over the whole Brillouin zone, the spatial and orbital compositions of the states, and the matrix elements of optical transitions. Moreover, the tight binding model is most appropriate for large scale electronic structure calculations, especially when implemented with O(N) strategies (see e.g. Ref. [5] and references therein, and Refs. [6, 7]).

However, there are cases (that will be described in detail in the following Chapters) when simpler but faster methods are more appropriate. In particular, we will describe and adopt for some selected applications a multiband $\mathbf{k} \cdot \mathbf{p}$ effective-mass model. The disadvantage of this model is that it is not as numerically accurate as the tight binding (see e.g. Refs. [8–11]). However, it has mainly two advantages. The first is that it significantly reduces the computation time. This is a strong requirement in the process of optimization of the design of complicated structures (see e.g. Secs. 3.4, 3.5 and 3.A): for such an application, the calculation has to be as real-time as possible, because we need to change many times the input parameters in order to obtain the best design. In practice, each run can last in the worst case tens of seconds, but not hours. The second advantage is that the $\mathbf{k} \cdot \mathbf{p}$ model can give a more intuitive description of many of the physical properties of the system, often allowing to understand their qualitative behavior or even providing for them analytic expressions.

In this Chapter, we describe both models for the calculation of the electronic properties of bulk and heterostructured semiconductors, with special attention to the case of Si and Ge. Furthermore, we also address some further theoretical models that will be adopted in the second Part of the Thesis.

**Table 1.1** – Lattice constants of some semiconductors which crystallize in the diamond structure, taken from Wyckoff [12].

| Crystal | | $a$(Å) | |
|---|---|---|---|
| C | Diamond | 3.566 79 | (20 °C) |
| Si | Silicon | 5.430 70 | (25 °C) |
| | | 5.445 | (1300 °C) |
| Ge | Germanium | 5.657 35 | (20 °C) |
| | | 5.656 95 | (18 °C) |
| $\alpha$–Sn | Tin (gray) | 6.4912 | |

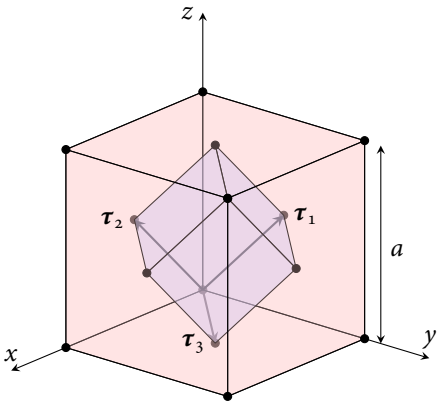


**Figure 1.1** – FCC lattice. The primitive vectors are $\boldsymbol{\tau}_1 = {}^{a}/_{2}(0,1,1)$, $\boldsymbol{\tau}_2 = {}^{a}/_{2}(1,0,1)$ and $\boldsymbol{\tau}_3 = {}^{a}/_{2}(1,1,0)$, where $a$ is the side of the conventional unit cell. The primitive cell is shown with a darker color.
The conventional unit cell, having a basis of four atoms in the positions $\mathbf{d}_1 = (0,0,0)$, $\boldsymbol{\tau}_1$, $\boldsymbol{\tau}_2$ and $\boldsymbol{\tau}_3$, emphasizes the full cubic symmetry $O_h$ of the lattice.

## 1.1 Crystal geometry of zincblende structures

This Thesis is focused on silicon (Si) and germanium (Ge), which are group IV semiconductors and crystallize in the diamond structure. Since this structure is a special case of the zincblende structure, typical of most group III-V semiconductors, like gallium arsenide (GaAs), indium arsenide (InAs), etc., in this Section we describe the more general zincblende structure.

The Bravais lattice of the zincblende structure is face centered cubic (FCC) with a basis of two atoms, so that it can be seen as two interpenetrating FCC lattices. We can choose the three translation vectors of the FCC lattice as

$$\boldsymbol{\tau}_1 = {}^{a}/_{2}(0,1,1), \qquad \boldsymbol{\tau}_2 = {}^{a}/_{2}(1,0,1), \qquad \boldsymbol{\tau}_3 = {}^{a}/_{2}(1,1,0), \tag{1.1}$$

as represented in Fig. 1.1; the primitive cell formed by these vectors has volume $a^3/4$. However, in order to emphasize the full cubic symmetry of the Bravais lattice, one often uses the larger conventional unit cell with side $a$, also shown in Fig. 1.1. The values of $a$ (the lattice constant) for some common semiconductors which crystallize in the diamond structure are given in Table 1.1.

As already mentioned, the zincblende structure has two atoms in the primitive cell, one in the origin $\mathbf{d}_1 = (0,0,0)$, and one at one fourth of the diagonal of the cube: $\mathbf{d}_2 = {}^{a}/_{4}(1,1,1)$; the resulting structure is shown in Fig. 1.2. In this Figure it is also

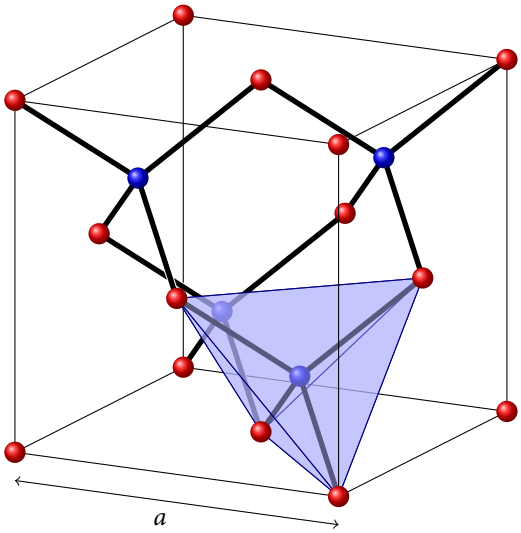


**Figure 1.2** – Conventional unit cell of the zincblende structure. First-neighbor bonds are also shown. In this structure, one kind of atoms (e.g. the anions, red in the Figure) form a FCC lattice. The other kind of atoms (cations, blue in the Figure) also form a FCC lattice, which is displaced by one fourth of the diagonal of the conventional unit cell with respect to the FCC lattice of the anions. If the two atoms are equal, one recovers the diamond structure. If we use the primitive cell with translation vectors given in Eq. (1.1) (see also Fig. 1.1), there are only two atoms in the primitive cell: the anion, lying at $\mathbf{d}_1 = (0,0,0)$, and the cation, lying at $\mathbf{d}_2 = {}^{a}/_{4}(1,1,1)$.
In the zincblende structure, each atom has four first neighbors of opposite kind, which form a regular tetrahedron centered on the atom. One of such tetrahedrons is shown in blue in the Figure.

possible to notice that each atom lies at the center of a regular tetrahedron formed by its four first neighbors. We emphasize here that the knowledge of the position of the first neighbors is of great importance for the application of the tight-binding model. We thus write explicitly the coordinates of the positions of the four first neighbors with respect to the reference atom. In the case of the atom centered on the origin, the four nearest-neighbor positions are

$$\begin{aligned} \mathbf{d}_2 = \mathbf{a}_1 &= (1/2, 1/2, 1/2), & \mathbf{d}_2 - \boldsymbol{\tau}_1 = \mathbf{a}_2 &= (1/2, -1/2, -1/2), \\ \mathbf{d}_2 - \boldsymbol{\tau}_2 = \mathbf{a}_3 &= (-1/2, 1/2, -1/2), & \mathbf{d}_2 - \boldsymbol{\tau}_3 = \mathbf{a}_4 &= (-1/2, -1/2, 1/2), \end{aligned} \tag{1.2}$$

while for the atom centered on $\mathbf{d}_2$ the relative positions are

$$\begin{aligned} -\mathbf{a}_1 &= (-1/2, -1/2, -1/2), & -\mathbf{a}_2 &= (-1/2, 1/2, 1/2), \\ -\mathbf{a}_3 &= (1/2, -1/2, 1/2), & -\mathbf{a}_4 &= (1/2, 1/2, -1/2). \end{aligned}$$

The two atoms in $\mathbf{d}_1$ and $\mathbf{d}_2$ are different in the case of group III-V materials (for instance, in the case of GaAs, we have an arsenic atom in the origin and a gallium atom in $\mathbf{d}_2$), and in this case we designate them as the anion and the cation,

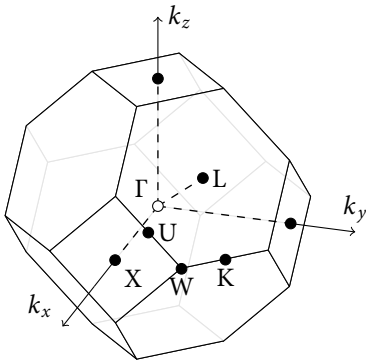


**Figure 1.3** – Brillouin zone of a crystal with a FCC Bravais lattice. The reciprocal lattice is a body-centered cubic (BCC) and the Brillouin zone is a truncated octahedron, centered on Γ.
The points of high symmetry are also shown.

respectively. For the diamond structure, the two atoms in the primitive cell are instead equal.

The corresponding primitive vectors of the FCC reciprocal lattice are

$$\mathbf{g}_1 = \frac{2\pi}{a}(-1,1,1), \qquad \mathbf{g}_2 = \frac{2\pi}{a}(1,-1,1), \qquad \mathbf{g}_3 = \frac{2\pi}{a}(1,1,-1),$$

which form a BCC lattice. The Brillouin zone is the well known truncated octahedron, depicted in Fig. 1.3. Some points of high symmetry in the Brillouin zone are denoted by conventional names:

$$\Gamma = (0,0,0), \qquad X = \frac{2\pi}{a}(1,0,0), \qquad L = \frac{2\pi}{a}\left(\frac{1}{2},\frac{1}{2},\frac{1}{2}\right),$$
$$W = \frac{2\pi}{a}\left(1,\frac{1}{2},0\right), \qquad K = \frac{2\pi}{a}\left(\frac{3}{4},\frac{3}{4},0\right), \qquad U = \frac{2\pi}{a}\left(1,\frac{1}{4},\frac{1}{4}\right).$$

## 1.2 Tight-binding model

One of the models that we use in this work in order to study the electronic and optical properties of Si–Ge nanostructures is the tight-binding model (TB).

When the atoms are brought together to form the crystal, their orbitals overlap and the energy levels spread leading to the formation of bands, i.e. the actual levels in the solid.

We denote by $\mathbf{r}_{n\nu}$ the position of a generic atom of the crystal, where $n$ indicates the cell to which the atom belongs and $\nu$ indexes the different atoms within the cell; in particular, $\mathbf{r}_{n\nu}$ can be written as $\mathbf{r}_{n\nu} = \boldsymbol{\tau}_n + \mathbf{d}_\nu$, where $\boldsymbol{\tau}_n$ is a translation vector of the FCC Bravais lattice and $\mathbf{d}_\nu$ is the position of the atom $\nu$ within the cell.

The Hamiltonian of an isolated atom of type $\nu$ centered on $\mathbf{r}_{n\nu}$ is $h_\nu(\mathbf{r}-\mathbf{r}_{n\nu})$ and the corresponding Schrödinger equation is given by

$$h_\nu\phi_{\nu m}(\mathbf{r}-\mathbf{r}_{n\nu}) = \left[\frac{p^2}{2m} + V^{(a)}(r-r_{\nu m})\right]\phi_{\nu m}(\mathbf{r}-\mathbf{r}_{n\nu}) = \tilde{E}_{\nu m}\phi_{\nu m}(\mathbf{r}-\mathbf{r}_{n\nu}), \quad (1.3)$$

where $m$ indexes the states and $V^{(a)}$ is the atomic potential acting on the electron, due to the nucleus and the other electrons. We know that we can choose solutions

with a definite angular symmetry (for example, if the Hamiltonian depends only on the magnitude of $\mathbf{r}$ and not on its angular part, we can separate the orbitals $\phi_{\nu m}$ in a radial and an angular part, and choose the angular part as a linear combination of spherical harmonics, so that the orbitals have symmetry $s$, $p_x$, $p_y$, $p_z$ and so on).

We always assume, moreover, that the atomic orbitals $\phi_{\nu m}(\mathbf{r} - \mathbf{r}_{n\nu})$ are Löwdin orbitals, i.e., different orbitals are orthogonal to each other. For orbitals centered on the same atom this is obvious, as we can always choose an orthonormal set of eigenfunctions for the problem (1.3). For atoms centered on different sites, we can first obtain a set of non-orthogonal orbitals simply solving Eq. (1.3). With a procedure shown in Ref. [13] we can at this point change the basis set to obtain the Löwdin orbitals with the requested property

$$\langle \phi_{\nu m}(\mathbf{r} - \mathbf{r}_{n\nu}) \,|\, \phi_{\nu' m'}(\mathbf{r} - \mathbf{r}_{n'\nu'}) \rangle = \delta_{mm'}\delta_{nn'}\delta_{\nu\nu'}. \tag{1.4}$$

The simple orthogonalization algorithm presented in [14] has moreover the advantage that the Löwdin orbitals $\phi_{\nu m}$ show the same symmetry properties as the original atomic orbitals, so that we can still speak of orbitals of $s$-symmetry, $p_x$-symmetry, and so on. This information is contained in the index $m$ of $\phi_{\nu m}$.

When we consider the full Hamiltonian of the crystal, the actual wavefunctions must satisfy the Bloch theorem because of the discrete translational symmetry of the lattice; we can write them in the form of Bloch sums

$$\Phi_{\nu m}(\mathbf{k}, \mathbf{r}) = \frac{1}{\sqrt{N}} \sum_n e^{i\mathbf{k}\cdot\mathbf{r}_{n\nu}} \phi_{\nu m}(\mathbf{r} - \mathbf{r}_{n\nu}) \tag{1.5}$$

where $N$ is the number of primitive cells in the crystal and the sum over $n$ runs over all the $N$ cells. Note that these Bloch sums are orthonormal because of Eq. (1.4).

We assume that the single-particle Hamiltonian $\mathcal{H}$ for an electron of the crystal can be written in the form

$$\mathcal{H} = \frac{\mathbf{p}^2}{2m} + V(\mathbf{r}),$$

where $V$ (the crystalline potential) is assumed to be the sum of the atomic potentials $V^{(a)}$:

$$V(\mathbf{r}) = \sum_{n,\nu} V^{(a)}(\mathbf{r} - \mathbf{r}_{n\nu}). \tag{1.6}$$

The eigenfunctions of the total Hamiltonian $\mathcal{H}$ with given $\mathbf{k}$ vector can be written as linear combinations of the orthonormal Bloch sums $\Phi_{\nu m}(\mathbf{k}, \mathbf{r})$

$$\Psi_{\mathbf{k}}(\mathbf{r}) = \sum_{\nu,m} C_{\nu m} \Phi_{\nu m}(\mathbf{k}, \mathbf{r})$$

and the coefficients $C_{\nu m}$ can be obtained by simply diagonalizing the Hamiltonian matrix $H_{\nu m,\nu' m'}(\mathbf{k})$, whose matrix elements are

$$H_{\nu' m',\nu m}(\mathbf{k}) = \langle \Phi_{\nu' m'}(\mathbf{k}, \mathbf{r}) | \mathcal{H} | \Phi_{\nu m}(\mathbf{k}, \mathbf{r}) \rangle .$$

Let us explicitly compute the matrix elements $H_{\nu' m',\nu m}(\mathbf{k})$ of the Hamiltonian.

We can split $V$, given in Eq. (1.6), in two parts, separating the contribution of the atom in $\mathbf{d}_{\nu'}$:

$$\mathcal{H} = \frac{\mathbf{p}^2}{2m} + V(\mathbf{r}) = \frac{\mathbf{p}^2}{2m} + V^{(a)}(\mathbf{r} - \mathbf{d}_{\nu'}) + V'(\mathbf{r}) = h_{\nu'} + V'$$

where $V'(\mathbf{r})$ contains all the remaining terms of the potential, i.e. the atomic potentials centered on sites different from $\mathbf{d}_{\nu'}$.

Using now the fact that $\phi_{\nu m}$ is eigenfunction of the atomic Hamiltonian $h_\nu$, as stated in Eq. (1.3), and the explicit expression for the orthonormal $\Phi_{\nu m}$ functions, given in Eq. (1.5), we obtain

$$\begin{aligned} H_{\nu' m', \nu m}(\mathbf{k}) &= \langle \Phi_{\nu' m'}(\mathbf{k}, \mathbf{r}) | \mathcal{H} | \Phi_{\nu m}(\mathbf{k}, \mathbf{r}) \rangle = E_{\nu' m'} \delta_{\nu \nu'} \delta_{m m'} + \\ &+ \sum_{\boldsymbol{\tau}_n} e^{i\mathbf{k}\cdot(\boldsymbol{\tau}_n + \mathbf{d}_\nu - \mathbf{d}_{\nu'})} \int \mathrm{d}\mathbf{r}\, \phi^*_{\nu' m'}(\mathbf{r} - \mathbf{d}_{\nu'}) V'(\mathbf{r}) \phi_{\nu m}(\mathbf{r} - \boldsymbol{\tau}_n - \mathbf{d}_\nu). \end{aligned} \tag{1.7}$$

The sum of the previous expression is over all translation vectors $\boldsymbol{\tau}_n$ such that $\nu$ and $\nu'$ belong to different sites. Note that the energy $E_{\nu' m'}$ contains the atomic eigenvalue $\tilde{E}_{\nu' m'}$ of the atom in $\mathbf{d}_{\nu'}$ corrected by the crystal field contribution, which originates from the term in Eq. (1.7) with $\boldsymbol{\tau}_n = 0$ and $\nu = \nu'$. This term is of the form

$$\int \mathrm{d}\mathbf{r}\, \phi^*_{\nu' m'}(\mathbf{r} - \mathbf{d}_{\nu'}) V'(\mathbf{r}) \phi_{\nu' m'}(\mathbf{r} - \mathbf{d}_{\nu'}), \tag{1.8}$$

where we stress again that $V'$ is the sum of all contributions to the potential coming from atoms other than the one sitting at $\mathbf{d}_{\nu'}$, and both orbitals are centered on the same position $\mathbf{d}_{\nu'}$. As a consequence, $E_{\nu' m'}$ feels its environment, i.e. it contains contributions due to the symmetry of the crystal structure in which the atom is embedded.

As already said, to get the energy levels we only need to solve the eigenvalue problem

$$\mathcal{H}\Psi(\mathbf{k}) = E(\mathbf{k})\Psi(\mathbf{k}),$$

i.e. diagonalize the Hamiltonian matrix $H_{\nu' m', \nu m}(\mathbf{k})$. This is, however, not simple at all.

The first difficulty that we encounter is in the evaluation of the last term of Eq. (1.7). This term rises two problems: first of all we have to work with the sum over $\boldsymbol{\tau}_n$ that, even if not infinite, is composed of an unmanageable large number of terms. However, we can make a first approximation considering only those orbitals centered on atoms that are not too far apart, because we are assuming that the orbitals of interest are quite localized and do not interact significantly if they are spatially well separated. We can then adopt the first-neighbor approximation, where we sum only on the nearest-neighbor atoms (in the case of the zincblende structure, only on four atoms), second-neighbor approximation and so on. A further approximation is the so called two-center approximation. Indeed, expanding $V'(\mathbf{r})$ using Eq. (1.6), we see that in general we have integrals in Eq. (1.7) where the two wavefunctions are centered on two different atoms, and interact through an atomic potential centered

on a third site. Always assuming well localized orbitals, we can neglect all those contributions where the three sites are different, and consider only the terms of the following form:

$$\left\langle \phi_{\nu' m'}(\mathbf{r} - \mathbf{d}_{\nu'}) \,\middle|\, V^{(a)}(\mathbf{r} - \mathbf{d}_{\nu} - \boldsymbol{\tau}_n) \,\middle|\, \phi_{\nu m}(\mathbf{r} - \mathbf{d}_{\nu} - \boldsymbol{\tau}_n) \right\rangle . \tag{1.9}$$

The second problem that we have to face with, is that we have an infinite number of Löwdin orbitals on each site, and therefore also the Hamiltonian matrix is infinite. To obtain a finite matrix, allowing us to diagonalize it with standard methods, we consider only a finite set of orbitals, in particular those of the outermost atomic shells. This choice is physically motivated by the fact that the inner orbitals are quite ineffective to provide relevant features in the electronic properties of the crystal, being tightly bound to the nuclei. If a calculation is performed taking into account also these orbitals, we would get that they generate dispersionless ($\mathbf{k}$–independent) core bands, that correspond to an infinite electronic effective mass. Moreover, these (completely filled) bands are deep well below the chemical potential level, and therefore also an excitation of an electron to a higher band is impossible using photons in the visible range or with lower frequency.

The topmost occupied valence bands show on the contrary a complicated dispersion relation $E(\mathbf{k})$; moreover there is the actual possibility that some electrons are transferred to the empty conduction bands, originating interesting transport and optical properties of the semiconductor.

The simplest choice of orbitals that produces reasonable results is the so called $sp^3$ tight-binding model, where we consider only one orbital with $s$ symmetry and three $p$ orbitals ($p_x$, $p_y$ and $p_z$) centered on each atom of the primitive cell, reducing the total number of orbitals to eight in the case of the zincblende structure. In this way we have to diagonalize only a $8 \times 8$ matrix, simplifying notably the computation.

This description, however, is quite poor, and indeed it lacks some of the most important features of the band dispersion of the group IV and III-V semiconductors. In the literature, there have been different attempts to solve this problem, typically increasing the order of neighbors which are taken into account in the calculation, or introducing additional orbitals for each atom. With this second method, at the expense of an increase of the dimension of the Hamiltonian matrix, one obtains a great improvement of the results of the computation, allowing for the description of some features that were missed by the simple $sp^3$ model.

The model that is used throughout this work is the $sp^3d^5s^*$ model in the first-neighbor approximation, that we now describe in detail.

### 1.2.1 Semiempirical approach

An upgrade of the minimal $sp^3$ basis set model has been obtained introducing, for each atom in the primitive cell, an unoccupied excited $s$-type orbital [15]; this gives a better description of the conduction bands of the semiconductors. Such orbitals are denoted by $s^*$ to distinguish them from the other lower-energy $s$ orbitals.

The major improvement in the description of the conduction bands, however, is obtained by the introduction of $d$-type orbitals, as explained in Jancu *et al.* [16]. One of the main achievements of such a choice is a better agreement with the known sequence of the energy levels, and a better reproduction of the transverse effective masses for the conduction band minima at the L point and along the Γ–X line in the Brillouin zone.

Throughout this work, we thus adopt ten atomic-like orbitals for each atom, denoted by their symmetry as

$$s; \quad \underbrace{x, y, z}_{p}; \quad \underbrace{xy, xz, yz, x^2 - y^2, 3z^2 - r^2}_{d}; \quad s^*. \tag{1.10}$$

To distinguish between orbitals belonging to different atoms, we use a specific site label. For zincblende structures, e.g., we denote with $s_a$ the $s$ orbital centered on the anion, and with $s_c$ the orbital centered on the cation, and similarly for the other orbitals. We will use this notation also for group IV semiconductors if we need to distinguish between the two atoms in the basis, even if the two atoms are of the same kind.

As already said, we limit ourselves to interactions between first neighbors and consider only two-center integrals. The generic integral that we must compute in order to obtain the matrix elements given by Eq. (1.7) is therefore of the form

$$\left\langle \phi_{\nu' m'}(\mathbf{r} - \mathbf{d}_{\nu'}) \,\middle|\, V^{(a)}(\mathbf{r} - \mathbf{d}_{\nu} - \boldsymbol{\tau}_n) \,\middle|\, \phi_{\nu m}(\mathbf{r} - \mathbf{d}_{\nu} - \boldsymbol{\tau}_n) \right\rangle. \tag{1.11}$$

In the semiempirical approach these integrals, as well as the energies $E_{\nu m}$ of Eq. (1.7), are taken as parameters, and are obtained by fitting specific features of the band dispersion of the bulk semiconductor under study. Typically, such features are the values of the energy bands at high-symmetry points of the Brillouin zone and the effective masses, which are obtained from experimental data or from other theoretical methods. The empirical tight-binding model, in this sense, can be seen as an interpolation method that gives the energy bands for all points in the Brillouin zone, starting from a limited set of energies. This semiempirical approach to the tight-binding method was first introduced by Slater and Koster [14].

Using this approach we want now to show that, for a $sp^3d^5s^*$ model with interactions limited to first neighbors, we need only a small set of independent two-center integrals to obtain the full band dispersion. These are denoted (for group IV crystals) by

$$\begin{array}{llllll} V(ss\sigma), & & & & & \\ V(sp\sigma), & V(pp\sigma), & V(pp\pi), & & & \\ V(sd\sigma), & V(pd\sigma), & V(pd\pi), & V(dd\sigma), & V(dd\pi), & V(dd\delta), \\ V(s^*s\sigma), & V(s^*s^*\sigma), & V(s^*p\sigma), & V(s^*d\sigma). & & \end{array} \tag{1.12}$$

What we mean is that all integrals of the form of Eq. (1.11) can be expressed by appropriate linear combinations of the independent integrals (1.12), where the

coefficients depend on the director cosines of the vector $\mathbf{R} = \mathbf{d}_\nu + \boldsymbol{\tau}_n - \mathbf{d}_{\nu'}$ that joins the two atoms at $\mathbf{d}_{\nu'}$ and at $\boldsymbol{\tau}_n + \mathbf{d}_\nu$.

To clarify this concept, we now discuss the meaning of the integrals (1.12). In the case of two $s$ orbitals, the angular momentum quantized in the direction of the vector joining the two atoms can only be zero. However, if we consider two $p$ orbitals (see Fig. 1.4), we can overlap them along the direction of the orbital; in this case we speak of a $\sigma$ bond, and the angular momentum along the axis is still zero. We can however let them overlap in a direction orthogonal to the orbitals, e.g. considering the interaction between two $p_x$ orbitals, but with the two atoms aligned along the $z$ direction: this type of bond is called a $\pi$ bond, and now the angular momentum along $z$ is $\hbar$.

In particular, if the vector $\mathbf{R}$ joining the two atoms is along the $z$ direction, we can define the two-center integrals introduced in (1.12) by

$$\begin{aligned} \langle s|H|s\rangle &= V(ss\sigma); & \langle s|H|p_z\rangle &= V(sp\sigma); \\ \langle p_z|H|p_z\rangle &= V(pp\sigma); & \langle p_x|H|p_x\rangle &= \langle p_y \,|\, H \,|\, p_y\rangle = V(pp\pi). \end{aligned}$$

Moreover, we have that

$$\langle s|H|p_x\rangle = \langle s|H|p_y\rangle = V(sp\pi) = 0 \tag{1.13}$$

because, if the Hamiltonian includes only the two interacting atoms, then it has a cylindrical symmetry along the axis $\mathbf{R} = \mathbf{d}_\nu + \boldsymbol{\tau}_n - \mathbf{d}_{\nu'}$ joining the two atoms. If we consider that the angular part of the orbitals is simply a spherical harmonic function $Y_{lm}$, with azimuthal direction $\mathbf{R}$, then we see that the matrix element (1.13) of the Hamiltonian vanishes because the two spherical harmonics of the orbitals at the two centers have different $m$.

In the crystal, however, the direction of the vectors $\mathbf{R}$ joining two atoms are in general neither parallel nor orthogonal to the directions of the axes $x$, $y$, $z$ that we have chosen to define the $p$ orbitals; to get the interaction parameter for a generic direction, we have to expand the spherical harmonics which define the angular part of our orbitals along the direction of $\mathbf{R}$. The matrix element is therefore a linear combination of the integrals of (1.12). A graphical representation of one possible case is given in Fig. 1.4.

A complete table of all matrix elements needed for a $sp^3d^5s^*$ basis is reported in Table 1.2, where $l$, $m$, and $n$ denote the director cosines of $\mathbf{R}$ with respect of the $x$, $y$, $z$ axes, as shown in Fig. 1.5. These matrix elements are known as the Slater–Koster parameters.

For the sake of completeness, we mention that in the case of group III-V semiconductors, the only difference is that we have to distinguish for instance between $V(s_a p_c \sigma)$ and $V(s_c p_a \sigma)$: we have indeed different energies depending on whether the $s$ orbital is centered on the anion or on the cation. The number of independent integrals will be slightly larger, but except for this there is no conceptual difference from what we have presented up to now for group IV semiconductors.

**Table 1.2** – Slater–Koster parameters up to $d$–type orbitals in terms of two-center integrals. In this table, we have denoted simply with $(ss\sigma)$ the independent integral $V_{ss\sigma}$, with $(pd\pi)$ the integral $V_{pd\pi}$ and so on.

| | |
|---|---|
| $E_{s,s}$ | $(ss\sigma)$ |
| $E_{s,x}$ | $l(sp\sigma)$ |
| $E_{x,x}$ | $l^2(pp\sigma)+(1-l^2)(pp\pi)$ |
| $E_{x,y}$ | $lm(pp\sigma)-lm(pp\pi)$ |
| $E_{x,z}$ | $ln(pp\sigma)-ln(pp\pi)$ |
| $E_{s,xy}$ | $\sqrt{3}lm(sd\sigma)$ |
| $E_{s,x^2-y^2}$ | $\frac{1}{2}\sqrt{3}(l^2-m^2)(sd\sigma)$ |
| $E_{s,3z^2-r^2}$ | $\left[n^2-\frac{1}{2}(l^2+m^2)\right](sd\sigma)$ |
| $E_{x,xy}$ | $\sqrt{3}l^2m(pd\sigma)+m(1-2l^2)(pd\pi)$ |
| $E_{x,yz}$ | $\sqrt{3}lmn(pd\sigma)-2lmn(pd\pi)$ |
| $E_{x,zx}$ | $\sqrt{3}l^2n(pd\sigma)+n(1-2l^2)(pd\pi)$ |
| $E_{x,x^2-y^2}$ | $\frac{1}{2}\sqrt{3}l(l^2-m^2)(pd\sigma)+l(1-l^2+m^2)(pd\pi)$ |
| $E_{y,x^2-y^2}$ | $\frac{1}{2}\sqrt{3}m(l^2-m^2)(pd\sigma)-m(1+l^2-m^2)(pd\pi)$ |
| $E_{z,x^2-y^2}$ | $\frac{1}{2}\sqrt{3}n(l^2-m^2)(pd\sigma)-n(l^2-m^2)(pd\pi)$ |
| $E_{x,3z^2-r^2}$ | $l\left[n^2-\frac{1}{2}(l^2+m^2)\right](pd\sigma)-\sqrt{3}ln^2(pd\pi)$ |
| $E_{y,3z^2-r^2}$ | $m\left[n^2-\frac{1}{2}(l^2+m^2)\right](pd\sigma)-\sqrt{3}mn^2(pd\pi)$ |
| $E_{z,3z^2-r^2}$ | $n\left[n^2-\frac{1}{2}(l^2+m^2)\right](pd\sigma)+\sqrt{3}n(l^2+m^2)(pd\pi)$ |
| $E_{xy,xy}$ | $3l^2m^2(dd\sigma)+(l^2+m^2-4l^2m^2)(dd\pi)+(n^2+l^2m^2)(dd\delta)$ |
| $E_{xy,yz}$ | $3lm^2n(dd\sigma)+ln(1-4m^2)(dd\pi)+ln(m^2-1)(dd\delta)$ |
| $E_{xy,zx}$ | $3l^2mn(dd\sigma)+mn(1-4l^2)(dd\pi)+mn(l^2-1)(dd\delta)$ |
| $E_{xy,x^2-y^2}$ | $\frac{3}{2}lm(l^2-m^2)(dd\sigma)+2lm(m^2-l^2)(dd\pi)+\frac{1}{2}lm(l^2-m^2)(dd\delta)$ |
| $E_{yz,x^2-y^2}$ | $\frac{3}{2}mn(l^2-m^2)(dd\sigma)-mn\left[1+2(l^2-m^2)\right](dd\pi)+$ $mn\left[1+\frac{1}{2}(l^2-m^2)\right](dd\delta)$ |
| $E_{zx,x^2-y^2}$ | $\frac{3}{2}nl(l^2-m^2)(dd\sigma)+nl\left[1-2(l^2-m^2)\right](dd\pi)-$ $nl\left[1-\frac{1}{2}(l^2-m^2)\right](dd\delta)$ |
| $E_{xy,3z^2-r^2}$ | $\sqrt{3}lm\left[n^2-\frac{1}{2}(l^2+m^2)\right](dd\sigma)-2\sqrt{3}lmn^2(dd\pi)+$ $\frac{1}{2}\sqrt{3}lm(1+n^2)(dd\delta)$ |
| $E_{yz,3z^2-r^2}$ | $\sqrt{3}mn\left[n^2-\frac{1}{2}(l^2+m^2)\right](dd\sigma)+\sqrt{3}mn(l^2+m^2-n^2)(dd\pi)-$ $\frac{1}{2}\sqrt{3}mn(l^2+m^2)(dd\delta)$ |
| $E_{zx,3z^2-r^2}$ | $\sqrt{3}ln\left[n^2-\frac{1}{2}(l^2+m^2)\right](dd\sigma)+\sqrt{3}ln(l^2+m^2-n^2)(dd\pi)-$ $\frac{1}{2}\sqrt{3}ln(l^2+m^2)(dd\delta)$ |
| $E_{x^2-y^2,x^2-y^2}$ | $\frac{3}{4}(l^2-m^2)^2(dd\sigma)+\left[l^2+m^2-(l^2-m^2)^2\right](dd\pi)+$ $\left[n^2+\frac{1}{4}(l^2-m^2)^2\right](dd\delta)$ |
| $E_{x^2-y^2,3z^2-r^2}$ | $\frac{1}{2}\sqrt{3}(l^2-m^2)\left[n^2-\frac{1}{2}(l^2+m^2)\right](dd\sigma)+$ $\sqrt{3}n^2(m^2-l^2)(dd\pi)+\frac{1}{4}\sqrt{3}(1+n^2)(l^2-m^2)(dd\delta)$ |
| $E_{3z^2-r^2,3z^2-r^2}$ | $\left[n^2-\frac{1}{2}(l^2+m^2)\right]^2(dd\sigma)+3n^2(l^2+m^2)(dd\pi)+$ $\frac{3}{4}(l^2+m^2)^2(dd\delta)$ |

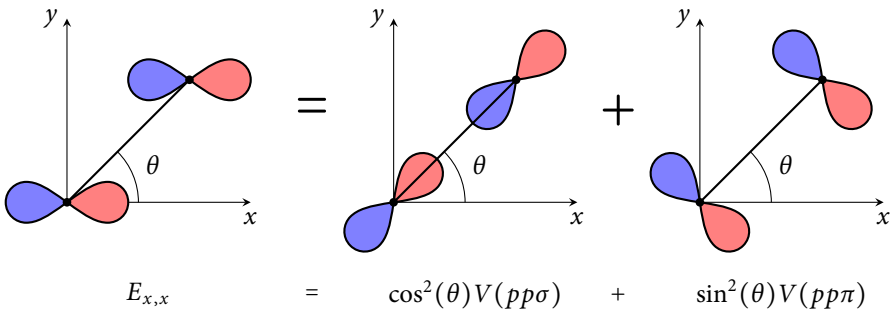


**Figure 1.4** – Graphical example of the interaction between orbitals on different sites. In this case, the interaction between two $p_x$ orbitals is shown and is decomposed into its two contributions $V(pp\sigma)$ and $V(pp\pi)$.

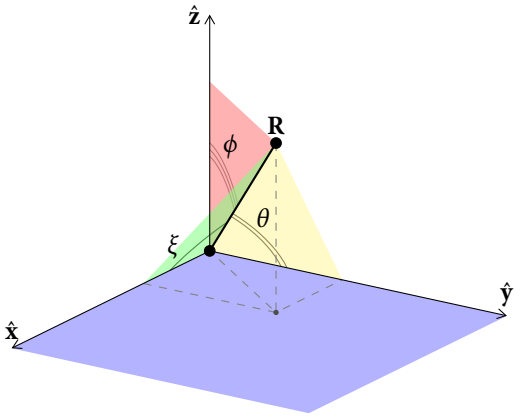


**Figure 1.5** – The director cosines of a given vector **R** with respect to the axis set $(x, y, z)$ are given by the cosines of the angles formed by **R** with the axes. In our notation, we have:
$l = \cos\xi$,
$m = \cos\theta$,
$n = \cos\phi$.

We can now apply these results in our specific case. For the zincblende structure, the director cosines of the vectors joining an anion at $\mathbf{d}_1 = 0$ to its four first neighbors are (see the relations (1.2)):

| | $l$ | $m$ | $n$ |
|---|---|---|---|
| $\mathbf{d}_2$ | $\frac{1}{\sqrt{3}}$ | $\frac{1}{\sqrt{3}}$ | $\frac{1}{\sqrt{3}}$ |
| $\mathbf{d}_2 - \boldsymbol{\tau}_1$ | $\frac{1}{\sqrt{3}}$ | $-\frac{1}{\sqrt{3}}$ | $-\frac{1}{\sqrt{3}}$ |
| $\mathbf{d}_2 - \boldsymbol{\tau}_2$ | $-\frac{1}{\sqrt{3}}$ | $\frac{1}{\sqrt{3}}$ | $-\frac{1}{\sqrt{3}}$ |
| $\mathbf{d}_2 - \boldsymbol{\tau}_3$ | $-\frac{1}{\sqrt{3}}$ | $-\frac{1}{\sqrt{3}}$ | $\frac{1}{\sqrt{3}}$ |

(1.14)

while for a cation at $\mathbf{d}_2$ the four vectors are $-\mathbf{d}_2$, $-(\mathbf{d}_2 - \boldsymbol{\tau}_1)$, $-(\mathbf{d}_2 - \boldsymbol{\tau}_2)$, $-(\mathbf{d}_2 - \boldsymbol{\tau}_3)$, i.e. the opposites of the vectors for an anion. We note here that we are assuming that the atom sitting in the origin is an anion; however, this is only a convention and we could choose to put instead the cation in the origin. The results are the same, because we can go from one description to the other by simply translating the origin of $\mathbf{d}_2$ and performing an inversion of the axes. Using this transformation, the anions take the place of the cations and vice versa.

Using these coefficients, we can express all integrals needed to obtain the Hamiltonian matrix as a function of the Slater–Koster parameters reported in Table 1.2, so that a generic interaction term between an orbital $i$ of the anion $a$, sitting in the origin, and an orbital $j$ of the cation $c$, is of the form

$$\begin{aligned} H_{ij}^{ac}(\mathbf{k}) &= \sum_{\substack{\text{first}\\ \text{neighbors}}} e^{i\mathbf{k}\cdot(\boldsymbol{\tau}_n+\mathbf{d}_2)} \langle \phi_i^a(\mathbf{r})|H|\phi_j^c(\mathbf{r}-\mathbf{d}_2-\boldsymbol{\tau}_n)\rangle = \\ &= \sum_{n=0,1,2,3} e^{i\mathbf{k}\cdot(\mathbf{d}_2-\boldsymbol{\tau}_n)} E_{ij}(\mathbf{d}_2-\boldsymbol{\tau}_n), \end{aligned} \tag{1.15}$$

where we have defined $\boldsymbol{\tau}_0 = (0,0,0)$ and $E_{ij}$ is a Slater–Koster parameter.

We notice, now, that all the integrals between the center atom and the four first neighbors have the same absolute value, and differ only in a sign. We can therefore rewrite Eq. (1.15) as

$$H_{ij}^{ac}(\mathbf{k}) = E_{ij}(\mathbf{d}_2) \sum_{n=0,1,2,3} e^{i\mathbf{k}\cdot(\boldsymbol{\tau}_n+\mathbf{d}_2)} \operatorname{sign}(n),$$

where $\operatorname{sign}(n)$ represents the relative sign of the integral for the atom in position $\mathbf{d}_2 - \boldsymbol{\tau}_n$ and that for the atom in position $\mathbf{d}_2$.

Considering all the possibilities for the relative signs, we obtain that the sum of the exponentials can assume only four different values, called phase factors[1]:

$$g_0 = 4(\cos x \cos y \cos z - i \sin x \sin y \sin z), \tag{1.16a}$$
$$g_1 = 4(-\cos x \sin y \sin z + i \sin x \cos y \cos z), \tag{1.16b}$$
$$g_2 = 4(-\sin x \cos y \sin z + i \cos x \sin y \cos z), \tag{1.16c}$$
$$g_3 = 4(-\sin x \sin y \cos z + i \cos x \cos y \sin z), \tag{1.16d}$$

where we have defined

$$x = \frac{ak_x}{4}, \qquad y = \frac{ak_y}{4}, \qquad z = \frac{ak_z}{4}.$$

Using the above definitions, we can now write the $20 \times 20$ Hamiltonian matrix for a zincblende crystal with two atoms in the primitive cell, in the $sp^3d^5s^*$ basis, as follows:

$$H_{ij} = \left(\begin{array}{c|c} H^{aa} & H^{ac} \\ \hline H^{ca} & H^{cc} \end{array}\right), \tag{1.17}$$

[1]The four phase factors are obtained in the following cases:

$$\begin{aligned} g_0: &\quad \operatorname{sign}(0) = \operatorname{sign}(1) = \operatorname{sign}(2) = \operatorname{sign}(3) = 1, \\ g_1: &\quad \operatorname{sign}(0) = \operatorname{sign}(1) = 1, \quad \operatorname{sign}(2) = \operatorname{sign}(3) = -1, \\ g_2: &\quad \operatorname{sign}(0) = \operatorname{sign}(2) = 1, \quad \operatorname{sign}(1) = \operatorname{sign}(3) = -1, \\ g_3: &\quad \operatorname{sign}(0) = \operatorname{sign}(3) = 1, \quad \operatorname{sign}(1) = \operatorname{sign}(2) = -1. \end{aligned}$$

where $H^{aa}$, $H^{ac}$, $H^{ca}$ and $H^{cc}$ are $10 \times 10$ matrices.

In particular, $H^{aa}$ is the diagonal matrix composed of the atomic eigenvalues corrected by the crystal field contribution; its elements are

$$E_s^a,\ E_p^a,\ E_p^a,\ E_p^a,\ E_d^a,\ E_d^a,\ E_d^a,\ E_d^a,\ E_d^a,\ E_{s^*}^a$$

and analogously $H^{cc}$ for the cation.

We have also that $H^{ca} = (H^{ac})^\dagger$, because the Hamiltonian is Hermitian.

The block $H^{ac}$ contains the interactions between the anion and the cation. Its explicit form is shown in Table 1.3.

Diagonalizing the matrix $H_{ij}(\mathbf{k})$ of Eq. (1.17) we obtain twenty (real) eigenvalues, which are the allowed energies for the electron.

If we plot these energies versus the $\mathbf{k}$ vector, we obtain the bands of the crystal; an example for silicon is reported in Fig. 1.6, where we have also shown the path followed in $\mathbf{k}$ space.

### 1.2.2 Spin–orbit coupling

For a more precise analysis of the electronic states, also relativistic effects should be included. Indeed this contribution, even if often negligible on the conduction bands, produces instead quite important effects especially at the top of the valence bands (which are mainly composed of $p$-type states). The correction due to relativistic effects is more important for heavy elements. For most semiconductors, however, these effects are small and we can limit to first-order perturbation theory: for instance, the separation at $\Gamma$ of the topmost valence bands is only 0.04 eV for silicon ($Z = 14$) and 0.29 eV for germanium ($Z = 32$).

To include these effects, we start from the Dirac relativistic equation

$$\left[c\boldsymbol{\alpha}\cdot\mathbf{p} + \beta mc^2 + V(\mathbf{r})\right]\psi = W\psi.$$

Here $\psi$ is a four-component spinor, $\mathbf{p}$ is the momentum operator $-i\hbar\nabla$, $W = E + mc^2$ is the total energy (including the rest energy $mc^2$) and $\boldsymbol{\alpha}$ and $\beta$ are given by

$$\boldsymbol{\alpha} = \begin{pmatrix} \mathbf{0} & \boldsymbol{\sigma} \\ \boldsymbol{\sigma} & \mathbf{0} \end{pmatrix}, \qquad \beta = \begin{pmatrix} \mathbf{1} & \mathbf{0} \\ \mathbf{0} & -\mathbf{1} \end{pmatrix},$$

where $\mathbf{1}$ is the $2 \times 2$ unit matrix and $\boldsymbol{\sigma}$ are the usual Pauli matrices

$$\sigma_x = \begin{pmatrix} 0 & 1 \\ 1 & 0 \end{pmatrix}, \qquad \sigma_y = \begin{pmatrix} 0 & -i \\ i & 0 \end{pmatrix}, \qquad \sigma_z = \begin{pmatrix} 1 & 0 \\ 0 & -1 \end{pmatrix}. \tag{1.18}$$

Using the Foldy–Wouthuysen transformation [17], we can decouple the strong and weak components of the Dirac spinor. If we consider only the first terms of an expansion in the ratio $\mathbf{p}/mc$, we obtain the following equation for the upper two-component spinor:

$$\left[\frac{\mathbf{p}^2}{2m} + V(\mathbf{r}) - \frac{\mathbf{p}^4}{8m^3c^2} - \frac{\hbar^2}{4m^2c^2}\nabla V\cdot\nabla + \frac{\hbar}{4m^2c^2}\boldsymbol{\sigma}\cdot(\nabla\mathbf{V}\times\mathbf{p})\right]\psi = E\psi.$$

**Table 1.3** – $H^{ac}$ matrix which describes the interaction between an anion in the origin and a cation in $\mathbf{d}_2$. We have denoted simply with $x^2$ the $x^2-y^2$ $d-$type orbital. If we are dealing with a group III-V semiconductor, the elements denoted with a tilde are to be defined with the first orbital centered on a cation and the second on an anion, i.e. we have to use, for instance, $V(s_c p_a \sigma)$ instead of $V(s_a p_c \sigma)$ (for those without tilde, the first center is instead on an anion). The order of the basis is that reported in Eq. (1.10), i.e. $s$, $p_x$, $p_y$, $p_z$, $d_{xy}$, $d_{xz}$, $d_{yz}$, $d_{x^2-y^2}$, $d_{3z^2-r^2}$, $s^*$ for each atom in the primitive cell.

$$
\begin{pmatrix}
g_0E_{s,s} & g_1E_{s,x} & g_2E_{s,x} & g_3E_{s,x} & g_3E_{s,xy} & g_2E_{s,xy} & g_1E_{s,xy} & 0 & 0 & g_0E_{s,s^*} \\
-g_1\tilde{E}_{s,x} & g_0E_{x,x} & g_3E_{x,y} & g_2E_{x,y} & g_2E_{x,xy} & g_3E_{x,xy} & g_0E_{x,yz} & g_1E_{x,x^2} & -\frac{g_1}{\sqrt{3}}E_{x,x^2} & -g_1\tilde{E}_{s^*,x} \\
-g_2\tilde{E}_{s,x} & g_3E_{x,y} & g_0E_{x,x} & g_1E_{x,y} & g_1E_{x,xy} & g_0E_{x,yz} & g_3E_{x,xy} & -g_2E_{x,x^2} & -\frac{g_2}{\sqrt{3}}E_{x,x^2} & -g_2\tilde{E}_{s^*,x} \\
-g_3\tilde{E}_{s,x} & g_2E_{x,y} & g_1E_{x,y} & g_0E_{x,x} & g_0E_{x,yz} & g_1E_{x,xy} & g_2E_{x,xy} & 0 & 2\frac{g_3}{\sqrt{3}}E_{x,x^2} & -g_3\tilde{E}_{s^*,x} \\
g_3\tilde{E}_{s,xy} & -g_2\tilde{E}_{x,xy} & -g_1\tilde{E}_{x,xy} & -g_0\tilde{E}_{x,yz} & g_0E_{xy,xy} & g_1E_{xy,xz} & g_2E_{xy,xz} & 0 & -2\frac{g_3}{\sqrt{3}}E_{xz,x^2} & g_3\tilde{E}_{s^*,xy} \\
g_2\tilde{E}_{s,xy} & -g_3\tilde{E}_{x,xy} & -g_0\tilde{E}_{x,yz} & -g_1\tilde{E}_{x,xy} & g_1E_{xy,xz} & g_0E_{xy,xy} & g_3E_{xy,xz} & g_2E_{xz,x^2} & \frac{g_2}{\sqrt{3}}E_{xz,x^2} & g_2\tilde{E}_{s^*,xy} \\
g_1\tilde{E}_{s,xy} & -g_0\tilde{E}_{x,yz} & -g_3\tilde{E}_{x,xy} & -g_2\tilde{E}_{x,xy} & g_2E_{xy,xz} & g_3E_{xy,xz} & g_0E_{xy,xy} & -g_1E_{xz,x^2} & \frac{g_1}{\sqrt{3}}E_{xz,x^2} & g_1\tilde{E}_{s^*,xy} \\
0 & -g_1\tilde{E}_{x,x^2} & g_2\tilde{E}_{x,x^2} & 0 & 0 & g_2E_{xz,x^2} & -g_1E_{xz,x^2} & g_0E_{x^2,x^2} & 0 & 0 \\
0 & \frac{g_1}{\sqrt{3}}\tilde{E}_{x,x^2} & \frac{g_2}{\sqrt{3}}\tilde{E}_{x,x^2} & -2\frac{g_3}{\sqrt{3}}\tilde{E}_{x,x^2} & -2\frac{g_3}{\sqrt{3}}E_{xz,x^2} & \frac{g_2}{\sqrt{3}}E_{xz,x^2} & \frac{g_1}{\sqrt{3}}E_{xz,x^2} & 0 & g_0E_{x^2,x^2} & 0 \\
g_0\tilde{E}_{s,s^*} & g_1E_{s^*,x} & g_2E_{s^*,x} & g_3E_{s^*,x} & g_3E_{s^*,xy} & g_2E_{s^*,xy} & g_1E_{s^*,xy} & 0 & 0 & g_0E_{s^*,s^*}
\end{pmatrix}
$$

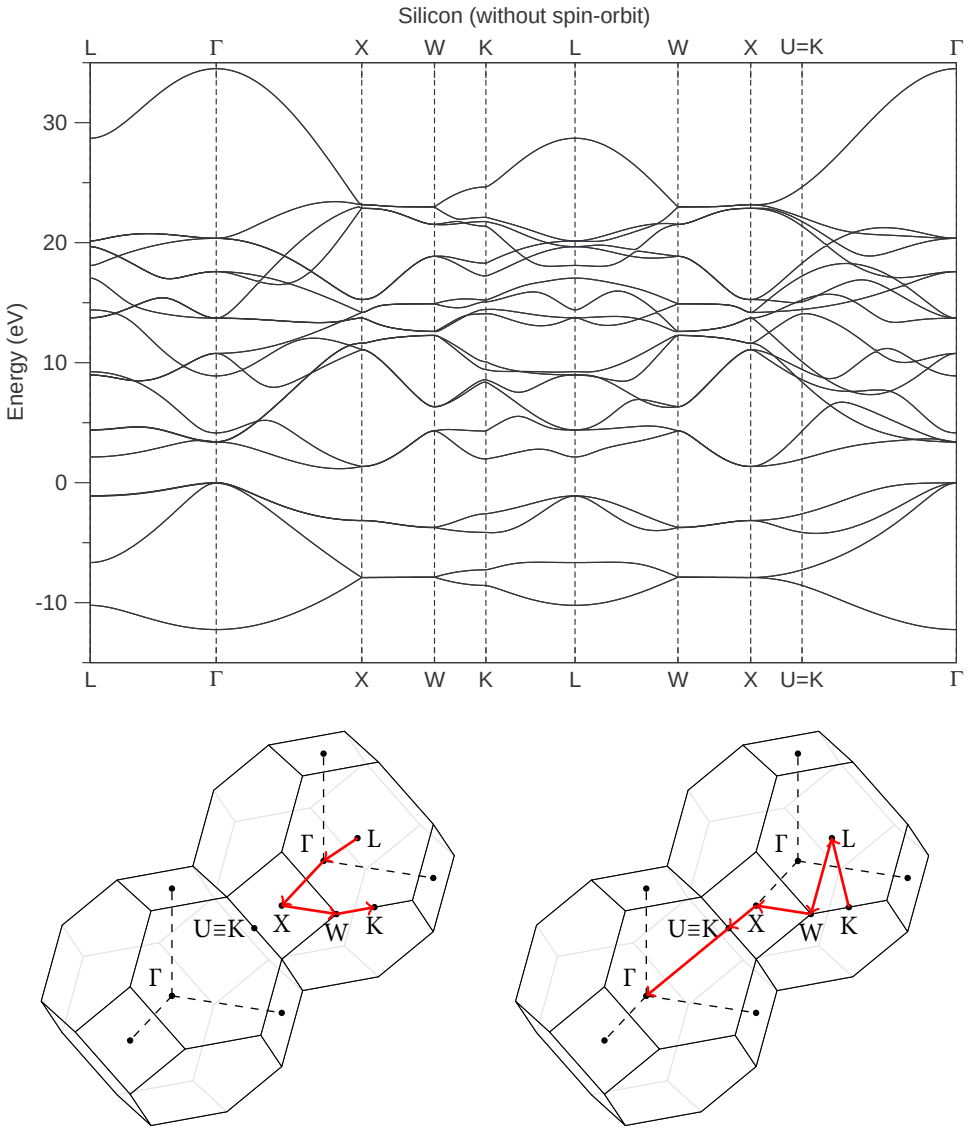


**Figure 1.6** – Band structure of silicon (without the introduction of spin–orbit interactions), using the parametrization of Jancu *et al.* [16]. The path followed in **k** space is also shown (it is split in two parts only for graphical reasons).

The first two terms on the left-hand side are the non-relativistic Hamiltonian. The three following terms

$$\mathcal{H}_v = -\frac{\mathbf{p}^4}{8m^3c^2}, \qquad \mathcal{H}_d = -\frac{\hbar^2}{4m^2c^2}\nabla V \cdot \nabla, \qquad \mathcal{H}_{\text{so}} = \frac{\hbar}{4m^2c^2}\boldsymbol{\sigma} \cdot (\nabla \mathbf{V} \times \mathbf{p}) \quad (1.19)$$

are the first-order relativistic corrections to the Schrödinger Hamiltonian. The first term $\mathcal{H}_v$ is the relativistic correction to the kinetic energy, as can be seen expanding the relativistic expression of the kinetic energy

$$\sqrt{c^2\mathbf{p}^2 + m^2c^4} = mc^2 + \frac{\mathbf{p}^2}{2m} - \frac{\mathbf{p}^4}{8m^3c^2} + \cdots$$

The second term $\mathcal{H}_d$ is a correction to the potential $V(\mathbf{r})$ and is known as the Darwin term. Finally, the third term $\mathcal{H}_{\text{so}}$ is the spin–orbit coupling and can be interpreted as the interaction between the spin magnetic moment of the electron and the magnetic field felt by the electron (originated from the Coulomb potential of the nucleus). This term can be understood also in a classical analysis [18], even if it leads to a wrong prefactor of two.

The terms $\mathcal{H}_v$ and $\mathcal{H}_d$ do not depend on the spin of the electron and do not change the symmetry properties of the non-relativistic Hamiltonian. Thus, they are not explicitly considered in a semiempirical tight-binding approximation. Indeed, $\mathcal{H}_v$ gives a negative expectation value on any electronic state; we expect a smooth deformation of the bands, but the degeneracy of the states remains unchanged. $\mathcal{H}_d$ gives instead a correction that depends strongly on the angular momentum, and is important only for $s$ states. Also in this case, no additional splitting is introduced; the only effect can be the inversion of the order of some levels. Both these effects, however, are automatically included when we fit the two-center integrals to the actual band structure of the crystal, so that we do not need to explicitly consider them.

The spin–orbit term couples instead real-space operators with spin-space operators: the symmetry is thus reduced and, when we classify the states with the irreducible representations of the symmetry group of the Hamiltonian, different groups must be considered. The simple group is used when spin–orbit interactions are discarded, while the corresponding double group is used when these effects are included. A detailed description of these groups and of how the states of the simple group split into the states of the double group is reported in Ref. [19].

For a spherically-symmetric potential $V_a(r)$, we can write the spin–orbit term of Eq. (1.19) as

$$\mathcal{H}_{\text{so}} = \frac{\hbar}{4m^2c^2}\frac{1}{r}\frac{\mathrm{d}V_a(r)}{\mathrm{d}r}\boldsymbol{\sigma} \cdot \mathbf{L},$$

where we have used the definition $\mathbf{L} = \mathbf{r} \times \mathbf{p}$ of the angular momentum operator. For this Hamiltonian, $m$ and $s_z$ are no more good quantum numbers, and the $2(2l+1)$ degeneracy of each state with angular momentum $l$ is lifted, originating a state with total angular momentum $j = l + \frac{1}{2}$ and degeneracy $2l + 2$, and a state with $j = l - \frac{1}{2}$ and degeneracy $2l$ (except for $s$ states, that do not split). In the case of a crystal, if

the crystal potential is approximated by sums of spherical potentials, the spin-orbit term can be written as

$$\mathcal{H}_{\mathrm{so}} = \frac{\hbar}{4m^2c^2}\sum_{\boldsymbol{\tau}_n}\sum_{\mathbf{d}_\nu}\frac{1}{|\mathbf{r}-\mathbf{d}_\nu-\boldsymbol{\tau}_n|}\frac{\mathrm{d}V_\nu(\mathbf{r}-\mathbf{d}_\nu-\boldsymbol{\tau}_n)}{\mathrm{d}(\mathbf{r}-\mathbf{d}_\nu-\boldsymbol{\tau}_n)}\boldsymbol{\sigma}\cdot\mathbf{L}(\mathbf{r}-\mathbf{d}_\nu-\boldsymbol{\tau}_n). \tag{1.20}$$

For the inclusion of spin–orbit, we must consider different orbitals for spin-up and spin-down electrons and the Bloch sums derived from these orbitals, since the degeneracy on $s_z$ is now removed. Moreover, this is important only near the nuclei, where $\mathrm{d}V_\nu(\mathbf{r})/\mathrm{d}\mathbf{r}$ is strong, thus only on-site integrals among degenerate Bloch sums are important and are considered in a first-order approximation. Using Eq. (1.20), one can easily compute matrix elements between states with same angular momentum $l$, but different $m$ and spin.

If we are interested in a semiempirical approach, however, we can simply assume that on each site the spin–orbit interaction term is of the form

$$h_{\mathrm{so}} = \alpha\mathbf{L}\cdot\mathbf{S}, \tag{1.21}$$

where $\mathbf{L}$ is the orbital angular momentum operator, $\mathbf{S} = \frac{1}{2}\hbar\boldsymbol{\sigma}$ is the spin angular momentum operator and $\boldsymbol{\sigma}$ are the Pauli matrices given in (1.18).

Here $\alpha$ is a new fitting parameter that is adapted to reproduce the experimental splittings, and can be considered as a constant. We consider the effect of spin–orbit only on $p$–type states, mainly because all the parametrizations that we adopt involve spin–orbitals only for $p$–states, since the effects are smaller for $d$–type states. As already pointed out at the beginning of this Section, we treat spin–orbit interaction in a perturbative approach, writing

$$\mathcal{H} = \mathcal{H}_{\mathrm{tb}} + \mathcal{H}_{\mathrm{so}},$$

where $\mathcal{H}_{\mathrm{tb}}$ is the tight-binding Hamiltonian described in the previous Section.

To evaluate the energy contribution of this perturbation, we introduce the total angular momentum $\mathbf{J} = \mathbf{L} + \mathbf{S}$ so that

$$\mathbf{J}^2 = (\mathbf{L}+\mathbf{S})^2 = \mathbf{L}^2 + \mathbf{S}^2 + 2\mathbf{L}\cdot\mathbf{S}$$

and from this Equation we obtain that the expectation value of the $\mathbf{L}\cdot\mathbf{S}$ operator is

$$\langle\mathbf{L}\cdot\mathbf{S}\rangle = \frac{1}{2}\langle\mathbf{J}^2 - \mathbf{L}^2 - \mathbf{S}^2\rangle = \frac{\hbar^2}{2}[j(j+1) - l(l+1) - s(s+1)], \tag{1.22}$$

where $j$, $l$ and $s$ are the quantum numbers of the operators $\mathbf{J}^2$, $\mathbf{L}^2$ and $\mathbf{S}^2$, respectively.

The new basis set of states includes both spin-up and spin-down states so that we now consider 20 orbitals for each atom in the unit cell, namely:

$$\begin{aligned} &s^{\uparrow}, \quad p_x^{\uparrow}, p_y^{\uparrow}, p_z^{\uparrow}, \quad d_{xy}^{\uparrow}, d_{xz}^{\uparrow}, d_{yz}^{\uparrow}, d_{x^2-y^2}^{\uparrow}, d_{3z^2-r^2}^{\uparrow}, \quad s^{*\uparrow}, \\ &s^{\downarrow}, \quad p_x^{\downarrow}, p_y^{\downarrow}, p_z^{\downarrow}, \quad d_{xy}^{\downarrow}, d_{xz}^{\downarrow}, d_{yz}^{\downarrow}, d_{x^2-y^2}^{\downarrow}, d_{3z^2-r^2}^{\downarrow}, \quad s^{*\downarrow}, \end{aligned}$$

where the arrows indicate spin-up and spin-down states.

In order to exploit Eq. (1.22), we need to express $p$ states as functions of $\Phi_{j,j_z}$, i.e. of eigenstates of the total angular momentum or, more precisely, of $\mathbf{J}^2$ and $J_z$:

$$\mathbf{J}^2\Phi_{j,j_z} = \hbar^2 j(j+1)\Phi_{j,j_z}$$
$$J_z\Phi_{j,j_z} = \hbar j_z\Phi_{j,j_z}$$

For this aim we first express the $p_x$, $p_y$ and $p_z$ states in terms of the spherical harmonics $Y_{lm}$:

$$p_x = \frac{1}{\sqrt{2}}(Y_{1,-1} - Y_{1,1}),$$
$$p_y = \frac{i}{\sqrt{2}}(Y_{1,-1} + Y_{1,1}),$$
$$p_z = Y_{1,0}.$$

We now use the Clebsch–Gordan coefficients to decompose these states (multiplied by their spin part) in terms of $\Phi_{j,j_z}$. We obtain[2]

$$\Phi_{3/2,3/2} = Y^{\uparrow}_{1,1} = \frac{1}{\sqrt{2}}(p^{\uparrow}_x + ip^{\uparrow}_y) \tag{1.23a}$$

$$\Phi_{3/2,1/2} = \frac{1}{\sqrt{3}}Y^{\downarrow}_{1,1} + \frac{\sqrt{2}}{\sqrt{3}}Y^{\uparrow}_{1,0} = -\frac{1}{\sqrt{6}}[(p^{\downarrow}_x + ip^{\downarrow}_y) - 2p^{\uparrow}_z] \tag{1.23b}$$

$$\Phi_{3/2,-1/2} = \frac{\sqrt{2}}{\sqrt{3}}Y^{\downarrow}_{1,0} + \frac{1}{\sqrt{3}}Y^{\uparrow}_{1,-1} = \frac{1}{\sqrt{6}}[(p^{\uparrow}_x - ip^{\uparrow}_y) + 2p^{\downarrow}_z] \tag{1.23c}$$

$$\Phi_{3/2,-3/2} = Y^{\downarrow}_{1,-1} = \frac{1}{\sqrt{2}}(p^{\downarrow}_x - ip^{\downarrow}_y) \tag{1.23d}$$

$$\Phi_{1/2,1/2} = -\frac{1}{\sqrt{3}}Y^{\uparrow}_{1,0} + \frac{\sqrt{2}}{\sqrt{3}}Y^{\downarrow}_{1,1} = -\frac{1}{\sqrt{3}}[(p^{\downarrow}_x + ip^{\downarrow}_y) + p^{\uparrow}_z] \tag{1.23e}$$

$$\Phi_{1/2,-1/2} = -\frac{\sqrt{2}}{\sqrt{3}}Y^{\uparrow}_{1,-1} + \frac{1}{\sqrt{3}}Y^{\downarrow}_{1,0} = -\frac{1}{\sqrt{3}}[(p^{\uparrow}_x - ip^{\uparrow}_y) - p^{\downarrow}_z] \tag{1.23f}$$

Inverting these relations, we obtain the expressions of our states in terms of the total angular momentum eigenstates:

$$p^{\uparrow}_x = \frac{1}{\sqrt{2}}\left[-\Phi_{3/2,3/2} + \frac{1}{\sqrt{3}}\Phi_{3/2,-1/2} - \frac{\sqrt{2}}{\sqrt{3}}\Phi_{1/2,-1/2}\right] \tag{1.24a}$$

$$p^{\downarrow}_x = \frac{1}{\sqrt{2}}\left[-\frac{1}{\sqrt{3}}\Phi_{3/2,1/2} - \frac{\sqrt{2}}{\sqrt{3}}\Phi_{1/2,1/2} + \Phi_{3/2,-3/2}\right] \tag{1.24b}$$

$$p^{\uparrow}_y = \frac{i}{\sqrt{2}}\left[\Phi_{3/2,3/2} + \frac{1}{\sqrt{3}}\Phi_{3/2,-1/2} - \frac{\sqrt{2}}{\sqrt{3}}\Phi_{1/2,-1/2}\right] \tag{1.24c}$$

$$p^{\downarrow}_y = \frac{i}{\sqrt{2}}\left[\frac{1}{\sqrt{3}}\Phi_{3/2,1/2} + \frac{\sqrt{2}}{\sqrt{3}}\Phi_{1/2,1/2} + \Phi_{3/2,-3/2}\right] \tag{1.24d}$$

[2] As an overall phase for the states has no physical effects, we could have chosen different Clebsch-Gordan coefficients. Another phase convention which is often used is that of Luttinger [20].

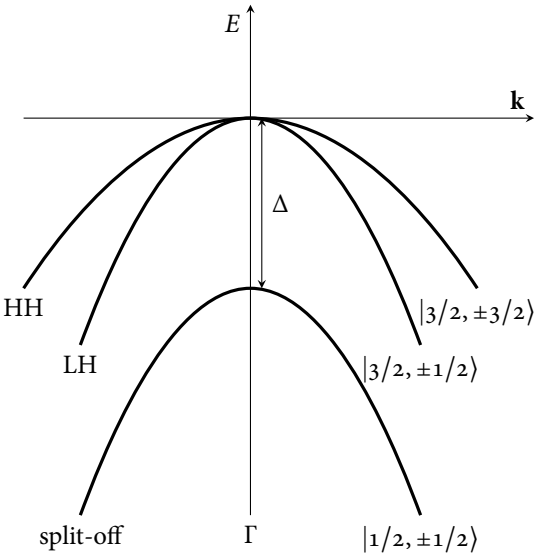


**Figure 1.7** – As a consequence of spin–orbit coupling, the degeneracy of the bands of zincblende or diamond semiconductors is lifted at Γ. The heavy hole (HH) and light hole (LH) states (with $j = 3/2$) remain degenerate at the zone center, while the split-off state (with $j = 1/2$) shifts down in energy. $\Delta$ represents the experimental splitting at Γ.

$$p_z^{\uparrow} = \frac{\sqrt{2}}{\sqrt{3}}\Phi_{3/2,1/2} - \frac{1}{\sqrt{3}}\Phi_{1/2,1/2} \tag{1.24e}$$

$$p_z^{\downarrow} = \frac{\sqrt{2}}{\sqrt{3}}\Phi_{3/2,-1/2} + \frac{1}{\sqrt{3}}\Phi_{1/2,-1/2} \tag{1.24f}$$

At this point, the evaluation of the matrix elements of $\mathcal{H}_{\text{so}}$ between these states becomes straightforward. In Eq. (1.22) we have $l = 1$ and $s = 1/2$ because we are considering $p$–type orbitals; $j$ is obtained from the expansions (1.23) and (1.24). We also use the fact that the eigenstates $\Phi_{j,j_z}$ are orthogonal and we finally obtain

$$\begin{aligned}
\langle p_x^{\uparrow}|\mathcal{H}_{\text{so}}|p_y^{\uparrow}\rangle &= -i\lambda,\\
\langle p_x^{\uparrow}|\mathcal{H}_{\text{so}}|p_z^{\downarrow}\rangle &= \lambda,\\
\langle p_y^{\uparrow}|\mathcal{H}_{\text{so}}|p_z^{\downarrow}\rangle &= -i\lambda,\\
\langle p_x^{\downarrow}|\mathcal{H}_{\text{so}}|p_y^{\downarrow}\rangle &= i\lambda,\\
\langle p_x^{\downarrow}|\mathcal{H}_{\text{so}}|p_z^{\uparrow}\rangle &= -\lambda,\\
\langle p_y^{\downarrow}|\mathcal{H}_{\text{so}}|p_z^{\uparrow}\rangle &= -i\lambda,
\end{aligned} \tag{1.25}$$

where $\lambda$ is the spin–orbit parameter which is provided by the parametrization, and is related to the parameter $\alpha$ of Eq. (1.21) by $\lambda = \alpha\hbar^2/2$.

The splitting of the states is easy to understand in the basis of $\Phi_{j,j_z}$, where we immediately see from Eq. (1.22) that the expectation value of the quadruplet with $j = 3/2$ and the doublet with $j = 1/2$ is different. We thus have four degenerate bands at the zone center and two bands at a lower energy, called the split-off state, as schematically represented in Fig. 1.7. From Eq. (1.22) one also obtains that $\Delta$, i.e. the splitting at Γ between the HH, LH states and the SO state, should be equal to $3\lambda$. Note

however that this is true only if the parametrization does not include $d$ orbitals. If the parametrization includes them, as in the case of the $sp^3d^5s^*$ parametrizations used in this Thesis, the value of the spin-orbit parameter $\lambda$ is not given by one third of the experimental splitting $\Delta$, even if we do not include spin-orbit interaction between $d$ orbitals (as it is the case in all parametrizations used in this Thesis). This discrepancy is due to the fact that valence states have non-zero components for the $d$ orbitals.

If we analyze the bands also for $\mathbf{k}$ values slightly different from zero, we see moreover that the four bands at the zone center have different curvatures, i.e. different effective masses, and are known as the light hole (LH) and heavy hole (HH) states. In particular, the heavy hole states are those with $|j_z| = 3/2$ ($\Phi_{3/2,3/2}$ and $\Phi_{3/2,-3/2}$), while the light hole states are those with $|j_z| = 1/2$ ($\Phi_{3/2,1/2}$ and $\Phi_{3/2,-1/2}$).

Using the results given in Eq. (1.25), we can now write the general form of the Hamiltonian matrix, which is of size $40 \times 40$. Its form is the following:

$$H_{ij} = \left(\begin{array}{cc|cc} H^{aa}_{\uparrow\uparrow} & H^{aa}_{\uparrow\downarrow} & H^{ac} & 0 \\ H^{aa}_{\downarrow\uparrow} & H^{aa}_{\downarrow\downarrow} & 0 & H^{ac} \\ \hline H^{ca} & 0 & H^{cc}_{\uparrow\uparrow} & H^{cc}_{\uparrow\downarrow} \\ 0 & H^{ca} & H^{cc}_{\downarrow\uparrow} & H^{cc}_{\downarrow\downarrow} \end{array}\right),$$

where $H^{ac}$ and $H^{ca}$ are the same $10 \times 10$ blocks of Eq. (1.17) and Table 1.3, while the $20 \times 20$ diagonal blocks contain also spin–orbit interaction terms and are reported in Table 1.4.

To conclude this Section, we note that the states at points of high symmetry of the Brillouin zone are denoted with different symbols in the literature, depending on whether we use the nomenclature of the simple group (i.e., we neglect spin–orbit effects, as it is usually done for silicon) or the nomenclature of the double group, including spin–orbit splittings. A detailed study of the state symmetries and of the simple and double groups can be found in [19, 21].

To make this clear, we show in Fig. 1.8 the names of some important states for silicon and germanium.

## 1.3 Strain

Up to now we have considered perfect Si/Ge crystals with diamond structure. We examine now small deviations from this arrangement. This is important e.g. for the analysis of the effect of a mechanical pressure on the materials, but in particular for the study of heterostructures strained due to the coherent growth in the epitaxial deposition process. Indeed, at the interface between two different materials, if the mismatch of the two lattice constants is not too large, the overlayer can grow (at least for small thicknesses of the grown material) matching its lattice constant to the one of the substrate. The lattice structure is therefore slightly distorted and we need to consider the consequences of this for a quantitative analysis of the electronic and optical properties of the heterostructure. The resulting effects are in many cases not negligible, also because the symmetry of the states will in general change, and this

**Table 1.4** – 20 × 20 on-site matrix of an anion, including spin–orbit coupling. The framed elements are actually 5 × 5 diagonal blocks. Elements that are not indicated are zero. A similar matrix is obtained for the self-interaction of cations. Notice that, in a semiempirical approach, there are two different spin-orbit coupling parameters $\lambda_a$ and $\lambda_c$, one for the anions and one for the cations.

$$
\begin{pmatrix} H^{aa}_{\uparrow\uparrow} & H^{aa}_{\uparrow\downarrow} \\ H^{aa}_{\downarrow\uparrow} & H^{aa}_{\downarrow\downarrow} \end{pmatrix} =
\left(\begin{array}{ccccc|ccccc}
E^a_s & & & & & 0 & & & & \\
 & E^a_p & -i\lambda & & & & 0 & & \lambda & \\
 & i\lambda & E^a_p & & & & & 0 & -i\lambda & \\
 & & & E^a_p & & & -\lambda & i\lambda & 0 & \\
 & & & & \boxed{E^a_d} & & & & & \boxed{0} \\
 & & & & & E^a_{s*} & & & & 0 \\
\hline
0 & & & & & E^a_s & & & & \\
 & 0 & & -\lambda & & & E^a_p & i\lambda & & \\
 & & 0 & -i\lambda & & & -i\lambda & E^a_p & & \\
 & \lambda & i\lambda & 0 & & & & & E^a_p & \\
 & & & & \boxed{0} & & & & & \boxed{E^a_d} \\
 & & & & & 0 & & & & E^a_{s*}
\end{array}\right)
$$

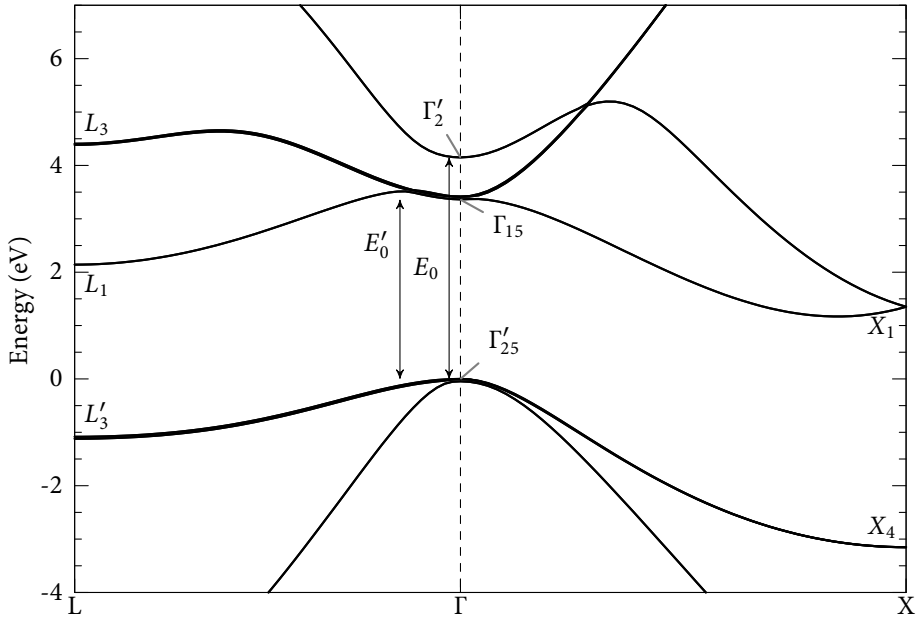


**(a)** Silicon, using the nomenclature of the simple group.

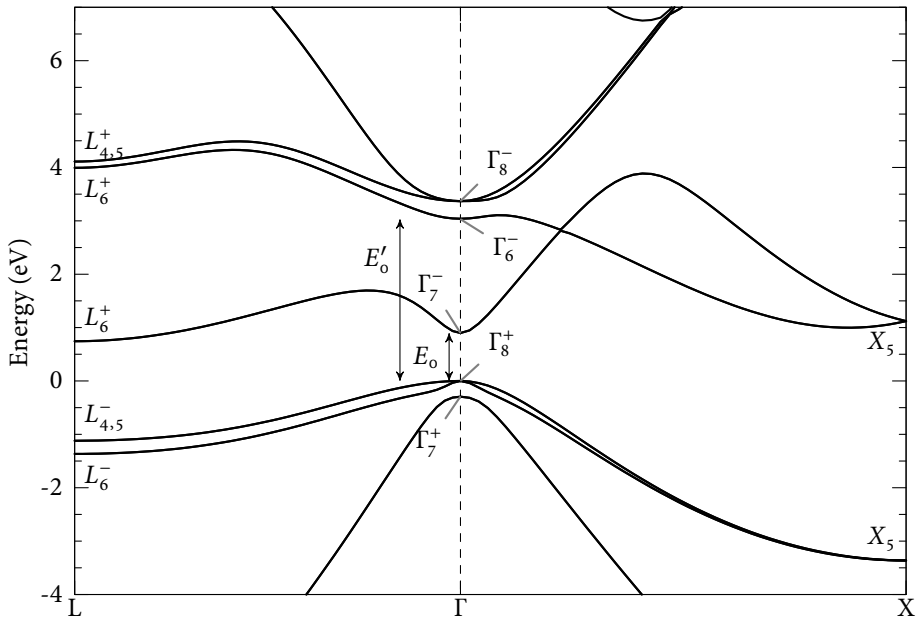


**(b)** Germanium, using the nomenclature of the double group.

**Figure 1.8** – Band structure of silicon and germanium crystals. In the case of silicon, we have used the simple group notation, widely used in the literature since the spin–orbit coupling effects are often discarded for silicon. A table of the decomposition of the states of the simple group into the states of the double group is provided in Ref. [19, 21]; we report here only some interesting cases: $\Gamma'_{25} \to \Gamma^+_7 + \Gamma^+_8$; $\Gamma'_2 \to \Gamma^-_7$, $\Gamma_{15} \to \Gamma^-_6 + \Gamma^-_8$, $X_1 \to X_5$, $X_4 \to X_5$, $L'_3 \to L^-_4 + L^-_5 + L^-_6$, $L_3 \to L^+_4 + L^+_5 + L^+_6$, $L_1 \to L^+_6$. Notice that the ordering of the $\Gamma'_2$ and $\Gamma_{15}$ states in germanium is opposite to that of silicon.

can affect in a substantial way the optical and transport properties of the system. We stress moreover that these strain effects are always present in SiGe heterostructures, since silicon and germanium have a quite large mismatch of $\approx 4\%$ of their lattice constants (see Table 1.1). Thus, every (coherently grown) heterostructure composed of silicon and germanium, or more in general of two $Si_{1-x}Ge_x$ alloys with different Ge content $x$, has at least a strained region.

We start with a short summary of the main definitions and results of the theory of elastic strains; we then focus on the analysis of the deformations in the case of epitaxial deposition of lattice mismatched crystals.

We start considering an orthonormal tern of vectors $(\hat{\mathbf{x}}, \hat{\mathbf{y}}, \hat{\mathbf{z}})$ which describes the unstrained structure of the crystal: after fixing an arbitrary origin, a generic atom of the crystal structure can be identified by a vector $\mathbf{r}$, which can be expressed as a linear combination of the three unit vectors: $\mathbf{r} = x\hat{\mathbf{x}} + y\hat{\mathbf{y}} + z\hat{\mathbf{z}}$.

If an uniform strain is applied, such that each primitive cell is deformed in the same way, the whole structure changes its shape and also the three vectors $\hat{\mathbf{x}}$, $\hat{\mathbf{y}}$ and $\hat{\mathbf{z}}$ change to three new vectors $\tilde{\mathbf{x}}$, $\tilde{\mathbf{y}}$, $\tilde{\mathbf{z}}$. This deformation can be described with the following equations:

$$\tilde{\mathbf{x}} = (1 + \varepsilon_{xx})\hat{\mathbf{x}} + \varepsilon_{xy}\hat{\mathbf{y}} + \varepsilon_{xz}\hat{\mathbf{z}} \tag{1.26a}$$

$$\tilde{\mathbf{y}} = \varepsilon_{yx}\hat{\mathbf{x}} + (1 + \varepsilon_{yy})\hat{\mathbf{y}} + \varepsilon_{yz}\hat{\mathbf{z}} \tag{1.26b}$$

$$\tilde{\mathbf{z}} = \varepsilon_{zx}\hat{\mathbf{x}} + \varepsilon_{zy}\hat{\mathbf{y}} + (1 + \varepsilon_{zz})\hat{\mathbf{z}}, \tag{1.26c}$$

so that the atom at $\mathbf{r}$, is now at the position

$$\tilde{\mathbf{r}} = x\tilde{\mathbf{x}} + y\tilde{\mathbf{y}} + z\tilde{\mathbf{z}}$$

with the same coefficients $x$, $y$, and $z$ because of the definitions (1.26). In general the new vectors $\tilde{\mathbf{x}}$, $\tilde{\mathbf{y}}$, $\tilde{\mathbf{z}}$ are however no more orthogonal, nor are of unit length.

The displacement $\mathbf{R}$ of the atom which was at $\mathbf{r}$ can be written as

$$\begin{aligned}\mathbf{R} = \tilde{\mathbf{r}} - \mathbf{r} &= x(\hat{\mathbf{x}} - \tilde{\mathbf{x}}) + y(\hat{\mathbf{y}} - \tilde{\mathbf{y}}) + z(\hat{\mathbf{z}} - \tilde{\mathbf{z}}) = \\ &= u(\mathbf{r})\hat{\mathbf{x}} + v(\mathbf{r})\hat{\mathbf{y}} + w(\mathbf{r})\hat{\mathbf{z}},\end{aligned}$$

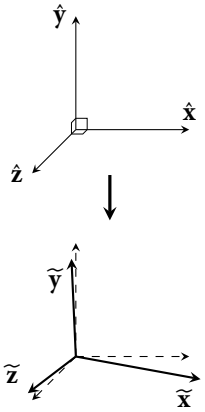


where we have defined the three quantities $u$, $v$, $w$ as

$$u(\mathbf{r}) = x\varepsilon_{xx} + y\varepsilon_{yx} + z\varepsilon_{zx} \tag{1.27a}$$

$$v(\mathbf{r}) = x\varepsilon_{xy} + y\varepsilon_{yy} + z\varepsilon_{zy} \tag{1.27b}$$

$$w(\mathbf{r}) = x\varepsilon_{xz} + y\varepsilon_{yz} + z\varepsilon_{zz}. \tag{1.27c}$$

In the following, we assume that the deformation is small, that is, every coefficient $\varepsilon_{ij}$ is much smaller than one, so that we can always expand the above expressions to first order in the coefficients $\varepsilon_{ij}$ and ignore higher-order terms.

For a non-uniform deformation, the tensor $\varepsilon_{ij}$ is not constant throughout the whole crystal, but it depends on the point $\mathbf{r}$. Taking the origin of the axes near the point $\mathbf{r}$ that we are interested in (that is, inside a small region in which the deformation is roughly uniform in space), we can expand the displacement $\mathbf{R}$ around $\mathbf{R}(0) = 0$, obtaining the definition for the coefficients $\varepsilon_{ij}$ in the non-uniform case:

$$\varepsilon_{xx} \approx \frac{\partial u}{\partial x}; \qquad \varepsilon_{yx} \approx \frac{\partial u}{\partial y}; \qquad \varepsilon_{zy} \approx \frac{\partial v}{\partial z}; \qquad \dots$$

Now, noticing that the $\varepsilon_{ij}$ matrix can be written in matrix form as the gradient of the displacement $\mathbf{R}$:

$$\varepsilon_{ij} = \nabla \mathbf{R} = \begin{pmatrix} \frac{\partial u}{\partial x} & \frac{\partial v}{\partial x} & \frac{\partial w}{\partial x} \\ \frac{\partial u}{\partial y} & \frac{\partial v}{\partial y} & \frac{\partial w}{\partial y} \\ \frac{\partial u}{\partial z} & \frac{\partial v}{\partial z} & \frac{\partial w}{\partial z} \end{pmatrix},$$

we see at glance that $\varepsilon_{ij}$ actually transforms as a tensor under rotations; it is called the strain tensor. Finally, it can be easily proven that the transformation from $\varepsilon_{ij}$ to its symmetric part, leaving unchanged both the length of the vectors and the angles between them, is simply a rotation, so that we always assume in the following that the $\varepsilon_{ij}$ tensor is symmetric.

### 1.3.1 Relation between strains and stresses

We want now to study the forces, or stresses, which are exerted on a unit area of the crystal. These forces are responsible for the strain of the structure, and in this Section we study the relation between strains and stresses.

Given a surface orthogonal to, say, the $z$ direction, we can decompose the force acting on it in its three components along the axes (see Fig. 1.9a): we denote these components as $\sigma_{xz}$, $\sigma_{yz}$ and $\sigma_{zz}$. If we do the same with surfaces orthogonal to the $x$ and $y$ directions, we end up with the $3 \times 3$ stress tensor:

$$\sigma_{ij} = \begin{pmatrix} \sigma_{xx} & \sigma_{xy} & \sigma_{xz} \\ \sigma_{yx} & \sigma_{yy} & \sigma_{yz} \\ \sigma_{zx} & \sigma_{zy} & \sigma_{zz} \end{pmatrix}.$$

With the notation introduced, the first letter of the subscript is the direction of the force, while the second one is the direction of the normal to the plane on which the force is acting. However, we do not need to worry about this, because this tensor is actually symmetric if we require that there is no torque applied to an elementary cube of the system, so that there is no angular acceleration due to the internal forces. This is graphically shown in Fig. 1.9b.

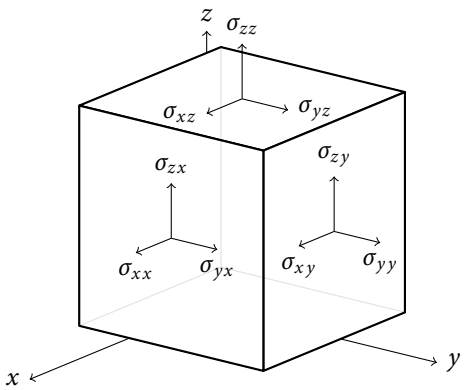


**(a)** Graphical representation of the stress components acting on the surfaces of an infinitesimal cube.

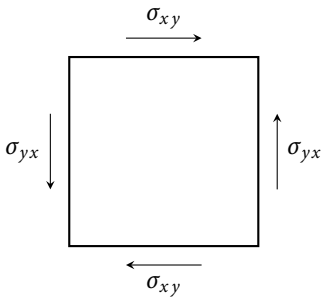


**(b)** In order for the torque to vanish on the $xy$–plane, we need $\sigma_{xy} = \sigma_{yx}$ and similarly for the other planes, so that $\sigma_{ij}$ must be a symmetric tensor.

**Figure 1.9** – Stress components

**Stiffness matrix: General form**

Since we are working with small strains, we assume the hypothesis of linear regime, so that we can apply Hooke's law and write the relation between strains and stresses by means of a fourth-order $C_{ijkl}$ tensor in the form: $\sigma_{ij} = C_{ijkl}\varepsilon_{kl}$.

Due to the various symmetries of the problem under consideration, however, the number of independent parameters defining the $C$ tensor can be greatly reduced.

First of all, we notice that the relation between strains and stresses is usually given in terms of the coefficients $\gamma_{ij}$ (called engineering strains), which are defined by

$$\gamma_{ii} = \varepsilon_{ii}, \qquad \gamma_{ij} = \varepsilon_{ij} + \varepsilon_{ji} = 2\varepsilon_{ij} \ (i \neq j).$$

As only the off-diagonal terms are multiplied by two, $\gamma_{ij}$ is not a tensor and to avoid confusion we do not write it in matrix form, but simply write its six independent components (only six because $\gamma_{ij} = \gamma_{ji}$) in vector form. We use the engineering strains because they are a measure of the total shear deformation, as shown in Fig. 1.10.

Using these conventions, we can write

$$\begin{pmatrix} \sigma_{xx} \\ \sigma_{yy} \\ \sigma_{zz} \\ \sigma_{yz} \\ \sigma_{zx} \\ \sigma_{xy} \end{pmatrix} = \begin{pmatrix} C_{11} & C_{12} & C_{13} & C_{14} & C_{15} & C_{16} \\ C_{21} & C_{22} & C_{23} & C_{24} & C_{25} & C_{26} \\ C_{31} & C_{32} & C_{33} & C_{34} & C_{35} & C_{36} \\ C_{41} & C_{42} & C_{43} & C_{44} & C_{45} & C_{46} \\ C_{51} & C_{52} & C_{53} & C_{54} & C_{55} & C_{56} \\ C_{61} & C_{62} & C_{63} & C_{64} & C_{65} & C_{66} \end{pmatrix} \begin{pmatrix} \gamma_{xx} \\ \gamma_{yy} \\ \gamma_{zz} \\ \gamma_{yz} \\ \gamma_{zx} \\ \gamma_{xy} \end{pmatrix} \tag{1.28}$$

where the $C_{\alpha\beta}$ are called elastic stiffness constants or moduli of elasticity.

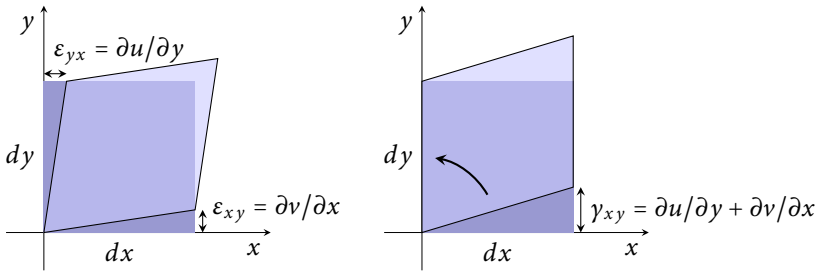


**Figure 1.10** – The engineering strain $\gamma_{xy} = \frac{\partial u}{\partial y} + \frac{\partial v}{\partial x}$ gives the total shear deformation on a given plane. Here is shown the case in which there is only shear deformation, that is $\varepsilon_{xx} = \varepsilon_{yy} = 0$.

### Number of independent parameters

First of all we prove that the $C_{\alpha\beta}$ matrix is symmetric. Let us start writing the elastic energy as a function of the strains. In the assumption of validity of the Hooke's law, the energy is a quadratic function of the total displacements:

$$U = \frac{1}{2} \sum_{\alpha,\beta=1}^{6} U_{\alpha\beta} \gamma_\alpha \gamma_\beta, \tag{1.29}$$

where the index of the $\gamma$'s identifies the six components of the vector given in (1.28):

$$\gamma_1 = \gamma_{xx}, \quad \gamma_2 = \gamma_{yy}, \quad \gamma_3 = \gamma_{zz}, \quad \gamma_4 = \gamma_{yz}, \quad \gamma_5 = \gamma_{zx}, \quad \gamma_6 = \gamma_{xy}.$$

The stresses are obtained from the derivative of the energy with respect to the corresponding strain component. For example,

$$\sigma_{xy} = \frac{\partial U}{\partial \gamma_{xy}} = \frac{\partial U}{\partial \gamma_6} = U_{66}\gamma_6 + \frac{1}{2} \sum_{\beta \neq 6} (U_{6\beta} + U_{\beta 6})\gamma_\beta =$$

$$= \sum_{\beta=1}^{6} \frac{1}{2} (U_{6\beta} + U_{\beta 6})\gamma_\beta.$$

Doing the same for all components and comparing the results with Eq. (1.28), we see that we can identify

$$C_{\alpha\beta} = \frac{1}{2}(U_{\alpha\beta} + U_{\beta\alpha}) = C_{\beta\alpha},$$

thereby proving that the stiffness matrix is symmetric.

The semiconductors under consideration have the atoms arranged in a FCC lattice and have accordingly specific symmetry operations. One of the transformations which leaves the system unchanged is the rotation of $\frac{2\pi}{3}$ around one of the diagonals of the cube (direction [111] and equivalent ones), which interchanges the axes according to

$$x \to y \to z, \qquad -x \to z \to -y, \qquad x \to z \to -y, \qquad -x \to y \to z$$

**Table 1.5** – Stiffness constants of silicon and germanium at 298 K, taken from [22].

| | $C_{11}(\mathrm{N/m^2})$ | $C_{12}(\mathrm{N/m^2})$ | $C_{44}(\mathrm{N/m^2})$ |
|---|---|---|---|
| Si | $1.6577 \cdot 10^{11}$ | $0.6393 \cdot 10^{11}$ | $0.7962 \cdot 10^{11}$ |
| Ge | $1.240 \cdot 10^{11}$ | $0.413 \cdot 10^{11}$ | $0.683 \cdot 10^{11}$ |

depending on the diagonal which is chosen.

A general term of the energy expansion (1.29) is proportional to a product of the form $\gamma_{ij}\gamma_{kl}$, where the indices can be $x$, $y$ or $z$. If a given index appears an odd number of times, we can always find a rotation around one of the diagonals which changes the sign of the term, since in general we have $\gamma_{xy} = -\gamma_{x(-y)}$ and so on. To be invariant under the symmetry operations of the cube, these terms must vanish, so that the only terms with a coefficient different from zero are

$$\gamma_{xx}^2, \quad \gamma_{yy}^2, \quad \gamma_{zz}^2, \quad \gamma_{yz}^2, \quad \gamma_{zx}^2, \quad \gamma_{xy}^2, \quad \gamma_{xx}\gamma_{zz}, \quad \gamma_{yy}\gamma_{zz}, \quad \gamma_{xx}\gamma_{yy}.$$

Furthermore using the same symmetry requirement it can be shown that $\gamma_{xx}^2$, $\gamma_{yy}^2$ and $\gamma_{zz}^2$ have the same coefficient; in the same way it is shown that the coefficient is the same for the three terms $\gamma_{yz}^2$, $\gamma_{zx}^2$ and $\gamma_{xy}^2$, and for $\gamma_{xx}\gamma_{zz}$, $\gamma_{yy}\gamma_{zz}$ and $\gamma_{xx}\gamma_{yy}$.

Thus the final form of the stiffness matrix in the case of cubic symmetry is

$$C_{ij} = \begin{pmatrix} C_{11} & C_{12} & C_{12} & 0 & 0 & 0 \\ C_{12} & C_{11} & C_{12} & 0 & 0 & 0 \\ C_{12} & C_{12} & C_{11} & 0 & 0 & 0 \\ 0 & 0 & 0 & C_{44} & 0 & 0 \\ 0 & 0 & 0 & 0 & C_{44} & 0 \\ 0 & 0 & 0 & 0 & 0 & C_{44} \end{pmatrix} \tag{1.30}$$

with only three independent parameters $C_{11}$, $C_{12}$ and $C_{44}$, which depend on the material and are experimentally known for a large set of cubic semiconductors. These stiffness constants are reported in Table 1.5 for silicon and germanium.

### 1.3.2 Strains in mismatched epitaxy and continuum elasticity theory

As already mentioned, one of the most important cases where strains are concerned is that of mismatched epitaxy, in which a semiconductor layer is epitaxially grown on a substrate with a (slightly) different lattice constant. Throughout this work, we consider planar heterostructures and we always assume the ideal case of coherent growth, schematically depicted in Fig. 1.11, meaning that the in-plane lattice constant of all materials in the system is the same and is fixed by the substrate lattice constant. From an experimental point of view, this condition is never exactly achieved, and various kinds of defects (dislocations, stacking faults, …) are always present in the grown crystal. However, the efforts of the experimentalists are oriented toward the realization of a growth process which is as close as possible to the ideal (coherent)

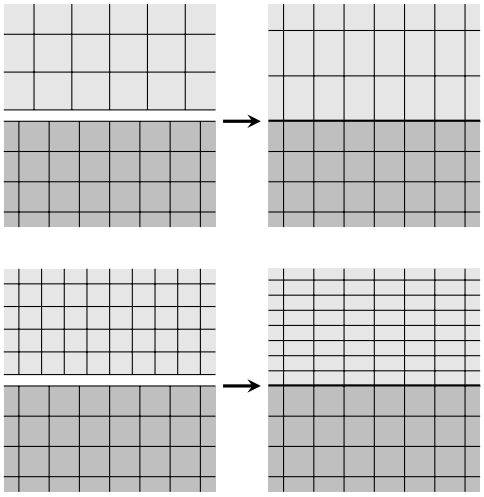

**Figure 1.11** – When we deposit some layers of a semiconductor on top of a substrate with a different lattice constant, if the lattice mismatch is not too large, the in-plane lattice constant of the overlayer changes, so that each atom of the overlayer bonds to one of the substrate: this is called a coherent growth. In order to minimize the total energy, also the lattice constant in the growth direction is modified: if the material is stretched on the plane, it contracts in the growth direction (and vice versa). A measure of this effect is given by the Poisson's ratio.

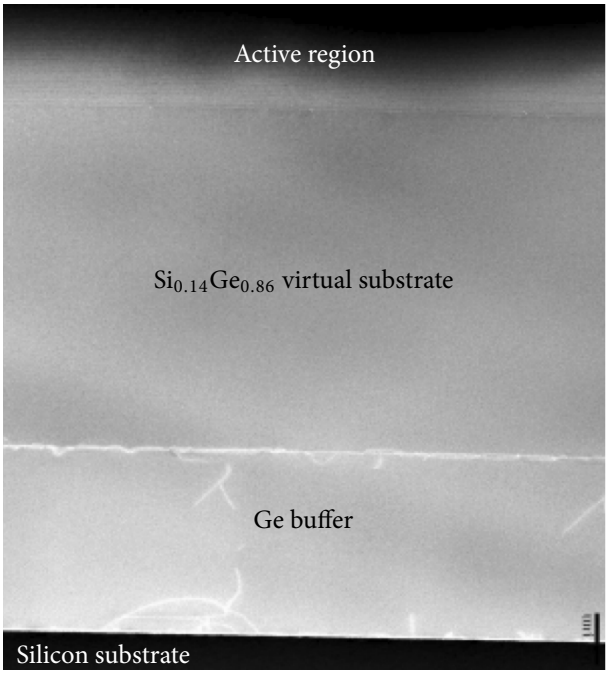


**Figure 1.12** – TEM micrograph of a Si/Ge quantum cascade sample grown on a virtual $Si_{0.14}Ge_{0.86}$ substrate. The adopted growth technique strongly reduces defects in the active region (the growth has been made at the University of Roma Tre and the TEM at the CNR-IMM of Catania).

one, mainly because the presence of defects degrades significantly the performances of the devices. Often, this is achieved using ingenious techniques that are able for instance to limit the defects within the buffer substrate, and suppress significantly their number in the active region. A TEM micrograph of a SiGe multilayer structure ("active region") grown on a SiGe virtual substrate is shown in Fig. 1.12, where we can see that the defects are mainly confined in the Ge buffer, whereas they are significantly reduced in the active region.

In the following, we show how to calculate the atomic positions in a strained structure using the continuum elasticity theory. This theory takes the stiffness con-

stants measured in the bulk to describe the elastic properties of the system, and does not consider the fact that the crystal is composed of atoms. However, it is known [23] that this theory reproduces correctly the atomic positions in the case of planar heterostructures, even if composed of a very small number of atomic monolayers. In the case of more complicated structures, one can employ other techniques, possibly exploiting an atomistic approach, as it is the case for instance of the valence force field (VFF) [24–27]. Systems that require to be modeled by such more complicated (but detailed) techniques include for instance nanowires, quantum dots, nanotubes (for this latter system, see for instance Appendix A.1).

Since this Thesis focuses mainly on planar heterostructures, we describe below the main results of the continuum elasticity theory that are needed to predict the strains (and thus the atomic positions) in multilayer systems.

We describe in particular biaxial strains in the case of planar heterostructures composed of a sequence of layers grown on a substrate along the [001] direction, which is the growth direction of interest for the integration of photonic devices in the present Si electronic technology. For this reason, all systems considered in this Thesis are grown along the [001] direction. Chosen a coordinate system with two vectors on the plane of the interface and the third vector along the [001] growth direction, the strain tensor $\varepsilon_{ij}$ within each layer is diagonal and has the following form:

$$\varepsilon_{ij} = \begin{pmatrix} \varepsilon_{\parallel} & 0 & 0 \\ 0 & \varepsilon_{\parallel} & 0 \\ 0 & 0 & \varepsilon_{\perp} \end{pmatrix}. \tag{1.31}$$

For heterostructures grown on a thick substrate, we can assume that the latter is not deformed, so that the in-plane lattice constant is the same for all layers, and the value of $\varepsilon_{\parallel}$ of a given overlayer is simply given by the lattice mismatch

$$\varepsilon_{\parallel} = \frac{a_S}{a_L} - 1,$$

$a_S$ and $a_L$ being the bulk lattice constants of the substrate and of the overlayer, respectively.

For common semiconductors, if the crystal is stretched along one direction, it tends to shorten in the other directions (for a graphical representation of this effect in the case of mismatched epitaxy, see Fig. 1.11). To give a measure of this tendency, we define the following ratio $\eta$:

$$\eta = -\frac{\varepsilon_{\parallel}}{\varepsilon_{\perp}}. \tag{1.32}$$

Just to avoid confusion, we note that this ratio is different from the one known in literature as the Poisson's ratio $\nu$. The latter is in fact defined as the ratio of the strain along the two orthogonal directions in the case of uniaxial strains, i.e. when the system is stretched or compressed along one direction and can relax along the two orthogonal directions. In the case of coherently-grown heterostructures, we have instead a biaxial strain, where the strains along two directions are fixed (i.e., those

on the growth plane), and only one direction can freely relax. In this case, the ratio of the two strains assumes the value $\eta$ defined in Eq. (1.32), and one can easily show that their relation is given by

$$\eta = \frac{1-\nu}{2\nu}. \tag{1.33}$$

We briefly prove here this formula, which is useful since the quantity $\nu$ is the most used in the literature; for more details one can refer for instance to [28]. We start considering a *uniaxial* stress along the $x$ direction. From Hooke's law, we can write $\sigma_{xx} = E\varepsilon_{xx}$, where $E$ is the modulus of elasticity, i.e. the coefficient $C_{11}$ of Eq. (1.28). The Poisson ratio $\nu$ is defined by the relation $\varepsilon_{yy} = \varepsilon_{zz} = -\nu\varepsilon_{xx} = -\nu(\sigma_{xx}/E)$.

I now apply three stresses $\sigma_{xx}$, $\sigma_{yy}$ and $\sigma_{zz}$ along the three Cartesian directions. Then, for any given direction, the strain is both controlled by the stress along the same direction (through the modulus of elasticity $E$), and by the stress along the orthogonal directions (through the Poisson ratio $\nu$). Writing all the contributions together, we obtain

$$\begin{cases} \varepsilon_{xx} = \frac{1}{E}\left[\sigma_{xx} - \nu(\sigma_{yy} + \sigma_{zz})\right] \\ \varepsilon_{yy} = \frac{1}{E}\left[\sigma_{yy} - \nu(\sigma_{xx} + \sigma_{zz})\right] \\ \varepsilon_{zz} = \frac{1}{E}\left[\sigma_{zz} - \nu(\sigma_{xx} + \sigma_{yy})\right] \end{cases}.$$

The coefficient $\eta$ defined above is obtained by the condition $\sigma_{zz} = 0$ (no stress along the growth direction), and imposing also $\varepsilon_{xx} = \varepsilon_{yy}$ and $\sigma_{xx} = \sigma_{yy}$ (same strains and stresses along the two in-plane directions). By simple substitutions we get

$$\begin{cases} \varepsilon_{xx} = \frac{1}{E}\sigma_{xx}(1-\nu) \\ \varepsilon_{zz} = \frac{1}{E}\sigma_{xx}(-2\nu) \end{cases}$$

from which we immediately obtain the expression of $\eta$ from its definition:

$$\eta = -\frac{\varepsilon_{\parallel}}{\varepsilon_{\perp}} = -\frac{\varepsilon_{xx}}{\varepsilon_{zz}} = \frac{1-\nu}{2\nu},$$

thus proving Eq. (1.33).

Going back to Eq. (1.31) and substituting Eq. (1.32), we get

$$\varepsilon_{ij} = \varepsilon \begin{pmatrix} 1 & 0 & 0 \\ 0 & 1 & 0 \\ 0 & 0 & -1/\eta \end{pmatrix},$$

where by definition $\varepsilon = \varepsilon_{\parallel}$.

We want to emphasize here that the $\eta$ ratio (or, equivalently, the Poisson's ratio $\nu$) does not depend only on the material, through its stiffness constants $C_{11}$, $C_{12}$ and $C_{44}$ of Eq. (1.30), but also on the growth direction with respect to the crystalline axes. The value of $\eta$ for a generic growth direction is obtained by first rotating the stress tensor $\sigma_{ij}$ to a reference frame where the third coordinate is along the growth direction, and then imposing the condition $\sigma_{33} = 0$. In particular, for the [001] direction, which

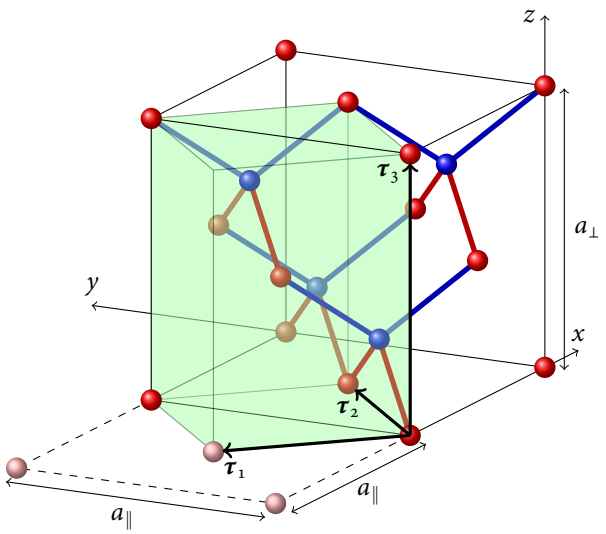


**Figure 1.13** – Unit cell (green shaded parallelepiped) having one atom on each plane orthogonal to $\boldsymbol{\tau}_3$ and containing a total of four atoms. The coordinates of the basis vectors are: $\boldsymbol{\tau}_1 = {}^{a_\parallel}/_2(-1,1,0)$, $\boldsymbol{\tau}_2 = {}^{a_\parallel}/_2(1,1,0)$, $\boldsymbol{\tau}_3 = {}^{a_\perp}/_2(0,0,2)$.

is the only one of interest in this Thesis, we do not need to rotate the tensor and we simply obtain from Eq. (1.28), (1.30) and the condition $\sigma_{zz} = 0$ that

$$\eta = \frac{C_{11}}{2C_{12}} \qquad \text{(for the [001] direction).}$$

### 1.3.3 Change of symmetry under biaxial strain

The bulk unstrained diamond structure has the cubic symmetry $O_h$, where in particular the $x$, $y$ and $z$ directions are equivalent. After the application of a biaxial strain, the $z$ direction is no more equivalent to the $x$ and $y$ ones, since the size of the unit cell is different along the different directions, see Eq. (1.31). To describe systems under biaxial strain, we choose not to use the primitive cell introduced in Sec. 1.1. It becomes instead more convenient to use basis vectors that emphasize the new symmetry of the strained crystal. In particular, we choose one vector $\boldsymbol{\tau}_3$ along the $z$ direction and the other two ($\boldsymbol{\tau}_1$ and $\boldsymbol{\tau}_2$) orthogonal to it, along the $[\bar{1}10]$ and $[110]$ directions, as shown in Fig. 1.13. The unit cell contains now four atoms (one for each atomic plane orthogonal to $\boldsymbol{\tau}_3$) and has thus twice the volume of the primitive cell; if we consider the corresponding Brillouin zone, its volume is thus halved. The new Brillouin zone, which is a parallelepiped and is depicted in red in Fig. 1.14a, can be obtained folding the BZ of Fig. 1.3 as illustrated in Fig. 1.14b.

In order to write the TB Hamiltonian, the first step is to calculate the new director cosines for this strained geometry. One can easily see that for the nearest-neighbor

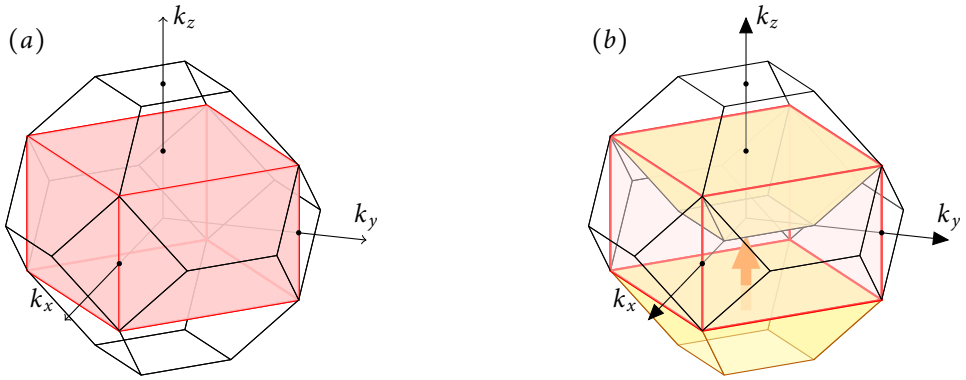


**Figure 1.14** – (a) Folded Brillouin zone (red parallelepiped) corresponding to a FCC Bravais lattice with a basis vector chosen along [001] and four atoms in the unit cell. The red parallelepiped can be obtained folding the truncated octahedron as shown in panel (b).

distances these are given by (for the atoms in the anion position):

| | $l$ | $m$ | $n$ |
|---|---|---|---|
| $\mathbf{v}_1$ | $\frac{a_\parallel}{\sqrt{2a_\parallel^2+a_\perp^2}}$ | $\frac{a_\parallel}{\sqrt{2a_\parallel^2+a_\perp^2}}$ | $\frac{a_\perp}{\sqrt{2a_\parallel^2+a_\perp^2}}$ |
| $\mathbf{v}_2$ | $-\frac{a_\parallel}{\sqrt{2a_\parallel^2+a_\perp^2}}$ | $-\frac{a_\parallel}{\sqrt{2a_\parallel^2+a_\perp^2}}$ | $\frac{a_\perp}{\sqrt{2a_\parallel^2+a_\perp^2}}$ |
| $\mathbf{v}_3$ | $\frac{a_\parallel}{\sqrt{2a_\parallel^2+a_\perp^2}}$ | $-\frac{a_\parallel}{\sqrt{2a_\parallel^2+a_\perp^2}}$ | $-\frac{a_\perp}{\sqrt{2a_\parallel^2+a_\perp^2}}$ |
| $\mathbf{v}_4$ | $-\frac{a_\parallel}{\sqrt{2a_\parallel^2+a_\perp^2}}$ | $\frac{a_\parallel}{\sqrt{2a_\parallel^2+a_\perp^2}}$ | $-\frac{a_\perp}{\sqrt{2a_\parallel^2+a_\perp^2}}$ |

where we have defined $a_\parallel = (1+\varepsilon_\parallel)a$ the in-plane lattice constant and $a_\perp = (1+\varepsilon_\perp)a$ the lattice constant along the growth direction (see also Fig. 1.13). For the atoms sitting in cation positions one just has to take the opposite signs, as discussed already below (1.14). The geometric phase factors introduced in Eqs. (1.16) and the matrix elements reported in Table 1.3 change in a similar way. It is straightforward to obtain the explicit form for the matrix using the same steps presented in Sec. 1.2, and we do not write this matrix explicitly.

The change of the TB parameters due to the change of bond lengths is discussed later in Sec. 1.3.4. Nonetheless, it is worth pointing out already here that the TB formalism, considering explicitly the geometric positions of the atoms through the director cosines of the vectors connecting them, takes automatically into account the symmetry properties of the system, and in particular describes correctly the reduction of the symmetry due to strain effects (which can for instance result in the splitting of degenerate states, see Sec. 1.3.6).

### 1.3.4 Hopping integrals under strain in the TB formalism

The semiempirical parameters that we have discussed in Sec. 1.2.1 are valid only for the relaxed bulk solids and give quantitatively correct results only if we do not have

strain and deformation effects.

In real situations, however, when strains play a crucial role, we need to know how the TB parameters change if the geometric structure of the crystal is modified. In fact, while we have already pointed out in Sec. 1.3.3 that the change of the bond angles is automatically taken into account in the TB model by use of the formulae of Table 1.2, the most important effect that must be taken into account is the dependence on the distance of the hopping integrals between orbitals on neighboring sites. In fact, when the distance between two atoms is changed, the overlap of the orbitals centered on them may change significantly, and the same holds for the integrals introduced in Eq. (1.9).

This dependence is usually given in the form of scale laws: if $ij\kappa$ is a generic independent Slater–Koster integral (e.g. $V(ss\sigma)$, $V(pd\pi)$, ...), $d_0$ is the unstrained distance between two neighboring atoms for which the bulk parametrization is obtained, and $d$ is the strained distance, we can obtain the new interaction energy in the presence of strain by the following generalization of Harrison's $d^{-2}$ law:

$$ij\kappa(d) = ij\kappa(d_0)\left(\frac{d_0}{d}\right)^{n_{ij\kappa}}.$$

Here, $n_{ij\kappa}$ are exponents that express how the interaction between orbitals $i$ and $j$ (centered on neighboring atoms) changes when the distance between the atoms is modified. These exponents reflect the localization of the two orbitals near their nuclei.

Harrison [29] chose for all these exponents the value 2 when working with a minimal $sp^3$ basis; in a semiempirical approach [16, 30–32], however, these coefficients are usually slightly modified (typically ranging from 1 to 4) to better reproduce some experimental data, as for example the $\mathrm{d}E/\mathrm{d}p$ pressure coefficients, which express how the different band edge energies change under hydrostatic or uniaxial pressure applied to the system.

### 1.3.5 Discussion of the parametrizations and diagonal parameters shifts

In the last years many first-neighbor $sp^3d^5s^*$ parametrizations for Si and Ge appeared in the literature. Since the parametrization of Jancu et al. [16], there have been various attempts to improve it [32–37]. When choosing the parametrization to use, one has to keep in mind that each parametrization tries to reproduce at best a given set of system parameters (e.g. effective masses, band edge energies, etc.) but can give inaccurate results for other parameters.

To give an example, the Si parametrization of Sacconi *et al.* [35] was developed with the aim of having more accurate results for the transport properties of $n^+$-Si/$SiO_2$/$p$-Si capacitors: in fact, for the study of the electron tunneling in such structures, it is essential to have precise values for the Si masses along the $\Delta$ line in order to avoid false estimations of transmission coefficients. Thus, the authors started from the parameters of Ref. [16] (which provide an incorrect mass at $\Delta$ for Si) and improved them in order to yield precise Si conduction band masses. On the

other hand, this new parametrization lacks the required precision for the conduction states at the L point. These, however, lie at a much higher energy than $\Delta$ states in Si and can thus be disregarded for the calculation of transport properties in Si structures. Yet, this inaccuracy at the L point is not tolerable if one is concerned with L-like states in Ge-rich SiGe layers. Moreover, in the mentioned Si capacitors, strain is not relevant and thus this parametrization does not provide the scaling exponents $n_{ij\kappa}$ for the hopping matrix elements, which are instead of the uttermost importance for the accurate evaluation of electronic and optical properties in strained SiGe heterostructures. For similar reasons, also the parametrization of [34] does not provide any scaling parameters (the extension of Ref. [34] in the presence of strain is presented in Ref. [37]).

As a second example, we quote the extrapolation of the results of a given parametrization outside its range of validity. For instance, since SiGe heterostructures are typically grown on SiGe substrates (and since Ge has a larger lattice constant than Si) the parametrizations fit the pressure coefficients for Ge only for compressive in-plane strains. Thus, is is not obvious whether the same parameters can be used also when studying tensile-strained Ge. For this case, discussed for instance in Chap. 4, it is more suitable to use for instance the parametrization provided in [36], developed specifically with the aim of improving the results of [16] for what concerns the effects of tensile strain on the band structure of Ge.

However, the most important difference among different parametrizations often consists in how they modify the on-site terms when a strain is applied. In fact, in the literature it has been pointed out [31] that keeping the on-site energies constant and independent of the strain is not a good approximation. In fact, even the behavior of the band edges would be wrongly reproduced. In particular, in the case of non-hydrostatic strains, we expect that the strain lifts the degeneracies of the on-site energies due to the modification of the crystal symmetry and to the fact that these diagonal terms include the crystal field, defined in Eq. (1.8). As discussed in that Section, in fact, the crystal field has the symmetry of the crystal and not the spherical symmetry of the atomic orbitals: in the presence of a biaxial strain, we thus expect some loss of degeneracy among the different $p$ or $d$ orbitals.

To be more specific, we describe how this effect is taken into account by Jancu *et al.* [16]. In their parametrization, they propose a simple correction only for $d-$type orbitals, valid in the case of biaxial strain for the [001] ($z$) growth direction. In this case, they suggest that the diagonal terms should change as

$$\begin{aligned} E_{xy} &= E_d[1 + 2b_d(\varepsilon_{zz} - \varepsilon_{xx})], \\ E_{yz} = E_{xz} &= E_d[1 - b_d(\varepsilon_{zz} - \varepsilon_{xx})], \\ E_{x^2-y^2} = E_{3z^2-r^2} &= E_d, \end{aligned}$$

where $b_d$ is another empirical parameter given in the paper [16]. An analogous treatment for the [111] growth direction can be found in Ref. [36]. This approach could be repeated also for other growth directions, and the relevant parameters could be provided: however, when we do not consider planar layered structures, but for

instance nanowires, quantum dots, … the strains are no more simply biaxial, and we need a more general treatment of the strain influence on the on-site energies. For instance, in Ref. [31] a possible modification of on-site energies is also presented, allowing to take into account generic strains; but the parameters are provided only for GaAs and InAs. Different approaches that are able to consider generic strains applied to Si and Ge are presented in Refs. [32, 37]. We do not discuss them in detail here, because for the case of planar layered structures grown along the [001] direction such a level of generality is not required. However, a brief discussion of the parametrization of Ref. [32] can be found in Appendix A.1, where we discuss Si/Ge rolled-up nanotubes.

### 1.3.6 Band structure of Si and Ge under [001] biaxial strain

We briefly discuss in this Section some results of the application of strain to silicon and germanium with a short discussion of the main effects on their band structure.

We focus our attention in particular on the $\Delta$ and $\Lambda$ directions, i.e. the direction from $\Gamma$ to $X$ (six $\langle 001 \rangle$ equivalent directions) and from $\Gamma$ to $L$ (eight $\langle 111 \rangle$ equivalent directions), respectively (see also Fig. 1.3), because the conduction band minima in Si and Ge occur along these lines.

Under biaxial strain for the $[001]$ growth direction, the six equivalent $\Delta$ lines are split in two groups: two $\Delta_2$ lines along $k_z$, with $k$ vector ranging from $(0, 0, -\pi/a_\perp)$ to $(0, 0, \pi/a_\perp)$, and four $\Delta_4$ lines on the $k_x k_y$ plane, ranging from $(-2\pi/a_\parallel, 0, 0)$ to $(2\pi/a_\parallel, 0, 0)$ and from $(0, -2\pi/a_\parallel, 0)$ to $(0, 2\pi/a_\parallel, 0)$, respectively. In the presence of strain, the $\Delta_2$ and $\Delta_4$ lines become non-equivalent, and the degeneracy of the six $\Delta$ states is thus split in 4+2, since the effects of the strain is different along the different directions. In fact, when we calculate the band structure, we obtain that the shift of the $\Delta_2$ minima is opposite to that of the $\Delta_4$ minima. In particular, for a compressive in-plane strain, the energy of the $\Delta_2$ minima increases, while the energy of $\Delta_4$ decreases; the opposite is true for a tensile in-plane strain. A scheme of the different splittings of the $\Delta$ conduction states under biaxial strains is presented in Fig. 1.15.

The eight $L$ lines remain instead equivalent: indeed, given one of these lines, we can obtain the other ones either rotating around $k_z$ or reflecting with respect to the $k_x k_y$ plane. The strain only introduces a shift of the energy, which is the same for all 8 lines.

Another important effect of strain is the lifting of the degeneracy at the zone center in the topmost valence bands, separating the heavy-hole and the light-hole states. This is of great importance, because the character of the two states is different ($|J^2, J_z\rangle = |3/2, 3/2\rangle$ for heavy-hole states, $|3/2, 1/2\rangle$ for light-hole states) and this strongly influences the selection rules for the optical transitions, as we discuss in Chap. 2. As an example, in Fig. 1.16 we report the behavior of the top of the valence band for germanium. From this Figure, we notice that the light-hole state is on top for a tensile in-plane strain ($\varepsilon_\parallel > 0$). For a compressive in-plane strain, corresponding to $\varepsilon_\parallel < 0$, the heavy-hole state is instead on top. Fig. 1.15 summarizes the effect of a

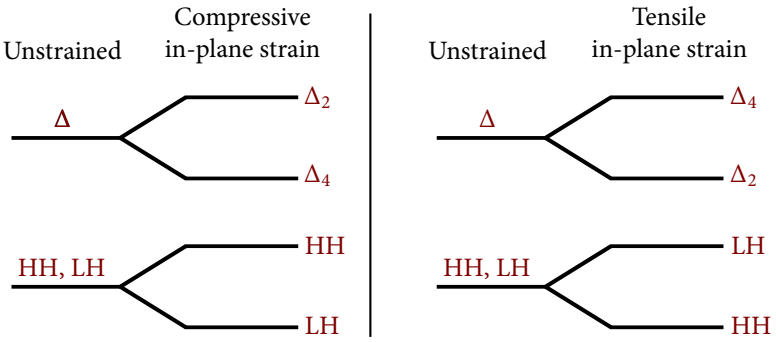


**Figure 1.15** – Schematic of the splitting of the Δ conduction edges and of the HH and LH valence edges under biaxial strain, both in the case of tensile and compressive in-plane strain fields.

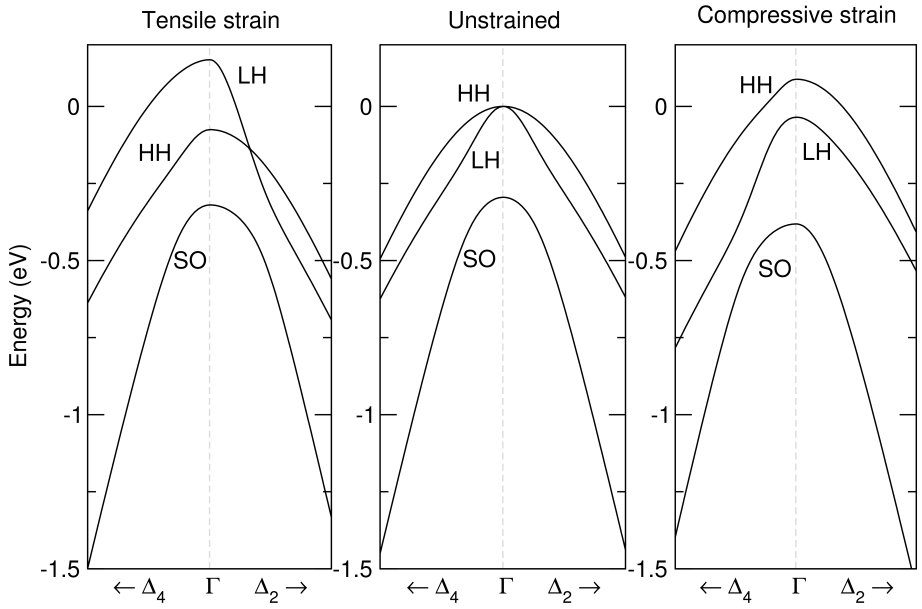


**Figure 1.16** – Top of the valence band of germanium for three different strains: from left to right, we have a tensile in-plane strain, corresponding to $\varepsilon_{\parallel} = 1.33\%$ and $\varepsilon_{\perp}$ calculated using the Poisson's ratio; an unstrained crystal; and a compressive in-plane strain, corresponding to $\varepsilon_{\parallel} = -1.33\%$.

biaxial strain also on the valence states.

Note that, in the presence of strain, outside the Γ point the bands are warped and the states strongly mix, so that the nomenclature "heavy hole" and "light hole" is strictly valid only at Γ. The two states can be distinguished at this point by the analysis of the corresponding eigenvectors at Γ, comparing them with Eqs. (1.23): the easiest thing to check is the presence or absence of a $p_z$-type component, since it contributes only to the light-hole states.

### 1.3.7 Strain balancing

When we grow a Ge/SiGe planar heterostructure, due to the different lattice constants of the two materials, the system cannot have infinite size since each layer adds an overall stress to the stack. This usually leads to the formation of dislocations or other defects at the top and bottom of the stack to relax the strain. However, by properly balancing the strain in one compressive layer by growing and adjacent tensile layer, the overall maximum stack thickness can be significantly increased. Then, in order to grow a large number of layers (as it is typically required for instance in quantum cascade systems, see Sec. 3.4), the substrate lattice constant has to be chosen in order to satisfy the strain balancing condition. We report here only the most important results that will be used in the Thesis; for a discussion of the different formulae that can be found in the literature concerning the strain-balancing condition, and for a discussion of their validity, we refer to [38].

The most simple formula that is often found for the optimal substrate lattice constant that fulfills the strain balancing condition is the average of the lattice constants of the layers, weighted by the respective layer thicknesses. In particular, in the case of an infinite stack of two different layers 1 and 2 with lattice constants $a_1$ and $a_2$, and thicknesses $t_1$ and $t_2$, the corresponding substrate lattice parameter $a_0$ is given by

$$a_0 = \frac{a_1 t_1 + a_2 t_2}{t_1 + t_2}.$$

This method is however strictly valid only if the two materials have identical elastic properties, which is however not true for Si and Ge (see Table 1.5). In any case, this formula has always a qualitative validity, stating that the substrate lattice constant should be intermediate between those of the two layers, so that in one layer the strain is compressive and in the other it is tensile.

A more sound expression can be obtained from the requirement of zero average in-plane stress in the system; this condition can be achieved by minimizing the total strain energy of the layered system. The complete calculation can be found in Ref. [38]; the final result for a two-layer system is that the average strain energy density in the two strained layers is

$$U_{\mathrm{av}} = \frac{A_1 \varepsilon_1^2 t_1 + A_2 \varepsilon_2^2 t_2}{t_1 + t_2}$$

where $\varepsilon_1$ and $\varepsilon_2$ are the in-plane strains in the two layers, and $A_1$ and $A_2$ are coefficients which depend only on the elastic constants of the layers 1 and 2, each of them given by

$$A = C_{11} + C_{12} - \frac{2C_{12}^2}{C_{11}},$$

where $C_{11}$ and $C_{22}$ are the elastic stiffness coefficients given in Table 1.5 for the layer under consideration.

The average in-plane stress due to the biaxial strain in the two-layer system is

defined by

$$X = \frac{\partial U_{\text{av}}}{\partial \varepsilon_1}$$

and the strain-balance condition is obtained by the requirement $X = 0$. The final result is that the substrate lattice constant $a_0$ must satisfy

$$a_0 = \frac{A_1 t_1 a_1 a_2^2 + A_2 t_2 a_2 a_1^2}{A_1 t_1 a_2^2 + A_2 t_2 a_1^2}.$$

The above method can be generalized to a periodic stack of more than two layers, as in the case of the quantum cascade structures presented in Sec. 3.4, allowing for the estimation of the best substrate lattice constant to be exploited to minimize strain relaxation effects.

## 1.4 SiGe alloys and the virtual crystal approximation

The discussion of the tight-binding model of Sec. 1.2 applies to perfect crystals composed solely of one kind of atoms (either Si or Ge). In real applications, however, SiGe alloys often play a significant role. For instance, a growth of a Ge layer on a Si substrate (or vice versa) would not be coherent for more than a few atomic layers, due to the large lattice mismatch between Si and Ge; on the contrary, Si-rich SiGe alloys can grow coherently on Si substrates for hundreds of angstrom (see e.g. Ref. [39]).

Si and Ge are perfectly miscible at any concentration. $\text{Si}_{1-x}\text{Ge}_x$ alloys are thus composed of a uniform random distribution of Si and Ge atoms, with an average fractional Ge composition given by the number $0 \leq x \leq 1$. Such an alloy does not possess any translational invariance, so that in principle one could not use the Bloch theorem. The Bloch theorem can be recovered considering a very large supercell containing Si and Ge atoms in the correct proportion, and calculating the electronic states for different random distributions of the atoms in the supercell. The properties of the bulk SiGe alloy would then be obtained as the limiting ones for a very large supercell. This kind of calculation is of course possible, but it is also much more complicated and computationally demanding than the one for a simple bulk crystal.

For SiGe alloys, however, there is a simple approximation, called the Virtual Crystal Approximation (VCA), which greatly simplifies the problem but is still able to produce very good results. This approximation will be always adopted in this Thesis when considering alloys. The VCA describes the alloy as a perfect crystal, where each atom is neither a Si nor a Ge one, but is a virtual atom whose properties are obtained by suitable interpolation of the Si and Ge properties. This allows us to use the same formalism of Sec. 1.2 also for the SiGe alloys.

In particular, the relaxed lattice constant $a_0(x)$ of a $\text{Si}_{1-x}\text{Ge}_x$ alloy is obtained (in Å units) by the formula [40, 41]:

$$a_0(x) = a_0(\text{Si}) + 0.200326x(1-x) + [a_0(\text{Ge}) - a_0(\text{Si})]x \tag{1.34}$$

where $a_0(\mathrm{Si})$ and $a_0(\mathrm{Ge})$ are the bulk lattice constants of Si and Ge given in Table 1.1, and the factor 0.200326 is a quadratic correction, which is introduced in order to reproduce the experimental deviation from the Vegard's law (i.e., the linear interpolation of the lattice constants of Si and Ge). Also the refractive index is not simply linearly interpolated, but we adopt instead the following formula given in Ref. [42]:

$$n_{\mathrm{Si}_{1-x}\mathrm{Ge}_x} \approx 3.42 + 0.37x + 0.22x^2. \tag{1.35}$$

A linear interpolation is instead adopted for the elastic constants (in order to obtain the alloy lattice parameter along the growth direction), and also for the on-site energies. Finally, Si and Ge hopping parameters are scaled as discussed in Sec. 1.3.4 according to the interatomic distances obtained for the SiGe alloys, and at this point the two sets of parameters are linearly interpolated to obtain the hopping parameters in the VCA.

Before concluding this discussion, we mention one of the weaknesses of the VCA, related to the prediction of the bandgap of SiGe alloys as a function of the Ge concentration $x$. From experiments, it is known that the bandgap of $\mathrm{Si}_{1-x}\mathrm{Ge}_x$ alloys is a decreasing function of $x$, and that there is a crossover between the $\Delta$ and L minima at $x \approx 0.85$. Moreover, as visible from the experimental data of Fig. 1.17, the region $x < 0.85$ is characterized by a "bowing", i.e. a downward deviation of the curve with respect to a linear interpolation. In Fig. 1.17 we also report the theoretical results for the fundamental bandgap in the VCA approximation, obtained using the two different parametrizations of Refs. [16, 32]. As it is evident, while the low and high-end parts of the graph are well reproduced (especially the Ge-rich region is well described), the bowing behavior is completely missed. To be able to describe it, a treatment beyond the VCA is needed. The most simple improvement consists of a quadratic interpolation of the TB parameters, as discussed in Ref. [43]. Another possibility is the supercell approach discussed above, whose effectiveness is for instance discussed in Ref. [32].

## 1.5 Valence band offsets

When building heterostructures, two different materials (or two alloys with different concentrations) are arranged face to face. In general, the electronic distribution near the interface differs from the bulk. This can result in a relative shift of the bulk states far from the interface and in a band energy discontinuity at the interface. To evaluate this effect, Van de Walle and Martin [23] have taken into account a suitable supercell containing both Si and Ge atoms and have calculated the energy discontinuity at the Si/Ge interface using local-density-functional theory with non-local norm-conserving pseudopotentials. The main result is that the average valence band, defined as $E_{\mathrm{av}} = (E_{HH} + E_{LH} + E_{SO})/3$, depends only weakly on the strain and is almost independent of the crystallographic direction of the interface. This result has also been checked both theoretically [45] and experimentally [46, 47]. This weak dependence of $E_{\mathrm{av}}$ suggests to adopt this quantity to define the band offsets.

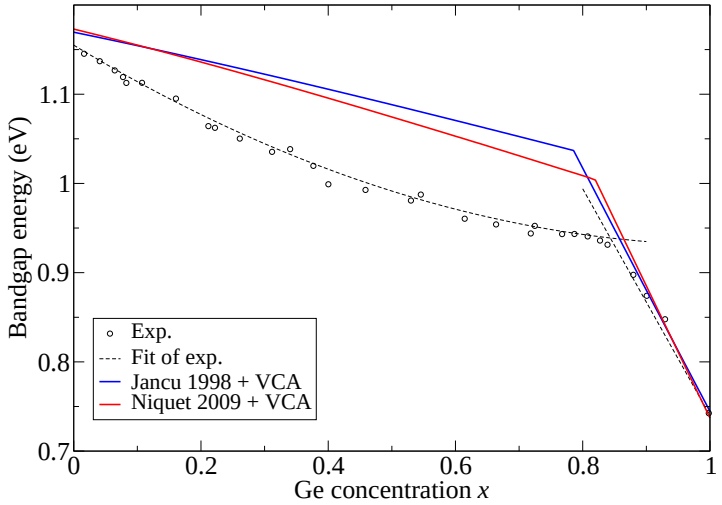


**Figure 1.17** – Comparison of the experimental fundamental bandgap of unstrained $Si_{1-x}Ge_x$ alloys with two theoretical results in the VCA approximation, using the parametrizations of Refs. [16, 32]. The experimental data is from Ref. [44] and is obtained from photoluminescence measurements at T=4.2 K. The dashed line is the fit of the experimental data provided in Ref. [44].

Typically, a linear interpolation both with respect to the strain and to the composition is adopted. For instance, in Ref. [41] the following formula is proposed:

$$\Delta E_{\text{av}} = (0.47 - 0.06y)(x - y), \tag{1.36}$$

which gives the discontinuity of the average valence band in eV of a $Si_{1-x}Ge_x$ strained alloy epitaxially grown on a $Si_{1-y}Ge_y$ substrate. The same functional dependence can be adopted to interpolate the band offset parameters of Ref. [23] and in this case we obtain

$$\Delta E_{\text{av}} = (0.54 - 0.03y)(x - y). \tag{1.37}$$

As we see, these values have a quite large inaccuracy, estimated to be of the order of 100 meV [23].

Practically, in the TB calculation, the average valence band $E_{\text{av}}$ is calculated for both the bulk materials across the interface, and then a suitable shift of the diagonal energies is applied in order to reproduce the $\Delta E_{\text{av}}$ value given by one of the above formulae.

Finally, we mention that these formulae are deduced for planar heterostructures with biaxial in-plane strain. For more complicated structures with more general strain fields, this assumption is not valid and one must find another rule for the evaluation of the band offsets. The most simple rule, which is widely used and is adopted for instance in the parametrization of Ref. [32], is to just add a constant diagonal energy shift to all Ge atoms with respect to Si atoms, independent of the strain status: while in the approaches of Eqs. (1.36) and (1.37), the formulae for $\Delta E_{\text{av}}$

already include the energy shift induced by the hydrostatic strain, in this second approach the shift only takes into account the differences in composition, while both the hydrostatic and uniaxial corrections to the band edges are to be included by the TB calculation.

## 1.6 $\mathbf{k}\cdot\mathbf{p}$ model

With the tight-binding model described in Sec. 1.2 (or with other methods as for instance pseudopotential) we can obtain the description of the electronic states of a crystal in the whole Brillouin zone. These methods possess a high degree of accuracy; however, it is often not possible to obtain explicit analytical expressions of many useful properties, as effective masses, absorption coefficients, … Moreover, these techniques can be computationally demanding in real systems. On the other hand, one is often not interested in the detailed description of the states in the whole BZ. Indeed, in a vast class of problems, only the properties near the band extrema are of relevance. In these cases, we expect that suitable approximations can be applied to significantly simplify the problem, with the advantage of obtaining a clearer physical insight of the system properties. Indeed, the $\mathbf{k}\cdot\mathbf{p}$ model has been developed precisely to this aim: starting from the exact knowledge of eigenstates and eigenvalues of a crystal at only one $\mathbf{k}_0$ point (typically a band extremum), the model allows to obtain a fairly accurate description of the states in a $\Delta\mathbf{k}$ neighborhood of the given $\mathbf{k}_0$ point. Moreover (as it is discussed in Sec.3.A, where an implementation of a multiband $\mathbf{k}\cdot\mathbf{p}$ model and its results are presented) the implementation of the model is fast enough to be employed in real-time calculations, even in the case of charged systems where self-consistent calculations are required to reproduce the band bending (see Sec. 1.9).

The purpose of this Section is not to give a thorough review of the $\mathbf{k}\cdot\mathbf{p}$ model, since this is outside the scope of this Thesis, but only to summarize the main results of the model for bulk systems and planar heterostructures (in the case of non-degenerate bands) that are employed in the next Chapters. The $\mathbf{k}\cdot\mathbf{p}$ method for degenerate (or almost degenerate) bands, as for instance at the top of the valence band of group IV or III-V materials, has been developed by Luttinger and Kohn [20] and by Kane [48]. A treatise on the $\mathbf{k}\cdot\mathbf{p}$ method, focusing in particular on its applications to semiconductor heterostructures, can be found in the book of Bastard [49].

More recently, more advanced models have been developed; we just mention here some of them for the sake of completeness, but we refer the reader to the literature for the details. For instance, in Ref. [50] a 14-band $\mathbf{k}\cdot\mathbf{p}$ model is developed, which considers the 14 near-gap states at $\Gamma$ with symmetry $\{\Gamma_8^-, \Gamma_6^-, \Gamma_7^-, \Gamma_8^+, \Gamma_7^+\}$ (see Fig. 1.8 for the nomenclature of the states). A further extension is the 30-band $\mathbf{k}\cdot\mathbf{p}$ model [51, 52], which allows to describe the near-gap valence and conduction bands over the whole BZ. Finally, we point to Ref. [9] for a discussion of the limits of $\mathbf{k}\cdot\mathbf{p}$ models and in particular on how the correct crystal symmetry has to be incorporated *a posteriori* in the standard $\mathbf{k}\cdot\mathbf{p}$ model (while in the TB formalism the correct symmetry is naturally imposed, since the atomic positions are employed in

constructing the Hamiltonian).

### 1.6.1 k · p model for bulk systems

For a crystalline system, we know that the Hamiltonian of a bulk electron can be written as $\mathcal{H} = p^2/m_0 + V(\mathbf{r})$, where the potential $V(\mathbf{r})$ has the same periodicity of the crystal, i.e. $V(\mathbf{r}+\mathbf{R}) = V(\mathbf{r})$ for all lattice translations $\mathbf{R}$. (Note that in this section we define the free-electron mass as $m_0$ to distinguish it from the various effective-masses.) Then, from the Bloch theorem, we know that for each $\mathbf{k}$ vector in the BZ we can write the solutions of the system Hamiltonian as

$$\mathcal{H}\psi^n_{\mathbf{k}} = E^n_{\mathbf{k}}\psi^n_{\mathbf{k}}, \tag{1.38}$$

where $n$ indexes the different bands, and the wavefunctions are of the Bloch form $\psi^n_{\mathbf{k}}(\mathbf{r}) = e^{i\mathbf{k}\cdot\mathbf{r}}u^n_{\mathbf{k}}(\mathbf{r})$ with the periodic functions $u^n_{\mathbf{k}}(\mathbf{r})$ having the same periodicity of $V(\mathbf{r})$.

We now assume that we know from some other method (e.g. from tight binding) the solutions of the problem at some point $\mathbf{k}_0$, which for notation simplicity we assume to be the Γ point, i.e. $\mathbf{k}_0 = 0$ (the extension to $\mathbf{k}_0 \neq 0$ is straightforward and it is briefly discussed at the end of this Section). Typically, this point $\mathbf{k}_0$ is chosen where an extremum for the bands is located, e.g. a local conduction band minimum. This means that we know all the energies $E^n_0$ at the Γ point, and the corresponding wavefunctions $\psi^n_0(\mathbf{r}) = u^n_0(\mathbf{r})$. We want to show that with only this knowledge, we can describe in a perturbation-theory approach the eigenfunctions and the eigenstates for $\mathbf{k}$ vectors not too far away from the Γ point (i.e., we can obtain the wavefunctions and the band structure near Γ). In order to do this, we find the Hamiltonian for the function $u^n_{\mathbf{k}}$. We first rewrite Eq. (1.38) as a function of the $u^n_{\mathbf{k}}(\mathbf{r})$:

$$\left(\frac{p^2}{2m_0} + V(\mathbf{r})\right) e^{i\mathbf{k}\cdot\mathbf{r}}u^n_{\mathbf{k}}(\mathbf{r}) = E^n_{\mathbf{k}}e^{i\mathbf{k}\cdot\mathbf{r}}u^n_{\mathbf{k}}(\mathbf{r}), \tag{1.39}$$

and we use $\mathbf{p} = -i\hbar\nabla$ to obtain

$$p^2\left(e^{i\mathbf{k}\cdot\mathbf{r}}u^n_{\mathbf{k}}(\mathbf{r})\right) = e^{i\mathbf{k}\cdot\mathbf{r}}(p^2 + 2\hbar\mathbf{k}\cdot\mathbf{p} + \hbar^2k^2)u^n_{\mathbf{k}}(\mathbf{r}).$$

Substituting this expression in Eq. (1.39) and dividing by $e^{i\mathbf{k}\cdot\mathbf{r}}$, we obtain

$$\left\{\left[\frac{p^2}{2m_0} + V\right] + \frac{\hbar}{m_0}\mathbf{k}\cdot\mathbf{p}\right\}u^n_{\mathbf{k}} = \left(E^n_{\mathbf{k}} - \frac{\hbar^2k^2}{2m_0}\right)u^n_{\mathbf{k}}. \tag{1.40}$$

With the definitions $\mathcal{H}_0 \equiv \mathcal{H}(\mathbf{k}=0)$, $W(\mathbf{k}) = \frac{\hbar}{m_0}\mathbf{k}\cdot\mathbf{p}$ and $\varepsilon^n_{\mathbf{k}} = E^n_{\mathbf{k}} - \hbar^2k^2/2m_0$, we can finally rewrite Eq. (1.40) as

$$[\mathcal{H}_0 + W(\mathbf{k})]u^n_{\mathbf{k}} = \varepsilon_{n\mathbf{k}}u^n_{\mathbf{k}}. \tag{1.41}$$

Up to know, we have only recast the Hamiltonian in a more convenient form for our next steps, but no approximations have been made and Eq. (1.41) is exact. In

this form, however, we immediately see that if $W(\mathbf{k})$ is small (i.e., if $\mathbf{k}$ is small), we can consider $W(\mathbf{k})$ as a perturbation to $\mathcal{H}_0$, for which we have assumed to know all eigenstates and eigenenergies, and obtain then the states and the bands near $\Gamma$ using perturbation theory. From now on we focus only on non-degenerate bands (apart from spin), which is valid for instance if we want to study the conduction band of Si and Ge. If we have chosen a local band extremum, the first order correction (proportional to $\mathbf{k}$) is zero, and then the second-order perturbative correction gives:

$$u_{n\mathbf{k}} = u_{n0} + \sum_{m\neq n} \frac{\langle u_{m0}|W(\mathbf{k})|u_{n0}\rangle}{\varepsilon_{n0}-\varepsilon_{m0}} u_{m0},$$
$$\varepsilon_{n\mathbf{k}} = \varepsilon_{n0} + \sum_{m\neq n} \frac{|\langle u_{m0}|W(\mathbf{k})|u_{n0}\rangle|^2}{\varepsilon_{n0}-\varepsilon_{m0}}.$$

Substituting the explicit expression of $W(\mathbf{k})$ and of $\varepsilon_{n\mathbf{k}}$, we finally obtain the band dispersion for the $n$–th band near $\mathbf{k}_0 = 0$:

$$E_{n\mathbf{k}} = E_{n0} + \frac{\hbar^2 k^2}{2m_0} + \frac{\hbar^2}{m_0^2}\sum_{m\neq n}\frac{|\mathbf{p}_{nm}\cdot\mathbf{k}|^2}{E_{n0}-E_{m0}}, \tag{1.42}$$

where we have defined the momentum matrix element

$$\mathbf{p}_{nm} = \langle u_{m0}|\mathbf{p}|u_{n0}\rangle .$$

A few comments are in order at this point. First of all, we can now quantify the meaning of "small" $\mathbf{k}$: from the previous perturbative approach, we see that the requirement is $|\varepsilon_{n\mathbf{k}} - \varepsilon_{n0}| \ll |\varepsilon_{n0} - \varepsilon_{m0}|$ for all $m$, i.e. we want that the energy dispersion of the band of interest be much smaller than all band gaps at $\mathbf{k}_0$. Secondly, we see that we do not actually need the explicit form of the $u_{n0}(\mathbf{r})$ at $\mathbf{k}_0$, but only the matrix elements $\mathbf{p}_{nm}$ of the momentum operator $\mathbf{p}$ between the periodic functions (and only at $\mathbf{k}_0$). As we show in Chap. 2, these matrix elements can be calculated in the TB formalism, so that we can start from the results of the TB at a given $\mathbf{k}_0$ point and obtain from these results a suitable $\mathbf{k}\cdot\mathbf{p}$ Hamiltonian. As a further remark, if the spin–orbit interaction term is included in the Hamiltonian, then the whole discussion is valid upon substitution of the $\mathbf{p}$ operator with the $\boldsymbol{\pi}$ operator [49], defined by

$$\boldsymbol{\pi} = \mathbf{p} + \frac{\hbar}{4m_0c^2}(\boldsymbol{\sigma}\times\nabla V).$$

Finally, we notice that in these simple approximations, we have obtained in Eq. (1.42) a quadratic expression for the band dispersion $E_{n\mathbf{k}}$ as a function of $\mathbf{k}$: this can be written as

$$E_{n\mathbf{k}} = E_{n0} + \frac{\hbar^2}{2}\sum_{i,j=x,y,z} k_i \left[\frac{1}{m_n^*}\right]_{ij} k_j$$

where $i$, $j$ run over the three components of the vector $\mathbf{k}$, and we have defined the inverse-mass tensor for the $n$−th band as

$$\left[\frac{1}{m_n^*}\right]_{ij} = \frac{1}{m_0}\delta_{ij} + \frac{2}{m_0^2}\sum_{m\neq n}\frac{(p_{mn})_i(p_{nm})_j}{E_{n0}-E_{m0}}. \tag{1.43}$$

Typically, for an evaluation of the inverse-mass tensor one limits the sum to near states (since farther bands give small contributions due to the energy denominator). For instance, the simplest approximation for the lowest conduction band at Γ in Ge (or in many III-V materials) is to sum only over the HH, LH and SO valence states. Note that practically, however, the whole process is often reversed: one measures experimentally the band edges and the effective masses, and employs directly these experimental values to define the parameters of the $\mathbf{k}\cdot\mathbf{p}$ Hamiltonian. We note that the inverse-mass tensor can be defined also as

$$\left[\frac{1}{m_n^*}\right]_{ij} = \frac{1}{\hbar^2}\left.\frac{\partial^2 E(\mathbf{k})}{\partial k_i \partial k_j}\right|_{\mathbf{k}=\mathbf{k}_0};$$

this expression is valid also if one relaxes some of the approximations made above, obtaining non-parabolic corrections to the energy dispersion [49].

Finally, we briefly show how the same formalism can be extended to a $\mathbf{k}_0$ point different from the Γ point. In this case, calling $\Delta\mathbf{k} = \mathbf{k} - \mathbf{k}_0$ and defining $w^n_{\mathbf{k},\mathbf{k}_0}(\mathbf{r}) \equiv e^{i\mathbf{k}_0\cdot\mathbf{r}}u^n_{\mathbf{k}}(\mathbf{r})$, we have

$$p^2\left(e^{i\mathbf{k}\cdot\mathbf{r}}u^n_{\mathbf{k}}(\mathbf{r})\right) = p^2\left(e^{i\Delta\mathbf{k}\cdot\mathbf{r}}w^n_{\mathbf{k},\mathbf{k}_0}(\mathbf{r})\right) = e^{i\Delta\mathbf{k}\cdot\mathbf{r}}(p^2 + 2\hbar\Delta\mathbf{k}\cdot\mathbf{p} + \hbar^2(\Delta\mathbf{k})^2)w^n_{\mathbf{k},\mathbf{k}_0}(\mathbf{r}),$$

so that the Hamiltonian for the function $w^n_{\mathbf{k},\mathbf{k}_0}$ is

$$\left\{\left[\frac{p^2}{2m_0} + V\right] + \frac{\hbar}{m_0}\Delta\mathbf{k}\cdot\mathbf{p}\right\}w^n_{\mathbf{k},\mathbf{k}_0} = \left(E^n_{\mathbf{k}} - \frac{\hbar^2(\Delta\mathbf{k})^2}{2m_0}\right)w^n_{\mathbf{k},\mathbf{k}_0}.$$

Now, as before, at the $\mathbf{k}_0$ point it holds $w^n_{\mathbf{k},\mathbf{k}_0} = \psi_{n\mathbf{k}_0}$, and we are assuming to know these wavefunctions and the respective eigenenergies $E^n_{\mathbf{k}_0}$. Then the same formalism described above can be applied, where the $\mathbf{k}$ variable (i.e. the displacement from the Γ point) is replaced by $\Delta\mathbf{k}$ (i.e. the displacement from $\mathbf{k}_0$). As a final remark, we note that the approximation of non-degenerate bands is valid also for the conduction band at the L point and at the band minima along the Δ lines, since at these points we have only a valley degeneracy, that is there are degenerate states, but at different $\mathbf{k}$ points and not at the same $\mathbf{k}_0$ point.

### 1.6.2 k·p model for heterostructures: the envelope-function approximation

The $\mathbf{k}\cdot\mathbf{p}$ model applied to heterostructures has been studied for many years, starting from very simple models up to the "thirty-band" models mentioned at the beginning of Sec. 1.6. We refer to the literature for a detailed description of them, and in

particular to the book of Bastard [49] and to the works of Burt (see for instance Ref. [53] for the justification of the application of the effective-mass approach to microstructures). Here, we just limit to a brief discussion on the derivation of the envelope-function equation when we consider states originating mainly from only one band (e.g., one conduction band), referring to the above-mentioned works for the discussion of the adopted approximations.

The complete Hamiltonian of a multilayer system is

$$\left[\frac{p^2}{2m_0} + V_{cr}(\mathbf{r}) + U(z)\right]\Psi(\mathbf{r}) = E\Psi(\mathbf{r}), \tag{1.44}$$

where $V_{cr}$ is the crystalline potential, which we assume periodic within each material, $m_0$ is the free-electron mass and $U(z)$ is a possibly non-zero external potential due for instance to an external electric field, to a charge rearrangement in the system which can induce a band bending, and so on.

We write the generic eigenstate $\Psi_i$ of the heterostructure as a linear combination of the complete set $\{u_{n'0}\}$ of the periodic part of the Bloch functions at $\Gamma$:

$$\Psi_i(\mathbf{r}) = \sum_{n'} F^i_{n'}(\mathbf{r}) u_{n'0}(\mathbf{r}), \tag{1.45}$$

where $F^i_{n'}$ is the $n'$−th component of the so-called envelope function associated to $\Psi_i$ (for simplicity, we focus on the minimum at $\Gamma$, and drop in the following the index 0 from the functions $u_{n'0}$, but the same reasoning applies to the other conduction-band minima).

Note that the functions $u_{n'0}(\mathbf{r})$ are in general different in the different materials that compose the heterostructure. The expansion (1.45) is a good approximation of the actual wavefunction if the external potentials and the system composition, and thus the envelope function $F$ vary very slowly with respect to the unit cell size. Alternatively, if the two neighboring materials are similar, one could assume as a first approximation that the periodic part of the bulk wavefunction is the same for the two materials.

The index $n'$ in Eq. (1.45) should run over all the eigenstates at $\Gamma$. However, for practical reasons, it is typically limited to a subset of $\Gamma$ eigenstates of the bulk crystal (e.g., the lowest conduction band and the HH, LH and SO valence bands), as already discussed in Sec. 1.6.1 in the bulk case. Note that we can write the envelope function as a vector $F = (F_1, \ldots, F_s)^t$ where $s$ is the number of bands that we are considering in the sum of Eq. (1.45), so that we can also write $\Psi = F \cdot (u_1, \ldots, u_s)$.

Let us discuss the equation that is satisfied by the functions $u_n$. If we are at position $\mathbf{r}$ in the region occupied by the $j$−th material of a multilayer system, and we are far from the interfaces separating different materials, then the following equation for the bulk $j$−th material holds (in absence of external fields):

$$\left(\frac{p^2}{2m_0} + V_{cr}(\mathbf{r})\right) u^j_{n'}(\mathbf{r}) = E^j_{n'} u^j_{n'}(\mathbf{r}). \tag{1.46}$$

Here, $V_{cr}(\mathbf{r})$ is the crystalline potential of the material $j$ and $E_n^j$ is the bulk energy of the $n-$th state at $k = 0$ for the $j-$th material. Due to the dependence on the material $j$, this energy is in fact dependent on $z$ (for planar heterostructures grown along $z$): $E_n^j \equiv W_n(z)$. This function of $z$ is the band profile for the $n-$th band. Basically, as we can deduce from Eq. (1.46), $W_n(z)$ gives the energy of the $n-$th band edge in the bulk of the material in the position $z$, correctly including the band offset (discussed in Sec. 1.5). Using this notation, we can rewrite Eq. (1.46) as

$$\left(\frac{p^2}{2m_0} + V_{cr}(\mathbf{r})\right) u_{n'}(\mathbf{r}) = W(z) u_{n'}(\mathbf{r}), \tag{1.47}$$

where we do not write anymore the index $j$ explicitly, since it can be deduced from the coordinate $\mathbf{r}$.

As a preliminary step, let us calculate the result of the action of the momentum operator and of its square modulus on a product of two functions:

$$\begin{aligned} &\mathbf{p}(Fu) = (\mathbf{p}F)u + F(\mathbf{p}u); \\ &p^2(Fu) = \mathbf{p}\left[(\mathbf{p}F)u + F(\mathbf{p}u)\right] = (p^2F)u + 2(\mathbf{p}F)\cdot(\mathbf{p}u) + F(p^2u). \end{aligned} \tag{1.48}$$

We now substitute the expression (1.45) for $\Psi$ in the Hamiltonian equation (1.44) and exploit the relation (1.48) to obtain

$$\sum_{n'}\left\{\frac{1}{2m_0}\left[(p^2F_{n'})u_{n'} + 2(\mathbf{p}F_{n'})\cdot(\mathbf{p}u_{n'})\right] + F_{n'}\left(\frac{p^2}{2m_0} + V_{cr}\right)u_{n'} + \right.$$
$$\left. + (U - E)F_{n'}u_{n'}\right\} = 0.$$

Substituting the result of Eq. (1.47) we rewrite the above equation as

$$\sum_{n'}\left\{\frac{1}{2m_0}\left[(p^2F_{n'})u_{n'} + 2(\mathbf{p}F_{n'})\cdot(\mathbf{p}u_{n'})\right] + F_{n'}u_{n'}(U(z) + W(z) - E)\right\} = 0.$$

We now multiply on the left by $u_n^*$ and integrate over a unit cell. In this integration, we use the approximation that the envelope functions $F_n$ are approximately constant over a unit cell due to their slow spatial variation, as discussed above, and the same holds for $U$. Moreover, we remind that (within a unit cell) the $u_n$ are orthogonal, being solutions of the Hamiltonian equation (1.46) for different eigenvalues, i.e. $\langle u_n|u_{n'}\rangle = \delta_{nn'}$. We thus obtain

$$\frac{p^2}{2m_0}F_n + \sum_{n'\neq n}\frac{1}{m_0}(\mathbf{p}F_{n'})\cdot\mathbf{p}_{n'n} + F_n(U + W - E) = 0, \tag{1.49}$$

where we have defined $\mathbf{p}_{n'n} = \langle u_n|\mathbf{p}|u_{n'}\rangle$ as in the previous section, and we have excluded in the sum the term $n' = n$ since $p_{nn} = 0$ for parity reasons.

We have thus obtained a set of coupled Hamiltonian-like equations for the components $F_n$ of the envelope function. We consider the Ben Daniel–Duke model

and focus on a state $\Psi$ of the conduction band of the heterostructure. We represent this state on a basis composed of a single conduction band ($n = c$) of the bulk material and of a finite set of valence bands labeled by the index $v$. Then, we expect that the main contribution to $\Psi$ comes from the envelope function $F_c$ with $n' = c$, and we can try to write an equation for $F_c$ only, eliminating the explicit dependence on the $\{F_v\}$. In fact, from Eq. (1.49) for the cases $n' = v$ (ignoring the free-electron term, i.e. the term $p^2/2m_0$, and also the coupling between valence bands $p_{vv'}$), we can easily obtain an expression for each valence component $F_v$ of the envelope function associated to $\Psi$ in terms of the conduction component $F_c$. With these approximations, we obtain:

$$F_v = \frac{1}{E - W_v(z) - U(z)} \frac{\mathbf{p}_{cv}}{m_0} \cdot (\mathbf{p}F_c).$$

We can now substitute this expression in the equation (1.49) and derive an equation for the conduction-part $F_c$ of the envelope function only. In particular the term $\sum_{n'\neq n} \frac{1}{m_0}(\mathbf{p}F_{n'}) \cdot \mathbf{p}_{n'n}$ of Eq. (1.49) gives, for $n = c$, $n' = v$:

$$\begin{aligned} &\frac{1}{m_0^2} \sum_v \mathbf{p}_{vc} \cdot \mathbf{p} \left[ \frac{1}{E - W_v(z) - U(z)} \mathbf{p}_{cv} \cdot (\mathbf{p}F_c) \right] = \\ =&\frac{1}{m_0^2} \sum_{\alpha,\beta} p^\alpha \sum_v \frac{p^\alpha_{vc} p^\beta_{cv}}{E - W_v(z) - U(z)} p^\beta F_c \end{aligned} \tag{1.50}$$

where the indices $\alpha$ and $\beta$ run over the spatial coordinates $x$, $y$ and $z$.

The simplest result can be obtained assuming that $E - W_v \approx W_c - W_v$ for heterostructure states $\Psi$ with energy $E$ in the conduction band, i.e. assuming that the energy $E$ of the heterostructure state is not too far away from the bulk eigenvalue $W_c$ with respect to the gap $W_c - W_v$ in the bulk[3]. Moreover, we neglect the $U(z)$ contribution in the denominator, assuming that the perturbations due to the external fields are small with respect to the energy gaps.

Then, we can exploit the definition of the effective mass tensor of Eq. (1.43) from which

$$\sum_v \frac{p^\alpha_{cv} p^\beta_{vc}}{W_c(z) - W_v(z)} = \frac{m_0^2}{2} \left[ \left( \frac{1}{m^*(z)} \right)_{\alpha\beta} - \frac{\delta_{\alpha\beta}}{m_0} \right],$$

where the $z$ dependence of $m^*$ accounts for the different effective masses in the different materials composing the heterostructure.

Substituting the above expression and Eq. (1.50) in Eq. (1.49) with $n = c$ and $n' = v$, we finally obtain:

$$\frac{p^2}{2m_0} F_c + [U(z) + W_c(z) - E]F_c + \frac{1}{2} \sum_{\alpha\beta} p^\alpha \left[ \left( \frac{1}{m^*(z)} \right)_{\alpha\beta} - \frac{\delta_{\alpha\beta}}{m_0} \right] p^\beta F_c = 0$$

[3]Note that this approximation gives parabolic subbands. In general, to take into account also non-parabolic effects, one should define an effective mass that depends also on the energy $E$. However, these effects are relevant only in materials with very narrow gap, or for heterostructure states with energy much larger than the energy minimum (e.g. due to a large in-plane momentum).

or, simplifying the first term and the term with $\delta_{\alpha\beta}$:

$$\frac{1}{2}\sum_{\alpha\beta} p^{\alpha}\left(\frac{1}{m^*(z)}\right)_{\alpha\beta} p^{\beta}F_c + [U + W_c]F_c = EF_c \tag{1.51}$$

which is the reduced Hamiltonian equation for the $F_c$ component of the eigenvector $\Psi$.

We assume now that the inverse mass tensor does not couple the growth direction $z$ with the motion on the $xy$ plane, and in particular that it has the form

$$\left(\frac{1}{m^*}\right)_{\alpha\beta} = \begin{pmatrix} 1/m_x^* & 0 & 0 \\ 0 & 1/m_y^* & 0 \\ 0 & 0 & 1/m_z^* \end{pmatrix};$$

the generalization with non-diagonal effective-mass tensor is given in Sec. 1.8.1. We can then separate the $z$ variable in Eq. (1.51) and choose the following form for the envelope function $F_c$:

$$F_c(x, y, z) = e^{ik_x x + ik_y y}\chi(z),$$

so that Eq. (1.51) becomes

$$\left\{-\frac{\hbar^2}{2}\frac{\partial}{\partial z}\frac{1}{m_z^*(z)}\frac{\partial}{\partial z} + [U(z) + W_c(z)]\right\}\chi(z) = E'\chi(z), \tag{1.52}$$

where the energy $E'$ is the $z$ contribution to the total energy:

$$E = E' + \frac{\hbar^2 k_x^2}{2m_x} + \frac{\hbar^2 k_y^2}{2m_y}.$$

Note that in Eq. (1.52) the kinetic operator has the form $\partial_z \frac{1}{m_z^*(z)}\partial_z$, i.e. the effective mass is between the two derivation operators. This is very important for what concerns the conditions to be satisfied by $\chi$ at the interfaces between materials with different $m^*$. In fact, multiplying Eq. (1.52) by $\chi^*(z)$ and taking the imaginary part, one gets

$$\mathrm{Im}\left[\chi^*(z)\partial_z\left(\frac{1}{m_z^*(z)}\partial_z\chi(z)\right)\right] = 0, \tag{1.53}$$

where we have used the fact that both $\chi^*\chi$ and the potential are real functions. Now, Eq. (1.53) can be rewritten as

$$\partial_z\left[\chi^*(z)\frac{1}{m_z}\partial_z\chi(z) - \chi(z)\frac{1}{m_z}\partial_z\chi^*(z)\right] = 0,$$

that is the conservation equation for the current $J$, which is proportional to the quantity between square brackets. Then, this quantity is conserved across an interface between two materials if both

$$\chi(z) \qquad \text{and} \qquad \frac{1}{m_z(z)}\frac{\partial}{\partial z}\chi(z) \tag{1.54}$$

**Table 1.6** – Relevant conduction-band masses for Si and Ge, in units of the electron mass. $m^{\Delta}_{l,t}$ are the longitudinal and transverse masses of the minima along the $\Delta$ line. $m^{\mathrm{L}}_{l,t}$ are the longitudinal and transverse masses of the minima at the L points. $m_{\Gamma}$ refers to the isotropic mass of the $\Gamma_7^-$ minimum (see Fig. 1.8). The theoretical data are from the parametrization of Ref. [41]. The experimental data are taken from Madelung [22].

| | Si (theory) | Si (exp.) | Ge (theory) | Ge (exp.) |
|---|---|---|---|---|
| $m^{\Delta}_{l}$ | 0.918 | 0.9163 (1.26 K) | 0.955 | |
| $m^{\Delta}_{t}$ | 0.197 | 0.1905 (1.26 K) | 0.203 | |
| $m^{\mathrm{L}}_{l}$ | 1.659 | | 1.742 | 1.59 (120 K) |
| $m^{\mathrm{L}}_{t}$ | 0.133 | | 0.0984 | 0.0823 (120 K) |
| $m_{\Gamma}$ | | | | 0.0380 (30 K) |

are continuous at the interface.

Summarizing, the envelope function is the product of a plane wave on the $xy$ plane and the function $\chi(z)$, that can be found numerically solving Eq. (1.52) and enforcing the continuity of the quantities (1.54) at the interfaces.

## 1.7 Effective-mass tensors in the conduction band of Si and Ge

We now focus on the effective masses around the most relevant conduction-band minima in bulk Si and Ge.

For what concerns the $\Gamma$ edges, the effective mass tensor is a multiple of the identity (i.e., it is isotropic). We then know that both Si and Ge have other (local or global) conduction-band minima along the $\Delta$ lines and at the L points (see e.g. Fig. 1.8). For these minima, the tensor is not a multiple of the identity. In both kind of valleys ($\Delta$ and L), the inverse-mass tensor is diagonal in a basis set which has one ("longitudinal") direction along the line connecting the $\Gamma$ point with the $\mathbf{k}$ point at which the minimum occurs, and two equivalent "transverse" directions[4]. Moreover, both for L and $\Delta$ minima, the longitudinal masses are larger than the transverse masses.

The values of the relevant masses for Si and Ge at the different conduction-band minima are reported in Table 1.6. In Fig. 1.18 we also plot the ellipsoids of constant energy around the energy minima along the $\Delta$ lines and at the L points.

[4]For strained $Si_{1-x}Ge_x$ alloys, the two transverse directions are no more equivalent, even if the difference between the two transverse masses is very small and can be often disregarded. For a parametrization of the longitudinal and transverse effective masses at $\Delta$ and L for strained SiGe alloys, see Ref. [41].

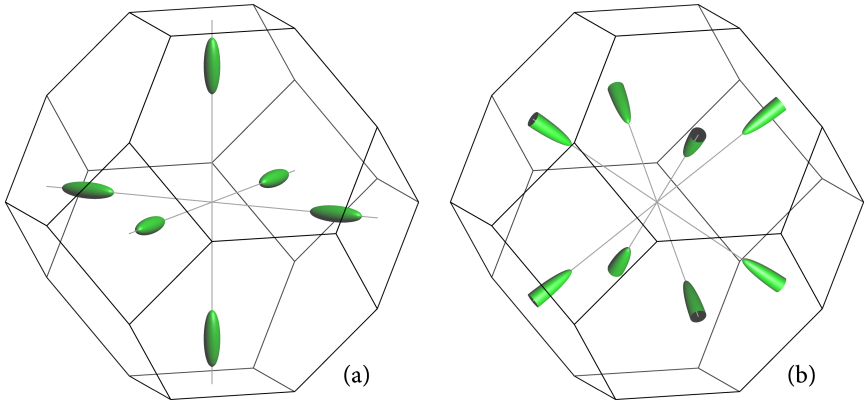


**Figure 1.18** – Schematic of the ellipsoids of constant energy around the energy minima along the Δ lines (panel a) or at the L points (panel b) for Si and Ge.

## 1.8 Evaluation of quasi-Fermi energies and effective masses

In the calculation of most electronic, optical and transport properties one has to evaluate an integral over the whole Brillouin zone (BZ) of a given quantity. This is true for instance for the calculation of the absorption or of the gain coefficient, as described in Sec. 2.1.

The most simple calculation of this kind is the counting up of filled states in a given band. To clarify this concept, let us consider a simple model system with one valence band and one conduction band. If the system is pumped with a light source (with energy larger than the bandgap) some electrons are excited from the valence to the conduction band. If the intraband relaxation channels (for instance via acoustic phonons) are much faster than the interband recombination, one can consider that a quasi-equilibrium is reached inside each of the two bands, so that we can define two quasi-Fermi energies $E_c^f$ and $E_v^f$ in the conduction and valence band, respectively. The values of $E_c^f$ and $E_v^f$ determine the number of electrons (holes) in the conduction (valence) band. This number can be calculated assuming a Fermi–Dirac distribution of the carriers within each band, so that the total number of electrons (holes) is given by:

$$N_{e,h} = \sum_{\mathbf{k}} \sum_{\sigma} f_{e,h}(E_{c,v}(\mathbf{k})), \tag{1.55}$$

i.e. by the sum over all states $(\mathbf{k}, \sigma)$ of the corresponding Fermi-Dirac distribution function defined by

$$f_{c,v}(E) = \frac{1}{1 + e^{(E - E_{c,v}^f)/k_B T}}, \qquad f_e(E) = f_c(E), \qquad f_h(E) = 1 - f_v(E).$$

In the above expressions, $k_B$ is the Boltzmann constant, $T$ is the electron temperature, $E_{c,v}(\mathbf{k})$ are the band energy dispersions of the conduction and valence bands and $f_h$ is the distribution function for holes, so that we have to count the empty states and then $f_h(E) = 1 - f_v(E)$. Finally, the sum over states $(\mathbf{k}, \sigma)$ is made over all $\mathbf{k}$ points

in the BZ and over the two spin polarizations; since the quantity to be summed does not depend on the spin in this case, we can simply replace this sum with a factor of 2.

The number of $\mathbf{k}$ points in the BZ is equal to the number of unit cells of the crystal and thus it is very large; hence, we can safely convert the sum of Eq. (1.55) with an integral over the whole BZ obtaining

$$N_{e,h} = \frac{V}{(2\pi)^3} 2 \int_{BZ} d^3\mathbf{k} f_{e,h}(E_{c,v}(\mathbf{k})), \tag{1.56}$$

where the factor of two takes into account the spin degeneracy as discussed above, and the factor $V/(2\pi)^3$ is the density of $\mathbf{k}$ points for a 3D crystal.

Since $f_{e,h}$ is a function of the energy, it would be much more convenient to convert this integral over all $\mathbf{k}$ points to an integral over energy. In order to do this, we have to know the expression of $E_{c,v}(\mathbf{k})$. To simplify the notation, we focus on the simple case of parabolic bands, that is often adopted in this Thesis when an analytical expression is needed, and moreover it is a quite good approximation near a band edge. Then, focusing for instance on the conduction band (and assuming for simplicity of notation that the band minimum is at the Γ point), we have

$$E_c(k) = E_c^0 + \frac{\hbar^2 k^2}{2m_c^*}, \tag{1.57}$$

where $m_c^*$ is the conduction effective mass. This form of $E_c(k)$ implies that the bands are isotropic (i.e., the energy dispersion does not depend on the direction of the $\mathbf{k}$ vector) so that the band energy depends only on $k = |\mathbf{k}|$. In this approximation we can rewrite Eq. (1.56) in spherical coordinates as

$$N_e = \frac{2V}{(2\pi)^3} \int_{BZ} 4\pi k^2 dk f_e(E_c(k)). \tag{1.58}$$

Then, using the inverse of Eq. (1.57):

$$k = \sqrt{\frac{2m_c^*(E_c(k) - E_c^0)}{\hbar^2}}$$

we can change the integration variable in Eq. (1.58) finally obtaining

$$n_e = \frac{1}{2\pi^2} \left(\frac{2m_c^*}{\hbar^2}\right)^{3/2} \int_{E_0}^{\infty} dE \sqrt{E - E_c^0} f_c(E),$$

where $n_e = N_e/V$ is the density of electrons in the conduction band, and we have extended the integral up to infinity thanks to the natural cutoff given by the Fermi–Dirac distribution.

From the last equation, we see that we can write the integral as

$$n_e = \int_{E_c^0}^{\infty} dE g_c^{3D}(E) f_e(E), \tag{1.59}$$

where

$$g_c^{3D}(E) = \frac{1}{2\pi^2}\left(\frac{2m_c^*}{\hbar^2}\right)^{3/2}\sqrt{E - E_c^0} \tag{1.60}$$

is the 3D density of states (DOS) for a parabolic isotropic band with effective mass $m_c^*$, including the factor of 2 for the sum over the spins. Note that we can implicitly take into account the bottom integration limit $E_c^0$ of Eq. (1.59) if in Eq. (1.60) we assume that the square root is defined as

$$\sqrt{x} = \begin{cases} \sqrt{x} & x \geq 0 \\ 0 & x < 0 \end{cases}. \tag{1.61}$$

Note that the same steps can be followed for any integrand factor that depends only on the energy, and not only for the Fermi–Dirac distribution $f_{e,h}$.

The same calculation can be performed also for a 2D gas, as for instance to calculate the occupation of a given subband of a quantum well. In this case, the density of $\mathbf{k}$ points is $S/(2\pi^2)$, where $S$ is the sample surface; the integral can be recast in cylindrical coordinates as $\int d^2\mathbf{k} \to \int 2\pi k dk$, and we finally obtain

$$n_e^{2D} = N_e/S = \int_{E_0}^{\infty} dE g_c^{2D}(E) f_e(E),$$

(where $E_0$ is now the subband edge and $n_c^{2D}$ is the surface charge density in the given subband), with

$$g_c^{2D}(E) = \frac{m_c^*}{\pi\hbar^2}\theta(E - E_0). \tag{1.62}$$

Here again we have inserted the Heaviside step function $\theta(E)$ to implicitly take into account the bottom integration limit $E_0$.

A (straightforward) generalization, which is very important for Si and Ge, is needed for the case of non-isotropic masses (as it happens at the L and Δ minima). In this case, it is convenient to write the (parabolic) energy dispersion in a orthogonal coordinate system 1, 2, 3 in which the effective-mass tensor is diagonal:

$$E\big(\mathbf{k} = (k_1, k_2, k_3)\big) = E_0 + \frac{\hbar^2 k_1^2}{2m_1^*} + \frac{\hbar^2 k_2^2}{2m_2^*} + \frac{\hbar^2 k_3^2}{2m_3^*}.$$

In this case, we can define $k_i' = k_i/\sqrt{m_i^*}$ for $i = 1, 2, 3$, so that $E(\mathbf{k}) = \hbar^2/2\big[(k_1')^2 + (k_2')^2 + (k_3')^2\big]$. Then, in this primed system the energy dispersion is isotropic, and we can perform the same steps as before; the final result is that the effective mass $m_c^*$ of Eq. (1.60) must be substituted in the non-isotropic case by the density-of-states effective-mass

$$m_{\mathrm{DOS}}^* = \sqrt[3]{m_1^* m_2^* m_3^*}$$

or, in the 2D case of Eq. (1.62), by

$$m_{\mathrm{DOS}}^* = \sqrt{m_1^* m_2^*}.$$

In the 2D case, $m_1^*$ and $m_2^*$ represent the two masses in the plane orthogonal to the growth axis. In Sec. 1.8.1 we describe how to evaluate these masses when the growth axis is not one of the principal axes of the inverse-mass tensor.

For more complicated (or realistic) calculations, taking into account also band non-parabolicities, band warping and so on, we have to numerically evaluate the DOS from a full TB band calculation. In this case, the electronic states on a 3D grid in $\mathbf{k}$ space can be calculated by diagonalization of the TB Hamiltonian matrix, and then we can evaluate the DOS directly from the sum in $\mathbf{k}$−space of Eq. (1.55) using a histogram technique. This is usually satisfactory in many cases, also thanks to the great computational power of modern computers. If however we want to reduce the number of $\mathbf{k}$ points for which the Hamiltonian matrix has to be diagonalized (or, equivalently, we want to increase the precision of the calculation for a fixed number of $\mathbf{k}$ points) we can use more sophisticated methods, as the tetrahedron method (for more details, see Ref. [54]).

### 1.8.1 Rotation of the effective-mass tensor

Let us consider the inverse-mass tensor in a basis $(\hat{\mathbf{x}}', \hat{\mathbf{y}}', \hat{\mathbf{z}}')$ in which it is diagonal:

$$\left(\frac{1}{m^*}\right)_{ij} = \begin{pmatrix} \frac{1}{m_T} & 0 & 0 \\ 0 & \frac{1}{m_T} & 0 \\ 0 & 0 & \frac{1}{m_L} \end{pmatrix}. \tag{1.63}$$

We are assuming here that two of the three masses (the transverse masses) are equal, while the third longitudinal one along the third basis vector can be in general different (even if the considerations below can be easily generalized to the case with three different masses). This is in fact the case for the conduction L valleys (with $\hat{\mathbf{z}}'$ axis along the Γ−L line) and for the Δ valleys (with $\hat{\mathbf{z}}'$ axis along the Γ−X line), as visible from the ellipsoids of constant energy shown in Fig. 1.18. Note that, due to the degeneracy on the $x'y'$ plane, in order to define the basis we simply have to give the coordinates of the versor $\hat{\mathbf{z}}'$: for instance, if we consider the L valley at $\frac{\pi}{a}(1,1,1)$, we choose $\hat{\mathbf{z}}' = \frac{1}{\sqrt{3}}(1,1,1)$. Note that we express the coordinates of the vectors in the system $xyz$ defined by the crystalline axes, so that the vector with components $(0,0,1)$ is along the [001] direction.

Our aim is to calculate the confinement mass $m_3^*$ along a generic growth direction $\hat{\mathbf{v}}$, possibly different from one of the three basis vectors, and the two principal masses $m_1^*$ and $m_2^*$ in the plane orthogonal to this direction. In this Thesis we consider structures grown along the [001] direction, so that $\hat{\mathbf{v}} = (0,0,1)$.

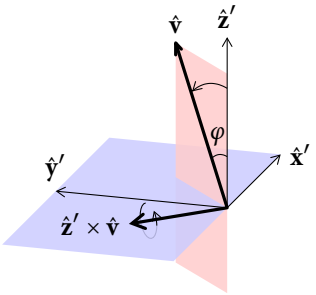


The first operation that we have to perform is to rotate the tensor so that one of the basis vectors (e.g. the third one $\hat{\mathbf{z}}'$) now points along $\hat{\mathbf{v}}$.

We thus need to find an orthogonal transformation which transforms the $(\hat{\mathbf{x}}', \hat{\mathbf{y}}', \hat{\mathbf{z}}')$ unit vectors to a new orthogonal set with $\hat{\mathbf{z}}' \equiv \hat{\mathbf{v}}$. We

call this new reference frame the growth reference frame. The simplest transformation is a rotation around the axis defined by $\hat{\mathbf{z}}' \times \hat{\mathbf{v}}$ (assuming, of course, that $\hat{\mathbf{v}}$ is not already in the $\hat{\mathbf{z}}'$ direction); the cosine of the angle of rotation $\varphi$ is given by $\hat{\mathbf{z}}' \cdot \hat{\mathbf{v}}$ (always assuming unit vectors).

To obtain an explicit form for the rotation given above (which brings $\hat{\mathbf{z}}'$ on $\hat{\mathbf{v}}$) we use the fact that the Lie algebra of the three-dimensional rotation group $SO_3$ is the group of the antisymmetric $3 \times 3-$matrices (satisfying $A^T = -A$).

Since the generators of the rotations around the axes are

$$A_{\mathbf{x}} = \begin{pmatrix} 0 & 0 & 0 \\ 0 & 0 & -1 \\ 0 & 1 & 0 \end{pmatrix}, \; A_{\mathbf{y}} = \begin{pmatrix} 0 & 0 & 1 \\ 0 & 0 & 0 \\ -1 & 0 & 0 \end{pmatrix}, \; A_{\mathbf{z}} = \begin{pmatrix} 0 & -1 & 0 \\ 1 & 0 & 0 \\ 0 & 0 & 0 \end{pmatrix},$$

the rotation around a unit vector of coordinates $(x, y, z)$ of an angle $\varphi$ can be written as

$$Q = e^{\varphi(xA_{\mathbf{x}} + yA_{\mathbf{y}} + zA_{\mathbf{z}})},$$

where we have to compute the exponential of a matrix.

It can be proven that the explicit form of this matrix is

$$Q = \begin{pmatrix} x^2(1-\cos\varphi) + \cos\varphi & xy(1-\cos\varphi) - z\sin\varphi & xz(1-\cos\varphi) + y\sin\varphi \\ xy(1-\cos\varphi) + z\sin\varphi & y^2(1-\cos\varphi) + \cos\varphi & yz(1-\cos\varphi) - x\sin\varphi \\ xz(1-\cos\varphi) - y\sin\varphi & yz(1-\cos\varphi) + x\sin\varphi & z^2(1-\cos\varphi) + \cos\varphi \end{pmatrix}$$

where, for our purposes, $(x, y, z)$ are the coordinates of the cross product $\hat{\mathbf{z}}' \times \hat{\mathbf{v}}$ after the normalization to one, and $\cos\varphi = \hat{\mathbf{v}} \cdot \hat{\mathbf{z}}'$.

In this way we have obtained the matrix which transforms the components of the vector from the growth reference frame, which coincides with the $xyz$ frame for $\hat{\mathbf{v}} = (0, 0, 1)$, to the $x'y'z'$ reference frame. Then, we can transform the inverse mass tensor from the $x'y'z'$ reference frame, in which it has the diagonal form given in Eq. (1.63), to the growth reference frame by means of the transformation[5] $Q(1/m^*)_{ij}Q^T$.

Since the case of $\Delta$ valleys is trivial, we discuss here in detail the particular case of $\hat{\mathbf{z}}' = \frac{1}{\sqrt{3}}(1, 1, 1)$, typical of L valleys. The final rotated matrix in the $xyz$ system, using the approach described above, is

$$\left(\frac{1}{m^*}\right)_{ij} = \begin{pmatrix} \frac{2m_L+m_T}{3m_Lm_T} & \frac{m_T-m_L}{3m_Lm_T} & \frac{m_T-m_L}{3m_Lm_T} \\ \frac{m_T-m_L}{3m_Lm_T} & \frac{2m_L+m_T}{3m_Lm_T} & \frac{m_T-m_L}{3m_Lm_T} \\ \frac{m_T-m_L}{3m_Lm_T} & \frac{m_T-m_L}{3m_Lm_T} & \frac{2m_L+m_T}{3m_Lm_T} \end{pmatrix}. \tag{1.64}$$

From this point on, since we discuss only of this growth reference frame, we call $x$, $y$, $z$ the three coordinates in this basis, so $i$ and $j$ indices run over $\{x, y, z\}$

[5] Note that the matrix $Q$ is expressed in the coordinate system defined by the crystalline directions $xyz$, while the tensor of Eq. (1.63) is in the $x'y'z'$ basis. Then, in general, if we want to use the $Q$ matrices to perform the transformation, we have to go through the crystalline coordinate system in each transformation, i.e. we have to perform the rotation in two steps, first bringing $\hat{\mathbf{v}}$ onto [001]$\equiv \hat{\mathbf{z}}$, and then from $\hat{\mathbf{z}}$ to $\hat{\mathbf{z}}'$: here, the first transformation is simply the identity.

and that $z$ indicates the growth direction. We want now to focus on the case of systems with a potential energy depending only on $z$, as inversion layers or multilayer systems. In this case, the Hamiltonian matrix for the envelope functions $\psi$ reads $[T+V(z)]\psi = E\psi$, with the potential energy depending only on the growth direction $z$ and the kinetic energy is

$$T = \frac{1}{2}\sum_{i,j} p_i w_{ij} p_j, \tag{1.65}$$

where $w_{ij} = (1/m^*)_{ij}$ is the inverse mass tensor in the coordinate system in which the growth direction is along the third axis, i.e. the one obtained with the steps above.

Using this form for $T$, the motions along $x$, $y$ and $z$ are coupled. In order to decouple the motion on the plane from the motion along $z$, we adopt the method described in Ref. [55] that we briefly summarize here.

Since the potential $V(z)$ depends on $z$ only, we can choose the solution $\psi$ of the form

$$\psi(x, y, z) = \xi(z) e^{ik_1 x + ik_2 y}. \tag{1.66}$$

Substituting this form in the Schrödinger equation and using the Eq. (1.65) for the kinetic energy $T$, we find the following equation for $\xi$:

$$-\frac{1}{2} w_{33}\hbar^2 \frac{d^2\xi}{dz^2} - i\hbar^2(w_{13}k_1 + w_{23}k_2)\frac{d\xi}{dz} + V(z)\xi(z) = E'\xi(z), \tag{1.67}$$

with

$$E = E' + \frac{1}{2}\hbar^2(w_{11}k_1^2 + 2w_{12}k_1k_2 + w_{22}k_2^2).$$

Eq. (1.67) is not in the usual "Schrödinger equation" form, since it has a first-order derivative with respect to $z$. To remove it, we make the further substitution

$$\xi(z) = \zeta(z) e^{-iz(w_{13}k_1 + w_{23}k_2)/w_{33}},$$

so that $\zeta$ satisfies

$$-\frac{\hbar^2}{2m_3^*}\frac{d^2\zeta}{dz^2} + V(z)\zeta(z) = E''\zeta(z), \tag{1.68}$$

with $m_3 = w_{33}^{-1}$ and

$$\begin{aligned} E(k_1, k_2) =& E'' + \frac{1}{2}\hbar^2\left[\left(w_{11} - \frac{w_{13}^2}{w_{33}}\right)k_1^2 + \right. \\ &\left. + 2\left(w_{12} - \frac{w_{13}w_{23}}{w_{33}}\right)k_1k_2 + \left(w_{22} - \frac{w_{23}^2}{w_{33}}\right)k_2^2\right]. \end{aligned} \tag{1.69}$$

We have then obtained with Eq. (1.68) a usual Schrödinger equation in $z$, whose solution gives the energies $E''$; we immediately see that the confinement mass $m_3^*$ is precisely given by the inverse of the (3,3) element of the rotated tensor, since it is the one that determines the energy levels $E''$. The actual energy $E$ of the electron

is given by Eq. (1.69): the term in square brackets basically takes into account the kinetic energy due to the motion in the $xy$ plane. Then, the two principal masses $m_1^*$ and $m_2^*$ can be found as the (inverse of) the eigenvalues of the following matrix:

$$\begin{pmatrix} w_{11} - \dfrac{w_{13}^2}{w_{33}} & w_{12} - \dfrac{w_{13}w_{23}}{w_{33}} \\ w_{12} - \dfrac{w_{13}w_{23}}{w_{33}} & w_{22} - \dfrac{w_{23}^2}{w_{33}} \end{pmatrix}.$$

In particular in the case of L valleys, using the coefficients $w_{ij} = (1/m^*)_{ij}$ of (1.64), the inverse of the eigenvalues are:

$$m_1^* = m_T, \qquad m_2^* = \frac{m_T + 2m_L}{3},$$

and for the confinement mass we get

$$m_3^* = \frac{3m_L m_T}{2m_L + m_T}.$$

## 1.9 Band bendings and Schrödinger–Poisson equation

When a MQW system is doped, the doping atoms can ionize and the resulting free electrons rearrange to reach an equilibrium condition. In particular, one common doping technique is the so-called modulation doping, where only the barriers are doped. Then, usually the doping charge is transferred into the well, so that the electrons are localized in a different spatial region with respect to the doping ions. This kind of doping scheme is often adopted because it provides a transport channel due to the free electrons which is located in the QW, while the charged ions remain in the barrier, separated from the transport channel. Since these ions act as scattering centers for the electrons, the spatial separation reduces the scattering and enhances the mobility of the system.

For large doping densities, however, one cannot neglect the effect of the electrostatic potential that builds up due to the charge localization. In this case, the approach that we describe here is needed to correctly calculate the band bendings that occur.

Due to the invariance of the system for translations along the growth plane, we consider only a one-dimensional problem along the growth direction $z$, which is sufficient and suitable for the study of MQWs and in general of planar heterostructures.

As we have described in Sec. 1.6.2, the envelope functions $\psi_{j,\alpha}(z)$ for the band $j$ satisfy the Schrödinger equation

$$\frac{\hbar^2}{2}\frac{d}{dz}\left(\frac{1}{m_j^*(z)}\frac{d}{dz}\right)\psi_{j,\alpha}(z) + V_j(z)\psi_{j,\alpha}(z) = E_{j,\alpha}\psi_{j,\alpha}(z), \tag{1.70}$$

where $E_{j,\alpha}$ is the eigenenergy of the $\alpha-$th state and $V_j(z) = -e\phi(z) + \Delta E_j(z)$ is the potential energy, which consists of a sum of the electrostatic contribution ($\phi(z)$ is the electrostatic potential) and of the energy $\Delta E_j(z)$ due to the band offset of the band $j$ under consideration.

The electrostatic potential $\phi(z)$ can be obtained solving the one-dimensional Poisson equation

$$\frac{d}{dz}\left(\varepsilon_s(z)\frac{d}{dz}\right)\phi(z) = \frac{-e}{\varepsilon_0}\big[N_D(z) - n(z)\big], \tag{1.71}$$

where $\varepsilon_s$ is the dielectric constant, $N_D$ the ionized donor concentration, and $n$ is the electron density distribution. Finally, the latter density is related to the wavefunctions $\psi_{j,\alpha}(x)$ by

$$n(z) = \sum_j \sum_\alpha \psi^*_{j,\alpha}(z)\psi_{j,\alpha}(z)n_{j,\alpha},$$

where $j$ runs over all bands under consideration, $\alpha$ indexes the different states and $n_{j,\alpha}$ is the electron occupation for each state. This occupation is obtained integrating the density of states times the Fermi distribution function. In particular, in 2D and under the assumption of parabolic bands, we can use the results for the DOS of Eq. (1.62) and solve analytically the integral, obtaining:

$$n_{j,\alpha} = \frac{m^*_{\mathrm{DOS}}}{\pi\hbar^2}\int_{E_{j,\alpha}}^{\infty}\frac{1}{1+e^{(E-E_F)/k_BT}}dE = \frac{m^*_{\mathrm{DOS}}k_BT}{\pi\hbar^2}\ln\left(1+e^{(E_F-E_{j,\alpha})/k_BT}\right),$$

where $E_F$ is the quasi Fermi energy in the conduction band. Note that, in the low-temperature limit $T \to 0$, the above expression further simplifies to

$$n_{j,\alpha} = \begin{cases} \frac{m^*_{\mathrm{DOS}}(E_F-E_{j,\alpha})}{\pi\hbar^2} & E_F > E_{j,\alpha} \\ 0 & E_F < E_{j,\alpha} \end{cases}.$$

The above equations (1.70) and (1.71) constitute a set of coupled equations, which must be solved together in order to find the final self-consistent solution. In the code, an iterative procedure is used, which has been carefully developed to be very stable and to converge to the correct solution also in strongly $n-$doped systems, as the ones that are discussed in Chap. 3. The details of the code are described in Sec. 3.A.

## 1.10 Evaluation of phonon scattering lifetimes

A key parameter in the design of quantum cascade structures, as those discussed in Chap. 3, are the non-radiative ISB relaxation lifetimes, which may originate from different mechanisms. One of them is the scattering due to the different kind of phonons in the crystal. The scattering rates between two subbands $i$ and $f$ belonging to the same valley (intravalley scattering) due to emission (upper sign) or absorption (lower sign) of optical and acoustic phonons can be respectively written as follows [56]

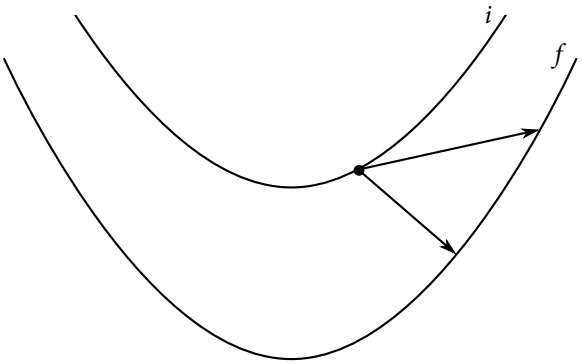


**Figure 1.19** – Some possible (intravalley) intersubband scattering processes involving acoustic or optical phonons between an initial subband $i$ and a final subband $f$.

(see also Fig. 1.19):

$$\frac{1}{\tau^{\pm}_{\text{opt}}} = \frac{D_0^2 m^* G}{4\pi\hbar^2\rho\omega_0}\left[n(\omega_0) + \frac{1}{2} \pm \frac{1}{2}\right]\Theta(E_i - E_f \mp \hbar\omega_0), \tag{1.72}$$

$$\frac{1}{\tau^{\pm}_{\text{ac}}} = \frac{\Xi_0^2 k_B T m^* G}{4\pi\hbar^3\rho v_s^2}\Theta(E_i - E_f).$$

In these equations $D_0$ and $\Xi$ are the scalar optical and acoustic deformation potentials, $\omega_0$ and $n(\omega_0)$ are the $q = 0$ optical phonon frequency and equilibrium number, $m^*$ is the two-dimensional DOS effective mass, $\rho$ is the mass density, $v_s$ is the sound velocity and $\Theta$ is the Heaviside step function. Some typical parameters for Si and Ge are collected in Ref. [56]. Finally, $G$ is the overlap factor defined by

$$G = \int dq_z \left|\langle f|e^{iq_z z}|i\rangle\right|^2. \tag{1.73}$$

In Si and Ge the phonon scattering is associated only to the mechanical deformations of the crystal, since Si and Ge are non-polar materials, and the energy dependence is simply given by a $\Theta$ function to take into account energy conservation. Instead, in the case of III-V compounds, due to polarization of the material associated to the longitudinal optical phonons, the scattering time shows a resonance at $\omega_0$.

In the above expressions, the only quantity to evaluate numerically from the wavefunctions is the overlap $G$ factor. The calculation requires the evaluation of an integral over the whole Brillouin zone of the square modulus of a matrix element (which is another integral). Moreover, the matrix element inside the integral contains the rapidly oscillating function $e^{iq_z z}$. It is then evident that a numerical evaluation of the $G$ factor can be problematic. A first approach that leads to accurate results for the evaluation of the matrix element

$$|\langle f|e^{iq_z z}|i\rangle|^2 = |\langle f|\cos(q_z z)|i\rangle|^2 + |\langle f|\sin(q_z z)|i\rangle|^2$$

consists in discretizing the $z$ axis and approximating the wavefunctions by linear interpolation of the sampling points. Then, the integrands in each interpolation interval are simply the products of a sin or cos function by a polynomial of degree

two, and can be evaluated analytically. Subsequently, the external integral $\int dq_z$ is performed (choosing a suitable finite region of integration, since the function $|\langle f|e^{iq_z z}|i\rangle|^2$ goes rapidly to zero for $|q_z| \to \infty$ [57]).

We emphasize here that for this problem, the routines that allow the evaluation of the integral of a generic function multiplied by a cos or sin function, as those implemented in the QuadPack library, cannot be implemented here: in fact, they require that the integrand function has continuous derivatives, otherwise large numerical errors may occur. However, the wavefunctions are usually evaluated solving the Schrödinger equation on a discretized set of values, so that the linear interpolation does not have a continuous derivative. Different interpolation schemes may partially solve the problem with increased computational time.

A better and easier method for the evaluation of Eq. (1.73) can however be found. In fact, we can think to the matrix element $\tilde{g}(q_z) = \langle f|e^{iq_z z}|i\rangle$ as the Fourier transform of the function $g(z) = \psi_i(z) \cdot \psi_f(z)$, where $\psi_i(z)$ and $\psi_f(z)$ are the envelope functions associated to the subbands $i$ and $f$. Then, $G$ is the square of the $\mathcal{L}_2$-norm of the function $\tilde{g}(q_z)$: $G = \|\tilde{g}(q_z)\|^2_{\mathcal{L}_2}$. We can thus apply the Parseval theorem, which relates the $\mathcal{L}_2$-norm of a function and of its Fourier transform by

$$\|\tilde{g}(q_z)\|^2_{\mathcal{L}_2} = 2\pi \|g(z)\|^2_{\mathcal{L}_2},$$

so that in conclusion $G$ can be rewritten as:

$$G = 2\pi \int dz |\psi_f(z)|^2 |\psi_i(z)|^2.$$

The advantage of this form is that now we need to evaluate only a single integral instead of a double integral, and most importantly all rapidly-oscillating factors have disappeared from the final expression, allowing in this way a fast and accurate evaluation of the $G$ overlap factors.

Finally, for intervalley scattering (e.g. between states belonging to different L valleys, or between L and $\Delta_2$ valleys), Jacoboni and Reggiani [58] propose to use the same functional forms given in Eq. (1.72), but with different phenomenological parameters based on an effective deformation potential that includes the contributions of both optical and acoustic phonons. In particular, an expression identical to Eq. (1.72) is used to compute the intervalley scattering rates into each $\Delta$ (L) valley with $\Delta_0$ and $\omega_0$ replaced by model parameters extrapolated from experimental data (see Refs. [56, 58] for a set of values for the parameters).

## 1.11 Interdiffusion due to annealing

In Sec. 4.6 we study the interdiffusion process caused by the thermal annealing of MQW structures. As a consequence of the interdiffusion, interfaces between layers are no more sharp; instead, the concentration profile, i.e. the value $x$ of the concentration of Ge in the $Si_{1-x}Ge_x$ alloy, becomes a smooth function of the growth

coordinate $z$. In this Section, we describe the model that was implemented and used in order to evaluate the concentration profile after the annealing process.

We call $\chi(z,t)$ the concentration profile as a function of the growth coordinate and of the time. Then, it must satisfy the following diffusion equation:

$$\frac{\partial \chi(z,t)}{\partial t} = D\nabla^2 \chi(z,t), \tag{1.74}$$

where $D$ is the diffusion coefficient. In order to obtain the simple form of Eq. (1.74), we have assumed that $D$ depends neither on the spatial coordinate (i.e., we assume a single diffusion coefficient for the whole MQW structure) nor on time. In particular, concerning this last approximation, we make the assumption that the diffusion coefficient $D$ is different from zero (and constant) only from $t = 0$ to $t = t_{\text{ann}}$, where $t_{\text{ann}}$ is the total annealing time. We furthermore assume a piecewise-constant profile $\chi(z, t = 0)$ before the annealing process, i.e. we assume a perfect growth of the sample, with sharp interfaces.

The value of $D$, which depends on the temperature, can be extrapolated from XRD measurements on experimental samples as discussed in [59]. Since in Sec. 4.6 we study $Ge/Si_{0.13}Ge_{0.87}$ MQW samples, we also fitted the results of Ref. [59] for the $T-$dependent linear diffusion coefficient, where the authors studied the interdiffusion of $Si_{0.02}Ge_{0.98}/Si_{0.16}Ge_{0.84}$ superlattice samples grown on $Si_{0.14}Ge_{0.86}$ substrates in the 600–700 °C temperature range.

The functional form of $D(T)$ for these kind of systems in the given temperature range is typically taken to be [60]

$$D(T) = D_0 e^{-E_A/(k_B T)},$$

where $k_B$ is the Boltzmann constant, $D_0$ is called the diffusion prefactor and $E_A$ is the activation energy. Note that the prefactor $D_0$ may have an uncertainty of several orders of magnitude [60] due to the exponential dependence of $D(T)$ on the temperature.

In particular, from the fit of the interdiffusion data of Ref. [59] for the superlattice samples cited above, we obtain

$$D_0 = 4.4\,\text{cm}^2/\text{s}, \qquad E_A = 3.2\,\text{meV}.$$

Using these values, we can calculate the profile $\chi(z, t > t_{\text{ann}})$ after the thermal annealing by numerical solution of Eq. (1.74).

The solution of Eq. (1.74) for constant $D$ is simple: in fact, calling $\tilde{\chi}(k,t) = \mathcal{F}[\chi(z,t)]$ the Fourier transform of $\chi$ with respect to the space coordinate, we can rewrite the diffusion equation in Fourier space as

$$\frac{\partial \tilde{\chi}(k,t)}{\partial t} = -Dk^2 \tilde{\chi}(k,t)$$

so that the solution $\tilde{\chi}(k,t)$ at time $t$ is related to the solution at time zero by

$$\tilde{\chi}(k,t) = \tilde{\chi}(k,t=0)e^{-k^2Dt}.$$

Going back to real space, and using the fact that the Fourier transform of the product of two functions is a convolution of their transforms, we finally get

$$\chi(z,t) = \int_{-\infty}^{\infty} dz' \chi(z',t=0) \frac{1}{\sqrt{4\pi Dt}} e^{-(z-z')^2/(4Dt)}. \tag{1.75}$$

In order to solve numerically the diffusion equation (1.74), two different approaches can be adopted.

**Real-space approach** In this first approach, we simply integrate Eq. (1.75) in real space. To this aim, we define the concentration profile $\chi(z, t = 0)$ over a large-enough number of periods (e.g., five or ten) to simulate the periodic conditions, and possibly terminate the structure on both sides by a capping layer. Then, after a discrete sampling of the $z$ axis, we calculate $\chi(z, t_{\text{ann}})$ by direct numerical integration of Eq. (1.75). Finally, the profile for one period can be obtained from the central region of the simulated system.

**Fourier-space approach** In this second approach we exploit the fact that, in Fourier transform, the solution $\tilde{\chi}(k,t)$ is simply a product of two functions, and therefore very easy to calculate. So, we start by calculating a discrete Fourier transform of the initial profile $\chi(z, t = 0)$ defined only over one period (note that in this approach, the periodic conditions are automatically enforced). Then, we multiply the obtained $\tilde{\chi}(k, t = 0)$ by the Fourier transform of the exponential function $g(z,t) = \frac{1}{\sqrt{4\pi Dt}} e^{-z^2/(4Dt)}$, and we finally perform an inverse Fourier Transform of the result to obtain the profile after a time $t$. For the numerical implementation of the discrete Fourier transform, we employ the FFTW library.

When adopting this method, one should pay attention to the magnitude of the time step $t$. In fact, if the annealing time is large, the Gaussian $g(z,t)$ is not well confined within the sampling domain (whose width is the same of the MQW period). Then, to ensure the correctness of the result, one has to divide the total annealing time $t_{\text{ann}}$ in $m$ steps (of length $\Delta t = t_{\text{ann}}/m$), where $m$ is chosen large enough so that $g(z, \Delta t)$ is almost zero outside the sampling period, and then calculate the inverse Fourier Transform of $\tilde{\chi}(k, t = 0) \cdot \tilde{g}(k, \Delta t)^m$ to obtain $\chi(z, t_{\text{ann}})$.

Both methods have been implemented, and the results are the same within the numerical accuracy. The second method, however, is much faster also thanks to the use of the optimized libraries for the calculation of the discrete Fast Fourier Transform. Note that to maximally optimize the computation time, one should choose a number of sampling points for the $z$ axis which is a power of two. To

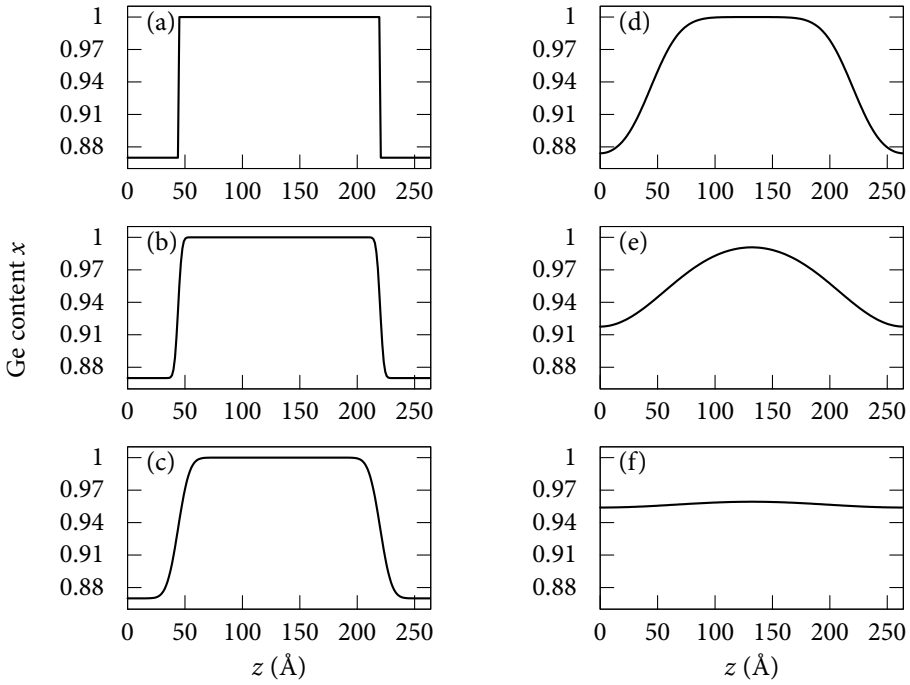


**Figure 1.20** – Concentration profile $\chi(z, t_{\text{ann}})$, i.e. the Ge content $x$ of the $Si_{1-x}Ge_x$ alloy, vs. the coordinate along the growth direction $z$, plotted for one period of a MQW structure (see text). (a): unannealed sample, with sharp interfaces. From (b) to (f): profiles obtained from sample (a) after annealing for $t_{\text{ann}} = 30$ s at 650, 700, 750, 800, 850 °C, respectively.

show a typical result, we plot in Fig. 1.20 the calculated profiles for an annealing time of $t_{\text{ann}} = 30$ s and different annealing temperatures. The unannealed sample of Fig. 1.20a, which is defined by the function $\chi(z, t = 0)$, is a $Ge/Si_{0.13}Si_{0.87}$ MQW system with well width of 176 Å and barrier width of 88 Å.

Finally, the TB code has been adapted to take as input a generic $\chi(z)$ profile. Using this profile, the code calculates for each atomic monolayer the $z$ coordinate of the atoms and the corresponding Ge content $x$, so to have the best approximation of the input profile $\chi$. We emphasize that the $z$-dependent lattice constant in the growth direction is evaluated by means of macroscopic elastic theory (as described in Sec. 1.3.2), where the Poisson ratio is calculated consistently from the input profile $\chi(z)$.

## 1.A Appendix: Basis reordering to optimize the diagonalization

In this Appendix we describe a technique that was implemented in the code, that allows to reduce significantly the time needed for the diagonalization of the TB Hamiltonian matrix.

Let us consider a planar heterostructure with *open* boundary conditions. Then, its Hamiltonian matrix is of the form

$$H = \left(\begin{array}{cc|cccc} a_1 & b_1 & 0 & 0 & 0 & 0 \\ b_1^\dagger & a_2 & b_2 & 0 & 0 & 0 \\ \hline 0 & b_2^\dagger & a_3 & b_3 & 0 & 0 \\ 0 & 0 & b_3^\dagger & a_4 & \ddots & 0 \\ 0 & 0 & 0 & \ddots & \ddots & b_{n-1} \\ 0 & 0 & 0 & 0 & b_{n-1}^\dagger & a_n \end{array}\right)$$

where the $a_i$'s and $b_i$'s are in general block matrices relative to a given monolayer and not simple numbers (for instance, they are $20 \times 20$ blocks in a $sp^3d^5s^*$ basis including spin-orbit interactions).

This form of the matrix is particularly convenient for the computation of eigenvalues and eigenvectors, since it is in *banded* form, i.e. the only elements which are different from zero are those in the main diagonal and in a small number of sub- and superdiagonals. Indeed, for these matrices special routines allow a faster calculation of eigenvalues and eigenvectors; for instance, in the standard LAPACK library the algorithm for Hermitian banded matrices (in complex double precision) is implemented by the ZHBEV subroutine, that can be used in place of the usual ZHEEV one. The advantage in terms of computation time is relevant, since the algorithm scales with a smaller power of the matrix size. Moreover, with ZHBEV the matrix is stored in RAM using a compact storage scheme (i.e., only the main diagonal and the relevant superdiagonals are stored) avoiding the need to allocate space for elements which are zero, and thus having less memory requirements if only eigenvalues are needed.

However, many interesting systems have instead *periodic* boundary conditions. In this case, the matrix has the following form:

$$H = \left(\begin{array}{cc|cccc} a_1 & b_1 & 0 & 0 & 0 & c \\ b_1^\dagger & a_2 & b_2 & 0 & 0 & 0 \\ \hline 0 & b_2^\dagger & a_3 & b_3 & 0 & 0 \\ 0 & 0 & b_3^\dagger & a_4 & \ddots & 0 \\ 0 & 0 & 0 & \ddots & \ddots & b_{n-1} \\ \hline c^\dagger & 0 & 0 & 0 & b_{n-1}^\dagger & a_n \end{array}\right)$$

where we now have an additional $20 \times 20$ block $c$ at the top-right angle of the matrix.

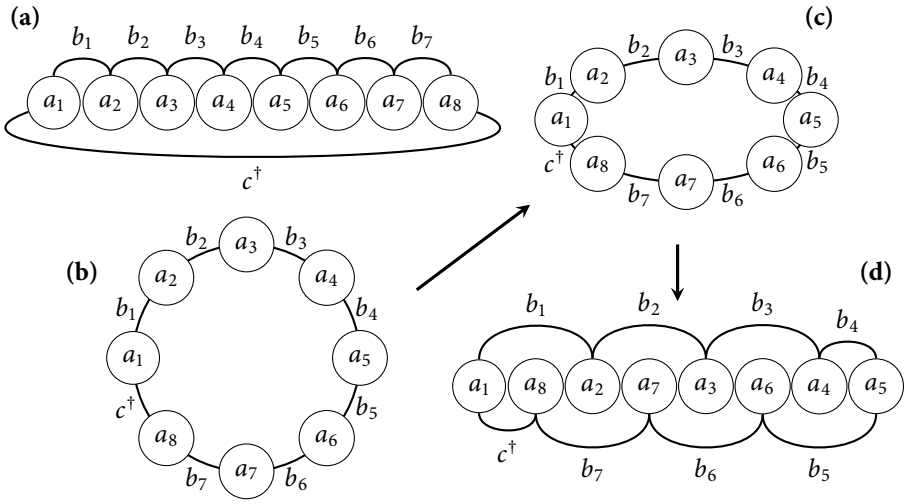


**Figure 1.21** – Graphical representation that illustrates the procedure used to reorder the basis and bring the matrix to banded form, in the simple case with only 8 sites. At the beginning, we have a system with only first-neighbor interactions $b_i$ and $c^\dagger$, as in (a) and (b). At the end, we have reordered the basis with a procedure that can be pictorially illustrated as a "squeezing" of the chain (c), so that each site is linked at most with a site of distance two from itself (d). What is most important, we have no more a link between the first and the last site.

This destroys the banded form of the matrix and it thus seems that we are forced back to employ the usual dense matrix routines, as ZHEEV for instance.

However, since we have only one new block $c$ that is different from zero, it is plausible that with a simple unitary transformation we can rewrite the matrix in banded form, allowing a considerable speed-up in the diagonalization.

The unitary transformation that we use in the code is plausibly one of the easiest ones (since it consists only in a reordering of the basis). This transformation has the only drawback that the number of sub- and superdiagonals is increased; however, we verified that the speed-up is still significant, and at the same time the unitary transformation (and its inverse) are so simple that we do not need to store in RAM the unitary matrix, which would require a lot of memory, but only to define the function that gives the new index of a basis element given the old index, and its inverse.

To better understand the strategy that we use to bring the matrix in banded form, let us describe the problem from a physical point of view. The diagonal terms $a_i$ are the layer self-energies, while all non-diagonal terms represent interactions between two (neighboring) layers. In particular $b_i$ is the interaction between the $i$-th and the $(i+1)$-th layer, and $c$ is the interaction between the first and the last layer (so that $c^\dagger$ is the "inverse" interaction between the last and the first layer).

We can make a graphical representation of this quasi-one-dimensional chain, as shown in Fig. 1.21. The periodic case can be represented by a circular ring with each site connected to its two first neighbors (Fig. 1.21b). If we draw it as a linear chain

(Fig. 1.21a), we see that each site is linked to its first neighbors, except for the first and the last one that are also linked together. Thus in the Hamiltonian matrix we have the top-right corner that is different from zero. If we now think to "squeeze" the ring (Fig. 1.21c-d), interleaving the sites of the chain so that the new order is

$$1, \quad n, \quad 2, \quad n-1, \quad 3, \quad n-2, \quad \ldots$$

we now see that each site is linked at most with a site of distance two from itself. But what is most important, we have no more a link between the first and the last site. This means that, if we write the Hamiltonian matrix in this new reordered basis, the non-zero elements are only those on the diagonal and on the two sub- and superdiagonals. For instance, again in the case $n = 8$, the matrix is:

$$H = \begin{pmatrix} a_1 & c & b_1 & & & & & \\ c^\dagger & a_8 & 0 & b_7^\dagger & & & & \\ b_1^\dagger & 0 & a_2 & 0 & b_2 & & & \\ & b_7 & 0 & a_7 & 0 & b_6^\dagger & & \\ & & b_2^\dagger & 0 & a_3 & 0 & b_3 & \\ & & & b_6 & 0 & a_6 & 0 & b_5^\dagger \\ & & & & b_3^\dagger & 0 & a_4 & b_4 \\ & & & & & b_5 & b_4^\dagger & a_5 \end{pmatrix}$$

What is important to notice is that now, for some pairs of sites, the relative order in the new basis is inverted (for instance in the above example the $7^{\text{th}}$ layer is before than the $6^{\text{th}}$): in these cases, we must remember to write $b_i^\dagger$ *above* the diagonal and $b_i$ *below* when we define the matrix, since the element above the diagonal now represents for instance the interaction from 7 to 6, i.e. $b_6^\dagger$.

We have thus again a matrix in banded form, even if we needed to increase the band width with respect to the original problem. For instance, in the case of $20 \times 20$ blocks, we go from a band width of $39 = 2 \cdot 20 - 1$ to a band width of $59 = 3 \cdot 20 - 1$. This, however, still allows for a faster calculation for typical-size systems, composed of a number of layers of the order of 100, for the reason discussed above (i.e., the different scaling of the computation time with the size of the matrix).

The reindexing function, i.e. the function that gives the new index of a block given the old one, and its inverse are quite simple to write and we report here their implementation in Fortran (77):

```
*     *****
      subroutine map_layer(i,n,inew)
*     Given a block  with index i in chain of length n,
*     returns in inew the new index in
*     the reordered chain
*     *****
      implicit none
      integer i, n, inew
*
      if (i .le. (n+1)/2) then
```

```
         inew = 2 * i - 1
      else
         inew = 2 * n - 2 * i + 2
      endif
      return
      end
```

```
*     *****
      subroutine map_layer_inverse(i,n,iorig)
*     Given a block  with index i in reordered chain of
*     length n, returns in iorig the original index
*     *****
      implicit none
      integer i, n, iorig
*
      if (mod(i,2).eq.0) then
         iorig = n + 1 - i/2
      else
         iorig = (i + 1)/2
      endif
      return
      end
```

# Chapter 2

# Optical properties of bulk and heterostructured semiconductors

In this Chapter, we discuss how the optical properties of semiconductor materials are defined and can be calculated using the methods and techniques described in the previous Chapter.

In particular, in Sec. 2.1 we focus on the derivation of the expressions for the absorption and gain spectra (for direct transitions); in Sec. 2.2 we specialize the expressions that we have obtained, explaining how the above-mentioned quantities can be evaluated both in the tight-binding (TB) formalism or using the $\mathbf{k} \cdot \mathbf{p}$ approximation.

Then, in Sec. 2.3 we calculate the expressions for the spontaneous recombination rate spectra including in this case also the contribution due to indirect transitions.

Sec. 2.4 is devoted to the inclusion of the excitonic effects to the calculated absorption spectra, with special attention to the case of 2D excitons that occur in multiple quantum well structures.

In Sec. 2.5 we discuss the form of the absorption coefficient in the special case of intersubband transitions, we define oscillator strengths and sum rules, and treat the case of a non-diagonal effective mass tensor.

Finally, in the Appendix to this Chapter (Sec. 2.A), we derive the general analytic form of the broadening function to be used when the line broadening is comparable to the transition frequency.

## 2.1 Absorption and gain

Let us start deducing the relationship between the imaginary part of the dielectric constant $\varepsilon_2(\omega)$ and the number of transitions per unit time $W(\omega)$. For more details, we refer to [61]; note that in this Thesis we use MKS units.

Let us consider a transverse plane wave described by the vector potential

$$\mathbf{A}(\mathbf{r}, t) = A_0 \hat{\mathbf{e}} e^{i(\mathbf{q}\cdot\mathbf{r} - \omega t)} + c.c., \tag{2.1}$$

where $\hat{\mathbf{e}}$ is the polarization vector (with $\mathbf{q} \perp \hat{\mathbf{e}}$), the amplitude $A_0$ is taken as real and $c.c.$ indicates the complex conjugate of the preceding expression. The electric field associated to this vector potential can be obtained from the relation $\mathbf{E}(\mathbf{r}, t) = -\partial\mathbf{A}/\partial t$, so that the electric field can be written as

$$\mathbf{E}(\mathbf{r}, t) = E_0 \hat{\mathbf{e}} e^{i(\mathbf{q}\cdot\mathbf{r}-\omega t)} + c.c.,$$

with $E_0 = i\omega A_0$. If this electric field is present within a (isotropic) medium, it induces a current $\mathbf{J}$ which is connected to the electric field through the complex transverse conductivity $\sigma(\mathbf{q}, \omega)$ by:

$$\mathbf{J}(\mathbf{r}, t) = \sigma(\mathbf{q}, \omega) E_0 \hat{\mathbf{e}} e^{i(\mathbf{q}\cdot\mathbf{r}-\omega t)} + c.c.$$

Let us now calculate the power dissipated in a medium where a current $\mathbf{J}$ flows and an electric field $\mathbf{E}$ is present: this is given by

$$\begin{aligned}\int_V \mathbf{J}\cdot\mathbf{E} d\mathbf{r} &= \int_V d\mathbf{r}(\sigma E_0 e^{i(\mathbf{q}\cdot\mathbf{r}-\omega t)} + c.c.)(E_0 e^{i(\mathbf{q}\cdot\mathbf{r}-\omega t)} + c.c.) = \\ &= \int_V d\mathbf{r}(\sigma|E_0|^2 + \sigma^*|E_0|^2) + \int_V d\mathbf{r}(\sigma E_0^2 e^{2i(\mathbf{q}\cdot\mathbf{r}-\omega t)} + c.c.).\end{aligned}$$

The second integral is zero, since it is the integral of a rapidly oscillating function over the volume $V$, and only the first integral remains, giving the final result

$$\int_V \mathbf{J}\cdot\mathbf{E} d\mathbf{r} = 2\sigma_1(\mathbf{q}, \omega)|E_0|^2 V, \tag{2.2}$$

with $\sigma_1 = \mathrm{Re}(\sigma) = (\sigma + \sigma^*)/2$.

To obtain the required relation between $\varepsilon_2$ and $W(\omega)$, we equate the dissipated power calculated macroscopically in Eq. (2.2) with the same quantity calculated microscopically, which is given by the number of transitions per unit time $W(\omega)$ multiplied by the photon energy $\hbar\omega$: we thus obtain

$$2\sigma_1(\mathbf{q}, \omega)|E_0|^2 V = \hbar\omega W(\omega) \quad \Rightarrow \quad \sigma_1(\mathbf{q}, \omega) = \frac{\hbar\omega W(\omega)}{2V\omega^2 A_0^2}.$$

To connect the real part of $\sigma$ with the imaginary part of the complex dielectric function $\varepsilon$, we observe that from the equations $\mathbf{D} = \varepsilon_0\mathbf{E} + \mathbf{P}$ and $\partial\mathbf{P}/\partial t = \mathbf{J}$ we have

$$\frac{\partial\mathbf{D}}{\partial t} = \varepsilon_0 \frac{\partial\mathbf{E}}{\partial t} + \mathbf{J}.$$

Since $\mathbf{D} = \varepsilon_0\varepsilon\mathbf{E}$ and $\mathbf{J} = \sigma\mathbf{E}$, we obtain

$$\varepsilon = 1 + \frac{i\sigma}{\omega\varepsilon_0}.$$

Taking the imaginary part of the above expression, we finally obtain $\varepsilon_2 = \sigma_1/(\omega\varepsilon_0)$, so that in conclusion

$$\varepsilon_2(\mathbf{q}, \omega) = \frac{\hbar W(\omega)}{2\varepsilon_0 V\omega^2 A_0^2}. \tag{2.3}$$

Before deriving the microscopic expression for the transition rate $W(\omega)$, we want to connect the $\varepsilon_2$ function to the absorption spectrum $\alpha(\omega)$, defined by the relation

$$I = I_0 e^{-\alpha(\omega)L}, \tag{2.4}$$

where $I_0$ is the initial intensity of a monochromatic beam of frequency $\omega$ and $I$ is the attenuated intensity after a path of length $L$ inside the material (which is assumed to be homogeneous).

The dispersion relation of a plane wave propagating along $z$, with amplitude dependence $e^{i(q_z z-\omega t)}$, is $q_z = \tilde{n}\omega/c$, where $\tilde{n}$ is the complex refractive index. The attenuation part of the wave amplitude comes from the imaginary part of $q_z$, that is $\mathrm{Im}\, q_z = n_2\omega/c$, with $n_2 = \mathrm{Im}\,\tilde{n}$. For the attenuation of the intensity, we have to consider the square modulus of the amplitude, so that (after a path $L$) we have $I = I_0 e^{-2(\mathrm{Im}\, q_z)L}$. Equating this expression with Eq. (2.4) we thus obtain that

$$\alpha(\omega) = \frac{2n_2\omega}{c}.$$

We now remind that the dielectric function is the square of the complex refractive index, so that

$$\varepsilon = \tilde{n}^2 = (n_1 + in_2)^2 \Rightarrow \begin{cases} \varepsilon_1 = n_1^2 - n_2^2 \\ \varepsilon_2 = 2n_1 n_2 \end{cases} \Rightarrow 2n_2 = \frac{\varepsilon_2}{n_1}.$$

Finally, substituting these results in Eq. (2.3), we obtain the final expression for the absorption coefficient as a function of the microscopic transition rate:

$$\alpha(\omega) = \frac{\hbar W(\omega)}{2n_1(\omega)c\varepsilon_0 V\omega A_0^2}. \tag{2.5}$$

For weak absorption, the frequency dependence of $n_1$ is weak and can be neglected. It turns out, however, that this approximation is a good one also in the case of strong absorption (e.g. from comparison with the experimental data), so that in general one simply uses the static refractive index of the material as $n_1$ in the above formula.

### 2.1.1 Calculation of the transition rate $W(\omega)$

We now calculate the transition rate $W(\omega)$. In a generic system described by the Hamiltonian $H_0 = p^2/(2m_0) + V(r)$, the presence of an electromagnetic field can be described via the minimal coupling, i.e. substituting $\mathbf{p}$ with $\mathbf{p} + e\mathbf{A}$, where $e > 0$ is the modulus of the elementary charge and $\mathbf{A}$ is the vector potential of the electromagnetic field. Using the form for $\mathbf{A}$ given in Eq. (2.1), we can write the Hamiltonian of the coupled system as

$$H = H_0 + \frac{eA_0}{m_0} e^{i(\mathbf{q}\cdot\mathbf{r}-\omega t)}\hat{\mathbf{e}}\cdot\mathbf{p} + \frac{eA_0}{m_0} e^{-i(\mathbf{q}\cdot\mathbf{r}-\omega t)}\hat{\mathbf{e}}\cdot\mathbf{p} \tag{2.6}$$

where we have neglected the term proportional to $A^2$: this is typically a very good approximation if the field intensity is not too large and thus we are not interested in non-linear effects. The Hamiltonian $H$ is then the sum of the uncoupled Hamiltonian $H_0$ and of two terms that account for the absorption and emission of photons of energy $\hbar\omega$, respectively. We can then treat the coupling of the system with the electromagnetic field using the time-dependent perturbation theory. In particular, let us consider two eigenstates of $H_0$, $|\psi_i\rangle$ and $|\psi_j\rangle$, with energy $E_i < E_j$, respectively. In the presence of the electromagnetic field, $|\psi_i\rangle$ and $|\psi_j\rangle$ are no more eigenstates of the total Hamiltonian $H$, and in fact the two perturbative terms induce electromagnetic transitions between these states. Indeed, using the Fermi golden rule, we can write the probability per unit time that an electron makes a transition from $|\psi_i\rangle$ to $|\psi_j\rangle$ with the absorption of a photon of energy $\hbar\omega$ as:

$$P_{i\to j} = \frac{2\pi}{\hbar}\left(\frac{eA_0}{m_0}\right)^2 |\langle\psi_j|e^{i\mathbf{q}\cdot\mathbf{r}}\hat{\mathbf{e}}\cdot\mathbf{p}|\psi_i\rangle|^2\delta(E_j - E_i - \hbar\omega). \tag{2.7}$$

Analogously, we can evaluate the probability per unit time for the inverse process, when an electron makes a transition from $|\psi_j\rangle$ to $|\psi_i\rangle$ with the emission of a photon of energy $\hbar\omega$ as:

$$P_{j\to i} = \frac{2\pi}{\hbar}\left(\frac{eA_0}{m_0}\right)^2 |\langle\psi_i|e^{-i\mathbf{q}\cdot\mathbf{r}}\hat{\mathbf{e}}\cdot\mathbf{p}|\psi_j\rangle|^2\delta(E_i - E_j + \hbar\omega). \tag{2.8}$$

As it is usual, we can adopt the electric dipole approximation, assuming that $e^{i\mathbf{q}\cdot\mathbf{r}} \approx 1$ since the momentum $\mathbf{q}$ carried by the photon is much smaller than the typical momenta of the electrons, $\mathbf{k}$, so that in $\mathbf{k}$−space the photons can induce only vertical transitions.

Let us now calculate the net transition rate involving photons of energy $\hbar\omega$. We call $f$ the distribution function for the electrons (this is typically the Fermi–Dirac distribution, but in many cases the situation may be slightly more complicated: for instance in an optically pumped semiconductor, it is convenient to introduce two different distribution functions for the electrons in the conduction band and for the holes in the valence band, see also Sec. 1.8). Then, in order for a transition to occur, we need that the initial state is occupied and the final state is empty: the net rate is then obtained summing over all pair of states the quantity

$$P_{i\to j}f(E_i)(1 - f(E_j)) - P_{j\to i}f(E_j)(1 - f(E_i)).$$

Substituting Eqs. (2.7) and (2.8) we obtain

$$W(\omega) = \frac{2\pi}{\hbar}\left(\frac{eA_0}{m_0}\right)^2 \sum_{ij} |\langle\psi_j|\hat{\mathbf{e}}\cdot\mathbf{p}|\psi_i\rangle|^2\delta(E_j - E_i - \hbar\omega)[f(E_i) - f(E_j)], \tag{2.9}$$

where the sum is over all possible initial and final states, and in particular the sum over the indices $i$ and $j$ includes also a sum over the two spin polarizations of each state.

Let us now specify the above formula for the case of interband transitions in a semiconductor. We consider as initial state a valence state $|\psi_{v,\mathbf{k},\sigma}\rangle$ and the corresponding final state is a conduction state $|\psi_{c,\mathbf{k},\sigma}\rangle$, where the index $v$ ($c$) labels the different valence (conduction) bands. Note that we are assuming that the $\mathbf{k}$ point is the same for both states due to the dipole approximation discussed above, and also that the spin polarization $\sigma$ is the same since the operator $\hat{\mathbf{e}}\cdot\mathbf{p}$ does not involve the spin. Then, we can rewrite Eq. (2.9) replacing the sum over all states $i$ and $j$ with

$$W(\omega) = \frac{2\pi}{\hbar}\left(\frac{eA_0}{m_0}\right)^2 2\sum_{c,v}\sum_{\mathbf{k}} |\langle\psi_{c,\mathbf{k}}|\hat{\mathbf{e}}\cdot\mathbf{p}|\psi_{v,\mathbf{k}}\rangle|^2 \delta(E_{c,\mathbf{k}}-E_{v,\mathbf{k}}-\hbar\omega)[f(E_{v,\mathbf{k}})-f(E_{c,\mathbf{k}})],$$

where the factor of two in front of the sums accounts for the two spin polarizations $\sigma$. We can make a further step converting the sum over all $\mathbf{k}$ points in the Brillouin zone (BZ) in an integral:

$$\begin{aligned} W(\omega) =& \frac{4\pi}{\hbar}\left(\frac{eA_0}{m_0}\right)^2 \sum_{c,v}\frac{V}{(2\pi)^3}\cdot \\ &\cdot\int_{BZ} d\mathbf{k}\,|\hat{\mathbf{e}}\cdot\mathbf{p}_{cv}(\mathbf{k})|^2\,\delta(E_{c,\mathbf{k}}-E_{v,\mathbf{k}}-\hbar\omega)[f(E_{v,\mathbf{k}})-f(E_{c,\mathbf{k}})], \end{aligned} \tag{2.10}$$

where we have defined the momentum matrix element

$$\mathbf{p}_{cv}(\mathbf{k}) = \langle\psi_{c,\mathbf{k}}|\mathbf{p}|\psi_{v,\mathbf{k}}\rangle\,. \tag{2.11}$$

Finally, using Eq. (2.5) and Eq. (2.10) together, we can obtain the required expression for the absorption coefficient:

$$\begin{aligned} \alpha(\omega) = \frac{e^2}{4\pi\varepsilon_0}\frac{1}{\pi n_1 m_0^2 c\omega}\sum_{c,v}\int_{BZ} d\mathbf{k}\,|\hat{\mathbf{e}}\cdot\mathbf{p}_{cv}(\mathbf{k})|^2\cdot \\ \cdot\,\delta(E_{c,\mathbf{k}}-E_{v,\mathbf{k}}-\hbar\omega)[f(E_{v,\mathbf{k}})-f(E_{c,\mathbf{k}})]. \end{aligned} \tag{2.12}$$

In the calculation, the Dirac's delta is often replaced by a suitable (normalized) lineshape function to take into account the different broadening mechanisms. A typical broadening curve is a Lorentzian function (for the justification and the limits of validity of this lineshape, see Sec. 2.A), so that the substitution reads

$$\delta(E_{c,\mathbf{k}}-E_{v,\mathbf{k}}-\hbar\omega) \to \mathcal{L}(E_{c,\mathbf{k}}-E_{v,\mathbf{k}}-\hbar\omega) \equiv \frac{\Gamma}{\pi}\frac{1}{(E_{c,\mathbf{k}}-E_{v,\mathbf{k}}-\hbar\omega)^2+\Gamma^2}, \tag{2.13}$$

where $\Gamma$ is the half width at half maximum (HWHM). Then, the problem of calculating the absorption spectrum is recast to the calculation of the momentum matrix elements $\mathbf{p}_{cv}(\mathbf{k})$ for each pair $(v,c)$ of bands, and the integration of the quantity reported in Eq. (2.12) over the whole BZ. The details of how this can be done in the TB or in the $\mathbf{k}\cdot\mathbf{p}$ formalism is discussed in the following Sections.

Before concluding this Section, we mention that there are cases in which the absorption coefficient assumes negative values: this is called a gain, and the gain spectrum is defined as

$$G(\omega) = -\alpha(\boldsymbol{\omega}). \tag{2.14}$$

In this case, the electromagnetic field is amplified when it propagates through the system. This is what typically happens when a population inversion condition is established (as for instance in a laser). This can also be easily seen by inspection of Eq. (2.12): in fact, all terms are positive except for the the difference of the Fermi functions $f(E_{v,\mathbf{k}}) - f(E_{c,\mathbf{k}})$.

In the applications described in Chap. 4, we study systems that display positive gain, i.e. negative absorption in a given frequency range.

## 2.2 Evaluation of the optical properties

### 2.2.1 Optical matrix elements in the tight-binding formalism

In Sec. 2.1 we have seen that, in order to calculate the absorption coefficient $\alpha(\omega)$, we need to compute the matrix elements (2.11) of the momentum operator. In the tight-binding model, the basis functions are Bloch sums built from the localized orbitals $\phi_{vm}(\mathbf{r} - \mathbf{r}_{nv})$ introduced at the beginning of Sec. 1.2, where we remind that $n$ indicates the unit cell, $v$ the atom within the unit cell and $m$ the symmetry of the orbital ($s$, $p_x$, $d_{yz}$ and so on). However, the $\mathbf{p}$ operator is not diagonal in this basis (as it would be instead in a plane-wave basis). To calculate the matrix element between localized states one should know the functional form of the orbitals $\phi_{vm}$. However in most semiempirical TB parametrizations, only the on-site energies of each orbital and the hopping integrals between neighboring orbitals are given. Nevertheless, a suitable approximation (that we describe in this Section) can be found in order to evaluate the $\mathbf{p}_{cv}$ matrix elements. This approximation has been first proposed for bulk systems in Ref. [62], and then extended also to confined systems (see Ref. [63] and references therein), and the good agreement between calculated and measured optical properties shows the reliability of the approximations that are used. In particular, typical quantities that have been compared in the literature are the imaginary part of the dielectric constant, $\varepsilon_2(\omega)$, and the absorption coefficient, $\alpha(\omega)$. An example of the comparison between the calculated and measured absorption coefficient for a quantum-confined Ge/SiGe MQW system can be found in this Thesis in Fig. 4.1a.

Let us start from the Bloch sums of Eq. (1.5):

$$\Phi_{vm}(\mathbf{k}, \mathbf{r}) = \frac{1}{\sqrt{N}} \sum_n e^{i\mathbf{k}\cdot\mathbf{r}_{nv}} \phi_{vm}(\mathbf{r} - \mathbf{r}_{nv}), \tag{2.15}$$

where $n$ runs over the $N$ unit cells of the crystal. We have already discussed in Sec. 1.2 how the eigenfunctions of the total Hamiltonian $H$ with given $\mathbf{k}$ vector can be written as linear combinations of the orthonormalized Bloch sums $\Phi_{vm}(\mathbf{k}, \mathbf{r})$, so that for the two states involved in the optical matrix element we have:

$$|\psi_{\mathrm{v},\mathbf{k}}\rangle = \sum_{v,m} C^{\mathrm{v}}_{vm}(\mathbf{k}) \Phi_{vm}(\mathbf{k}, \mathbf{r}) \tag{2.16}$$

$$|\psi_{c,\mathbf{k}}\rangle = \sum_{v',m'} C^{c}_{v'm'}(\mathbf{k}) \Phi_{v'm'}(\mathbf{k}, \mathbf{r}) \tag{2.17}$$

where the $C^{\mathrm{v}}_{\nu m}(\mathbf{k})$ and $C^{c}_{\nu' m'}(\mathbf{k})$ are the coefficients of the linear combinations, obtained from the diagonalization of the $H$ matrix.

Substituting Eqs. (2.15), (2.16) and (2.17) in the expression (2.11) for $\mathbf{p}_{cv}(\mathbf{k})$ we obtain:

$$\mathbf{p}_{cv}(\mathbf{k}) = \sum_{m,m'} \sum_{\nu,\nu'} [C^{c}_{\nu' m'}(\mathbf{k})]^{*} C^{\mathrm{v}}_{\nu m}(\mathbf{k}) \cdot \cdot \left[ \sum_{n} e^{i\mathbf{k}\cdot(\boldsymbol{\tau}_n + \mathbf{d}_\nu - \mathbf{d}_{\nu'})} \langle \phi_{\nu' m'}(\mathbf{r} - \mathbf{d}_{\nu'}) | \mathbf{p} | \phi_{\nu m}(\mathbf{r} - \boldsymbol{\tau}_n - \mathbf{d}_\nu) \rangle \right].$$

We are now left with the problem of calculating the matrix elements of the momentum operator, $\langle \phi_{\nu' m'}(\mathbf{r} - \mathbf{d}_{\nu'}) | \mathbf{p} | \phi_{\nu m}(\mathbf{r} - \boldsymbol{\tau}_n - \mathbf{d}_\nu) \rangle$, which as we have already discussed cannot be evaluated exactly since we do not know the explicit form of the localized orbitals $\phi$. In order to obtain an approximate relation, we convert the momentum matrix element to a matrix element involving the position operator using the commutation relation

$$\mathbf{p} = \frac{m_0}{i\hbar} [\mathbf{r}, \mathbf{H}],$$

so that we obtain

$$\langle \phi_{\nu' m'}(\mathbf{r} - \mathbf{d}_{\nu'}) | \mathbf{p} | \phi_{\nu m}(\mathbf{r} - \boldsymbol{\tau}_n - \mathbf{d}_\nu) \rangle = \frac{m_0}{i\hbar} \left\{ \langle \phi_{\nu' m'}(\mathbf{r} - \mathbf{d}_{\nu'}) | \mathbf{r} H | \phi_{\nu m}(\mathbf{r} - \boldsymbol{\tau}_n - \mathbf{d}_\nu) \rangle - \langle \phi_{\nu' m'}(\mathbf{r} - \mathbf{d}_{\nu'}) | H \mathbf{r} | \phi_{\nu m}(\mathbf{r} - \boldsymbol{\tau}_n - \mathbf{d}_\nu) \rangle \right\}.$$

We introduce now the approximation of assuming the localized orbitals $\phi$ eigenstates of the position operator $\mathbf{r}$, so that

$$\mathbf{r} \, | \phi_{\nu m}(\mathbf{r} - \boldsymbol{\tau}_n - \mathbf{d}_\nu) \rangle = (\boldsymbol{\tau}_n + \mathbf{d}_\nu) \, | \phi_{\nu m}(\mathbf{r} - \boldsymbol{\tau}_n - \mathbf{d}_\nu) \rangle .$$

This approximation is reasonable since the $\phi$ orbitals are localized; the validity of this approximation is discussed in Ref. [63]. In this way, we finally obtain that the $\mathbf{p}$ matrix element between localized orbitals is given by

$$\langle \phi_{\nu' m'}(\mathbf{r} - \mathbf{d}_{\nu'}) | \mathbf{p} | \phi_{\nu m}(\mathbf{r} - \boldsymbol{\tau}_n - \mathbf{d}_\nu) \rangle = = \frac{i m_0}{\hbar} (\boldsymbol{\tau}_n + \mathbf{d}_\nu - \mathbf{d}_{\nu'}) \langle \phi_{\nu' m'}(\mathbf{r} - \mathbf{d}_{\nu'}) | H | \phi_{\nu m}(\mathbf{r} - \boldsymbol{\tau}_n - \mathbf{d}_\nu) \rangle .$$

The last matrix element of $H$ between functions localized on nearest-neighbor atoms is simply one of the hopping integrals discussed in Sec. 1.2, see e.g. the integral (1.9). In conclusion the matrix element $\hat{\mathbf{e}} \cdot \mathbf{p}_{cv}(\mathbf{k})$ can be expressed in terms of the tight-binding semiempirical parameters:

$$\hat{\mathbf{e}} \cdot \mathbf{p}_{cv}(\mathbf{k}) = \frac{i m_0}{\hbar} \sum_{m,m'} \sum_{\nu,\nu'} [C^{c}_{\nu' m'}(\mathbf{k})]^{*} C^{\mathrm{v}}_{\nu m}(\mathbf{k}) \left[ \sum_{n} e^{i\mathbf{k}\cdot(\boldsymbol{\tau}_n + \mathbf{d}_\nu - \mathbf{d}_{\nu'})} \hat{\mathbf{e}} \cdot (\boldsymbol{\tau}_n + \mathbf{d}_\nu - \mathbf{d}_{\nu'}) \langle \phi_{\nu' m'}(\mathbf{r} - \mathbf{d}_{\nu'}) | H | \phi_{\nu m}(\mathbf{r} - \boldsymbol{\tau}_n - \mathbf{d}_\nu) \rangle \right]. \quad (2.18)$$

For the evaluation of the above expression, we consider only those $n$ in the sum such that $(\boldsymbol{\tau}_n + \mathbf{d}_\nu - \mathbf{d}_{\nu'})$ is a vector connecting two first-neighbor atoms.

### 2.2.2 Absorption and gain in the tight-binding model

Using the general formula given in Eq. (2.12) and the result of Eq. (2.18) for the $\mathbf{p}_{cv}$ matrix element, it is now easy to calculate the absorption (or the gain) spectrum of a given material using the TB code.

The integration in $\mathbf{k}$ space can involve a significantly large number of $\mathbf{k}$ points of the BZ and thus can be extremely demanding. The way to simplify the calculation depends on the particular system that we are simulating. The most simple strategy to evaluate the numerical integral is to calculate the matrix elements on a regular 3D grid, possibly exploiting all the symmetries of the system so to make the calculations only in the irreducible wedge of the BZ. Moreover, we can further limit the integration to a smaller region of $\mathbf{k}$ points for which the transition energy is below a chosen threshold. For instance, if we study the direct-gap absorption at $\Gamma$, and we are interested in the spectrum only for photon energies $\hbar\omega$ smaller than, say, 1.5 eV, we can consider only those $\mathbf{k}$ points lying in the corresponding suitable neighborhood of the $\Gamma$ point, since all interband vertical transitions at larger $|\mathbf{k}|$ typically occur at a much larger transition energy and thus do not contribute to the $\alpha(\boldsymbol{\omega})$ spectrum in the energy range of interest.

However, in the calculations of Chap. 4, when we study the contribution due to confined states in systems with thick barriers, we often use a different integration scheme: in particular, we can reasonably assume that the $k_z$ dispersion of these states is flat, so that we only have to perform an integration in two dimensions $(k_x, k_y)$. Moreover, we can reasonably assume that the dependence of the matrix elements on the angle $k_\theta$ (defined by $\tan k_\theta = k_y/k_x$) is weak, so that we can perform an integral in radial coordinates $\left(k_\rho = \sqrt{k_x^2 + k_y^2}, k_\theta\right)$, sampling only a few lines with fixed $k_\theta$ (e.g. eight lines at $k_\theta$ =0°, 45°, 90°, …) and with a finer sampling along the $k_\rho$ coordinate. This allows to significantly reduce the number of $\mathbf{k}$ points for which the evaluation has to be done, and thus to reduce the computational time without a large error on the resulting evaluated spectrum.

### 2.2.3 Absorption and gain in the effective-mass approximation

We have discussed in the previous Section how to calculate the absorption spectrum using the tight-binding code. This calculation is quantitatively precise and it takes into account all the relevant effects (as the dependence of the $\mathbf{p}$ matrix element on $\mathbf{k}$, the non-parabolicities of the bands and so on). However, the evaluation of a single spectrum may require in general the calculation of the matrix elements at hundreds of thousands of $\mathbf{k}$ points and, even if the computation is parallelized on several processors, it results to be extremely demanding.

When we are instead interested in obtaining the optical spectra in a much faster way (possibly obtaining analytical expressions) we can work in the effective mass

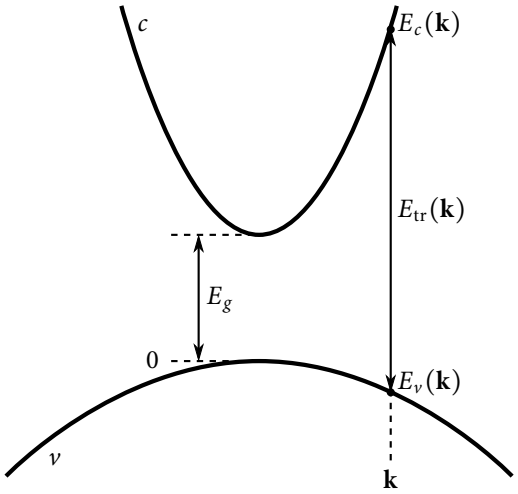


**Figure 2.1** – Scheme of a direct interband transition between a pair of parabolic bands, occurring at a wavevector $\mathbf{k}$. The gap at $\Gamma$ is denoted by $E_g$.

approximation discussed in Chap. 1 (see also Ref. [64]). In particular, in Sec. 1.8 we have shown that the density of states (DOS) can be exploited to convert an integral over $\mathbf{k}$ into an integral over the energy (in the simple case of parabolic bands). Using those results, we now specialize Eq. (2.12) in the context of the effective-mass approximation. We consider a 3D system: the same results can be analogously obtained also for a quantum-confined 2D system, using the appropriate expression for the DOS.

To obtain the final expression, we generalize the 3D DOS of Eq. (1.60) defining the joint density of states, i.e. choosing as integration variable the transition energy between a conduction and a valence band rather than simply the band energy.

Indeed, if both the conduction-band energy $E_c(\mathbf{k})$ and the valence-band energy $E_v(\mathbf{k})$ are parabolic (and isotropic), also their difference $E_{\mathrm{tr}}(\mathbf{k}) = E_c(\mathbf{k}) - E_v(\mathbf{k})$ has a parabolic dispersion, and in particular it holds (see Fig. 2.1)

$$E_{\mathrm{tr}}(\mathbf{k}) = E_g + \frac{\hbar^2 k^2}{2m_c^*} - \left(-\frac{\hbar^2 k^2}{2m_v^*}\right) = E_g + \frac{\hbar^2 k^2}{2m_{cv}^*}, \tag{2.19}$$

where $E_g$ is the bandgap energy at $\Gamma$ (which in general depends on $v$ and $c$), and $m_{cv}^*$ is the reduced effective mass given by

$$\frac{1}{m_{cv}^*} = \frac{1}{m_c^*} + \frac{1}{m_v^*}. \tag{2.20}$$

Since the energy dispersion has the same functional form, the results of Sec. 1.8 can be applied here by simply substituting in Eq. (1.60) the DOS effective mass with the reduced effective mass $m_{cv}^*$.

Hence, we can rewrite Eq. (2.12) for the absorption coefficient as

$$\alpha_{3D}(\omega) = \frac{e^2}{4\pi\varepsilon_0}\frac{|\hat{\mathbf{e}}\cdot\mathbf{p}_{cv}|^2}{\pi n_1 m_0^2 c\omega}\sum_{c,v}\frac{1}{2\pi^2}\left(\frac{2m_{cv}^*}{\hbar^2}\right)^{3/2}\int_{E_g}^{\infty} dE_{\mathrm{tr}}\sqrt{E_{\mathrm{tr}}-E_g}\cdot$$
$$\cdot\,\delta(E_{\mathrm{tr}}-\hbar\omega)\left[f\big(E_v(E_{\mathrm{tr}})\big)-f\big(E_c(E_{\mathrm{tr}})\big)\right], \quad (2.21)$$

where we remind that $m_0$ is the free-electron mass. Moreover, we have assumed that the $\mathbf{p}_{cv}(\mathbf{k})$ matrix element does not depend significantly on $\mathbf{k}$, and thus we can take its value at $\Gamma$ and consider $\mathbf{p}_{cv}$ as a constant. For its evaluation, we can either use the results of Sec. 1.6.1 and deduce its value from the effective masses and the energy of the bandgap, or more simply we can calculate the $\mathbf{p}_{cv}$ value at $\Gamma$ with the TB code for the relevant band edges (e.g. where $c$ is the bottom conduction band and $v$ runs over the HH, LH and SO valence bands).

Note that it is possible to substitute the integral in $\mathbf{k}$−space with an integral over energy only because (in our approximation of parabolic and isotropic bands) we can write the valence energy $E_v(E_{\mathrm{tr}})$ and the conduction energy $E_c(E_{\mathrm{tr}})$ as functions of the integration variable $E_{\mathrm{tr}}$, since $E_c$ and $E_v$ are the arguments of the distribution functions. Indeed, inverting Eq. (2.19) we can easily prove that

$$E_v(E_{\mathrm{tr}}) = -(E_{\mathrm{tr}}-E_g)\frac{m_{cv}^*}{m_v^*}, \quad (2.22)$$

$$E_c(E_{\mathrm{tr}}) = E_g + (E_{\mathrm{tr}}-E_g)\frac{m_{cv}^*}{m_c^*} \quad (2.23)$$

where we have set the zero of the energy at the top of the valence band; analogous equations can be obtained for the valence split-off (SO) band.

As an example, we show that at $T = 0$ (and without optical pumping) we can easily obtain an analytical expression for the absorption coefficient. We calculate here only the contribution from one given pair of bands $(v, c)$; the total absorption coefficient is given by the sum of the contributions of all band pairs.

At $T = 0$ in an undoped semiconductor without optical pumping, the valence band is full and the conduction band is empty, so that $f(E_v) - f(E_c) = 1$. Eq. (2.21) then becomes

$$\alpha_{3D}(\omega) = \frac{e^2}{4\pi\varepsilon_0}\frac{|\hat{\mathbf{e}}\cdot\mathbf{p}_{cv}|^2}{\pi n_1 m_0^2 c\omega}\frac{1}{2\pi^2}\left(\frac{2m_{cv}^*}{\hbar^2}\right)^{3/2}\int_{E_g}^{\infty} dE_{\mathrm{tr}}\sqrt{E_{\mathrm{tr}}-E_g}\,\delta(E_{\mathrm{tr}}-\hbar\omega) =$$
$$= \frac{e^2}{4\pi\varepsilon_0}\frac{|\hat{\mathbf{e}}\cdot\mathbf{p}_{cv}|^2}{2\pi^3 n_1 m_0^2 c\omega}\left(\frac{2m_{cv}^*}{\hbar^2}\right)^{3/2}\sqrt{\hbar\omega-E_g},$$

where we are using the convention of Eq. (1.61) so that $\alpha(\hbar\omega < E_g) = 0$.

Analogously, generalizing the above discussions also to the 2D case and using the expression for the 2D DOS of Eq. (1.62), we can obtain the absorption coefficient of a quantum-confined unexcited system at $T = 0$, associated to a given pair of bands $(v, c)$, one in the valence and one in the conduction band, as

$$\alpha_{2D}(\omega) = \frac{e^2}{4\pi\varepsilon_0}\frac{|\hat{\mathbf{e}}\cdot\mathbf{p}_{cv}|^2}{\pi n_1 m_0^2 c\omega}\frac{m_{cv}^*}{\pi\hbar^2}\theta(\hbar\omega-E_g'), \quad (2.24)$$

where $E'_g$ is the energy difference at Γ between the two bands, which is the sum of the bulk gap energy $E_g$ and of the confinement energies of the two involved bands $\nu$ and $c$.

## 2.3 Spontaneous recombination rate

In this Section we evaluate the spontaneous recombination rate in a semiconductor, comparing the direct contribution (due to the transitions that are vertical in $\mathbf{k}$−space and involve only one photon) and the indirect contribution (arising from second-order processes involving both one photon and one phonon). We assume that a given population of electrons and holes is present in the conduction and valence band, respectively, either due to doping or due to an optical pump. We assume that the photon energy of the pump is larger than the relevant energy region in which the recombination occurs, so that we can neglect the stimulated emission and consider only the spontaneous recombination rate. We furthermore assume that fast relaxation mechanisms exist, that allow a fast thermalization of the electrons and holes within the conduction and valence band.

The results of this Section are used in Sec. 4.5, where we describe the code that we have implemented to calculate the photoluminescence (PL) spectra of Ge bulk systems as a function of the doping charge, the pump power and the temperature. For definiteness, in this Section we focus on Ge systems, i.e. we consider the direct transitions at Γ and the indirect transitions between the four conduction L valleys and the topmost valence states (HH, LH and SO) at Γ.

We start with the derivation of the optical density of states $G_\Omega(\hbar\omega)$ of the electromagnetic field, where $G_\Omega(\hbar\omega)d\Omega_q d(\hbar\omega)$ is the total number of photons per unit volume contained in the energy interval $d(\hbar\omega)$ and with wavevector $\mathbf{q}$ in the solid angle $d\Omega_q$, for a given polarization. This density can be obtained observing that from the dispersion relation connecting energy and momentum of a photon, we have

$$q = n\frac{\omega}{c} \quad \Rightarrow dq = \frac{n}{\hbar c} d(\hbar\omega), \tag{2.25}$$

where $n$ is the refractive index of the material, and we are neglecting its frequency dependence. Then, using (2.25), we can count the number of modes per unit volume of one given polarization:

$$\frac{d^3\mathbf{q}}{(2\pi)^3} = \frac{q^2 dq d\Omega_q}{(2\pi)^3} = \frac{n^3(\hbar\omega)^2}{(2\pi\hbar c)^3} d\Omega_q d(\hbar\omega) \equiv G_\Omega(\hbar\omega) d\Omega_q d(\hbar\omega),$$

that is the definition of $G_\Omega(\hbar\omega)$.

To work out the expression for the recombination rate, it is more convenient to adopt the second quantization formalism, writing the vector potential for a plane wave of frequency $\omega$ and polarization $\hat{\mathbf{e}}$ as

$$\mathbf{A}(\omega) = \left(\frac{\hbar}{2V\omega\varepsilon_0\varepsilon}\right)^{1/2} [a^\dagger_{\hat{\mathbf{e}}}(\omega) + a_{\hat{\mathbf{e}}}(\omega)]\hat{\mathbf{e}}, \tag{2.26}$$

where $\varepsilon = n^2$ is the material dielectric constant; the creation operator $a^\dagger_{\hat{\mathbf{e}}}(\omega)$ for a photon of frequency $\omega$ and polarization vector $\hat{\mathbf{e}}$, and the respective annihilation operator $a_{\hat{\mathbf{e}}}(\omega)$ satisfy the commutation relation

$$[a, a^\dagger] = 1.$$

The prefactor of the expression Eq. (2.26) can be obtained semiclassically. Indeed, for a state with $N$ photons of energy $\hbar\omega$ in a volume $V$, we expect that the energy density is given by

$$U = \frac{N\hbar\omega}{V}. \tag{2.27}$$

On the other hand, the (time-averaged) energy density for an electromagnetic wave is

$$U = \frac{1}{2}(\mathbf{E}\cdot\mathbf{D} + \mathbf{B}\cdot\mathbf{H}) = \varepsilon_0\varepsilon E^2 = \varepsilon_0\varepsilon\omega^2 A^2,$$

where we have used the relation $\mathbf{E} = -\partial A/\partial t$. Then, in second quantization the energy density can be obtained calculating the average value of the operator $\varepsilon_0\varepsilon\omega^2 A^\dagger A$ on a state $|N\rangle$ with $N$ photons:

$$U = \varepsilon_0\varepsilon\omega^2 \frac{\hbar}{2V\omega\varepsilon_0\varepsilon}\langle N|(a_{\hat{\mathbf{e}}} + a^\dagger_{\hat{\mathbf{e}}})(a^\dagger_{\hat{\mathbf{e}}} + a_{\hat{\mathbf{e}}})|N\rangle = \frac{\hbar\omega}{V}\frac{\langle N|a_{\hat{\mathbf{e}}}a^\dagger_{\hat{\mathbf{e}}} + a^\dagger_{\hat{\mathbf{e}}}a_{\hat{\mathbf{e}}}|N\rangle}{2} =$$
$$= \frac{\hbar\omega}{V}\frac{2N+1}{2},$$

and we see that in the semiclassical limit $N \gg 1$ this expression is the same of Eq. (2.27).

Analogously to what has been done in Eq. (2.6), we can write the interaction Hamiltonian with the electromagnetic field: in second quantization, for a given light polarization $\hat{\mathbf{e}}$ and frequency $\omega$, this is

$$H^{\text{e.m.}}_{\text{int}}(\hat{\mathbf{e}}, \omega) = \frac{e}{m_0}\mathbf{A}(\omega)\cdot\mathbf{p}. \tag{2.28}$$

### 2.3.1 Direct transitions

We first address direct transitions from the bottom of the conduction to the top of the valence band, in a neighborhood of the Γ point. We consider an initial state $|i\rangle$ with only one electron excited in the conduction band at $\mathbf{k}$ with energy $E^\Gamma_c(\mathbf{k})$ (leaving a hole at energy $E^\Gamma_v(\mathbf{k})$), and no photons in the system; and a final state $|f\rangle$ with all electrons in the valence band and with one photon of energy $\hbar\omega = E^\Gamma_c(\mathbf{k}) - E^\Gamma_v(\mathbf{k})$:

$$|i\rangle = |\psi^\Gamma_c\rangle\,|0\rangle$$
$$|f_\omega\rangle = |\psi^\Gamma_v\rangle\,|0\cdots 1_\omega\cdots 0\rangle\,,$$

where the convention is to indicate first the electron states and then the photon states, and the notation $|0\cdots 1_\omega\cdots 0\rangle$ indicates that there is only one photon at frequency $\omega$.

The states $|i\rangle$ and $|f_\omega\rangle$ are eigenstates of the uncoupled system, but the interaction of Eq. (2.28) allows transitions between the two states, with matrix element

$$\langle f_\omega|H_{\text{int}}^{\text{e.m.}}(\hat{\mathbf{e}},\omega)|i\rangle = \frac{e}{m_0}\left(\frac{\hbar}{2V\omega\varepsilon_0\varepsilon}\right)^{1/2}(\mathbf{p}_{cv}^{\Gamma}\cdot\hat{\mathbf{e}})\cdot\langle 1_\omega|a_{\hat{\mathbf{e}}}^{\dagger}|0\rangle = \\ = \frac{e}{m_0}\left(\frac{\hbar}{2V\omega\varepsilon_0\varepsilon}\right)^{1/2}(\mathbf{p}_{cv}^{\Gamma}\cdot\hat{\mathbf{e}}). \tag{2.29}$$

Here, $\mathbf{p}_{cv}^{\Gamma}$ is the matrix element defined in Eq. (2.11) calculated at the $\Gamma$ point, where we assume that its value does not depend significantly on $\mathbf{k}$ in a neighborhood of the $\Gamma$ point. Note moreover that in the last step we have used $\langle 1_\omega|a_{\hat{\mathbf{e}}}(\omega)|0\rangle = 1$.

Using the Fermi golden rule, we can calculate the transition probability per unit time between the two states: we then have that

$$P_{i\to f_\omega} = \frac{2\pi}{\hbar}|\hat{\mathbf{e}}_i\cdot\mathbf{p}_{cv}^{\Gamma}|^2\delta(E_c^{\Gamma}(\mathbf{k})-E_v^{\Gamma}(\mathbf{k})-\hbar\omega)\frac{e^2\hbar}{2Vm_0^2\varepsilon_0\varepsilon\omega}.$$

Since in the spontaneous emission process the direction and the polarization of the emitted photon is arbitrary, we have to calculate the probability summed over all possible directions and polarizations. We then discuss preliminarily the quantity

$$\sum_{\hat{\mathbf{e}}}|\hat{\mathbf{e}}_i\cdot\mathbf{p}_{cv}^{\Gamma}|^2 = \sum_{i=1,2}\int d\Omega|\hat{\mathbf{e}}_i\cdot\mathbf{p}_{cv}^{\Gamma}|^2, \tag{2.30}$$

where $\hat{\mathbf{e}}_1$ and $\hat{\mathbf{e}}_2$ are two orthogonal polarizations, both orthogonal to the light wavevector $\mathbf{q}$. In particular, fixing the $z$ axis along the direction of the vector $\mathbf{p}_{cv}^{\Gamma}$, we can take $\hat{\mathbf{e}}_1$ parallel to $\mathbf{q}\times\mathbf{p}_{cv}^{\Gamma}$ and $\hat{\mathbf{e}}_2$ orthogonal to $\hat{\mathbf{e}}_1$. We then see immediately that $|\hat{\mathbf{e}}_1\cdot\mathbf{p}_{cv}^{\Gamma}|^2 = 0$, while $|\hat{\mathbf{e}}_2\cdot\mathbf{p}_{cv}^{\Gamma}|^2 = \sin^2\theta|\mathbf{p}_{cv}^{\Gamma}|^2$, where $\theta$ is the azimuthal angle in spherical coordinates. Then, the integral (2.30) becomes

$$2\pi\int_0^{\pi}\sin\theta d\theta\cdot\sin^2\theta|\mathbf{p}_{cv}^{\Gamma}|^2 = \frac{8\pi}{3}|\mathbf{p}_{cv}^{\Gamma}|^2. \tag{2.31}$$

The spontaneous transition rate $R_{\text{sp}}(\hbar\omega)d(\hbar\omega)$ per unit volume for photon emission in a frequency range $d(\hbar\omega)$ can be then written as:

$$R_{\text{sp}}(\hbar\omega)d(\hbar\omega) = \frac{1}{V}\sum_{c,v}\sum_{\mathbf{k},\sigma}\sum_{\hat{\mathbf{e}}}P_{i\to f_\omega}f_e(\mathbf{k})f_h(\mathbf{k})G_\Omega(\hbar\omega)Vd(\hbar\omega). \tag{2.32}$$

In this expression, $f_e$ is the distribution for electrons in the conduction band and represents the number of initial states, $f_h$ is the distribution for holes in the valence band and is the number of final states for the electronic part of the wavefunction, and $G_\Omega(\hbar\omega)Vd(\hbar\omega)$ is the number of final photonic states. Note that we are summing over all $(\mathbf{k},\sigma)$ electronic states and over all conduction and valence bands.

Substituting all the expressions found above in Eq. (2.32) we finally obtain

$$\begin{aligned} R_{\mathrm{sp}}(\hbar\omega)d(\hbar\omega) =& \frac{1}{V}\sum_{c,v}\sum_{\mathbf{k},\sigma}\frac{2\pi}{\hbar}\frac{8\pi}{3}|\mathbf{p}_{cv}^{\Gamma}|^2\delta(E_c^{\Gamma}(\mathbf{k})-E_v^{\Gamma}(\mathbf{k})-\hbar\omega)\cdot \\ & \cdot\frac{e^2\hbar}{2m_0^2\varepsilon_0\varepsilon\omega}f_e(\mathbf{k})f_h(\mathbf{k})\frac{n^3(\hbar\omega)^2}{(2\pi\hbar c)^3}d(\hbar\omega) = \\ =& \frac{1}{V}\sum_{c,v}\sum_{\mathbf{k},\sigma}\frac{e^2}{4\pi\varepsilon_0\hbar c}\frac{4n|\mathbf{p}_{cv}^{\Gamma}|^2\hbar\omega}{3m_0^2c^2\hbar}\delta(E_{\mathrm{tr}}^{\Gamma}(\mathbf{k})-\hbar\omega)f_e(\mathbf{k})f_h(\mathbf{k})d(\hbar\omega) \end{aligned}$$

where we have substituted $\varepsilon = n^2$ and we have used the definition $E_{\mathrm{tr}}^{\Gamma}(\mathbf{k}) = E_c^{\Gamma}(\mathbf{k}) - E_v^{\Gamma}(\mathbf{k})$.

Finally, in the case of parabolic bands in the $\mathbf{k}\cdot\mathbf{p}$ approximation, we can use the 3D joint density of states as we did in (2.19) and in following Equations, obtaining

$$\begin{aligned} R_{\mathrm{sp}}(\hbar\omega)d(\hbar\omega) =& \sum_{c,v}\frac{1}{2\pi^2}\left(\frac{2m_{cv}^*}{\hbar^2}\right)^{3/2}\int dE_{\mathrm{tr}}\sqrt{E_{\mathrm{tr}}-E_g^{cv}}\,\theta(E_{\mathrm{tr}}-E_g^{cv}) \\ & \frac{e^2}{4\pi\varepsilon_0\hbar c}\frac{4n|\mathbf{p}_{cv}^{\Gamma}|^2\hbar\omega}{3m_0^2c^2\hbar}\delta(E_{\mathrm{tr}}^{\Gamma}(\mathbf{k})-\hbar\omega)f_e\big(E_c(E_{\mathrm{tr}})\big)f_h\big(E_v(E_{\mathrm{tr}})\big) = \\ =& \sum_{c,v}\frac{1}{2\pi^2}\left(\frac{2m_{cv}^*}{\hbar^2}\right)^{3/2}\sqrt{\hbar\omega-E_g^{cv}}\,\theta(\hbar\omega-E_g^{cv})\cdot \\ & \frac{e^2}{4\pi\varepsilon_0\hbar c}\frac{4n|\mathbf{p}_{cv}^{\Gamma}|^2\hbar\omega}{3m_0^2c^2\hbar}f_e\big(E_c(E_{\mathrm{tr}})\big)f_h\big(E_v(E_{\mathrm{tr}})\big) \end{aligned}$$

with $E_v(E_{\mathrm{tr}})$ and $E_c(E_{\mathrm{tr}})$ given in Eqs. (2.22) and (2.23), and $E_g^{cv}$ is the gap at $\Gamma$ between the two bands $v$ and $c$.

### 2.3.2 Indirect transitions

Si and Ge have an indirect gap (see e.g. Fig. 1.8), thus direct optical transitions between states at the bottom of the conduction band (at $\mathbf{k} = \mathbf{k}_c$) and states at the top of the valence band (at $\mathbf{k} = \mathbf{k}_v$) are forbidden. Nevertheless, lattice vibrations relax this selection rule, allowing indirect transitions between these two electronic states via a two-step process where both a photon and a phonon are involved and the required momentum $\mathbf{q} = \mathbf{k}_c - \mathbf{k}_v$ is carried by the phonon.

In order to evaluate the spontaneous transition rate due to indirect transitions, let us start to write the interaction Hamiltonian of the electronic system with both the radiation field and the lattice vibrations as a sum of two terms:

$$H_{\mathrm{int}} = H_{\mathrm{int}}^{\mathrm{e.m.}} + H_{\mathrm{int}}^{\mathrm{ph}}, \tag{2.33}$$

where $H_{\mathrm{int}}^{\mathrm{e.m.}}$ is the interaction Hamiltonian with the electromagnetic field (2.28), while $H_{\mathrm{int}}^{\mathrm{ph}}$ is the interaction Hamiltonian with the phonons, whose explicit form is given later in this Section.

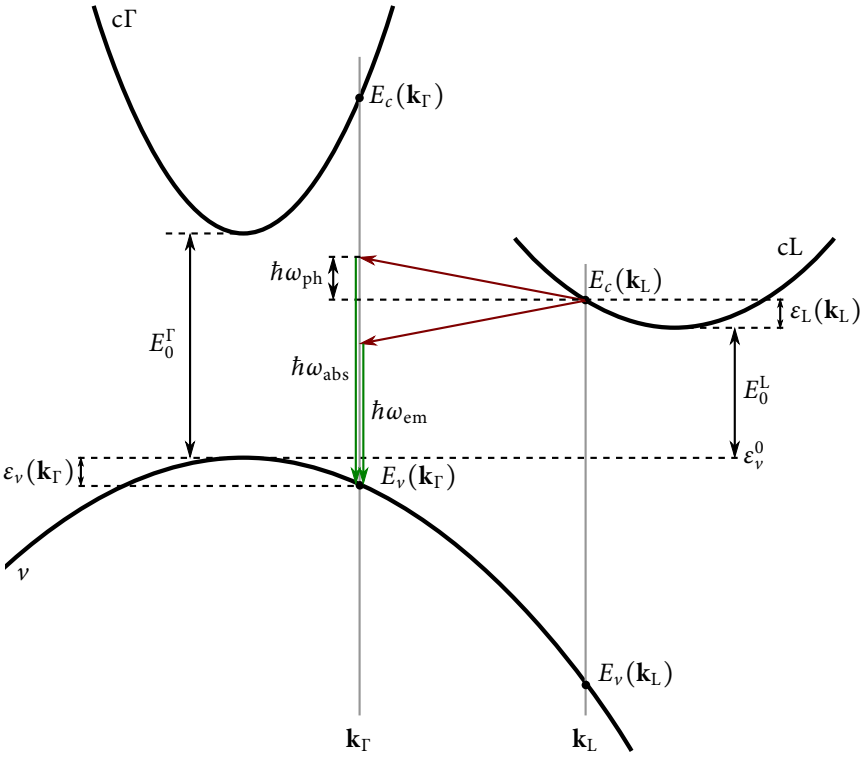


**Figure 2.2** – Schematic of a indirect transition occurring between a state in a conduction L valley at $\mathbf{k} = \mathbf{k}_\mathrm{L}$ and energy $E_c(\mathbf{k}_\mathrm{L})$, and a valence state (in the band $v$) at $\mathbf{k} = \mathbf{k}_\Gamma$ and energy $E_v(\mathbf{k}_\Gamma)$. The red arrows represent the emission or absorption of a phonon, while the green arrows represent the emission of a photon. The direct and indirect gaps are denoted with $E_0^\Gamma$ and $E_0^\mathrm{L}$, respectively; $\omega_{\mathrm{ph}}$ is the phonon frequency, while $\omega_{\mathrm{abs}}$ ($\omega_{\mathrm{em}}$) is the photon frequency in a process involving a phonon absorption (emission). The shown process is of type I, i.e. the first process is the absorption/emission of a phonon, and subsequently the photon is emitted. Analogously, a type-II process may occur (not shown) where the emission of the photon precedes the emission/absorption of the phonon, and then the intermediate state is at $\mathbf{k} = \mathbf{k}_\mathrm{L}$.

As discussed above, the indirect transitions are forbidden in first-order perturbation theory due to the momentum selection rule. Then, let us evaluate the transition rate in second-order perturbation theory, where the resulting net transition rate $W(\omega)$ is obtained substituting the matrix element of Eq. (2.29) with [65]

$$H_{if}^{(2)} = \sum_m \frac{\langle i|H_{\rm int}|m\rangle \langle m|H_{\rm int}|f\rangle}{E'_m - E'_f}, \tag{2.34}$$

where $|i\rangle$ and $|f\rangle$ are the initial and final states, respectively, and the sum is over all possible intermediate states $|m\rangle$. The energies $E'_i$, $E'_m$ and $E'_f$ denote the total energies of the system, i.e. including the contribution of the electronic system, of the radiation field and of the phonon field. In particular the conservation of energy implies that $E'_i = E'_f$, and then the denominator $E'_m - E'_f = E'_m - E'_i$ quantifies the deviation of the intermediate state $|m\rangle$ from the energy-conservation condition.

For definiteness, in the following we focus on a Ge bulk crystal, and we model the system by a single conduction band with one Γ valley and four degenerate L valleys (at lower energy). In the valence, all considered bands have maximum at Γ (and typically we include the three HH, LH and SO bands). A schematic of some possible indirect processes for the bulk Ge system are shown in Fig. 2.2.

For the evaluation of the indirect recombination rate, we choose the following initial and final states:

$$|i\rangle = |\psi_c(\mathbf{k}_{\rm L})\rangle\,|0\rangle\,|\cdots n_{\rm ph}(\mathbf{q})\cdots\rangle\,, \tag{2.35a}$$

$$|f^{\rm abs}\rangle = |\psi_v(\mathbf{k}_\Gamma)\rangle\,|0\cdots 1_{\omega_{\rm abs}}\cdots 0\rangle\,|\cdots(n_{\rm ph}(\mathbf{q})-1)\cdots\rangle\,, \tag{2.35b}$$

$$|f^{\rm em}\rangle = |\psi_v(\mathbf{k}_\Gamma)\rangle\,|0\cdots 1_{\omega_{\rm em}}\cdots 0\rangle\,|\cdots(n_{\rm ph}(\mathbf{q})+1)\cdots\rangle\,. \tag{2.35c}$$

In the above expressions, we are indicating first the electronic part of the wavefunction, then the electromagnetic part (where $|0\cdots 1_{\omega_{\rm abs}}\cdots 0\rangle$ indicates that only one photon with energy $\hbar\omega_{\rm abs}$ is present), and the third part is the phonon component, where $|\cdots n_{\rm ph}(\mathbf{q})\cdots\rangle$ indicates a state with $n_{\rm ph}(\mathbf{q})$ phonons with wavevector $\mathbf{q}$ and energy $E_{\rm ph}(\mathbf{q})$. Moreover, we are considering two possible final states: both are obtained from $|i\rangle$ emitting a photon, but while in $|f^{\rm em}\rangle$ also one phonon is emitted, in $|f^{\rm abs}\rangle$ one phonon is absorbed. Finally, for what concerns the electronic states, $|\psi_c(\mathbf{k}_{\rm L})\rangle$ indicates a state in a conduction L valley, with $\mathbf{k} = \mathbf{k}_{\rm L}$ in the neighborhood of the L point, while $|\psi_v(\mathbf{k}_\Gamma)\rangle$ is a state in the valence band labeled by $v$, with $\mathbf{k} = \mathbf{k}_\Gamma$ in the neighborhood of the Γ point. The spin of the initial and final states is assumed to be the same (and is not indicated explicitly), since only states with the same spin are coupled by the interaction Hamiltonian (2.33).

The total energies of the initial and final states are:

$$E'_i = E_c(\mathbf{k}_{\rm L}) + n_{\rm ph}\hbar\omega_{\rm ph} \tag{2.36a}$$

$$E'_{f^{\rm abs}} = E_v(\mathbf{k}_\Gamma) + (n_{\rm ph}-1)\hbar\omega_{\rm ph} + \hbar\omega_{\rm abs}, \tag{2.36b}$$

$$E'_{f^{\rm em}} = E_v(\mathbf{k}_\Gamma) + (n_{\rm ph}+1)\hbar\omega_{\rm ph} + \hbar\omega_{\rm em}. \tag{2.36c}$$

From the energy conservation condition $E'_i = E'_f$, we deduce that

$$\hbar\omega_{\text{abs}} = E_c(\mathbf{k}_\text{L}) - E_v(\mathbf{k}_\Gamma) + \hbar\omega_{\text{ph}}, \tag{2.37a}$$
$$\hbar\omega_{\text{em}} = E_c(\mathbf{k}_\text{L}) - E_v(\mathbf{k}_\Gamma) - \hbar\omega_{\text{ph}}, \tag{2.37b}$$

as it can also be deduced by inspection of Fig. 2.2.

Let us consider now the possible intermediate states $|m\rangle$ that have non-zero matrix element with both the initial and the final state, so that (2.34) is non-zero. There are two kinds of such intermediate states. In the first case (that we call of type I), the first process is a phonon scattering, followed by a photon emission, as the one shown in Fig. 2.2. Then, we see that for these type-I processes

$$\langle f|H_{\text{int}}|m_\text{I}\rangle = \langle f|H^{\text{e.m.}}_{\text{int}}|m_\text{I}\rangle\,, \qquad \langle m_\text{I}|H_{\text{int}}|i\rangle = \langle m_\text{I}|H^{\text{ph}}_{\text{int}}|i\rangle\,. \tag{2.38}$$

Moreover, due to the momentum conservation rule and to the verticality of the electromagnetic transitions, we see immediately that the electronic part of $|m_\text{I}\rangle$ must be at $\mathbf{k} = \mathbf{k}_\Gamma$ (see Fig. 2.2).

Analogously, we can have type-II processes, in which the first process is the photon emission, which is followed by the phonon scattering. In this case, the electronic part of $|m_\text{II}\rangle$ must be at $\mathbf{k} = \mathbf{k}_\text{L}$.

The complete expressions of the allowed intermediate states (both for the phonon absorption and emission processes) are:

$$|m^{\text{abs}}_\text{I}\rangle = |\psi_c(\mathbf{k}_\Gamma)\rangle\,|0\rangle\,|\cdots(n_{\text{ph}}-1)\cdots\rangle\,, \tag{2.39a}$$
$$|m^{\text{em}}_\text{I}\rangle = |\psi_c(\mathbf{k}_\Gamma)\rangle\,|0\rangle\,|\cdots(n_{\text{ph}}+1)\cdots\rangle\,, \tag{2.39b}$$
$$|m^{\text{abs}}_\text{II}\rangle = |\psi_v(\mathbf{k}_\text{L})\rangle\,|0\cdots 1_{\omega_{\text{abs}}}\cdots 0\rangle\,|\cdots n_{\text{ph}}\cdots\rangle\,, \tag{2.39c}$$
$$|m^{\text{em}}_\text{II}\rangle = |\psi_v(\mathbf{k}_\text{L})\rangle\,|0\cdots 1_{\omega_{\text{em}}}\cdots 0\rangle\,|\cdots n_{\text{ph}}\cdots\rangle\,, \tag{2.39d}$$

with energies

$$E'_{m^{\text{abs}}_\text{I}} = E_c(\mathbf{k}_\Gamma) + (n_{\text{ph}}-1)\hbar\omega_{\text{ph}}, \tag{2.40a}$$
$$E'_{m^{\text{em}}_\text{I}} = E_c(\mathbf{k}_\Gamma) + (n_{\text{ph}}+1)\hbar\omega_{\text{ph}}, \tag{2.40b}$$
$$E'_{m^{\text{abs}}_\text{II}} = E_v(\mathbf{k}_\text{L}) + n_{\text{ph}}\hbar\omega_{\text{ph}} + \hbar\omega_{\text{abs}}, \tag{2.40c}$$
$$E'_{m^{\text{em}}_\text{II}} = E_v(\mathbf{k}_\text{L}) + n_{\text{ph}}\hbar\omega_{\text{ph}} + \hbar\omega_{\text{em}}. \tag{2.40d}$$

We now want to show that, in first approximation, type-II processes can be neglected in Ge systems. To this aim, we calculate the denominator $(E'_m - E'_f)$ of Eq. (2.34) both for type-I and type-II processes. Using Eqs. (2.36), (2.37) and (2.40) we can easily obtain that

$$|E'_{m_\text{I}} - E'_f| = |E_c(\mathbf{k}_\Gamma) - E_c(\mathbf{k}_\text{L}) \mp \hbar\omega_{\text{ph}}| \approx 0.1\,\text{eV}, \tag{2.41a}$$
$$|E'_{m_\text{II}} - E'_f| = |E_v(\mathbf{k}_\text{L}) - E_v(\mathbf{k}_\Gamma) \pm \hbar\omega_{\text{ph}}| \approx 1\,\text{eV}, \tag{2.41b}$$

where the top (bottom) sign accounts for processes involving the absorption (emission) of a phonon. The numerical estimate has been done using the band structure of Ge (see Fig. 1.8) and considering that a typical value for the phonon energy in Ge is $\hbar\omega_{\rm ph} \approx 30\,$meV. Then, the contribution of type-II processes is expected to be much smaller than the contribution of type-I processes, also because in the final transition rates the matrix element (2.34), and thus in particular the denominator given in Eqs. (2.41), is squared.

Therefore in the following (also for notation simplicity) we consider only type-I processes and we do not write anymore the subscript I, even if type-II processes can be included with a straightforward generalization of the results reported below.

Let us now write explicitly the form of the electron–phonon interaction $H_{\rm int}^{\rm ph}$. One can derive that the electron-phonon scattering is described by a Hamiltonian of the form [66]:

$$H_{\rm int}^{\rm ph} = \sum_{\mathbf{q}} \sum_{\mathbf{k}} D_{\mathbf{q}} (b_{\mathbf{q}} + b_{\mathbf{q}}^{\dagger}) C_{\mathbf{q},\mathbf{k}},$$

where $b_{\mathbf{q}}$ is the bosonic annihilation operator for a phonon with wavevector[1] $\mathbf{q}$, and $C_{\mathbf{q},\mathbf{k}}$ contains the electronic part of the interaction Hamiltonian, with terms of the form $c_{\mathbf{k}+\mathbf{q}}^{\dagger} c_{\mathbf{k}}$ (where $c_{\mathbf{k}}$ is the fermion annihilation operator for the electrons). Consequently, the matrix elements $\langle m|H_{\rm int}^{\rm ph}|i\rangle$ are of the form

$$\langle m^{\rm abs}|H_{\rm int}^{\rm ph}|i\rangle = D_{\mathbf{q}}\sqrt{n_{\rm ph}}, \qquad \langle m^{\rm em}|H_{\rm int}^{\rm ph}|i\rangle = D_{\mathbf{q}}\sqrt{n_{\rm ph}+1}, \tag{2.42}$$

where $\mathbf{q}$ is the wavevector that allows a transition between $|i\rangle$ and $|m\rangle$ conserving the momentum, i.e. $\mathbf{q} = \mathbf{k}_{\rm L} - \mathbf{k}_{\Gamma}$.

In general, one should now consider all possible scattering mechanisms (e.g. both due to acoustic and optical phonons) and the dispersion relation of the phonon branches. Here we instead consider the simplified approach discussed in Refs. [67,68]. In particular, the overall action of all phonons is modeled by a single dispersionless phonon with energy $\hbar\omega_{\rm ph} = 27.56\,$meV [67] for what concerns the $\Gamma$–L scattering. The coefficient $D_{\mathbf{q}}$ for this single effective phonon is written as [66]

$$D_{\mathbf{q}} = D_{\rm eff}\sqrt{\frac{\hbar^2}{2\rho V \hbar\omega_{\rm ph}}},$$

with $\rho$ is the mass density and $V$ the volume of the crystal; $D_{\rm eff}$ is an effective deformation potential, whose value is $D_{\rm eff} = 2\cdot 10^8\,$eV/cm [67] (note that $D_{\rm eff}$ and $D_{\mathbf{q}}$ have different units).

Then, the square of the matrix elements (2.42) can be written as

$$|\langle m^{\rm abs}|H_{\rm int}^{\rm ph}|i\rangle|^2 = n_{\rm ph}\frac{\hbar^2 D_{\rm eff}^2}{2\rho V\hbar\omega_{\rm ph}}, \tag{2.43a}$$

$$|\langle m^{\rm em}|H_{\rm int}^{\rm ph}|i\rangle|^2 = (n_{\rm ph}+1)\frac{\hbar^2 D_{\rm eff}^2}{2\rho V\hbar\omega_{\rm ph}}. \tag{2.43b}$$

[1] In general, we should also have a further index to label the phonon branch, but for simplicity we do not indicate it in the expressions of this Section.

Moreover, from Eq. (2.38) we see that the matrix elements $|\langle f^{\text{abs,em}}|H_{\text{int}}|m^{\text{abs,em}}\rangle|^2$ involve only the electromagnetic part $H_{\text{int}}^{\text{e.m.}}$ of the interaction Hamiltonian and we then already know the expression for this matrix element, see Eq. (2.29).

With the knowledge of these matrix elements, the transition probability per unit time between the $|i\rangle$ and $|f\rangle$ states can be obtained using the Fermi golden rule:

$$\begin{aligned} P_{i\to f^{\text{abs,em}}} =& \frac{2\pi}{\hbar}|H^{(2)}_{if^{\text{abs,em}}}|^2\delta(E_c(\mathbf{k}_\text{L}) - E_v(\mathbf{k}_\Gamma) - \hbar\omega \pm \hbar\omega_{\text{ph}}) = \\ =& \frac{2\pi}{\hbar}\left|\frac{\langle f^{\text{abs,em}}|H_{\text{int}}^{\text{e.m.}}|m^{\text{abs,em}}\rangle\langle m^{\text{abs,em}}|H_{\text{int}}^{\text{ph}}|i\rangle}{E_c(\mathbf{k}_\Gamma) - E_c(\mathbf{k}_\text{L}) \mp \hbar\omega_{\text{ph}}}\right|^2 \cdot \\ & \cdot \delta(E_c(\mathbf{k}_\text{L}) - E_v(\mathbf{k}_\Gamma) - \hbar\omega \pm \hbar\omega_{\text{ph}}), \end{aligned} \tag{2.44}$$

where the sum over all intermediate states $|m\rangle$ is reduced to one state only for each phonon absorption or emission process, and also here the top (bottom) sign refers to processes involving a phonon absorption (emission). The spontaneous transition rate $R_{\text{sp}}^{\text{ind}}$ due to indirect transitions is obtained analogously to Eq. (2.32) as

$$R_{\text{sp}}^{\text{ind}}(\hbar\omega)d(\hbar\omega) = \frac{1}{V}\sum_{i,f}\sum_{\hat{\mathbf{e}}} P_{i\to f} f_e(\mathbf{k}_\text{L}) f_h(\mathbf{k}_\Gamma) G_\Omega(\hbar\omega) V d(\hbar\omega).$$

In the case of Ge systems, the sum over all possible initial and final states becomes

$$\sum_{i,f} \to 2N_V \sum_{\mathbf{k}_\text{L}}\sum_{\mathbf{k}_\Gamma}\sum_{\nu}\sum_{\text{abs,em}},$$

where the factor of two takes into account the spin degeneracy, $N_V = 4$ is the number of equivalent L valleys in which the initial state $|i\rangle$ can be chosen, and the sum over $\mathbf{k}_\text{L}$ runs only within one given L valley. Finally, the sum over $\nu$ is over all valence bands included in the model.

Substituting the matrix elements in Eq. (2.44) and using Eq. (2.31) for the sum over all polarizations, we finally get that the net spontaneous recombination rate per unit volume and energy is

$$\begin{aligned} R_{\text{sp}}^{\text{ind}}(\hbar\omega) = F_{\text{ind}}\cdot\hbar\omega \sum_{\text{abs,em}}\sum_{\nu}(n_{\text{ph}} + 1/2 \mp 1/2)|p_{c\nu}^\Gamma|^2 \frac{1}{V^2}\sum_{\mathbf{k}_\Gamma,\mathbf{k}_\text{L}} f_e(\mathbf{k}_\text{L}) f_h(\mathbf{k}_\Gamma)\cdot \\ \cdot \delta(E_c(\mathbf{k}_\text{L}) - E_v(\mathbf{k}_\Gamma) - \hbar\omega \pm \hbar\omega_{\text{ph}}) \frac{1}{(E_c(\mathbf{k}_\Gamma) - E_c(\mathbf{k}_\text{L}) \mp \hbar\omega_{\text{ph}})^2}, \end{aligned} \tag{2.45}$$

where $|p_{c\nu}^\Gamma|$ is the optical matrix element between the $\Gamma$ conduction band and the $\nu$ valence band calculated at the $\Gamma$ point, and the prefactor $F_{\text{ind}}$ is given by

$$F_{\text{ind}} = \frac{4N_V}{3}\frac{e^2}{4\pi\varepsilon_0\hbar c}\frac{\hbar|D_{\text{eff}}|^2 n}{m_0^2 c^2 \rho\hbar\omega_{\text{ph}}}.$$

We remind here that $n$ is the refractive index of the material, and that the physical units of $F_{\text{ind}}$ are volume·time$^{-1}$·mass$^{-1}$. Moreover, we can convert the two sums over

the **k** vectors in Eq. (2.45) to integrals with the substitution

$$\frac{1}{V^2}\sum_{\mathbf{k}_\Gamma,\mathbf{k}_\mathrm{L}} \to \int \frac{d\mathbf{k}_\Gamma}{(2\pi)^3}\int \frac{d\mathbf{k}_\mathrm{L}}{(2\pi)^3}.$$

To obtain an analytical expression, we now assume parabolic bands and convert the two integrals over $\mathbf{k}_\Gamma$, $\mathbf{k}_\mathrm{L}$ to two integrals over the energies $\varepsilon_v(\mathbf{k}_\Gamma)$ and $\varepsilon_\mathrm{L}(\mathbf{k}_\mathrm{L})$, respectively; these latter energies are shown in Fig. 2.2 and represent the energy of the valence (conduction) state at $\mathbf{k}_\Gamma$ ($\mathbf{k}_\mathrm{L}$) measured from the top of the valence band (bottom of the L band), respectively. We then obtain

$$R_\mathrm{sp}^\mathrm{ind}(\hbar\omega) = F_\mathrm{ind}\cdot\hbar\omega\sum_{\mathrm{abs,em}}\sum_{v}(n_\mathrm{ph}+1/2\mp 1/2)|p_{cv}^\Gamma|^2\int_0^\infty d\varepsilon_\mathrm{L}$$
$$g(\varepsilon_v,m_v^*)g(\varepsilon_\mathrm{L},m_\mathrm{L}^*)f_e(\varepsilon_\mathrm{L})f_h(\varepsilon_v)\frac{1}{(E_c(\mathbf{k}_\Gamma)-E_v(\mathbf{k}_\Gamma)-\hbar\omega)^2}. \quad (2.46)$$

In the latter expression, we have defined the factor $g(E,m)$ as the 3D DOS *without* the sum over the spin, i.e.

$$g(E,m) = \frac{1}{4\pi^2}\left(\frac{2m}{\hbar^2}\right)^{3/2}\sqrt{E};$$

$m_v^*$ is the valence effective mass of the band $v$, and $m_\mathrm{L}^*$ is the 3D DOS effective mass associated to one L valley. We have moreover used the Dirac's delta to remove the integral over the valence energy $\varepsilon_v$, from which we can obtain the following relation to express $\varepsilon_v$ as a function of $\varepsilon_\mathrm{L}$ (see also Fig. 2.2):

$$\varepsilon_v = -\left(E_0^\mathrm{L}+\varepsilon_\mathrm{L}-\hbar\omega\pm\hbar\omega_\mathrm{ph}\right).$$

Using this latter expression, we see that the integral over $\varepsilon_\mathrm{L}$ does not extend to infinity, but it has a natural cutoff: indeed, $g(\varepsilon_v,m_v^*)$ is zero for $\varepsilon_\mathrm{v}<0$, i.e. for $\varepsilon_\mathrm{L}>\hbar\omega\mp\hbar\omega_\mathrm{ph}-E_0^\mathrm{L}$.

The only final issue that we point out here is that the denominator can have a $1/x^2$ (non-integrable) divergence within the integration domain when the photon energy is large enough. This occurs when the intermediate state is no more virtual, but a phonon can induce a first-order transition between the conduction L and Γ valleys. The effect of these processes is to thermalize the L and Γ valleys, and thus these processes are already taken into account by the fact that we consider a single conduction quasi-Fermi energy, common to both the L and the Γ valleys. We then substitute the denominator in Eq. (2.46) with the value that it assumes for a transition between the bottom of the L valley and the top of the valence band [65], i.e. with $(E_0^\Gamma-\hbar\omega)^2=(E_0^\Gamma-E_0^\mathrm{L}\mp\hbar\omega_\mathrm{ph})^2$, so that we finally have

$$R_\mathrm{sp}^\mathrm{ind}(\hbar\omega) = F_\mathrm{ind}\cdot\hbar\omega\sum_{\mathrm{abs,em}}\sum_{v}(n_\mathrm{ph}+1/2\mp 1/2)|p_{cv}^\Gamma|^2\frac{1}{(E_0^\Gamma-E_0^\mathrm{L}\mp\hbar\omega_\mathrm{ph})^2}\cdot$$
$$\cdot\int_0^{\hbar\omega\mp\hbar\omega_\mathrm{ph}-E_0^\mathrm{L}} d\varepsilon_\mathrm{L}\, g(\varepsilon_v,m_v^*)g(\varepsilon_\mathrm{L},m_\mathrm{L}^*)f_e(\varepsilon_\mathrm{L})f_h(\varepsilon_v). \quad (2.47)$$

Finally, if we consider a thermalized bath of phonons at a given lattice temperature $T$, the number of phonons $n_{\mathrm{ph}}$ is given by the Bose–Einstein distribution

$$n_{\mathrm{ph}} = \frac{1}{e^{E_{\mathrm{ph}}/K_B T} - 1}.$$

We now have all ingredients for the calculation of the spontaneous transition rate due to indirect transitions, which simply requires the numerical evaluation of the definite integral of Eq. (2.47).

## 2.4 2D excitons

In real systems, the optical absorption spectrum is significantly modified by the presence of excitons. Thus, in order to obtain realistic $\alpha(\omega)$ spectra, the excitonic contribution has to be included. For the theory on 3D and 2D excitons, we refer for instance to the book of Haug and Koch [69]: we report here only the final results and we discuss the details of the implementation in the code for the evaluation of the optical spectra of MQW systems.

The binding energy of bound excitonic states depends on the dimensionality of the system. In particular, when we consider a given pair of bands $(v, c)$, the binding energy $\tilde{E}_n$ of the $n-$th bound state is given by

$$\tilde{E}_n = -E_0 \frac{1}{n^2}, \qquad n = 1, 2, \ldots \qquad \text{(3D bound states)}$$

$$\tilde{E}_n = -E_0 \frac{1}{(n + 1/2)^2}, \qquad n = 0, 1, \ldots \qquad \text{(2D bound states)}$$

where

$$E_0 = \frac{\hbar^2}{2 m_{cv} a_0^2}, \qquad a_0 = \frac{\hbar^2 4\pi\varepsilon_0 \varepsilon}{e^2 m_{cv}} :$$

here, $\varepsilon$ is the dielectric constant of the material and $m_{cv}$ is the reduced mass of the $v$ and $c$ bands, introduced in Eq. (2.20). Note that the largest binding energy (which is $-\tilde{E}_1$ in 3D and $-\tilde{E}_0$ in 2D) is $E_0$ in the 3D case, while it is $4E_0$ in the 2D case. For typical Ge/SiGe MQW systems, the binding energy is approximately 4 meV (i.e. $E_0 \approx 1\,\mathrm{meV}$).

As discussed in detail in Ref. [69], we expect that the absorption spectrum is modified by the presence of $\delta-$like absorption features in correspondence of the bound excitonic states below the onset of the absorption calculated in the previous Sections. In particular, in 2D the excitonic correction below the gap (for each given band pair) is given by

$$\alpha^{\mathrm{exc}}_{\mathrm{bound}}(\omega) = \alpha^0_{\mathrm{2D}} \sum_{n=0}^{\infty} \frac{4}{(n + 1/2)^3} \delta\left(\Delta + \frac{1}{(n + 1/2)^2}\right) \tag{2.48}$$

with

$$\Delta = \frac{\hbar\omega - E'_g}{E_0} \tag{2.49}$$

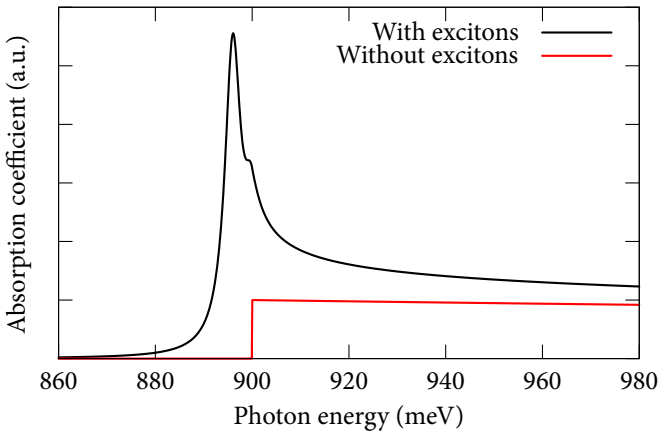


**Figure 2.3** – Comparison of the 2D interband absorption coefficient due to a single pair of subbands, with and without the excitonic contribution. The gap energy is set to $E_g' = 900\,\text{meV}$ and the binding energy is $4E_0 = 4\,\text{meV}$. The Lorentzian broadening is set to $\Gamma = 2\,\text{meV}$.

and $\alpha_{2D}^0$ defined here as the value of the absorption coefficient just above the gap, $\alpha_{2D}^0 \equiv \alpha_{\text{free}}(\hbar\omega = E_g')$, where $\alpha_{\text{free}}(\omega)$ is the absorption spectrum of Eq. (2.24). Note that each peak associated to an excitonic bound state contributes to the spectrum with intensity proportional to $1/(n + 1/2)^3$, and in the limit of $E \to E_g'$ the $\delta$ peaks tend to form a continuum, whose value tends to $\alpha_{\text{bound}}^{\text{exc}}(\omega \to E_g'/\hbar) \to 2\alpha_{2D}^0$.

Moreover, a correction is expected also above the onset of the one-particle absorption $\alpha_{\text{free}}$, due to fact that the Coulomb attraction between holes and electrons has effects also in the continuum: in fact, above the gap energy, we have [69]

$$\alpha_{\text{cont}}^{\text{exc}}(\omega) = \alpha_{\text{free}}(\omega)C(\omega),$$

where $\alpha_{\text{cont}}^{\text{exc}}(\omega)$ is the absorption spectrum including the excitonic contributions in the continuum ($\hbar\omega > E_g'$), and $C(\omega)$ is the Coulomb enhancement factor, that in 2D is

$$C(\omega) = \frac{e^{\pi/\sqrt{\Delta}}}{\cosh(\pi/\sqrt{\Delta})},$$

where $\Delta$ is the same of Eq. (2.49) (note that the 3D Coulomb enhancement form has a different expression, see Ref. [69]). Note that $C(\omega \to E_g'/\hbar) \to 2$, so that the two parts of $\alpha^{\text{exc}}$ connect continuously at $E_g'$.

In the numerical implementation, the Dirac's delta functions in Eq. (2.48) are substituted with Lorentzian peaks with suitable width as discussed in (2.13), where the width is chosen by comparison with the experimental data. Moreover, only the first few bound states (typically up to four) are included in Eq. (2.48), since the contribution of all remaining states with larger $n$ is negligible. Furthermore, to avoid discontinuities in the simulated spectrum, the contribution of the Coulomb enhancement factor, which should be exactly zero below $E_g'$, is instead smoothed with a Lorentzian tail (with same width as the one used for the delta functions). A comparison of the interband absorption spectrum of a 2D system (originating only from one pair of subbands) with and without the excitonic contribution is reported in Fig. 2.3.

In practice, the electronic states are calculated using the TB code, and the excitonic contribution is evaluated for all couples of valence and conduction bands. Actually, the choice of the unit cell in MQW systems implies a folding of states with $\Delta$ symmetry at the $\Gamma$ point of the BZ of the multilayer structure: then at $\Gamma$ we find both these folded states and the genuine $\Gamma$ states. The matrix dipole element between the folded states and the valence states is zero, and thus they are not optically active. A suitable filtering of the conduction states (based on the magnitude of the dipole matrix element) is thus applied to exclude these folded bands and then the excitonic contribution is added only to the transitions to genuine $\Gamma$ states.

Finally, for an example of a comparison of an experimental and theoretical absorption spectrum, including the 2D excitonic contribution, see Fig. 4.1a of this Thesis.

## 2.5 Intersubband absorption and oscillator strengths

The aim of this Section is to calculate the form of the absorption coefficient for intersubband transitions, with particular focus on the case of non-diagonal effective-mass tensors since this is the case for Ge-rich systems (see Sec. 1.7) as those discussed in Chap. 3. In the following we assume that the heterostructures are grown along the $z$ direction. Moreover, we do not consider explicitly the case of a spatially-varying $m^*(z)$, even if this is in general of interest for heterostructures. For a discussion of the generalization of the expressions in this case, see Ref. [70].

### 2.5.1 Intersubband absorption

In this Section we derive the expression of the intersubband absorption coefficient $\alpha(\omega)$ (see also Ref. [71]).

We need to calculate the transition rate $W(\omega)$ for intersubband transitions: once we know this quantity, we obtain the absorption coefficient using Eq. (2.5).

In the effective-mass approximation with a non-isotropic effective mass, we have seen in Eq. (1.65) that the Hamiltonian for the envelope function $\psi_i$ can be written as

$$H\psi_i = E_i\psi_i, \qquad H = \frac{1}{2}\mathbf{p}\cdot w^\gamma \cdot \mathbf{p} + V(z),$$

where $w^\gamma$ is the $3\times 3$ inverse mass tensor for a given band and valley (see Sec. 1.8.1), and we use the symbol $\gamma$ to denote the valley. Note that each valley has in general a different mass tensor. For instance, for $\Delta_4$ states in Si, the two valleys along $k_x$ have the longitudinal mass along $x$, while the two valleys along $k_y$ have the longitudinal mass along $y$. Hence the inverse mass tensors are different, and electrons in different valleys couple differently with a given light polarization.

Using the minimal coupling and the form for $\mathbf{A}$ of Eq. (2.1), we obtain that the

perturbation due to the presence of the electromagnetic field is given by

$$\frac{1}{2}eA_0\sum_{\alpha,\beta}\left(p_\alpha w^\gamma_{\alpha\beta}\hat{e}_\beta+\hat{e}_\alpha w^\gamma_{\alpha\beta}p_\beta\right)e^{i(\mathbf{q}\cdot\mathbf{r}-\omega t)},$$

where the indices $\alpha$ and $\beta$ run over the three coordinates $x$, $y$ and $z$.

Let us consider two states $\psi_i = \psi_{n,\mathbf{k}_\parallel,\sigma}$ and $\psi_j = \psi_{m,\mathbf{k}_\parallel,\sigma}$, where $n$ and $m$ are the subband indices, and we assume that $n \neq m$. We are interested in the optical transitions between the two states (note that we have assumed that the two states have same in-plane momentum $\mathbf{k}_\parallel$ and spin $\sigma$ for the reasons discussed in Sec. 2.1). In particular, the absorption probability from $\psi_i$ to $\psi_j$, with $E_i < E_j$, for the valley $\gamma$ is given by

$$P^\gamma_{n\to m}(\mathbf{k}_\parallel,\sigma)=\frac{2\pi}{\hbar}A_0^2\left|\sum_\alpha\hat{e}_\alpha w^\gamma_{\alpha z}\right|^2\cdot|p^z_{nm}|^2\cdot e^2\delta(E_m-E_n-\hbar\omega), \tag{2.50}$$

where $p^z_{nm}$ is the matrix element $\langle\psi_{n,\mathbf{k}_\parallel,\sigma}|p_z|\psi_{m,\mathbf{k}_\parallel,\sigma}\rangle$: note that, if we assume the form (1.66) for the $\psi$ envelope functions, the only component that gives non-zero matrix element is $p_z$, since we have assumed that the two states belong to two different subbands $n \neq m$. As a consequence, this matrix element does not depend neither on $\mathbf{k}_\parallel$ nor on $\sigma$. Moreover, we are assuming parabolic and parallel subbands, so that $E_j - E_i = E_m - E_n$ ($E_n$ and $E_m$ are the energy at the bottom of the respective subbands). Therefore, the energy difference in the Dirac's delta depends only on the subband indices $n$ and $m$ and as a consequence also $P^\gamma_{n\to m}(\mathbf{k}_\parallel,\sigma)$ depends only on $n$ and $m$. However, we have left the indices $\mathbf{k}_\parallel$ and $\sigma$ explicitly indicated to remind that this is a quantity that is evaluated for a transition between two single states and not between all states of the two subbands $n$ and $m$.

To take into account the broadening of the states, also in this case we substitute the $\delta$ function with the Lorentzian of (2.13). Note however that this substitution holds only if the broadening $\Gamma$ is much smaller than the level separation $E_m - E_n$. In the opposite case, which may happen for instance for intersubband transitions in the THz range, the more general lineshape expression given in Sec. 2.A is appropriate.

For the emission from $\psi_j$ to $\psi_i$, it is easy to show that $P^\gamma_{n\to m}(\mathbf{k}_\parallel,\sigma) = P^\gamma_{m\to n}(\mathbf{k}_\parallel,\sigma)$. The net transition rate $W(\omega)$ between the two subbands $n$ and $m$, which occurs at the same frequency $\omega$ for all $\mathbf{k}_\parallel$ due to the mentioned hypothesis of parallel bands, is then given by

$$W^\gamma_{n\to m}(\omega)=P^\gamma_{n\to m}\sum_{\mathbf{k}_\parallel,\sigma}\left[f(E_i,\mathbf{k}_\parallel)-f(E_j,\mathbf{k}_\parallel)\right]:$$

here, $f$ is the Fermi distribution function, and we remind that $E_i = E_n + \frac{\hbar^2}{2}\mathbf{k}_\parallel\cdot\tilde{w}\cdot\mathbf{k}_\parallel$, where $\tilde{w}$ is the $2\times 2$ mass tensor on the $xy$ plane described in Eq. (1.69).

Using these results, we can write the 2D (adimensional) absorption coefficient, defined as the usual absorption coefficient multiplied by the length $L_z$ of the het-

erostructure. Its expression is

$$\alpha_{2\mathrm{D}}(\omega) = \sum_{\substack{n<m \\ \gamma}} \sum_{\mathbf{k}_\parallel} 2P^{\gamma}_{n\to m} \frac{\hbar}{2Scn\varepsilon_0 A_0^2 \omega} [f(E_i, \mathbf{k}_\parallel) - f(E_j, \mathbf{k}_\parallel)],$$

where $S = V/L_z$ is the sample surface and the factor of two accounts for the sum over the spins.

### 2.5.2 Oscillator strengths

Before going on to determine an explicit expression for $\alpha_{2\mathrm{D}}(\omega)$, we define the oscillator strength (OS) that is useful to express $\alpha(\omega)$ in a more compact form; in fact, often in the literature the absorption coefficient is not written explicitly as a function of the matrix element contained in $P^{\gamma}_{n\to m}$ but as a function of the OS. Since the definition of the OS is not unique in the literature, we report here its expressions together with the respective Thomas–Kuhn sum rule for the different cases that are of interest.

#### Oscillator strength and Thomas–Kuhn rule in the simplest case

Let us consider a system with the simple Hamiltonian

$$H\phi(z) = E\phi(z), \qquad H = -\frac{\hbar^2}{2m_0}\frac{\partial^2}{\partial z^2} + V(z), \tag{2.51}$$

i.e. a simple one-dimensional Schrödinger equation with fixed isotropic mass, equal to the free-electron mass $m_0$.

In this case, it is usual to define the (adimensional) oscillator strength between two eigenstates $\phi_n$ and $\phi_m$ of the Hamiltonian (2.51) as

$$f_{nm} = \frac{2}{m_0 \hbar \omega_{mn}} |\langle \phi_n | p_z | \phi_m \rangle|^2 \tag{2.52}$$

where $\hbar\omega_{mn}$ is defined as $(E_m - E_n)$ (with the correct sign, so that $\omega_{nm} = -\omega_{mn}$), and $p_z$ is the usual momentum operator

$$p_z = -i\hbar\frac{\partial}{\partial z}.$$

If the system is bounded, so that the wavefunctions are normalizable and bounded, we can also use (within the dipole approximation) the interaction Hamiltonian $H' = -e\mathbf{E}\cdot\mathbf{r}$, using the relation between the matrix elements:

$$\mathbf{p}_{nm} = im_0\omega_{nm}\mathbf{r}_{nm} \tag{2.53}$$

so that the oscillator strength can also be written as

$$f_{nm} = \frac{2m_0\omega_{mn}}{\hbar} |\langle \phi_n | z | \phi_m \rangle|^2.$$

Note that this substitution is not strictly correct for periodic systems (for instance for systems described by the Kronig–Penney model, as superlattices), and in this case the $\mathbf{A}\cdot\mathbf{p}$ interaction should be used. For a detailed discussion of the error introduced when using the $z$ matrix element, see Ref. [72].

The above-defined oscillator strength satisfies the sum rule

$$\sum_m f_{nm} = 1, \tag{2.54}$$

known as the Thomas–Kuhn sum rule, which is valid for all initial states $n$ and where the sum extends over all final states $m$.

We prove this sum rule in the case of a finite bounded system by writing the oscillator strength as in (2.52):

$$\sum_m f_{nm} = \sum_m \frac{2}{m_0\hbar\omega_{mn}} |\langle\phi_n|p_z|\phi_m\rangle|^2 = \sum_m \frac{2}{m_0\hbar\omega_{mn}} \langle\phi_n|p_z|\phi_m\rangle\langle\phi_m|p_z|\phi_n\rangle .$$

Using now Eq. (2.53), we can write

$$\begin{aligned}\langle\phi_m|p_z|\phi_n\rangle &= im_0\omega_{mn}\langle\phi_m|z|\phi_n\rangle ;\\ \langle\phi_n|p_z|\phi_m\rangle &= im_0\omega_{nm}\langle\phi_n|z|\phi_m\rangle = -im_0\omega_{mn}\langle\phi_n|z|\phi_m\rangle\end{aligned}$$

and thus the sum rule becomes

$$\begin{aligned}\sum_m f_{nm} &= \sum_m \frac{1}{m_0\hbar\omega_{mn}}(\langle\phi_n|p_z|\phi_m\rangle\langle\phi_m|p_z|\phi_n\rangle + \langle\phi_n|p_z|\phi_m\rangle\langle\phi_m|p_z|\phi_n\rangle) =\\ &= \sum_m \frac{i}{\hbar}(\langle\phi_n|p_z|\phi_m\rangle\langle\phi_m|z|\phi_n\rangle - \langle\phi_n|z|\phi_m\rangle\langle\phi_m|p_z|\phi_n\rangle) = \frac{i}{\hbar}\langle\phi_n|[p_z,z]|\phi_n\rangle\end{aligned}$$

where in the last step we have used the completeness relation $\sum_m |\phi_m\rangle\langle\phi_m| = 1$.

Finally, using the commutator relation

$$[p_z, z] = -i\hbar \tag{2.55}$$

and the fact that the states $|\phi_n\rangle$ are normalized to one, we get the sum rule (2.54).

**Oscillator strength in the case $m^* \neq m_0$**

We consider now a system with an effective mass $m^*$ different from the bare electron mass $m_0$, but still limiting the analysis to an isotropic mass. In this case, the Hamiltonian is

$$H\phi(z) = E\phi(z), \qquad H = -\frac{\hbar^2}{2m^*}\frac{\partial^2}{\partial z^2} + V(z).$$

In the literature, slightly different definitions of the oscillator strength are used.

Apparently, the simplest extension of the definition of the previous section is to substitute $m_0$ with $m^*$: we thus get the definition of the oscillator strength

$$\tilde{f}_{nm} = \frac{2}{m^* \hbar \omega_{mn}} |\langle \phi_n | p_z | \phi_m \rangle|^2 \stackrel{*}{=} \frac{2m^* \omega_{mn}}{\hbar} |\langle \phi_n | z | \phi_m \rangle|^2$$

where the second equality holds exactly only for finite bounded systems. With this definition the sum rule has the same form of Eq. (2.54), i.e. $\sum_m \tilde{f}_{nm} = 1$. This definition is used for instance in Ref. [73].

However, as discussed below, this definition cannot be easily extended to the case of a non-isotropic effective mass. Sometimes, in the literature one finds a different expression of the oscillator strength, that actually coincides with that of Eq. (2.52):

$$\overset{\triangle}{f}_{nm} = \frac{2}{m_0 \hbar \omega_{mn}} |\langle \phi_n | p_z | \phi_m \rangle|^2$$

which satisfies the modified Thomas–Kuhn sum rule

$$\sum_m \overset{\triangle}{f}_{nm} = \frac{m^*}{m_0}.$$

Even this form, however, is not suitable to be extended to the case of a non-isotropic mass; we instead choose the following form:

$$f_{nm} = \frac{2m_0}{\hbar \omega_{mn}} \frac{1}{(m^*)^2} |\langle \phi_n | p_z | \phi_m \rangle|^2 \tag{2.56}$$

with the modified Thomas–Kuhn sum rule

$$\sum_m f_{nm} = \frac{m_0}{m^*}. \tag{2.57}$$

We use this expression in the following since, as we are going to see in a moment, it can be naturally extended to the case of a non-isotropic mass. We stress again that in the literature all the three forms of the oscillator strength can be found, and one must be careful to check the one that is used.

**Oscillator strength for a non-diagonal inverse mass tensor**

We now consider the case in which the inverse-mass tensor $w$ is no more a multiple of the identity.

In this case, the envelope function (for a given fixed valley $\gamma$ and band) is the eigenfunction of a Hamiltonian of the form

$$H = \frac{1}{2} \mathbf{p} \cdot w^\gamma \cdot \mathbf{p} + V(z),$$

where $\mathbf{p}$ is the vector momentum operator $\mathbf{p} = -i\hbar\nabla$ and $w^\gamma$ is the $3 \times 3$ inverse mass tensor relative to the given band and valley $\gamma$, as discussed at the beginning of Sec. 2.5.1.

In the general case of two and three dimensions, we have to consider explicitly the polarization vector $\hat{\mathbf{e}}$ of the photon which is involved in the transitions between the two states.

Following Ref. [74], we thus define the oscillator strength for a given fixed valley $\gamma$ and a given polarization $\hat{\mathbf{e}}$ as

$$\begin{aligned} f_{nm}^{\gamma} &= \frac{2m_0}{\hbar\omega_{mn}} |\langle\psi_n|\hat{\mathbf{e}}\cdot w^{\gamma}\cdot\mathbf{p}|\psi_m\rangle|^2 = \\ &= \frac{2m_0}{\hbar\omega_{mn}} (\hat{e}_x w_{xz}^{\gamma} + \hat{e}_y w_{yz}^{\gamma} + \hat{e}_z w_{zz}^{\gamma})^2 |p_{nm}^z|^2, \end{aligned} \tag{2.58}$$

where $p_{nm}^z$ is the matrix element of the $p^z$ component of the momentum operator between the states $|n\rangle$ and $|m\rangle$, that are the parts of the envelope function $\psi$ that depend only on $z$ after the variable separation, as described in Sec. 1.8.1.

The motivation for this definition can be understood looking at the expression for the intersubband absorption coefficient $\alpha_{2\mathrm{D}}(\omega)$ given in Sec. 2.5.1: $f_{nm}$ is defined in a way that it reduces to Eq. (2.56) for isotropic $m^*$, and that it is an "ingredient" of the equation that we will obtain for $\alpha_{2\mathrm{D}}(\omega)$, i.e. Eq. (2.63).

Let us now derive the expression of the oscillator strength as a function of the position matrix element instead that of $\langle p_z\rangle$. As a first step, we express the commutator $[H,z]$ in terms of $\mathbf{p}$:

$$[H,z] = \sum_{i,j}\left[\frac{1}{2}p_i w_{ij}^{\gamma} p_j + V(z), z\right] = \sum_{i,j}\left[\frac{1}{2}p_i w_{ij}^{\gamma} p_j, z\right] = \frac{1}{2}(A+B+C), \tag{2.59}$$

where

$$A = \sum_{j=x,y}[p_z w_{zj}^{\gamma} p_j, z], \quad B = \sum_{i=x,y}[p_i w_{iz}^{\gamma} p_z, z], \quad C = [p_z w_{zz}^{\gamma} p_z, z].$$

Let us calculate the three contributions. For the first two terms, since $[p_i, z] = 0$ for $i = x, y$, we have that the terms $A + B$ can be written as

$$A + B = \sum_{j=x,y} w_{zj}^{\gamma} p_j [p_z, z] + \sum_{i=x,y} w_{iz}^{\gamma} p_i [p_z, z] = -2i\hbar \sum_{j=x,y} w_{zj}^{\gamma} p_j \tag{2.60}$$

where we have used the fact that the tensor $w^{\gamma}$ is symmetric, and we have substituted the commutation relation of Eq. (2.55).

For the term $C$ we have instead

$$C = [p_z w_{zz}^{\gamma} p_z, z] = p_z w_{zz}^{\gamma}[p_z, z] + [p_z, z] w_{zz}^{\gamma} p_z = -2i\hbar p_z w_{zz}^{\gamma}, \tag{2.61}$$

so that, inserting Eqs. (2.60) and (2.61) in Eq. (2.59) we obtain

$$[H,z] = -i\hbar \sum_{j=x,y,z} w_{zj}^{\gamma} p_j.$$

We can now express the $p_z$ matrix element as a function of the $z$ matrix element:

$$\langle n|p_z|m\rangle \overset{\star}{=} \sum_j \frac{\langle n|w^\gamma_{zj}p_j|m\rangle}{w^\gamma_{zz}} = \frac{i}{\hbar}\frac{\langle n|[H,z]|m\rangle}{w^\gamma_{zz}} = \frac{i}{\hbar}\frac{1}{w^\gamma_{zz}}(E_m - E_n)\langle n|z|m\rangle\,, \quad (2.62)$$

where the equality marked with a star holds since the matrix elements of $p_x$ and $p_y$ vanish, due to the symmetry of the eigenfunctions $|n\rangle$, $|m\rangle$.

Using Eq. (2.62), we can finally rewrite the oscillator strength of Eq. (2.58) as

$$\begin{aligned} f^\gamma_{nm} &= \frac{2m_0\omega_{mn}}{\hbar}\frac{(\hat{e}_x w^\gamma_{xz} + \hat{e}_y w^\gamma_{yz} + \hat{e}_z w^\gamma_{zz})^2}{w^2_{zz}}|\langle n|z|m\rangle|^2 = \\ &= \frac{2m_0 E^{\mathrm{tr}}_{mn}}{\hbar^2}\frac{(\hat{e}_x w^\gamma_{xz} + \hat{e}_y w^\gamma_{yz} + \hat{e}_z w^\gamma_{zz})^2}{w^2_{zz}}|\langle n|z|m\rangle|^2 \end{aligned}$$

where the transition energy $E^{\mathrm{tr}}_{mn}$ is defined as usual: $E^{\mathrm{tr}}_{mn} = \hbar\omega_{mn} = \hbar(\omega_m - \omega_n)$.

Finally, we derive the Thomas–Kuhn sum rule fulfilled exploiting this definition of the oscillator strength. We have from Eq. (2.58):

$$\begin{aligned} \sum_m f^\gamma_{nm} &= (\hat{e}_x w^\gamma_{xz} + \hat{e}_y w^\gamma_{yz} + \hat{e}_z w^\gamma_{zz})^2\frac{2m_0}{\hbar}\sum_m \frac{\langle n|p_z|m\rangle\langle m|p_z|n\rangle}{\omega_{nm}} = \\ &= D\frac{i}{\hbar}\sum_m \frac{\omega_{mn}\langle n|z|m\rangle\langle m|p_z|n\rangle + \omega_{nm}\langle n|p_z|m\rangle\langle m|z|n\rangle}{\omega_{nm}} \end{aligned}$$

where we have substituted Eq. (2.62) once for the first matrix element and once for the second one, and we have defined

$$D = \frac{(\hat{e}_x w^\gamma_{xz} + \hat{e}_y w^\gamma_{yz} + \hat{e}_z w^\gamma_{zz})^2 m_0}{w^\gamma_{zz}}.$$

Now we use $\omega_{mn}/\omega_{nm} = -1$ and the completeness relation $\sum_m |m\rangle\langle m| = 1$, so that the sum rule becomes

$$\sum_m f^\gamma_{nm} = D\frac{i}{\hbar}(\langle n|p_z z|n\rangle - \langle n|z p_z|n\rangle) = D\frac{i}{\hbar}\langle n|[p_z, z]|n\rangle$$

and since from Eq. (2.55) we have $[p_z, z] = -i\hbar$, we finally obtain the final form for the sum rule

$$\sum_m f^\gamma_{nm} = \frac{(\hat{e}_x w^\gamma_{xz} + \hat{e}_y w^\gamma_{yz} + \hat{e}_z w^\gamma_{zz})^2 m_0}{w^\gamma_{zz}}.$$

To verify this result, we check what happens when the effective mass is isotropic. In this case, the $w^\gamma$ tensor is diagonal and thus $w^\gamma_{xz} = w^\gamma_{yz} = 0$, and moreover $w^\gamma_{zz} = 1/m^*$. The sum rule becomes

$$\sum_m f^\gamma_{nm} = \hat{e}_z^2 m_0 w^\gamma_{zz} = \hat{e}_z^2\frac{m_0}{m^*}\left(= \frac{m_0}{m^*} \text{ for a TM polarization}\right),$$

that shows that in this limit only the light polarized along the growth direction $z$ (pure TM mode) can produce intersubband transitions, and in this case the sum rule has the same form of Eq. (2.57).

### 2.5.3 Absorption coefficient as a function of the oscillator strength

We can now continue the derivation of the expression of the absorption coefficient, that we started in Sec. 2.5.1, using the expression of the oscillator strength derived in the previous Section.

Using the definition of Eq. (2.58), we can rewrite the probability per unit time $P^{\gamma}_{n\to m}(\mathbf{k}_{\parallel},\sigma)$ of Eq. (2.50) as

$$P^{\gamma}_{n\to m}(\mathbf{k}_{\parallel},\sigma) = \frac{\pi e^2 \omega_{mn}}{m_0} A_0^2 f^{\gamma}_{nm} \delta(E_m - E_n - \hbar\omega).$$

The adimensional absorption coefficient thus becomes (substituting the Dirac's delta with the Lorentzian function, see also Sec. 2.A for a discussion on the validity of this substitution):

$$\begin{aligned}\alpha_{2D}(\omega) &= \sum_{\substack{n<m\\ \gamma}} \sum_{\mathbf{k}_{\parallel}} \frac{f^{\gamma}_{nm}}{cn\varepsilon_0\omega} \frac{\hbar e^2 \omega_{mn}}{m_0 S} \frac{\Gamma}{(E_m - E_n - \hbar\omega)^2 + \Gamma^2} [f_n(\mathbf{k}_{\parallel}) - f_m(\mathbf{k}_{\parallel})] = \\ &= \sum_{\substack{n<m\\ \gamma}} \int \frac{d^2\mathbf{k}_{\parallel}}{(2\pi)^2} \frac{f^{\gamma}_{nm} e^2 \omega_{mn} \hbar}{cn\varepsilon_0\omega m_0} \frac{\Gamma}{(E_m - E_n - \hbar\omega)^2 + \Gamma^2} [f_n(\mathbf{k}_{\parallel}) - f_m(\mathbf{k}_{\parallel})].\end{aligned}$$

Note that $f^{\gamma}_{nm}$ is the oscillator strength, while $f_n(\mathbf{k}_{\parallel})$ is the Fermi distribution for the state of the subband $n$ with in-plane momentum $\mathbf{k}_{\parallel}$.

We now substitute the integral over $\mathbf{k}_{\parallel}$ with an integral over the energy: calling $m^{*\gamma}_{DOS}$ the DOS mass for a single valley (it has the same value for all valleys), and correctly taking into account the spin degeneracy, we obtain

$$\begin{aligned}\alpha_{2D}(\omega) = \sum_{\substack{n<m\\ \gamma}} \int_{E_n}^{\infty} dE' \frac{m^{*\gamma}_{DOS}}{\pi\hbar^2} \cdot \frac{e^2 \omega_{mn} \hbar}{2cn\varepsilon_0\omega m_0} \cdot \\ \cdot \frac{f^{\gamma}_{nm}\Gamma}{(E_m - E_n - \hbar\omega)^2 + \Gamma^2} [f(E') - f(E' + E_m - E_n)]\end{aligned}$$

where we have used again the assumption that the bands are parabolic and parallel. Under these assumptions, we can perform explicitly the integration:

$$\begin{aligned}\alpha_{2D}(\omega) = &\frac{e^2}{2cn\varepsilon_0\omega m_0 \pi\hbar} \sum_{\substack{n<m\\ \gamma}} m^{*\gamma}_{DOS} \omega_{mn} \frac{f^{\gamma}_{nm}\Gamma}{(E_m - E_n - \hbar\omega)^2 + \Gamma^2} \cdot \\ &\cdot \int_{E_n}^{\infty} dE' \left[ \frac{1}{e^{(E'-E_f)/KT} + 1} - \frac{1}{e^{(E'+E_m-E_n-E_f)/KT} + 1} \right]\end{aligned}$$

where $E_f$ is the Fermi energy, and integrating we finally obtain:

$$\begin{aligned}\alpha_{2D}(\omega) = \frac{e^2}{2\varepsilon_0 cn\hbar} \sum_{\substack{n<m\\ \gamma}} \frac{m^{\gamma}_{DOS}}{m_0} \cdot \frac{\omega_{mn}}{\omega} \cdot \frac{\Gamma/\pi}{(E_m - E_n - \hbar\omega)^2 + \Gamma^2} \cdot \\ \cdot f^{\gamma}_{nm} \cdot KT \log\left[ \frac{e^{(E_f - E_n)/KT} + 1}{e^{(E_f - E_m)/KT} + 1} \right].\end{aligned} \tag{2.63}$$

### 2.5.4 Low-temperature limit

In the low temperature limit $T \to 0$, assuming that only the lowest state $n = 1$ is filled, we get the following limit:

$$\log\left[\frac{e^{(E_f-E_n)/KT}+1}{e^{(E_f-E_m)/KT}+1}\right]\cdot KT \to (E_f - E_1)\delta_{n,1}$$

so that the absorption coefficient becomes (if we focus only to transitions to the first empty state $m = 2$):

$$\lim_{T\to 0}\alpha_{2D}(\omega) = \frac{e^2}{2\varepsilon_0 cn\hbar\pi}\sum_\gamma\left[\frac{m^\gamma_{DOS}}{\pi\hbar^2}(E_f - E_1)\right]\frac{\pi\hbar^2}{m_0}\frac{\omega_{21}}{\omega}\frac{\Gamma}{(E_{21}-\hbar\omega)^2+\Gamma^2}f^\gamma_{12}.$$

Now we note that the square bracket is the surface density of the electrons filling the first subband up to energy $E_f$ in a given valley $\gamma$, i.e. its value is $n_{2\mathrm{D}}/N^\gamma$, where $N^\gamma$ is the number of degenerate valleys and $n_{2\mathrm{D}}$ is the total number of free electrons per unit surface in the sample. The expression thus becomes

$$\lim_{T\to 0}\alpha_{2D}(\omega) = \frac{n_{2\mathrm{D}}e^2\hbar}{2\varepsilon_0 cn}\left[\frac{\sum_\gamma f^\gamma_{12}}{N^\gamma m_0}\right]\cdot\frac{\Gamma}{(E_{21}-\hbar\omega)^2+\Gamma^2}\cdot\frac{\omega_{21}}{\omega}$$

and its maximum value (reached at $\omega_{21} = \omega$) is

$$\alpha^{\max}_{2D} = \frac{n_{2\mathrm{D}}e^2\hbar}{2\varepsilon_0 cn\Gamma}\left(\frac{\sum_\gamma f^\gamma_{12}/m_0}{N^\gamma}\right).$$

i.e. the formula given also in Ref. [73], averaged over all valleys.

To have a rough estimate of this value, we note that in most cases for quantum well systems we can consider that the largest part of the sum rule is saturated by $f_{12}$, so that we can substitute $f^\gamma_{12} \approx \sum_m f^\gamma_{1m}$. Note moreover that in the case of a pure TM radiation (field along $\hat{z}$), the expression of the sum rule of the oscillator strength reduces to

$$\sum_m f^\gamma_{1m} = m_0 w_{zz} = \frac{m_0}{m^*_z}$$

so that in this simple case the system behaves as if it had an isotropic mass equal to the $m^*_z$ mass.

## 2.A Appendix: Lineshape function for large broadenings

In Eq. (2.13) we have discussed that often the broadening effects on the absorption coefficient are simply taken into account by substituting the Dirac's delta $\delta(E_{ij} - \hbar\omega)$ with the Lorentzian $\frac{\Gamma}{\pi}\frac{1}{(E_{ij}-\hbar\omega)^2+\Gamma^2}$.

We discuss in this Appendix why this substitution is reasonable, and the limits of its validity. We can see directly by inspection of the expressions for $\alpha_{2D}$ that the Lorentzian broadening cannot correct describe systems with small transition energy and large broadening. Indeed, if the Lorentzian broadening $\Gamma$ is comparable (or even larger) than the intersubband transition energies $E_{ij}$, we have a divergence of $\alpha_{2D}(\omega)$ at zero frequency due to the factor $1/\omega$ in its expression, see for instance Eq. (2.63). If instead $\Gamma$ is small, then we can assume that the Lorentzian provides an effective damping of the $\alpha$ coefficient, and (far from $\omega = 0$) the expression is valid.

Let us then start again from Eqs. (2.7) and (2.8). We remind the limit [61]

$$\lim_{\Gamma\to 0^+} \frac{1}{x - i\Gamma} = P\frac{1}{x} + i\pi\delta(x). \tag{2.64}$$

Then, we can substitute the $\delta(E_{ij} - \hbar\omega)$ that we are using to describe the imaginary part $\varepsilon_2$ of the dielectric constant with $\frac{1}{E_{ij}-\hbar\omega-i\Gamma}$, and then at the end we will take the imaginary part to have the expression of $\varepsilon_2$ and thus of $\alpha$.

If we make this substitution, we see that in the sum of Eq. (2.9) we have that each

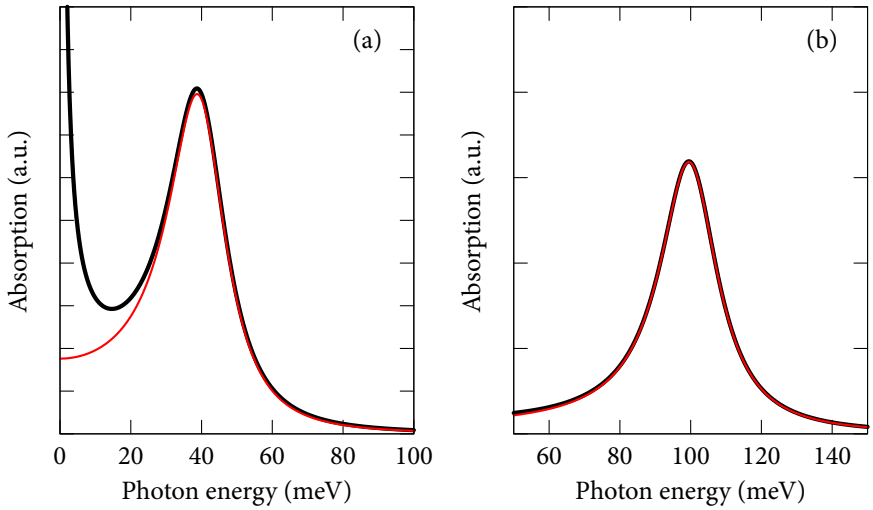


**Figure 2.4** – Comparison of the absorption coefficient obtained adopting different lineshapes, as discussed in Sec. 2.A. We have chosen $E_{ji} = 40$ meV in panel (a) and $E_{ji} = 100$ meV in panel (b). The black curve is obtained using a Lorentzian lineshape of (2.67), while the red curve is obtained using the lineshape of (2.65). In both panels, the broadening is set to $\Gamma = 10$ meV.

pair of states $(i, j)$ contributes with two terms:

$$\sum_{ij} |\langle\psi_j|\hat{\mathbf{e}}\cdot\mathbf{p}|\psi_i\rangle|^2 \frac{1}{E_{ji}-\hbar\omega-i\Gamma}[f(E_i)-f(E_j)] =$$
$$\sum_{i<j} |\langle\psi_j|\hat{\mathbf{e}}\cdot\mathbf{p}|\psi_i\rangle|^2 \left\{\frac{1}{E_{ji}-\hbar\omega-i\Gamma}-\frac{1}{-E_{ji}-\hbar\omega-i\Gamma}\right\}[f(E_i)-f(E_j)],$$

where we the sum is now only on $i < j$ and we have used $E_{ij} = -E_{ji}$, and $f(E_j) - f(E_i) = -[f(E_i) - f(E_j)]$.

The term in curly brackets can be rewritten as

$$\left\{\frac{2E_{ji}}{E_{ji}^2-(\hbar\omega+i\Gamma)^2}\right\}$$

and to obtain the expression for the lineshape of $\alpha$ we have to take its imaginary part divided by $\pi$, see Eq. (2.64), obtaining

$$\frac{\Gamma}{\pi}\frac{2E_{ji}\cdot 2\hbar\omega}{(E_{ji}^2-\hbar^2\omega^2+\Gamma^2)^2+(2\hbar\omega\Gamma)^2}. \tag{2.65}$$

This is the more correct lineshape to be used when $\Gamma$ is comparable to $E_{ji}$: in fact, now we have a factor $\omega$ at the numerator which removes the degeneracy at $\omega = 0$ discussed above for Eq. (2.63).

To justify the Lorentzian approximation, we consider the limit $\Gamma \ll E_{ji}$ and $\Gamma \ll \hbar\omega$, which is for instance a very good approximation for interband transitions, where $\Gamma$ is typically of the order of 10 meV while $E_{ji} \approx 1$ eV. Then, we can discard the $\Gamma^2$ term in the first bracket at the denominator of Eq. (2.65), and moreover we can assume that

$$E_{ji} + \hbar\omega \approx 2\hbar\omega \approx 2E_{ji} \tag{2.66}$$

near the resonance, where $\alpha$ is non-zero. Then, for the first bracket at the denominator of Eq. (2.65) it holds

$$(E_{ji}^2-\hbar^2\omega^2)^2 = (E_{ji}-\hbar\omega)^2(E_{ji}+\hbar\omega)^2 \approx (E_{ji}-\hbar\omega)^2(2E_{ji})^2$$

and then, approximating Eq. (2.65) using (2.66) we get that the lineshape is approximately given by

$$\frac{\Gamma/\pi}{(E_{ji}-\hbar\omega)^2+\Gamma^2}, \tag{2.67}$$

which is the Lorentzian lineshape discussed in Eq. (2.13).

In Fig. 2.4, a comparison of the absorption coefficient obtained using the two lineshapes is reported for a broadening $\Gamma = 10$ meV and for different values of $E_{ji}$. We see in Fig. 2.4a that near $\omega = 0$ the correct lineshape (red curve) must be taken into account to avoid divergences. In Fig. 2.4b we can instead notice that the difference between the two lineshapes is very small already for $E_{ji} = 100$ meV, if we are not interested in the absorption in regions of the spectrum near $\omega = 0$.

# Part II

# Applications

# Chapter 3

# THz emission from Si-compatible multilayer SiGe heterostructures

## 3.1 Introduction

In the last years, there has been an increasing interest in the development of unipolar photonic devices based on intersubband (ISB) transitions and operating in a quantum cascade (QC) architecture.

The first quantum cascade laser (QCL), emitting in the mid-infrared, was developed at Bell Labs in 1994 [75]. A few years later, in 2002, the first THz QCL (fabricated with a GaAs/AlGaAs heterostructure) was demonstrated by Köhler et al. [76]. This device opened a whole new field of research and applications, since for the first time cheap and compact sources in the THz region of the electromagnetic spectrum (1–10 THz, $\lambda \approx 300$–$30\,\mu$m, $E \approx 4$–$40$ meV) became easily available. In just a few years, in fact, the development of THz devices has grown incredibly fast [77].

This rapid development has also been driven by the rather large number of applications of the THz radiation, which are mainly of two categories: imaging and sensing. In fact, since THz radiation has a low diffusion in inhomogeneous materials, it is particularly suited for imaging applications; moreover, it can be used for sensing since many complex molecules have rovibrational absorption lines in this frequency range.

The unprecedented performance of these devices for what concerns the linewidth and the output power has already given rise to applications in local oscillators [78,79], real-time imaging [80] and molecular spectroscopy [81]. Detailed review of the applications of THz radiation can be found for instance in Refs. [42, 82].

The key requirement for most applications is the availability of cheap, high-power and compact THz sources, and the THz ISB lasers have these features. Moreover, the possibility of tailoring the emission frequency when designing the structure is another great advantage of these solid state devices: for instance, since the first THz QCL operating at 4.4 THz [76], there have been demonstrations of devices emitting even below 1 THz [83]. However, THz QCLs have one main issue which has not been

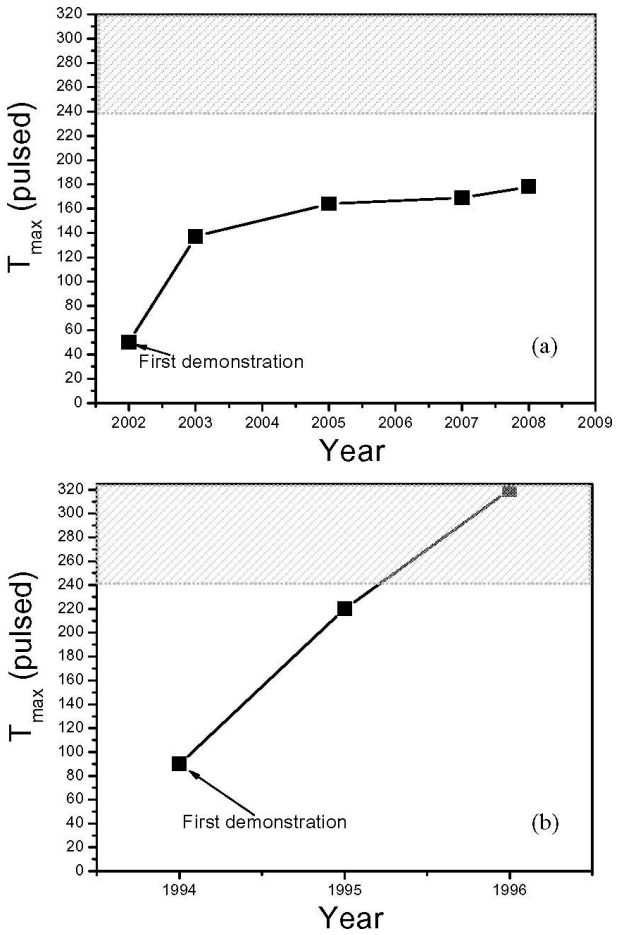


**Figure 3.1** – Timeline for the maximum operating temperature in pulsed mode for (a) THz QCLs and (b) mid-IR QCLs. The shaded area represents the temperature region achievable with thermoelectric coolers. Figure reproduced from [87].

solved yet: they can operate only at low temperature (in contrast to mid-IR QCLs). In fact, the first THz QCL was able to operate up to 50 K. Nowadays, even if many critical improvements have been made, mainly to the design of the active region and of the waveguide, the present maximum operating temperature is only slowly increasing, as evident in Fig. 3.1. The highest operating temperature at the moment of writing is 186 K [84], even if there has been a recent claim at the ITQW2011 conference of a new record temperature of 193 K [85]; note however that higher temperatures (225 K) have been reached by the application of a strong magnetic field to reduce the non-radiative scattering [86]. Thus THz lasing still needs cryogenic operation since it has not reached the temperature range accessible with thermoelectric (Peltier) coolers.

This is a very important issue that needs to be solved, since in many market and industrial applications (as the ones discussed above) devices working at room

temperature are required. However, it is commonly believed that further incremental developments to the current devices will not lead to significant improvements for what concerns the operating temperature; innovative approaches must be developed [87].

One interesting and promising possibility is to exploit new materials in the QC design, which can have better characteristics and overcome the intrinsic limitations of the usual GaAs/AlGaAs heterostructures. For instance, to take advantage of the lower effective masses, InP-based InGaAs/AlGaAs THz lasers are being investigated [88].

But also Si, Ge and their alloys are now attracting increasing efforts towards the realization of QC lasers. These materials were not usually considered suitable for photonics applications due to their indirect band gap, preventing an efficient recombination of electrons and holes and thus precluding the realization of efficient interband optical devices. (For more details on interband transitions in SiGe structures, see Chap. 4.) However, the exploitation of intersubband transitions either in the valence or in the conduction band allows to overcome this limitation. One of the reasons which pushes towards the realization of Si- and Ge-based optical devices is the possibility of integrating the optical part of the device with its control electronics. In fact, nowadays the largest part of the electronics is based on Si, and in particular the complementary metal-oxide-semiconductor (CMOS) technology is well established for the realization of integrated circuits. This is due to many factors, as the low static power supply drawn by CMOS devices (since the power is drawn only when switching between *on* and *off* states) and their quite high degree of immunity to noise [89]. Moreover silicon is particularly suited to the realization of these devices because its high thermal conductivity allows to dissipate efficiently the heat. Due to the enormous development of CMOS technology, a CMOS-compatible light-emitting device is particularly appealing, since it would allow the complete integration of the photonics devices on the same chip, with benefits in terms of manufacturing costs, device performance and robustness, etc.

Silicon-germanium multilayer heterostructures, and in particular those grown along the [001] direction, are thus quite appealing from this point of view, since they are highly compatible with CMOS processing [89].

For what concerns SiGe QC devices based on ISB transitions, these are not meant to overcome existing III-V lasers used in fiber-based telecommunications, since for these applications the operating wavelength is fixed by technological reasons in the near-infrared and thus requires lasers operating with interband transitions (see Chap. 4). On the other hand, chip-to-chip optical interconnects in electronic circuits are at the moment the object of intense research in order to overcome the current limitations of electronic connections. THz lasers could be an interesting opportunity, since THz radiation can be easily guided by metallic waveguides, and most integrated circuits elements (substrates, plastic cover, ...) are quite transparent in this frequency range; moreover Si-based lasers are the optimal choice thanks to their possibility of being directly integrated on the chips.

However, the most important advantage in the adoption of Si and Ge is that they are non-polar materials and thus the interaction of electrons with polar lon-

gitudinal optical (LO) phonons is absent. This is the main source of non-radiative intersubband relaxation for electrons, which reduces the population inversion and thus the possibility of device operation at high temperatures. Hence, SiGe lasers could give the possibility of obtaining THz emission at room temperature. Moreover a Ge/SiGe QCL, having no reststrahlen absorption, could allow the emission in the reststrahlen band of typical III-V semiconductors ranging from 23 to 65 μm (≈20–50 meV), closing the wavelength gap of QCLs existing today.

We remark here that, since silicon and germanium have different lattice constants, the resulting QW structures will be subject to strain fields. From the experimental point of view, this has to be carefully taken into account to avoid formation of defects. Moreover, also when designing cascade structures, one should try to balance the strain (alternating compressively and tensile strained layers) in order to minimize the total elastic energy, and allow the growth of structures with large number of periods without dislocations. In fact, strain can also be exploited as another degree of freedom to adjust the material properties, for instance to shift the band edges or to remove the degeneracies of the states, as it is discussed later in this Chapter.

Electroluminescence from Si-rich Si/SiGe QC structures was observed both in the mid-infrared [90] and in the THz [91], but up to now there have been significant difficulties in demonstrating laser emission. It is important to highlight that in the experiments of Refs. [90, 91], only valence-band ISB transitions were used. One of the reasons is that the valence effective masses are typically smaller than the Δ conduction masses along the tunneling direction in Si-based systems. A large mass, in fact, makes it very difficult to design devices which exploit the mechanism of resonant tunneling injection, since large masses imply small tunneling probabilities and thus small currents; that is, the injection is suppressed. Moreover, since the gain is inversely proportional to the effective mass, we expect that the gain is much more significant in structures with small masses.

However, exploiting valence ISB transitions has some big disadvantages: first, the presence of different valence bands (HH, LH) with similar energy introduces non-radiative scattering channels which reduce the performance of the device. Moreover, these bands have a very large non-parabolicity so that the behavior of a device based on ISB transitions in the valence band is very difficult to predict and describe. Furthermore, in these systems the quantum wells (where the holes are localized) are in the SiGe alloy material regions, whereas the pure Si layers act as barriers: this implies that also alloy scattering will be significant in these systems.

To overcome these difficulties, we will instead address intersubband transitions in $n$–doped Ge-rich Ge/SiGe heterostructures (even if in Sec. 3.5 we also address a Si-rich structure). In fact, when working in the conduction band of SiGe heterostructures, we can think of two main designs. In the first one, realized by Si QWs embedded in Si-rich SiGe barriers, the electrons are confined in the Si Δ valleys. The second possibility is to consider Ge QWs embedded in Ge-rich SiGe barriers, and in this case the electrons are instead confined in the L valleys of Ge.

The first advantage of both conduction-band schemes is that the electrons are not confined in the alloy materials, but either in the Si or in the Ge pure materials, re-

ducing thus significantly the alloy scattering. Moreover, analyzing the band structure of the systems, one sees that devices can be designed so that only one kind of states (e.g. only electrons at L) participate to charge transport, while the other conduction states are higher in energy and can be ignored, simplifying significantly the design of the QCLs (see Sec. 3.4).

The main advantage of Ge-rich structures is that the confinement mass at the L point of Ge along the growth direction is much smaller ($\approx 0.12m_0$) than the effective mass at the $\Delta$ valley in Si, which is $\approx 0.92m_0$, and we have already discussed the importance of having small effective masses in QC structures.

Moreover, the choice of Ge-rich structures has another positive "side effect". Since the inverse-mass tensor at the L point is not diagonal in a reference system where one vector is along the growth direction [001] (see Sec. 1.7), the usual selection rule for intersubband transitions, which forbids the TE mode emission in such structures, no more holds. Hence, it could be possible to observe light emission along the growth direction of a QCL.

Of course, the growth of Ge-rich structures poses non-trivial technical problems, mainly for the realization of a Ge-rich virtual substrate (VS) with small defect density. Only recently the technique of reverse grading has been developed [92], extending to the high Ge-content ($x$) regime the technique used for $x < 0.5$. In this procedure, the VS is obtained varying the composition of the deposited alloys with gradients of the order of 5%/micron [89] up to the desired value.

Most of the work presented in this Chapter has been done in tight collaboration with different experimental groups, in particular the "LFTS" group (Rome, Italy) for what concerns the growth and the spectroscopic analysis of SiGe MQWs, the "CNR-IMM" (Catania, Italy) group for the characterization spectroscopy, the "NEST" (Pisa, Italy) group for what concerns the design phase and the transport measurements, and the "HZDR" (Dresden, Germany) for the time-resolved pump and probe measurements.

## 3.2 ISB transitions in Ge/SiGe MQWs

As a first step towards the realization of a Ge-rich $n-$type THz QCL, the theoretical study and experimental demonstration of ISB transitions in the conduction band of Ge/$Si_{1-x}Ge_x$ MQW structures is needed. Moreover, it is fundamental to acquire a precise knowledge of the bands lineup at the $Si_{1-x}Ge_x$/Ge interface, a difficult task in the high Ge composition range. In fact, in relaxed $Si_{1-x}Ge_x$ alloys, the absolute conduction-band minimum has a $\Delta-$L crossover at $x = 0.85$. Furthermore, the strain in the structure changes significantly the energy of all conduction-band minima. Given a layer sequence, it is therefore crucial to investigate the relative energy position of the $\Delta$ and L states in the strained barriers and wells. Indeed, their relative energy position plays a crucial role in phenomena such as carrier tunneling and transfer doping effectiveness, determining in turn the performance of optoelectronic devices based on this kind of systems.

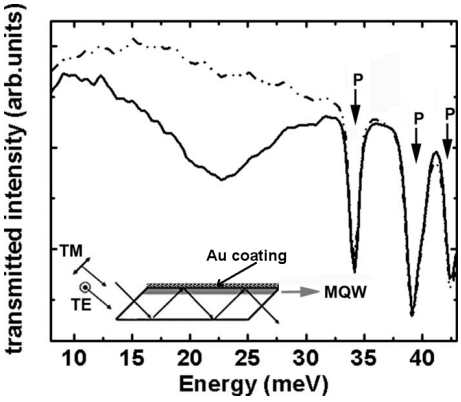


**Figure 3.2** – Normalized transmission spectra for sample 1598: $T_{TE}(E)$ (dashed-dotted line) and $T_{TM}(E)$ (solid line). The absorption peaks due to the dopant levels in the Si substrate are labeled with P. The inset shows a scheme of the optical path inside the sample. The MQWs position is indicated as well as the Au coating.

To this aim, in Refs. [93,94] we have shown experimental evidence of conduction band intersubband transitions in compressively-strained Ge quantum wells confined between Ge-rich SiGe barriers, and reported an extensive study of electronic and optical properties of $Ge/Si_{0.2}Ge_{0.8}$ MQWs, with well width in the range 8.5–24 nm. The absorption measurements have been interpreted by means of the $k \cdot p$ code described in Appendix 3.A of this Chapter. The observed features and the agreement between theoretical and experimental data demonstrate the high quality of the grown Ge/SiGe MQWs, the presence of a significant conduction-band offset and the effectiveness of the adopted theoretical models for evaluating band profiles, electronic structures, and self-consistent spatial distribution of charge carriers due to transfer doping. Furthermore, the careful determination of the strain conditions of the heterostructures has allowed the evaluation of the relative position of the $\Delta$ and L minima in the barriers and in the wells. In particular, we provided a quantitative understanding of why, in a modulation doped Ge/SiGe MQW, only a small fraction of the donor electrons in the barriers transfers into the well region, due to the relative positioning of the $\Delta$ and L states.

The SiGe heterostructures were grown by means of ultra-high vacuum chemical vapor deposition from high purity silane and germane on Si(001) substrates. The MQW structures were deposited at 500 °C on a partially relaxed reverse graded virtual substrate grown on silicon [95,96]. The MQWs were made of 10 repetitions of Ge wells and $Si_{0.2}Ge_{0.8}$ barriers (8 repetitions for sample 1598) with thicknesses reported in Table 3.1. The doping has been obtained by codeposition, adding phosphine to the reacting gases. In selected samples, we have inserted an undoped SiGe spacer layer between the $n$–doped barriers and the Ge wells. For the details of the structural characterization of the samples by means of transmission electron microscopy, x-ray diffraction and Raman spectroscopy we refer to Ref. [94]. We only point out here that these investigations have allowed us to calculate the in-plane lattice parameter $a_{\parallel}$ of each sample (which is the lattice parameter of a relaxed cubic $Si_{1-x}Ge_x$ alloy with $x_{eq} = 0.93$). Moreover, the wells and barriers have always been found to be lattice matched and also coherent with the underlying VS.

Low-temperature intersubband-transition absorption spectra have been mea-

**Table 3.1** – Well ($Si_{0.2}Ge_{0.8}$ barrier) widths $d_w$ ($d_b$) and 2D doping concentrations in the barriers ($\tilde{n}_{2D} = N_D \cdot d_b$) for the investigated samples, where $N_D$ is the donor density in the doped portion of the barriers. Samples 1617 and 1619 have two 4 nm-thick undoped $Si_{0.2}Ge_{0.8}$ spacers on each side of the barrier, and in these two cases $d_b$ includes the spacer layer thickness. Measured values at $T = 10$ K for the two-dimensional carrier densities transferred into the well region ($n_{2D}$), the intersubband absorption energies ($E_{abs}$) and the FWHM ($2\gamma$) of the absorption peaks, are also reported.

| Sample | $d_w$ (nm) | $d_b$ (nm) | $\tilde{n}_{2D}$ ($10^{12}$ cm$^{-2}$) | $n_{2D}$ ($10^{11}$ cm$^{-2}$) | $E_{abs}$ (meV) | FWHM (meV) |
|---|---|---|---|---|---|---|
| 1617 | 8.5 | 29.6 | 12 | 1.5 | 49.5 | 13 |
| 1630 | 10.0 | 22.5 | 1.9 | 1.4 | 45.5 | 13.5 |
| 1616 | 10.2 | 22.0 | 5.5 | 3.4 | 46.0 | 11.5 |
| 1619 | 12.0 | 28.0 | 11 | 2.2 | 39.7 | 10.5 |
| 1596 | 15.0 | 30.0 | 14 | 1.8 | 32.8 | 10.5 |
| 1594 | 18.5 | 30.0 | 12 | 3 | 28.1 | 11 |
| 1597 | 19.5 | 30.0 | 15 | 3.9 | 26.2 | 9.5 |
| 1598 | 24.0 | 30.0 | 15 | 4.7 | 22.2 | 10.5 |

sured on the samples of Table 3.1. In Fig. 3.2 we report the normalized TE ($T_{TE}(E)$) and TM ($T_{TM}(E)$) spectra of sample 1598. In the energy range of 30–50 meV the TE and TM spectra are dominated by narrow absorption features due to the dopant levels of the Si substrate. In addition, a large dip located at 22.2 meV is clearly visible in the TM spectrum. This absorption feature, which is not evident in the TE spectrum, is related to intersubband electronic transitions in the conduction band at the L point. It is worth to point out here that (as already mentioned before) while for Si/SiGe wells ISB transitions are forbidden for TE-polarized light, theoretical calculations indicate that in $n$–type Ge-rich Ge/SiGe MQWs the intersubband absorption of radiation with polarization vector parallel to the QW growth plane becomes visible in the TE spectrum, even if with a weak oscillator strength (≈ 20% of its TM counterpart [74]). Moreover in our samples, this intensity is further reduced because the field component parallel to the MQW plane is strongly suppressed at the surface by phase-matching effects due to the presence of the Au top layer [73]. We then expect that no signal is visible in the TE spectra.

Polarization-independent transitions, such as the narrow absorption features related to the dopant levels mentioned above, can be eliminated by calculating the linear dichroic transmission spectrum $T_D(E) = T_{TM}(E)/T_{TE}(E)$. The linear dichroic spectra of some of the investigated samples are shown in Fig. 3.3 in the energy range where intersubband transitions are predicted by numerical calculations. Although in this region several absorption lines are observed in the TM and TE spectra, the dichroic signal is characterized by a single pronounced transmission dip which is due to a reduced transmission of the TM mode and which monotonically blueshifts upon decreasing the well width. We attribute this feature to optical transitions from the ground to the first excited subband state at the L point. Depending on the number of periods in the MQW structure, on the waveguide length, and on the density of

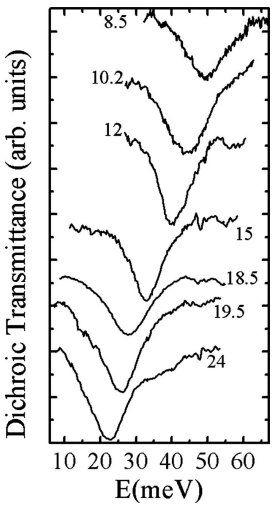


**Figure 3.3** – Measured dichroic transmittance spectra measured for some of the Ge/SiGe MQWs with different well width (reported in nm).

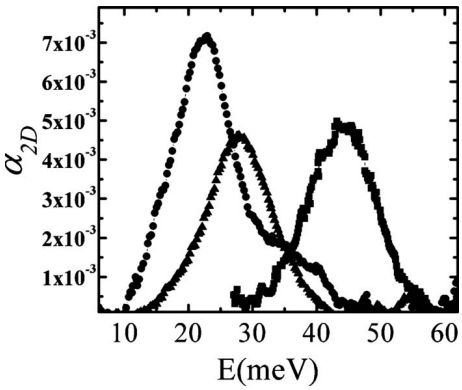


**Figure 3.4** – Single well dimensionless absorption coefficient (see text) for selected samples of Table 3.1: 1598 (circles), 1594 (triangles), 1616 (squares).

charges transferred into the wells, the observed transmission varies in the 50–90% range. For the investigated well widths (8.5–24.0 nm) the intersubband transition energies cover the 22–50 meV energy interval. The typical absorption line width [full width at half maximum (FWHM)] is about 10 meV with a maximum of 13.5 meV obtained for sample 1630.

For the adopted waveguide geometry the dimensionless absorption coefficient $\alpha_{2D}(E)$ (discussed in Sec. 2.5), associated to each QW, can be evaluated from the transmission data using the relation [73]

$$\alpha_{2D}(E) = \frac{-\ln[T(E)]\cos(\theta)}{CMN_W \sin^2(\theta)}, \tag{3.1}$$

where $N_w$ is the number of QWs in the sample, $M$ is the number of internal reflections in the waveguide, $\theta = 45°$ is the angle between the incident radiation and the growth direction, and $C$ is a parameter between 1 and 2 which accounts for the field enhancement due to the surface metallization. The $\alpha_{2D}$ spectra of three representative samples obtained from transmittance data using Eq. (3.1) are reported in Fig. 3.4. We have used the value $C = 1.5$ since this value well reproduces the

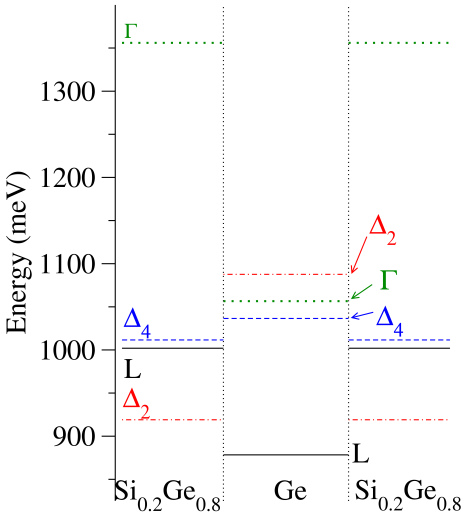


**Figure 3.5** – L (black, solid), $\Delta_2$ (red, dotted-dashed), $\Delta_4$ (blue, dashed), and $\Gamma$ (green, dotted) conduction-band edge profiles for the investigated Ge/$Si_{0.2}Ge_{0.8}$ MQW structures grown on [001] relaxed $Si_{0.07}Ge_{0.93}$ substrates. The zero of energy is set at the average of the top valence bands in the substrate.

absorption spectra that were previously measured [97] in strained Si MQW samples with the same waveguide geometry and known electron density in the well, obtained from Hall-effect measurements. Following the scheme of Refs. [73, 98], the energy integral of the low-temperature dimensionless absorption coefficient $\alpha_{2D}(E)$ can be related to the two-dimensional carrier density in the well $n_{2D}$ through the relation (see also Sec. 2.5.4):

$$\int \alpha_{2D}(E)dE = \frac{\pi n_{2D} e^2 \hbar}{2n\varepsilon_0 c m_z} f_{12}, \tag{3.2}$$

which holds under the assumption that carriers populate only the ground subband and for electric fields oriented along the growth direction; in the above expression $n = 4$ is the static Ge refractive index, $m_z = 0.12m_0$ is the [001] confinement effective mass of the L valley electrons and $f_{12}$ is the dimensionless oscillator strength (with Thomas–Kuhn sum rule $\sum_m f_{1m} = 1$, see discussion in Sec. 2.5.2). The $n_{2D}$ carrier density of our samples evaluated from Eq. (3.2) assuming $f_{12} = 1$ is reported in Table 3.1. The used value for the oscillator strength is compatible with the values obtained by our numerical calculations, which for the investigated sample are in the 0.92–0.98 range. We find that $n_{2D}$ is in the range $1.5 \cdot 10^{11}$–$5 \cdot 10^{11}$ $cm^{-2}$.

An important experimental result is the apparent ineffectiveness of induced charge transfer in these heterostructures: comparing the $n_{2D}$ values with the 2D donor concentrations $\tilde{n}_{2D}$ reported in Table 3.1, we deduce that most of the donor electrons are not transferred into the wells.

In order to understand this phenomenon, we have exploited the multiband self-consistent $k \cdot p$ code developed for this study, and described in Appendix 3.A of this Chapter, where we also describe the reasons for the choice of this method.

The obtained L, $\Delta_2$, $\Delta_4$, and $\Gamma$ conduction-band edge profiles are shown in Fig. 3.5. The in-plane compressive (tensile) strain in the well (barrier) region moves upward (downward) the $\Delta_2$ states while the opposite holds for the $\Delta_4$ levels. Note also that for [001] biaxial strain the four L valleys remain degenerate (valley splitting effects

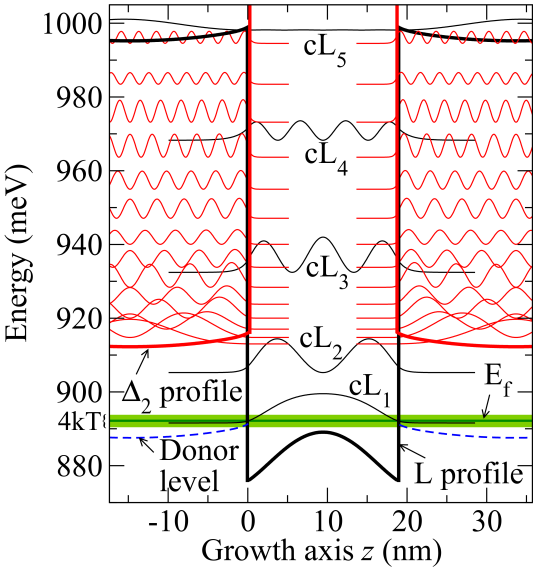


**Figure 3.6** – L (black) and $\Delta_2$ (red) band profiles and squared wave functions for the 1594 sample calculated at $T = 10\,\mathrm{K}$. The green shaded region of width $4k_BT$ is centered on the Fermi energy. The donor level in the barriers is represented by a blue dashed line.

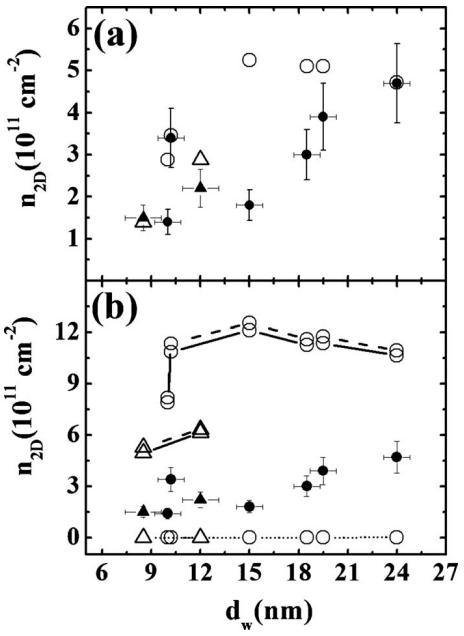


**Figure 3.7** – (a) Measured (closed symbols) and calculated (open symbols) two-dimensional carrier densities $n_{2D}$ in the well region plotted as a function of the well width for the samples of Table 3.1. Calculations have been carried out using the parameter values reported in Table 3.4. (b) Two-dimensional carrier densities as measured (closed symbols) and calculated (open symbols) modifying the parameter values of Table 3.4 as follows: $\Xi_u^{\Delta} = 5\,\mathrm{eV}$ (dashed line); $\Delta E_{v,\mathrm{avg}} = 0.060\,\mathrm{eV}$ (solid line); and $\Delta E_{v,\mathrm{avg}} = 0.104\,\mathrm{eV}$ (dotted line). Samples with spacer layers (1617 and 1619) are represented by triangles.

can be safely disregarded for well widths of the order of those of Table 3.1). From Fig. 3.5 it is evident that the conduction minimum in the doped barrier material, where the donor levels are located, is along the $\Delta_2$ lines. The $\Gamma$ and $\Delta_4$ states are higher in energy and thus at low temperature are expected to play a negligible role for charge redistribution. We find that the band offset between the L edges in the well and in the barrier is 124 meV and the energy difference between the $\Delta_2$ minima in the barrier and the L minima in the well is only $\approx 40$ meV.

The results of the self-consistent calculation for the conduction electronic states

at 10 K in the sample 1594 are reported in Fig. 3.6. The dashed line at about 25 meV below the $\Delta_2$ band edge represents the donor level. The Fermi energy is also shown. Note that far from the interfaces the donor level in the barriers is below the Fermi energy. As a consequence a very small fraction of the donor impurity states is ionized. In other words the electronic density in the well due to the transfer doping is limited by the small energy difference between the $\Delta_2$ minima in the barrier and the L minima in the well. The two-dimensional carrier densities for the samples of Table 3.1 are reported in Fig. 3.7a for samples having different well widths.

Measured (closed symbols) as well as calculated (open symbols) $n_{2D}$ values are both in the range $1 \cdot 10^{11}$–$5 \cdot 10^{11}$ cm$^{-2}$. We point out that the absence of a general trend of the $n_{2D}$ values as a function of the well width is to be attributed to the different doping levels and geometries of the samples. For instance, as expected, the insertion of a spacer between the well and the doped barrier region [triangles in Figs. 3.7a and 3.7b] reduces the charge transferred into the well, despite the larger number of donors with respect to the samples with similar well width. The overall agreement between the predicted and the measured values of $n_{2D}$ is satisfactory.

The discrepancies between theoretical and measured densities observed for some of the investigated samples in Fig. 3.7a may be mainly attributed to the unavoidable uncertainties affecting their compositional and structural parameters, in particular those related to the precise evaluation of the $\Delta_2$–L energy separation. In fact, our simulations indicate that the amount of charge transferred into the well region critically depends on the energy difference between the L and $\Delta_2$ conduction valleys in the well and barrier materials, respectively. As an example, for the sample 1596 (whose calculated $n_{2D}$ is $5.2 \cdot 10^{11}$ cm$^{-2}$), the experimental value $n_{2D} = 1.8 \cdot 10^{11}$ cm$^{-2}$ is exactly reproduced decreasing the $\Delta_2$–L energy difference by only 8 meV. This small change in the $\Delta_2$–L separation can be for instance related to a variation in the Ge content in the barrier from 80% to 79%, a quantity which is within our experimental uncertainty [96]. From the measured carrier densities we deduce that only the lowest ($E_1$) conduction subband is populated at low temperature. This confirms that the measured absorption peaks are related to the $E_1 \rightarrow E_2$ transitions at the L point in the Ge region. Neglecting the minor contribution due to the excitonic interaction, and in the two-level model [73], the energy of the absorption resonance $E_a$ is given by

$$E_a^2 = E_{21}^2(1 + \alpha),$$

where $E_{21}$ is the bare intersubband transition energy and $\alpha = \frac{2e^2 n_{2D}}{\varepsilon\varepsilon_0 E_{21}} S$ accounts for the blueshift induced by the depolarization effect. $S$ is an effective length given by

$$S = \int_{-\infty}^{+\infty} dz \left[ \int_{-\infty}^{z} dz' \psi_2(z') \psi_1(z') \right]^2$$

and $\psi_1$ and $\psi_2$ are the ground and first excited L subband wavefunctions, respectively.

In Fig. 3.8a we compare the theoretical evaluation of the intersubband absorption energies with the corresponding measured values. We observe that the theoretical model satisfactorily reproduces the measured data, especially for small $d_w$ where

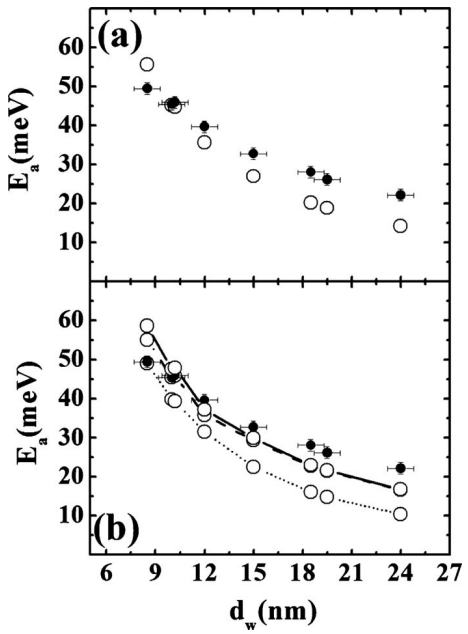


**Figure 3.8** – (a) Measured (closed symbols) and calculated (open symbols) intersubband absorption energies as a function of the quantum well width $d_w$. Calculations have been carried out using the parameter values reported in Table 3.4. (b) Intersubband absorption energies as measured (closed symbols) and calculated (open symbols) modifying the parameter values of Table 3.4 as follows: $\Xi_u^{\Delta}$ = 5 eV (dashed line); $\Delta E_{v,\mathrm{avg}}$ = 0.060 eV (solid line); and $\Delta E_{v,\mathrm{avg}}$ = 0.104 eV (dotted line).

depolarization effects are negligible and the transition energy is more sensitive to the conduction-band offset [97]. Note however that in the large-well region, absorption energies are systematically underestimated.

In the investigated samples the Hartree potential and the plasmon effect are responsible of significant deviations of the intersubband absorption resonances from the bare intersubband transition energies as calculated in the flat band approximation. These two effects cannot be separated and depend on the amount of charge transferred into the well region. On the other hand, since the $n_{2\mathrm{D}}$ carrier densities in the well depend critically on the $\Delta_2$–L energy differences, besides the uncertainties related to the structural and chemical composition of the samples, also those affecting the other input parameters used in the model play an important role in the calculated $n_{2\mathrm{D}}$ values. Indeed, several material parameters jointly contribute to determine the $\Delta_2$–L energy difference, as for instance the hydrostatic and uniaxial deformation potentials of $\Delta$ states in Ge, for which no experimental values are reported in the literature, or the valence-band offsets $\Delta E_{v,\mathrm{avg}}$ of the strained SiGe interface, whose precise values are still under debate [99, 100]. For this reason one can think to tune within the known uncertainty a subset of the model parameters in order to simultaneously fit the numerical results with the measured $n_{2\mathrm{D}}$ densities and intersubband absorption energies. In this way the model could be exploited to suggest more precise values for these fitting material parameters. However, we found that the introduction of one fitting parameter in the model does not lead to a substantially better agreement between measured and calculated absorption energies. More precisely, if the $\Delta_2$–L energy difference is increased, higher absorption energies in the large well region are found due to the enhancement of the plasmonic blueshift. Nevertheless, for reasonable values of the fitting parameter, this improvement remains modest while

the evaluated 2D carrier densities significantly change. As a consequence the good agreement previously obtained with the measured densities is lost.

Among the different material parameters which influence the $\Delta_2$–L energy difference, we have tested as fitting variables the $\Xi_u^{\Delta}$ deformation potential for Ge and the $\Delta E_{v,\mathrm{avg}}$ valence offset, due to the relatively large indeterminacy which affects them. As one can easily get convinced, larger $\Delta_2$–L energy differences can be obtained if smaller values of $\Xi_u^{\Delta}$(Ge) or $\Delta E_{v,\mathrm{avg}}$ are assumed.

As an example in Fig. 3.8b (dashed line) numerical absorption energies calculated diminishing the uniaxial deformation potential $\Xi_u^{\Delta}$ of Ge to the tentative fit value of 5 eV are reported. In this case the $\Delta_2$ donor states have higher energies and the carrier densities become 2–4 times larger than the measured ones, as reported in Fig. 3.7b, but the improvement in the energy differences between the measured and calculated absorption energies for the large well region is only on the order of 5%. We point out that the relative insensitiveness of the absorption energies with respect to $n_{2\mathrm{D}}$ in the $10^{11}$–$10^{12}$ cm$^{-2}$ density range here investigated, can be attributed to the opposite sign of the Hartree potential and the plasmonic effect contributions to the absorption energies.

Similar results are found if the valence-band offset between the well and barrier materials $\Delta E_{v,\mathrm{avg}}$ is decreased from the value of 0.083 eV, obtained by means of Eq. (1.36), to the tentative fit value of 0.060 eV (see Figs. 3.7b and 3.8b, solid lines).

For the sake of completeness we also report in Fig. 3.8b (dotted line) absorption energies obtained with a larger $\Delta E_{v,\mathrm{avg}}$. In this case the $\Delta_2$–L difference diminishes and then the amount of transferred charge rapidly decreases. For instance at $\Delta E_{v,\mathrm{avg}}$ = 0.104 eV, a value calculated according to the relation for the offsets between the *topmost* valence bands given in Ref. [99], $n_{2\mathrm{D}}$ values result to be less than $10^{10}$ cm$^{-2}$ (see Fig. 3.7b). Therefore the absorption resonances, which are now practically coincident with the flat band transition energies, become even more underestimated (see Fig. 3.8b).

In summary, the use of material parameters as fitting variables of the model does not remove the small systematic deviation between measured and calculated intersubband absorption energies observed in the large well width region. Then we conclude that from the present experiments there is no evidence to invoke new values for the material parameters since the literature data [Table 3.4 and Eq. (1.36)] allow a sound theoretical description of the measurements. The discrepancy in the absorption energies found for the large well samples could be more profitably addressed by means of first-principles calculations. In fact, it is well known that when the collective (plasmon) energies become as large as $E_{21}$, as it happens for the investigated samples with large wells, the intersubband resonances cannot be described in a single-particle framework anymore [73].

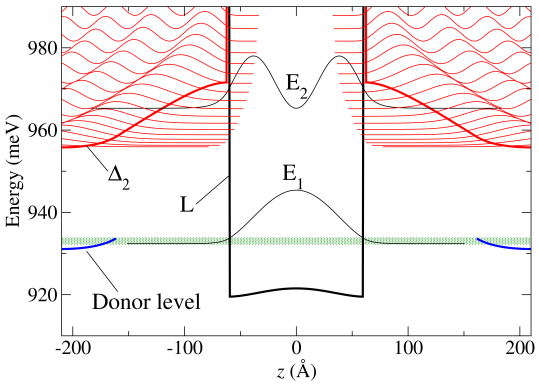


**Figure 3.9** – Self-consistent band edge profiles (thick lines) and squared modulus of the wavefunctions (thin lines) calculated for sample S1776 at $T = 10$ K in the absence of optical excitation. Profiles and states at L point (black lines, confined levels at energies $E_1$, $E_2$) and at $\Delta_2$ band edge (red lines) are displayed. The donor level in the doped portion of the barrier is also represented (blue line). The green shaded area represents the energy region from the Fermi level to $2k_BT$ above it.

## 3.3 Non-radiative lifetimes in Ge/SiGe MQWs

A further important step towards the realization of a THz QCL is the estimate and measurement of the non-radiative relaxation lifetimes $\tau$ between different subbands. Previous experimental determinations of $\tau$ in Si/SiGe heterostructures by time-resolved pump-probe transmission experiments were restricted to $p-$type systems [101–104] and very short $\tau < 1$ ps were reported [102, 103] for ISB transition energies above the longitudinal optical (LO) phonon energies $h\nu_{\mathrm{LO}}^{\mathrm{Si}} = 63$ meV, $h\nu_{\mathrm{LO}}^{\mathrm{Ge}} = 37$ meV and attributed to the scattering with LO phonons. At ISB transition energies below $h\nu_{\mathrm{LO}}$, the main scattering channel has been instead attributed to alloy disorder in the SiGe wells, with values of $\tau$ around 10 ps [101, 104].

Scattering by alloy disorder should be strongly reduced in $n-$type Ge QWs with thickness $d_{\mathrm{QW}} > 10$ nm since the wavefunctions are mainly confined in the pure-Ge well: longer lifetimes, desirable for the QCL design, are then expected for such structures. We have thus grown $n-$type modulation-doped strained Ge/$Si_{0.2}Ge_{0.8}$ MQW samples and we have determined the non-radiative $\tau$ using narrow-band picosecond pulses provided by the Dresden free-electron laser (FEL) "FELBE" [105]. The laser photon energy $h\nu_{\mathrm{FEL}}$ was tuned at the ISB transition energy to measure the transient bleaching signal by means of far-infrared degenerate pump-probe measurements.

The SiGe heterostructures were grown by means of the same technique described in Sec. 3.2. The MQWs were made of 20 repetitions of Ge/$Si_{0.2}Ge_{0.8}$ with $d_{\mathrm{QW}} = 13$ nm (sample S1776) or $d_{\mathrm{QW}} = 24$ nm (samples S1745 and S1750). The 30 nm-thick $Si_{0.2}Ge_{0.8}$ barriers were doped by phosphine codeposition resulting in a dopant concentration of $N_d \approx 1 \cdot 10^{18}$ cm$^{-3}$. The barriers were either doped uniformly, or alternatively 10 nm-thick $Si_{0.2}Ge_{0.8}$ spacers were left undoped on each side of the QW (see Table 3.2). We just stress here that there have been major improvements to the growth technique with respect to the samples of Table 3.1, as it is reflected on the much narrower lineshape of the ISB absorption feature: FWHM down to 3 meV have been measured in these new samples, see Fig. 3.10 (to be compared to 10–13 meV for the samples of Table 3.1).

**Table 3.2** – Parameters and results for the samples discussed in this section. The ISB transition energy is determined from both FTIR experiments (exp) and band calculations (theo) including the depolarization shift. $\tau$ is the non-radiative relaxation time as determined from pump-probe experiments. The TM-mode transmittance $T_{TM}$ at the used FEL photon energy is also reported.

| Sample | $d_{QW}$ (nm) | Spacer | T (K) | ISBT theo (meV) | ISBT exp (meV) | $h\nu_{FEL}$ (meV) | $T_{TM}$ | $\tau$ (ps) |
|---|---|---|---|---|---|---|---|---|
| S1745 | 24 | no | 4 | 15 | 16.2 | 14.1 | 0.71 | 27 |
| | | | 30 | | 17.9 | 14.1 | 0.71 | 34 |
| | | | 90 | | 20 | 18.2 | 0.66 | 30 |
| S1750 | 24 | yes | 30 | 13 | 14.7 | 14.1 | 0.67 | 34 |
| | | | 90 | | 18.0 | 18.2 | 0.64 | 34 |
| S1776 | 13 | yes | 4 | 32 | 28.4 | 28.8 | 0.73 | 33 |
| | | | 50 | | 28.5 | 28.8 | 0.72 | 33 |
| | | | 130 | | 28.5 | 28.8 | 0.71 | 33 |

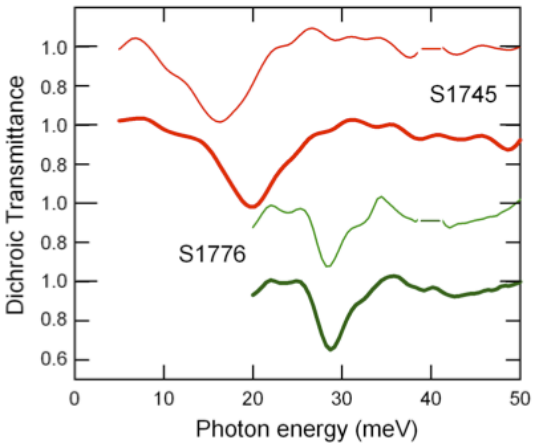


**Figure 3.10** – TM to TE waveguide mode transmittance ratio for two samples at $T$ = 10 K (thin lines) and $T$ = 90 K (thick lines). Lorentzian-shape dips are the signature of the $E_1 \rightarrow E_2$ intersubband transition. Spectra are vertically offset in steps of 0.4 for clarity. Data around 41 meV for $T$ = 10 K are discarded, as the transmitted signal is zero because of absorption by donor impurity levels in the Si substrate.

Electronic states calculations were performed by means of the effective-mass self-consistent approach with the code described in Appendix 3.A of this Chapter. States originating both from the L and $\Delta_2$ band edges are included in the model ($\Gamma$ and $\Delta_4$ states are much higher in energy and can be disregarded in this context). As an example we show in Fig. 3.9 the band edge profiles and the square modulus of the near-gap states for the conduction band of sample S1776 calculated at $T$ = 10 K. The QW ground state at energy $E_1$ and the first excited state at $E_2$ are clearly visible. In the doped portion of the barrier, the donor levels lie 24.7 meV below the $\Delta_2$ bands. We find that for the chosen temperature the donors are partially ionized, so that only a fraction of the doping charge is transferred into the well.

Low-temperature absorption spectra were measured by FTIR in order to identify the ISB transition energy. The radiation was coupled to the samples adopting a waveguide geometry with lateral facets at 70° with respect to the growth plane. The top (growth) side was coated with a 5 nm-thick Ti layer followed by an 80 nm-thick

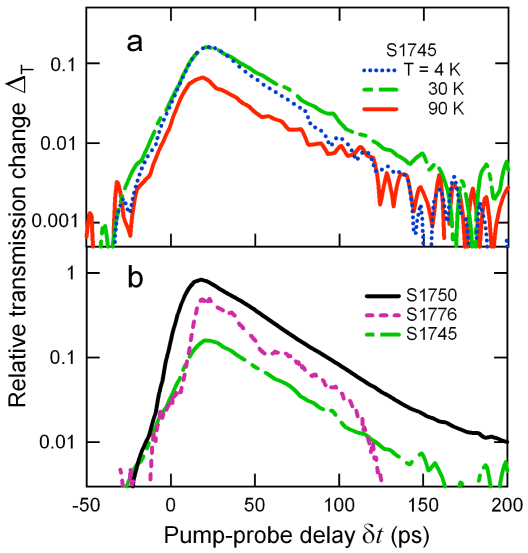


**Figure 3.11** – Relative transmission change $\Delta_T$ (see text) measured with the FEL photon energy tuned close to the ISB transition energy for each sample and temperature (see Table 3.2). A fit to a single-exponential decay provides the intersubband transition lifetimes $\tau$. (a) Temperature dependence for S1745. (b) Results for different samples at $T = 30$ K ($T = 50$ K for S1776). The maximum value of $\Delta_T$ is indicative of the fraction of confined electrons excited by the pump pulse.

Au metallization in order to ensure a good overlap of the optical mode with the active MQWs region [94]. The waveguide length and thickness were designed to allow only one light reflection inside the waveguide, as required for a precise determination of $\tau$ [106]. The dichroic transmittance shown in Fig. 3.10 is obtained as the ratio between the transmitted beam intensity with non-vanishing component of the polarization parallel to the growth direction (TM mode), and the transmitted intensity with orthogonal polarization (TE mode) as described in Sec. 3.2. One single absorption feature with Lorentzian lineshape and full width of about 3 (5) meV was observed in samples with (without) undoped spacers at all $T$ up to 130 K. As shown in Table 3.2 the measured ISB transition energies agree well with the theoretical values, obtained including the depolarization shift.

The intersubband non-radiative lifetimes were measured in a degenerate pump-probe scheme [106] with the FEL emitting a continuous train of pulses (duration from 4.8 ps for $h\nu_{\mathrm{FEL}} = 28.8$ meV to 13 ps for 14.1 meV, with separation of 77 ns). The pump power was reduced by a set of attenuators to 40 mW (pulse energy$\approx$ 3 nJ, power density at focus around 6 kW/cm$^2$). The transmission change $\Delta_T$ relative to the absolute TM-mode transmittance $T_{\mathrm{TM}}(\nu_{\mathrm{FEL}})$ (see Table 3.2) obtained from FTIR data (so that $|\Delta_T| < 1$) was determined as a function of the pump-probe delay $\delta t$.

All curves presented in Fig. 3.11 show $\Delta_T > 0$ (bleaching) indicating a decreased population of the lower subband at $\delta t = 0$ and subsequent relaxation towards equilibrium [106, 107]. In Fig. 3.11a we plot the measured $\Delta_T$ for sample S1745. The exponential decrease of $\Delta_T$ vs. $\delta t$ is extremely clear at all measured temperatures and the exponential fitting of each curve in Fig. 3.11a provides the non-radiative relaxation time $\tau$ with relative uncertainty below 5% (see Table 3.2). In Fig. 3.11b we plot $\Delta_T$ for all three samples ($T = 30$ K for S1745 and S1750, $T = 50$ K for S1776); exponential decays with very similar relaxation times are obtained. We found values of the order of $\tau \approx 30$ ps independent of the value of $T$ and $d_{\mathrm{QW}}$ and of the presence

of a spacer layer. We stress again that a $T-$independent value of $\tau$ is beneficial for high-$T$ operation of QCLs [42, 56, 102] (note that $\tau^{-1}$ is an exponentially decreasing function of $1/T$ in III-V QCL heterostructures with single-well transition [108]).

We shall now consider all scattering processes separately. First of all we note that in all our samples $E_2 - E_1$ is smaller than the Ge LO phonon energy $h\nu_{\mathrm{LO}} = 37$ meV. Therefore, LO-phonon scattering is strongly suppressed [107, 109, 110] for S1745 and S1750, while it might play a role in S1776, where $E_2 - E_1$ is only 8 meV lower than $h\nu_{\mathrm{LO}}$. Since we did not see appreciable difference in the lifetime of S1776, the LO-phonon scattering channel seems not to contribute to the observed lifetime. A second phonon-mediated scattering channel may be related to intervalley transitions [109] between the first-excited L ($E_2$) level and the quasi-continuum of $\Delta_2$ states, represented by red curves in Fig. 3.9. Note that in sample S1776, $E_2$ is in the energy region where $\Delta_2$ levels are present, while samples with larger $d_{\mathrm{QW}}$ (S1745 and S1750) have the first-excited L level well below the $\Delta_2$ continuum (not shown). Therefore if $\tau$ would be dominated by the $E_2 - \Delta_2$ scattering channel, we should expect large differences in the relaxation times. Since the observed $\tau$ are approximately sample-independent, we conclude that the time scale is not set by the intervalley scattering. Indeed, the $\Delta_2$ states are localized in a different spatial region. Therefore, the phonon-assisted intervalley $E_2 - \Delta_2$ scattering processes are strongly suppressed due to the small overlap factor $G$ [56,110] discussed in Sec. 1.10. We calculated the overlap $G$ factors for $E_2 - \Delta_2$ intervalley scattering processes and found them to be approximately 2 orders of magnitude smaller than the corresponding quantity evaluated by using $E_1$ as the final state. Concerning other inelastic interactions, we are left with acoustic-phonon intersubband scattering followed by hot-carrier thermalization [107, 110], which is thought to play a key role in group-IV conduction-band materials at electron energies well below $h\nu_{\mathrm{LO}}$ [56, 109, 111]. However, the predicted temperature dependence of the phonon-mediated relaxation time is not observed in our measurements (see Fig. 3.11), indicating that also this channel is not the dominant one.

Elastic scattering channels due to static potential energy perturbations such as interface roughness, ionized impurities and/or alloy disorder can also contribute to intersubband relaxation, in conjunction with fast intrasubband thermalization [42, 109]. The temperature independence of the measured $\tau$ seems to suggest that such elastic scattering processes dominate the intersubband relaxation. However, since we used a modulation-doped scheme, impurity scattering rates should be strongly dependent on the presence of undoped spacers. Moreover alloy disorder effects, which in pure-Ge wells are active only in the barrier region, and interface roughness scattering should both depend on $d_{\mathrm{QW}}$. The fact that these dependencies are not measured in our samples suggests that the predominant intersubband scattering channel is related to static potential energy perturbations inside the Ge well, such as dislocations and background impurities. If this is the case, even longer relaxation times could be achieved optimizing further the sample growth process.

In conclusion, we have measured the non-radiative ISB relaxation times for electrons in Ge quantum wells displaying intersubband transition energy between 14 and 29 meV, i.e. within the frequency range of the reststrahlen absorption of typical III-V

semiconductors used for existing quantum cascade lasers. We obtained relaxation times up to 33 ps at 130 K nearly independent of temperature, well width and presence of undoped spacers. These results indicate that $n-$type Ge/SiGe heterostructures are very promising for the realization of Si–based emitters in a wide far-infrared range, eventually capable of high temperature operation.

## 3.4 Design of a Ge/SiGe quantum cascade emitter

In the previous Sections, we have discussed different experiments and measurements that are preliminary to the realization of a $n-$type Ge-based QCL: in particular, the intersubband absorption between confined states in the conduction band, and the measurements of the non-radiative lifetimes. The following step is the measurement of the electroluminescence. To this aim, we have designed a quantum cascade (QC) structure with Ge wells and SiGe barriers that, under bias, should be able to emit photons in the desired THz energy region.

In the design of the QC emitter, different constraints must be taken into account. We have discussed in detail in the previous Sections how the lowest-lying levels in such structures originate from L states. The first constraint comes then from the requirement of a large enough conduction band offset (CBO) at the L point, so that the potential profile can confine at least two levels. Following the results of the previous Sections, we choose concentration of Ge in the $Si_{1-x}Ge_x$ barriers of $x \approx 0.8$ (the reason for the choice of this value is discussed below in more detail).

Then, we have to take into account the limits of the coherent growth process. In order to maximize the number of emitted photons, the largest possible number of structure periods must be grown. However, due to the different lattice constants of the well (Ge) and barrier (SiGe) materials, strain balancing is required in order to allow the growth of a large enough number of periods without formation of dislocations or other defects (for the evaluation of the optimal substrate lattice constant that minimizes the elastic energy of the stack of layers, see Sec. 1.3.7): then, the lattice constant of the substrate cannot be arbitrary. Furthermore, we also need the design to be very simple, with the lowest possible number of wells in each period, so as to minimize the total structure length.

Moreover, in order to reduce all scattering mechanisms that would reduce the performance of the device, we want to suppress all scattering from L states to states of different valleys, in particular to the $\Delta_2$ states that, as we have discussed, are very near to the L states. To this aim, the material parameters must be optimized so that these $\Delta_2$ levels are shifted to higher energy and thus are not involved in the transport of electrons through the cascade structure. The key parameter to tune is also in this case the substrate Ge content (i.e., the strain of the structure). In fact, varying the $x$ content of the substrate $Si_{1-x}Ge_x$ alloy in the 80 – 100% range, the conduction band offsets at L and $\Delta_2$ do not change substantially (see Table 3.3), so that the electronic levels are not significantly influenced by this parameter. On the contrary, the energy difference between the L band edge in the Ge well and the $\Delta_2$ edge in

**Table 3.3** – L and $\Delta_2$ conduction-band offsets (CBOs) between Ge and $Si_{0.2}Ge_{0.8}$. The minus sign for the $\Delta_2$ CBO indicates that the $\Delta_2$ level in Ge is at higher energy than in the SiGe alloy. Also the energy difference between the $\Delta_2$ edge in the SiGe alloy and the L band edge in Ge is reported.

| Substrate Ge content | L CBO (meV) | $\Delta_2$ CBO (meV) | $\Delta_2$–L (meV) |
|---|---|---|---|
| 97% | 123.8 | −168.8 | 30 |
| 95% | 123.6 | −169.1 | 35 |
| 93% | 123.5 | −169.4 | 40 |
| 92% | 123.4 | −169.6 | 42 |
| 91% | 123.3 | −169.7 | 45 |
| 84% | 122.8 | −170.6 | 62 |

the SiGe barriers is strongly affected by the strain, due to the reduction of the $\Delta_2$ energy for large tensile strains (in the barriers). Then, compatibly with the previous requirement of strain balancing, we want to reduce the Ge content of the substrate so to increase the $\Delta_2$–L energy difference, as can be also deduced inspecting Table 3.3 which reports the $\Delta_2$–L difference for different values of the substrate Ge content.

In order to reduce the Ge content of the substrate while keeping the strain balancing requirement, one should either have larger barrier thicknesses or reduce the Ge content of the barriers. Both strategies, however, are detrimental for different reasons. For what concerns the Ge content of the barriers, we have identified the $Si_{0.2}Ge_{0.8}$ alloy as the best compromise between a sufficiently large offset for the L states and a large separation between L and $\Delta_2$ states. In fact, considering a $Si_{0.05}Ge_{0.95}$ substrate (i.e. the one that fulfills the strain-balancing conditions in the final structure), a reduction of the Ge content of the barriers to 78% gives a L–$\Delta_2$ separation of only 10 meV (while an increase to 82% gives a significant reduction of the L CBO to less than 110 meV). Secondly, for what concerns the barrier thickness, we cannot have barriers that are too thick, otherwise the resonant tunneling mechanisms that are fundamental for the operation of a QC structure would be strongly suppressed. Note, however, that thin barriers are in fact beneficial for what concerns the positioning of the $\Delta_2$ states. In fact, as already discussed, these states are confined within the SiGe alloy materials; if the thickness of these layers is small, a large confinement energy for the $\Delta_2$ levels is obtained, and consequently all these undesired levels are shifted to a higher energy.

Due to the above mentioned considerations, many parameters of the design are locked. With these constraints, we have then designed a three-well strain-balanced QC emitter. The structure is designed to work under a bias of 6.5 kV/cm, with emission frequency around 30 meV; the structure and the resulting levels under this bias are shown in Fig. 3.12. In the Figure, the first-confined $\Delta_2$ levels in the SiGe layers are also displayed, showing that they are higher in energy than the relevant L states. In particular, the structure is composed by one larger well ("transition well"), where the emission of photons should occur involving transitions between the first excited and the ground state of this well; the other two (narrower) wells act

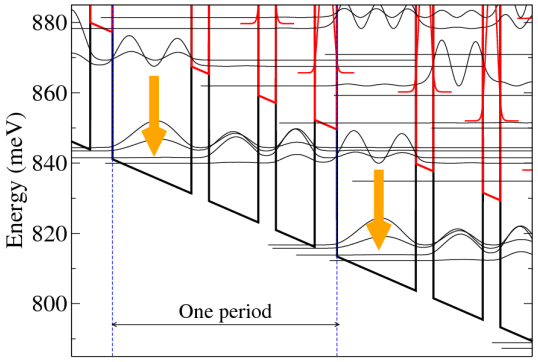


**Figure 3.12** – Band profile (thick lines) and squared moduli of the wavefunctions for the L (black) and $\Delta_2$ (red) states under a bias of 6.5 kV/cm. The orange arrows represent the optical transitions. The $\Delta_2$ states confined in the SiGe layers are visible and are at higher energy than the relevant L states also due to the large confinement energy.

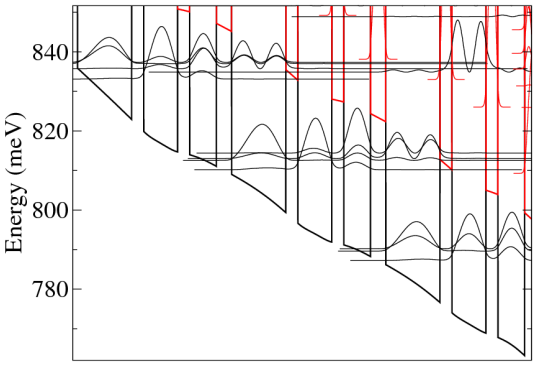


**Figure 3.13** – Band profile and squared moduli of the wavefunctions for the L (black) and $\Delta_2$ (red) states under a bias of 8.5 kV/cm, taking into account also the band bending as discussed in the text.

as extractor and injector.

The stability of the design has been verified by varying by ±10% the layer thicknesses: in all cases, a slightly different electric field can be found that allows the alignment of the levels. Moreover, also a self-consistent calculation taking into account the band bendings due to the presence of the doping charge ($2 \cdot 10^{17}$ cm$^{-3}$) in the extractor well has been performed: the resulting profile is shown in Fig. 3.13, proving that (even if for a different electric field value of 8.5 kV/cm) we have again a level alignment. Note that this calculation has been performed under the assumption of a fast equilibrium reached within each period, so that each set of four levels in each period has its own quasi-Fermi level, and moreover assuming a complete ionization of the doping charge.

### 3.4.1 Contacts in the Ge/SiGe quantum cascade structure

A sample with 20 periods, according to the design described above, has been grown in Rome and measured at NEST laboratory in Pisa in order to reveal the electroluminescence signal under bias. However, no electroluminescence could be distinguished from the background blackbody radiation.

In order to understand the possible reasons for the absence of an electroluminescence signal, we also investigated the electronic structure of the contact layers. An important point has to be emphasized regarding the bottom contact. In order to obtain a parallel lattice constant equivalent to a $Si_{0.05}Ge_{0.95}$ alloy, in the experiments

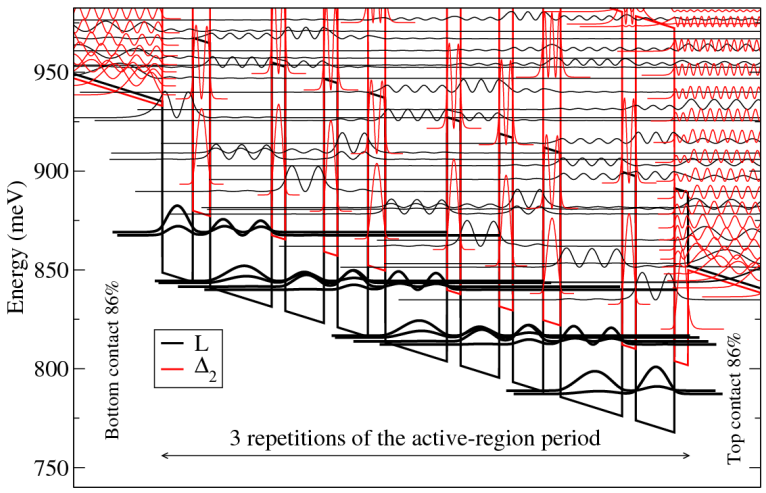


**Figure 3.14** – Band edges and states of the grown Ge/SiGe QC structure (only three periods are shown) to emphasize the position of the states in the contacts. Note that the lowest-lying states in the contacts are at a much higher energy than the relevant states within the active region.

a reverse-graded buffer is realized, with final Ge content equal to $x = 0.86$. However, since the strain relaxation is not complete in this buffer layer, the resulting parallel lattice constant is the same of a SiGe alloy with $x = 0.95$. While this subtlety is not a problem for the active region, since the substrate enters only through its lattice constant, it becomes very important when the charge injection from the contacts is taken into account.

In fact, the band structure of the contact region is not the one of a relaxed $Si_{0.05}Ge_{0.95}$ alloy, but the one of a strained $Si_{0.14}Ge_{0.86}$ alloy. The calculations then show that in the contacts the $\Delta_2$ states are below the L states. Moreover, the relevant states in the active region are at a much lower energy with respect to the electronic states in the contacts. This can imply that the electronic transport in the structure can occur without a relaxation into the relevant states of the active region, and even more importantly electrons cannot be easily extracted from the top contact. To better clarify the problem, we report in Fig. 3.14 the scheme of the states in the grown structure, where both the bottom and top layer contacts are composed of a $Si_{0.14}Ge_{0.86}$ alloy; for clarity, only three repetitions of the active region between the top and bottom contacts are shown. Note that in all Figures of this Section, for simplicity we have shown the contacts as non-conductive, and consequently their band edges are not flat.

In order to solve this problem, we have proposed a new modified design, where the active region is left unchanged with respect to what described in the previous Section, while all changes are meant to improve both the injection and extraction regions.

The first modification consists in an inversion of the growth order of the layer

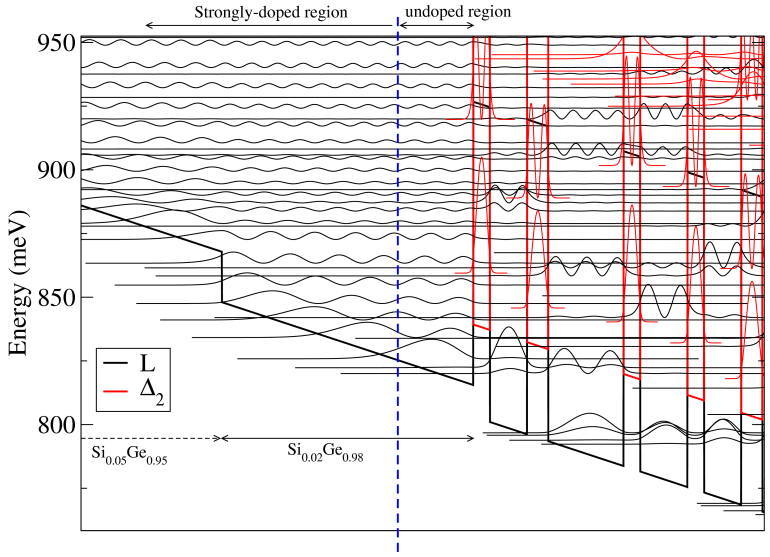


**Figure 3.15** – Improved design for the injector region (top contact layer) of the QC emitter.

stack, so that the injection of electrons occurs *from* the top contact *to* the bottom contact layer.

Then, a second modification involves the injection region (now located at the top contact layer). This layer must be realized with a $Si_{0.05}Ge_{0.95}$ alloy (note that, due to the value of the in-plane lattice constant in the structure, this layer is relaxed). Moreover, between the top contact layer and the beginning of the active region, a $Si_{0.02}Ge_{0.98}$ layer should be inserted, so that the bottom at L in this layer is approximately at the same energy of the first excited state in the first quantum well of the active region. Finally, the region should start with a barrier so that also the first Ge region (injector) is able to confine electrons. For what concerns the doping, the total length of the top contact layer can be of about 2000 Å, with a very large doping ($\approx 5 \cdot 10^{18}$–$1 \cdot 10^{19}$ cm$^{-3}$), but leaving undoped a small region between the contact and the active region. All these requirements are summarized in Fig. 3.15.

Finally, the third set of modifications involves the extraction region (bottom contact layer). Between the $Si_{0.14}Ge_{0.86}$ virtual substrate and the active region, a 8000 Å-thick $Si_{0.05}Ge_{0.95}$ (unstrained) layer should be inserted. In this way, also in the extraction region the bottom levels are at L. Moreover, between the active region and the bottom contact layer, a $Si_{0.03}Ge_{0.97}$ layer should be inserted, so that the electrons can be more easily extracted from the ground state of the last extractor well. Also in this case, the whole bottom contact should be $n$–doped with a very large doping ($\approx 5 \cdot 10^{18}$–$1 \cdot 10^{19}$ cm$^{-3}$), but leaving undoped a small region between the active region and the contact. These requirements are summarized in Fig. 3.16.

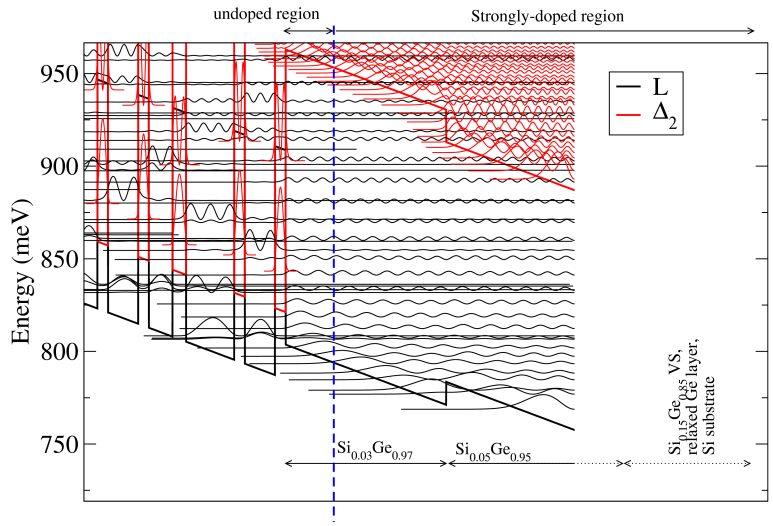


**Figure 3.16** – Improved design for the extractor region (bottom contact layer) of the QC emitter.

## 3.5 Design of a Si/SiGe quantum cascade emitter

We have proposed three possible designs of Si/SiGe QC structures, with low-Ge content $Si_{1-x}Ge_x$ barriers ($x$ typically in the range 20–40%).

In this kind of systems, the L edge is at high energy and can be disregarded; the relevant states to be taken into account are the $\Delta_2$ and $\Delta_4$ edges. Since in general the Si QWs are tensile strained (due to the growth on SiGe virtual substrates, with typical Ge content $x \approx 10\%$), the lowest states (that are exploited for the electronic transport) are of $\Delta_2$ symmetry, while we try to keep the $\Delta_4$ states (with reversed profile: the quantum wells are the SiGe layers) high enough in energy so that the $\Delta_2 \rightarrow \Delta_4$ scattering is suppressed.

These designs rely on diagonal (in real space) transitions, i.e. between the fundamental levels of two adjacent wells. To have a significant overlap between the wavefunctions, we need a very thin barrier between the two wells. A thicker well acts both as injector and extractor, allowing the transport from the bottom level of one period to the upper one of the next period.

In the first design of Fig. 3.17, the barriers are composed of a $Si_{0.8}Ge_{0.2}$ alloy. While the two (thinner) wells where the transition occurs are composed of pure silicon, the thick well has a small Ge content $x = 0.05$; this non-zero $x$ value was chosen to allow the injection of electrons in the upper transition level. The structure is grown on a $Si_{0.8}Ge_{0.2}$ substrate, implying that it is not strain-compensated. This substrate is needed to keep the $\Delta_4$ states at higher energy with respect to $\Delta_2$ states. Indeed, as already pointed out, the $\Delta_4$ band profile is inverted with respect to the $\Delta_2$ profile ($\Delta_4$ electrons localize in the SiGe thin barrier regions). Moreover, since the barriers are relaxed, the bottom of the $\Delta_4$ band profile coincides with the top of

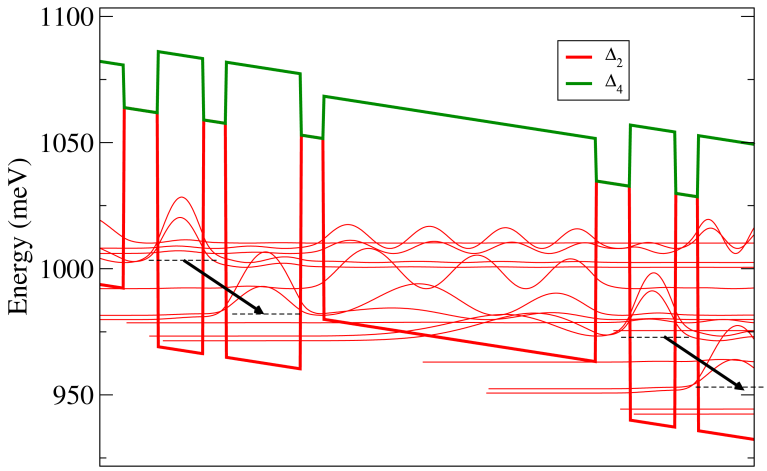


**Figure 3.17** – First Si/SiGe QC design. The substrate is a $Si_{0.8}Ge_{0.2}$ alloy and the thick well is $n$–doped. The operating field is 14 kV/cm. The black arrows indicate the optical transitions.

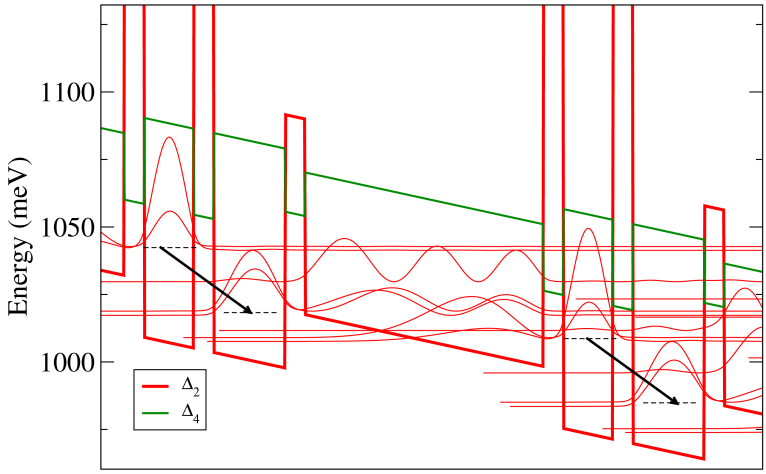


**Figure 3.18** – Second Si/SiGe QC design. The substrate is a $Si_{0.76}Ge_{0.14}$ alloy and the thick well is $n$–doped. The operating field is 16 kV/cm. The black arrows indicate the optical transitions.

the $\Delta_2$ profile (see Fig. 3.17). As a consequence, the lowest $\Delta_4$ states lie far away in energy from the active $\Delta_2$ levels. The operating field for this structure is of 14 kV/cm and the transition energy of 21 meV.

The second design, reported in Fig. 3.18, is a modification of the previous one to obtain a partial strain compensation. This has been achieved by decreasing the substrate Ge content to 14%, and increasing the Ge content of two of the barriers from 20% to 40%. We stress, however, that even this structure does not obtain a complete strain balancing, which would require a $Si_{0.93}Ge_{0.07}$ substrate. This substrate, however, would shift the $\Delta_4$ states in the SiGe layers much lower in energy, reaching the range of the $\Delta_2$ states. The chosen value $x$ = 14% for the substrate

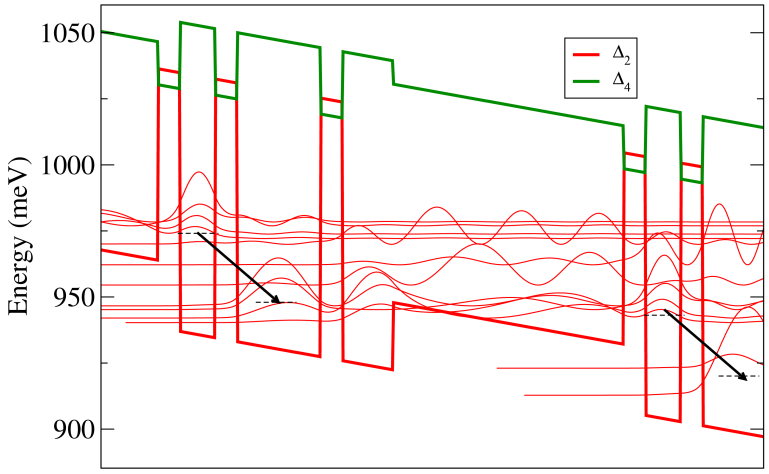


**Figure 3.19** – Third Si/SiGe QC design. The substrate is a $Si_{0.8}Ge_{0.2}$ alloy and the thick well is $n$–doped. The operating field is 15 kV/cm. The black arrows indicate the optical transitions.

lattice constant guarantees instead that the first $\Delta_4$ confined states are at least 35 meV above the active levels localized in the adjacent spatial regions. Note that, in order to compensate for the increased barrier height, we have reduced the injection barrier thickness.The above argument on the competitiveness between strain compensation and $\Delta_2 - \Delta_4$ level separation shows clearly that a Si/SiGe QC design is pretty difficult to obtain. The operating field for this system is of 16 kV/cm and the transition energy of 24 meV.

Finally, the third design, reported in Fig. 3.19, contains an additional small well of pure Si between the extraction barrier and the big $Si_{0.95}Ge_{0.05}$ well. This configuration allows a finer tuning of the levels overlapping and relative positioning. In fact, this additional well allows to reduce the energy of the final state of the transitions, since the electron extraction is now facilitated by the new well. As a consequence, the radiative transition energy is slightly larger than in the previous structures. However, in the design, one has to avoid that the energy levels are lowered too much, since in this case the electronic states would remain confined in the additional well, and the injection in the following cascade period would be hindered. We also stress that this type of design has never been reported previously in the literature. The operating field for this system is of 15 kV/cm and the transition energy of 35 meV.

We have proposed these three designs and now the experimentalists are planning the growth of samples according to what reported here, in order to measure the possible electroluminescence out of these structures.

## 3.6 Conclusion of the Chapter

In conclusion, in this Chapter we have discussed critically why the choice of Si and Ge materials could be beneficial to overcome the present limitations of THz QCLs.

We have theoretically supported the first important experiments to realize a QCL in the conduction band of Ge/SiGe systems and we have thoroughly described and interpreted the results by means of numerical simulations.

In particular, we have first discussed the absorption between the first and the second subband in the conduction band (at the L point) of Ge/SiGe MQW systems, and we have studied in detail the interplay between the position of the L states in the Ge well and of the $\Delta_2$ states in the SiGe barriers. We have then shown that long $\approx$ 30 ns non-radiative lifetimes can be achieved in these systems for the relaxation from the first-excited subband, and we have discussed the most important mechanism that could be at the origin of this non-radiative relaxation. Then, we have presented a design for a Ge/SiGe quantum cascade emitter, that could allow the experimental measurement of electroluminescence out of this system and pave the way to the first Ge/SiGe QCL. Regarding this point, we have not only discussed the active region design (and the importance of removing the $\Delta_2$ states from the relevant energy range), but we have also optimized the contact regions so to have efficient injection and extraction of electrons in the system. We have also presented three possible designs for a Si/SiGe emitter (with electrons in the $\Delta_2$ states), showing that such systems have much more stringent requirements (for instance, a complete strain compensation cannot be achieved, otherwise $\Delta_4$ states would we in the same energy region of the active $\Delta_2$ states). Finally, in Appendix 3.A we discuss in detail the motivations for the choice of the self-consistent multiband $\mathbf{k} \cdot \mathbf{p}$ code that we have implemented for the present study, and the most important details of the code.

## 3.A Appendix: details of the k · p multiband code

The TB code developed as described in Sec. 1.2 is a very powerful and quantitatively precise tool for the determination of the electronic and optical properties of SiGe heterostructures. However, it has the drawback of being computationally quite intensive.

While designing a QC structure, however, one often needs to change many of the parameters of the system (Ge content of the barriers, layer widths, substrate lattice constant, …); it is therefore necessary to have a tool that, even if less precise, is fast and interactive enough to allow for a real-time calculation of the properties of the system. Another case in which a fast code is needed is when we want to perform self-consistent calculations, as we have shown in the previous Sections to be necessary for modulation-doped MQW systems, so to take into account the band bending due the doping charge. These calculations require the iterative solution of a self-consistent Schrödinger–Poisson equation (see Sec. 1.9), and can involve a large number of iterations before convergence is attained. Also the TB formalism is of course suitable to this goal, but for instance if each calculation requires some tens of minutes, one has to wait for days to obtain a single result.

In the choice of the theoretical method to be implemented in the code, the requirement was to be able to address the systems described in Sec. 3.2, where very large $n$–dopings of the barriers lead to modest charge transfer in the quantum wells. It has been thus necessary to write a code with the following properties:

- It must be a *multiband calculation*, which takes into account the L, Δ (and possibly Γ) conduction valleys. In fact, these conduction band minima have very close energies in the heterostructures that we have investigated and must all be considered simultaneously. In this way, partial ionization of the dopants can be properly taken into account for a self-consistent evaluation of the Fermi energies and of the electronic carrier densities in the wells.

- It must be *fast*, but at the same time *accurate* enough to give quantitatively meaningful results.

- It must include a *1D Poisson solver* to calculate the electric field and the electrostatic potential due to the distribution of the doping charge in the structure, which is calculated starting from the probability distribution $|\psi|^2$ obtained from the solution of the Schrödinger equation.

- It must adopt a *stable self-consistent iterative algorithm* to solve the self-consistent 1D Schrödinger–Poisson equation. In fact, we have discussed how changes of only a few meV in the band edge positions can lead to changes of orders of magnitude in the amount of charge transferred into the QWs. Thus, in these unlucky (but common) situations, the iterative algorithm has to be devised carefully in order to be able to reach convergence even under these extremely unstable conditions.

To this aim, we have implemented a code in the **k**·**p** envelope function framework. In this model the band alignments of the L, Δ, and Γ conduction minima between a biaxially strained $Si_{1-x}Ge_x$ layer grown on a relaxed $Si_{1-y}Ge_y$ substrate are evaluated according to Ref. [23]:

$$E_c^{\mathrm{L},\Delta,\Gamma}(x,y) = E_{v,\mathrm{avg}}^{\mathrm{L},\Delta,\Gamma}(x,y) + \frac{1}{3}\Delta_0(x) + E_g^{\mathrm{L},\Delta,\Gamma}(x) + E_h^{\mathrm{L},\Delta,\Gamma}(x,y) + E_u^{\mathrm{L},\Delta,\Gamma}(x,y),$$

where $E_g^{\mathrm{L},\Delta,\Gamma}(x,y)$ are the band gaps at the L, Δ and Γ points, $\Delta_0(x)$ is the spin-orbit splitting of the unstrained bulk $Si_{1-x}Ge_x$ alloy; $E_h^{\mathrm{L},\Delta,\Gamma}(x,y)$ is the band-gap shift due to the hydrostatic component of the strain, and $E_u^{\mathrm{L},\Delta,\Gamma}(x,y)$ is the contribution from the uniaxial part. $E_{v,\mathrm{avg}}^{\mathrm{L},\Delta,\Gamma}(x,y)$ is the offset between the barycenters of the heavy, light, and split-off valence bands in the substrate and in the strained layer and is given by Eq. (1.36).

The $E_g^{\mathrm{L},\Delta,\Gamma}(x)$ band gaps (in eV) for unstrained $Si_{1-x}Ge_x$ alloys are parametrized to reproduce the experimental data according to Ref. [44]:

$$\begin{aligned} E_g^{\mathrm{L}}(x) &= 2.01 - 1.27x, \\ E_g^{\Delta}(x) &= 1.155 - 0.43x + 0.206x^2, \\ E_g^{\Gamma}(x) &= 3.37 - 2.48x. \end{aligned}$$

Finally, for the hydrostatic, $E_h^{\mathrm{L},\Delta,\Gamma}(x,y)$, and the uniaxial, $E_u^{\mathrm{L},\Delta,\Gamma}(x,y)$, strain terms for the well and barrier regions, it holds [23]

$$\begin{aligned} E_h^{\mathrm{L},\Delta,\Gamma}(x,y) &= (a_c^{\mathrm{L},\Delta,\Gamma} - a_v)\cdot(2\varepsilon_\parallel + \varepsilon_\perp), \\ E_u^{\Delta_2}(x,y) &= \frac{2}{3}\Xi_u^{\Delta}(\varepsilon_\perp - \varepsilon_\parallel), \\ E_u^{\Delta_4}(x,y) &= -\frac{1}{3}\Xi_u^{\Delta}(\varepsilon_\perp - \varepsilon_\parallel), \\ E_u^{\mathrm{L}}(x,y) &= E_u^{\Gamma}(x,y) = 0, \end{aligned}$$

where $\varepsilon_\parallel$ and $\varepsilon_\perp$ are the strain components along the parallel and growth directions, respectively; $a_c$, $a_v$, and Ξ are the deformation potentials. To take into account the $z$ dependence of the longitudinal and perpendicular effective masses of the strained SiGe and Ge materials, we use the mass parametrization reported in Ref. [41] for Δ and L electrons. Densities of states for the confined states are calculated as discussed in Sec. 1.8 in the parabolic band approximation.

The values adopted for the spin-orbit splitting and for the deformation potentials are summarized in Table 3.4 for Si and Ge bulk crystals. The corresponding parameters for the SiGe barrier material are obtained by linear interpolation. Nonlinear interpolations are instead adopted for the lattice constant, see Eq. (1.34), and the static refractive index, see Eq. (1.35).

For what concerns the solution of the coupled Schrödinger–Poisson equations, the Schrödinger equation for the envelope function is solved numerically for each

**Table 3.4** – Spin-orbit splitting $\Delta_0$ and deformation potentials for Si and Ge bulk crystals adopted in the code. Values for SiGe alloys have been obtained by linear interpolation. a: Data from Ref. [112]; b: Data from Ref. [23]; c: Data from Ref. [113].

| | Silicon | Germanium |
|---|---|---|
| $\Delta_0$ (eV) | 0.044[a] | 0.296[a] |
| $a_c^{\mathrm{L}} - a_v$ (eV) | −3.12[b] | −2.78[b] |
| $a_c^{\Delta} - a_v$ (eV) | 1.72[b] | 1.31[b] |
| $\Xi_u^{\Delta}$ (eV) | 8.7[c] | 9.42[c] |

conduction valley, using the standard technique of discretizing the wavefunctions along the growth direction $z$ and diagonalizing the resulting Hamiltonian matrix to obtain eigenenergies and eigenstates. The model for the solution of the self-consistent equations is described in detail in Sec. 1.9. Exchange-correlation effects are included in the local-density approximation [114] only for the 2D electrons at the L point since at low temperature the free electron density is mostly due to the confined carriers at L.

The Fermi level $E_f$ is evaluated as a function of temperature taking into account also the occupation of the impurity levels in the barriers. We assume that the energies of the impurity states are $E_b$ meV below the $z$–dependent conduction minimum of the barrier material; we adopt for $E_b$ the value of the binding energy of phosphorus in a $Si_{0.2}Ge_{0.8}$ bulk alloy (see Refs. [115,116]). Moreover, the occupancy of bound impurity states is evaluated avoiding double occupation due to Coulomb repulsion [61].

The obtained L, $\Delta_2$, $\Delta_4$, and $\Gamma$ conduction-band edge profiles for the grown samples are shown in Fig. 3.5, and in Fig. 3.6 we display the results of the self-consistent calculation for the conduction electronic states at 10 K in one of the samples. From the comparison between the donor level and the Fermi energy $E_f$, it is clear that only a very small fraction of the donor impurity states is ionized. This in turn implies that the final equilibrium solution is quite unstable (from a numerical point of view), and in fact typically up to 50–100 iterations are needed. We finally point out that, even if the algorithm can be optimized to reduce the number of required iterations, the present version was able to reach the final solution within any given required accuracy in all the different systems that we have simulated.

# Chapter 4

# Achieving direct-gap Si/Ge systems

## 4.1 Introduction

As already discussed in the Introduction of this Thesis, a CMOS-compatible laser based on group-IV materials is extremely desirable for the monolithic integration of the photonics part of the devices with their control electronics.

We have already examined in Chapter 3 the possibility of using Ge/SiGe heterostructures in the intersubband regime, with light emission in the THz range of the electromagnetic spectrum. In this Chapter we focus instead on the possibility of light emission exploiting interband transitions.

In fact, present research efforts are focused on the development of energy-efficient and CMOS-compatible LED or laser sources in the 1.55 μm C-band, since this band is routinely used for long-range optical fiber communications (the band is defined as 1.530–1.565 μm, i.e. with energy 810–792 meV). Indeed, at these wavelengths the losses in silica-based fibers are reduced. Moreover, the most used fiber amplifier, the erbium-doped fiber amplifier (EDFA) has its amplification window precisely in the C-band. The realization of a new device emitting in this frequency range would thus ensure its compatibility with the existing telecommunication infrastructure.

However, emission at this energy cannot be obtained with intersubband SiGe devices, since the band offset are not large enough, and then we must wisely exploit interband transitions. The main obstacle for optical emission in systems based on silicon or germanium is their indirect gap, which is at the basis of the very poor recombination efficiency observed in these materials. In fact, in Si the direct gap at $\Gamma$ has an energy larger than 3 eV, much above the fundamental gap at $\approx 1.13$ eV (with conduction band minimum along the $\Delta$ line). On the other hand, in bulk Ge the conduction band minimum at the $\Gamma$ point is only 136 meV higher in energy than the bottom of the conduction band at the L point, which is located (at low temperature) at about 900 meV above the top of the valence band. Thus Ge has two advantages: first, the direct gap energy is not too far from the required C-band, considering also

that, increasing the temperature, the energy of the direct gap decreases. Moreover, even if the minimum is not at the Γ point, the direct gap has an energy not much larger than the indirect gap. This motivates the study of Ge-rich systems for the realization of Si-compatible photonics applications. We just mention here that several other strategies have been adopted to obtain Si-based optically active materials, such as exploiting erbium doping [117], reduced dimensionality [118], hybrid Si/III-V systems [119], $\beta$-$FeSi_2$ alloying [120] and porous structures [121].

In the following Sections, we discuss different avenues that could allow the realization of optically-active systems based on Si and Ge. In particular, this Chapter is organized as follows: as a first step we discuss in Sec. 4.2 the type-I alignment of the band structure at the Γ point for Ge/SiGe MQWs grown along the [001] direction, by comparing the simulated absorption spectrum with the experimental absorbance spectrum. Then, we analyze in Sec. 4.3 how to exploit large strain fields in order to reach the direct-gap condition in Ge/SiGe MQW systems. In Sec. 4.4 we then discuss the possibility of the exploitation, in bulk and MQW systems, of smaller strain fields in combination with large $n-$type dopings, to achieve light amplification. To this aim, we developed a code (described in Sec. 4.5) for the evaluation of the luminescence spectra of Ge-based systems. In Sec. 4.6 we the discuss whether a rapid thermal annealing of Ge/SiGe MQW systems can increase the tensile strain without damaging the structure, in order to shift the lowest excitonic feature inside the C-band. Finally, in Sec. 4.7 we describe an interesting possibility of obtaining direct-gap Si-based systems by the use of short-period superlattices (SL).

Some of the studies are supported by experimental results, which have originated from collaborations with different experimental groups. In particular, for what concerns interband devices, we mention both the "L-NESS" (Como, Italy) group and the "LFTS" (Rome, Italy) group for the growth of SiGe heterostructures, and the "PSI" (Villigen, Switzerland) group for the x-ray and optical characterization of the samples.

## 4.2 Type-I alignment and calculation of the absorption coefficient

Recently, robust offsets for both Γ and L electrons in [001] Ge-rich Ge/SiGe multilayer structures have been reported [122,123]. In particular, Kuo *et al.* have first demonstrated a type-I profile for the Γ point band edges in Ge QWs and then exploited this result to propose Ge/SiGe MQW high-speed optical modulators based on the Quantum Confined Stark Effect [122,124]

In order to verify the type-I alignment of Ge/SiGe MQWs at the Γ point, we have investigated in Ref. [94] the optical absorption coefficient of a 30 MQW sample with 19.0 nm–thick Ge QWs and 19.0 nm–thick $Si_{0.2}Ge_{0.8}$ barriers on a $Si_{0.05}Ge_{0.95}$ equivalent substrate.

The comparison between the experimental and theoretical data is reported in Fig. 4.1a and shows a good quantitative agreement. For the electronic-states cal-

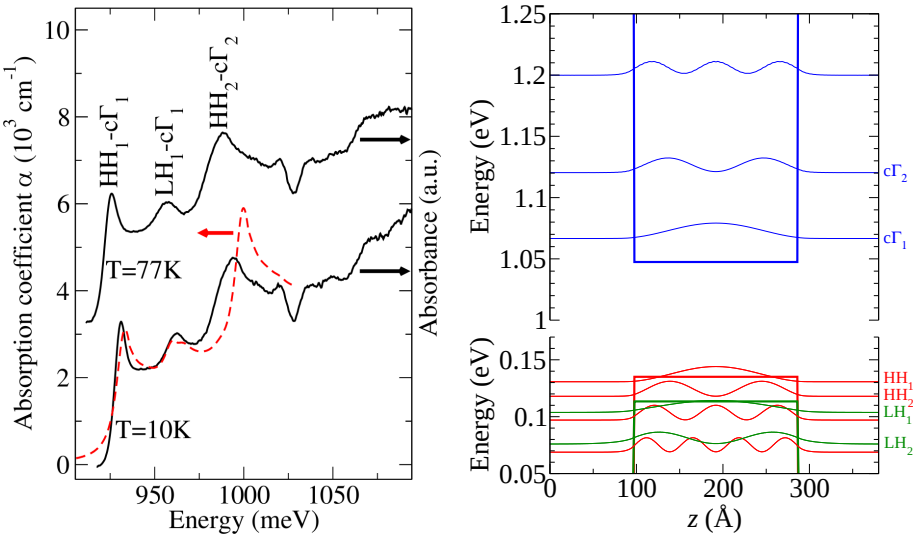


**(a)** Experimental absorbance spectra and theoretical absorption spectrum.

**(b)** Band edges and wavefunctions at Γ.

**Figure 4.1** – (a) Interband absorbance spectra (right vertical axis) of the MQW sample described in the text, measured at 10 and 77 K (black solid lines). The spectrum at $T$ = 77 K has been displaced along the vertical axis for clarity. Peaks attribution and the low-temperature theoretical absorption spectrum (left vertical axis) are also shown (dashed line). (b): LH, HH and cΓ band edges (thick lines) and squared moduli of the wavefunctions at Γ for the same MQW system. Relevant states are labeled.

culation, we have adopted the TB $sp^3d^5s^*$ model described in Sec. 1.2, using the parametrization of Ref. [16] for both Si and Ge. The calculated LH, HH and cΓ band-edge profiles and the squared moduli of the wavefunctions at Γ are reported in Fig. 4.1b. To the aim of calculating the optical absorption spectrum of Fig. 4.1a, the model described in Sec. 2.1 has been adopted, with the inclusion of the 2D exciton contribution as described in Sec. 2.4. The very good prediction of the absorption spectrum constitutes a check of the reliability of the material parameters that we are using to predict the properties of these systems in the neighborhood of the Γ point. Moreover, the comparison of the experimental spectrum with our calculation allows to assign the different excitonic features to the respective transitions, and this interpretation in terms of transitions between quantum-confined states both in the conduction and in the valence band provides a verification of the type-I band alignment for the electrons and holes at Γ.

## 4.3 Large tensile strain for optical gain in Ge

If we want to obtain direct-gap light emission from Ge structures, we have to conceive clever ways to reduce the Γ–L energy difference, in order to fill the Γ valley with

electrons and reach the population inversion regime. One appealing possibility is to apply a tensile strain field to the Ge material. In fact, when such a strain field is applied, both the L and Γ conduction states lower their energy but, due to the larger deformation potential of the Γ state, the fundamental gap becomes direct for an in-plane strain of about 2% [125] (see also solid lines of Fig. 4.2). This effect can be obtained for instance by means of a mechanical stress deformation on a germanium thin film [126]. However, while this may be an adequate technique for the investigation of the effects of strain on Ge, application of a mechanical strain is not appropriate for the integration in final devices. Instead, the embedding of strain by means of a coherent heteroepitaxial growth (see Sec. 1.3.2) would be much more effective. However, since Si has a smaller lattice constant than Ge, if we grow Ge on a SiGe substrate, we would expect only compressively-strained Ge layers. Actually, it is possible to obtain (small) tensile strains growing epitaxial Ge layers on Si substrates exploiting the thermal expansion mismatch between Ge and Si [127] (a discussion on the application of this technique is presented in Sec. 4.4 and following Sections). Such thermally induced tensile strain can reach values up to ≈ 0.25% and is moreover insensitive to the Ge film thickness [128]. However, with the values of the tensile strain attainable with this technique, the difference between the Γ and L valleys of Ge can be decreased to ≈115 meV, but we are yet quite far from the direct-gap regime. Presently, the most promising possibility to grow Ge layers on Si substrates with large tensile strain is to use $Ge_{1-x-y}Si_xSn_y$ alloys, due to the larger lattice constant of $\alpha$-Sn (6.489 Å) with respect to Si (5.430 Å) and Ge (5.6563 Å) [129–131]. Moreover the Sn concentration, $y$, represents an additional degree of freedom for band engineering [132–137]. Indeed, through simultaneous control of the $x$ and $y$ molar fractions, relaxed $Ge_{1-x-y}Si_xSn_y$ alloys grown on Ge-buffered silicon have already been optimized to obtain tunable direct gap structures [137].

We would like to point out here that often in the literature one refers to "thin" Ge layers, where the word "thin" means a few μm thick. For what concerns the electronic properties, however, such systems are not thin at all, and in fact they display bulk-like properties. Instead of growing "thin" Ge layers on a buffer substrate, a very attractive route towards a direct-gap Ge laser is represented by suitably designed silicon-germanium multilayer heterostructures, which are highly compatible with CMOS processing [89]. In fact, the exploitation of confined nanostructures such as Ge-rich SiGe MQWs could benefit from larger oscillator strengths due to the reduced dimensionality. Moreover, as discussed in Sec. 4.2, [001] Ge-rich Ge/SiGe multilayer structures present robust offsets for both Γ and L electrons and a type-I profile for the Γ point band edges. Motivated by these arguments, we study in this Section the possibility of obtaining a direct-gap material when a significant tensile-strain is applied to a Ge/SiGe MQW system. The results of this work have been published in Ref. [138].

For this study, we adopt the $sp^3d^5s^*$ tight-binding Hamiltonian described in Sec. 1.2. In fact, it fully considers strain, alloy effects, spin-orbit coupling, interface potentials and band non-parabolicities, and moreover it is particularly suitable for the whole Brillouin zone description of the multivalley conduction bands of tensile

strained Ge-rich Ge/SiGe MQWs. In this way the leakages in the gain coefficient, related to the occupation of the electronic states near the L point, can be correctly taken into account. Also, the analysis of the spatial and orbital contributions of the near-gap states allows us to give a transparent interpretation of the numerical results for the strain-dependent TE/TM gain ratio.

The systems investigated in this Section are multiple quantum well heterostructures with alternating Ge and SiGe layers, coherently grown along the [001] direction on SiGeSn relaxed virtual substrates.

Appropriate periodic boundary conditions are assumed along the lateral (parallel) and growth (orthogonal) $z$ directions. The in-plane lattice constant is determined by the SiGeSn substrate, and the inter-plane separations along $z$ are evaluated according to the macroscopic elasticity theory (see Sec. 1.3.2). Interfaces are assumed flat and sharp.

For the evaluation of the electronic states, we adopt here the TB parametrization of Ge given in Ref. [36], which has been developed to improve the results of Ref. [16] in the presence of tensile strains ad discussed in Sec. 1.3.5. This is of particular relevance in our case, where intense strain fields are present. For Si, we use the parametrization reported in Ref. [35], with the scaling coefficients for the hopping energies of Ref. [16]. For the valence band offset between the average of the valence-band edges in a strained $Si_{1-x}Ge_x$ and in a relaxed SiGe substrate, we adopt the formula of Eq. (1.37). Note, however, that in order to describe the case of a SiGeSn substrate, we extend to the $a_\parallel \gtrsim a_{Ge}$ range the above expression, which was originally derived for $a_{Si} \leq a_\parallel \leq a_{Ge}$. Since we are interested only in the relative offsets between the SiGe layers of the MQW (which do not contain Sn) and actually not with the substrate, the extension provides the correct result, since the substrate enters in this formula only through its lattice constant. Finally, dipole matrix elements and gain coefficients are calculated as described in Chap. 2.

As an useful starting point we have evaluated the $\Delta_\perp$, L and $\Gamma$ energy gaps for Ge and $Si_{0.2}Ge_{0.8}$ bulk crystals with the same parallel lattice constant as a function of the in-plane Ge tensile strain. The results are shown in Fig. 4.2. All these gaps decrease in energy with increasing strain, but in Ge, due to the larger deformation potential of the $\Gamma$ states with respect to the L states, an indirect–direct band gap transition occurs at $\varepsilon_\parallel \simeq 1.8\%$.

We have then considered MQW structures, composed of a sequence of alternating regions of Ge and $Si_{0.2}Ge_{0.8}$ materials, of thickness 110 Å each. For both L and $\Gamma$ electrons, the band edge of the SiGe alloy is higher in energy than the corresponding value of pure Ge, so that the Ge layers act as quantum wells and the alloy layers as barriers. The situation is reversed for the $\Delta_\perp$ edges, which are however much higher in energy. Therefore for the evaluation of the gain spectra, only electrons filling the $\Gamma$ and L valleys have to be taken into account. As evident from Fig. 4.2, where the MQW conduction confinement energies have been added to the corresponding bulk gaps, the larger confinement energy of $\Gamma$ electrons due to their lighter mass pushes the indirect–direct crossover to a higher strain value, at about $\varepsilon_\parallel \simeq 2.68\%$ (see the arrow in Fig. 4.2).

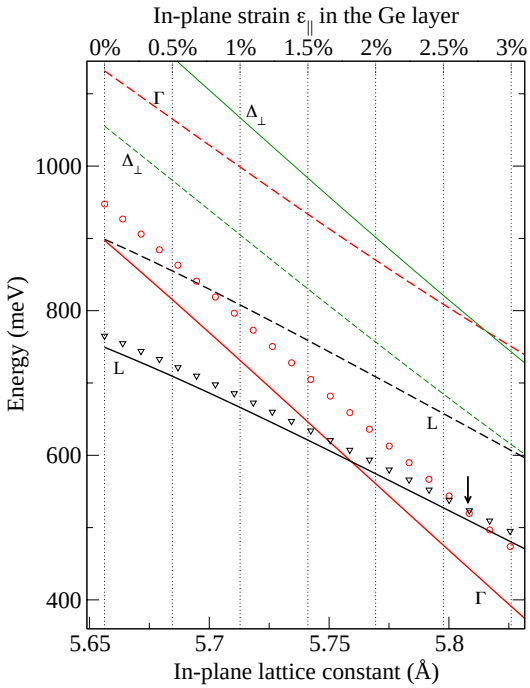


**Figure 4.2** – Band gaps as a function of the in-plane lattice constant (bottom $x$-axis) for in-plane biaxial tensile strained bulk materials. Solid (dashed) lines refer to Ge ($Si_{0.2}Ge_{0.8}$). The in-plane strain indicated in the top $x$-axis refers to germanium. Band gaps at the Γ and L points, and along the $\Delta_\perp$ line are indicated by red, black and green lines, respectively. Band minima along the $\Delta_\parallel$ line are higher in energy and are not shown in the Figure. The contribution to the L and Γ energy due to confinement in the MQW systems are represented as triangles and circles for $cL_1$ and $c\Gamma_1$, respectively. The arrow indicates the crossover between the indirect and direct gap regions in the MQW system.

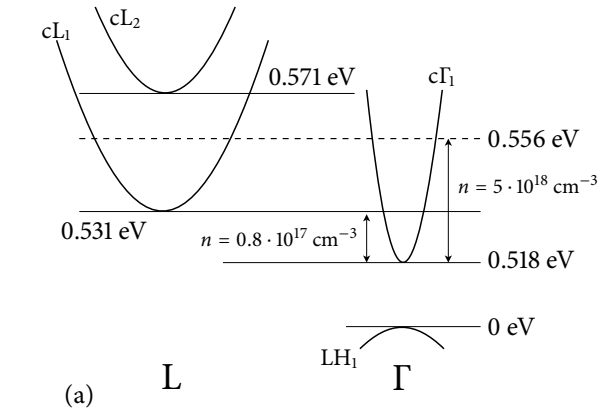


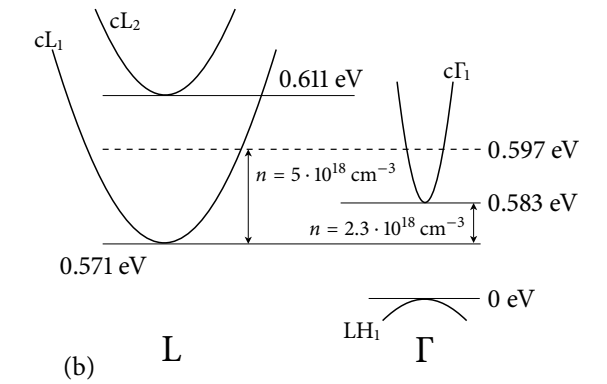


**Figure 4.3** – Schematic band profile (not to scale) at the L and Γ points of the MQW for systems A ($a_\parallel$ = 5.818 Å, panel (a)) and for system B ($a_\parallel$ = 5.794 Å, panel (b)). The injected carrier densities corresponding to the $|c\Gamma_1 - cL_1|$ energies difference are quoted. The energy difference corresponding to the maximum value of the carrier density discussed in the text ($5 \cdot 10^{18}$ cm$^{-3}$) is also reported. Energies are referred to the topmost valence state ($LH_1$).

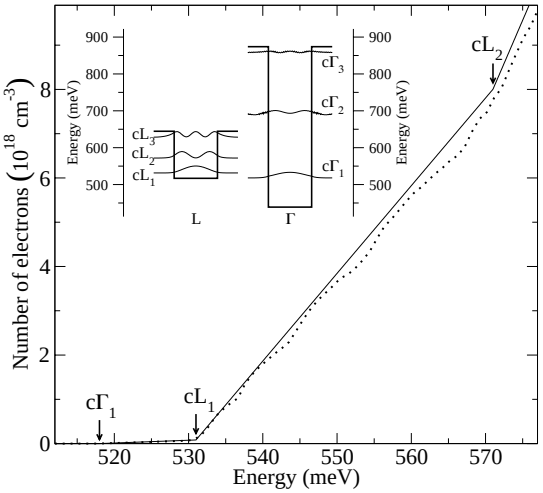


**Figure 4.4** – Integrated electronic density of states for system A, plotted as a function of the quasi-Fermi energy. The dotted line has been obtained integrating the DOS resulting from the electronic spectrum of the tight-binding Hamiltonian. The solid line is calculated from the DOS obtained with the 2D effective mass model. The energies of the $c\Gamma_1$, $cL_1$ and $cL_2$ states are indicated with arrows. In the inset, conduction band edge profiles and square modulus of the confined wavefunctions at L and Γ points are reported.

From now on, we focus on two MQW systems whose $\varepsilon_{\parallel}$ are chosen at opposite sides of the indirect–direct gap crossover shown in Fig. 4.2. For system A we set $\varepsilon_{\parallel} = 2.86\%$, so that $E(c\Gamma_1) < E(cL_1)$, while system B corresponds to $\varepsilon_{\parallel} = 2.43\%$, and thus $E(c\Gamma_1) > E(cL_1)$. The relevant energies at the Γ and L points are summarized in Fig. 4.3a and Fig. 4.3b for systems A and B, respectively. It is worth to notice that both the A and B MQWs are not strain compensated, since in both cases not only the active Ge region but also the barrier material are tensile strained. It follows that in the practical realization of the above structures one has to limit the total thickness of the MQW stack so to preserve coherent growth. Strain compensation can be realized exploiting SiGeSn alloys for the barrier material, as proposed for instance in [139], where tensile-strained Ge MQW systems with similar $a_{\parallel}$ lattice constant are studied within an effective mass approach. We note that the authors of [139] find L and Γ band edge alignments comparable to those obtained here. Also their reported gain spectra are similar to our findings, as one may expect since the optically active states are well confined in the Ge layer. This suggests that the results discussed in the following do not depend critically on the chemical composition of the barrier material, provided that enough confinement in the near gap valence, and Γ and L conduction states exists.

We report in Fig. 4.4 the integrated DOS for system A, obtained from the TB Hamiltonian taking into account the joint contribution of the L and Γ conduction valleys. As shown in the inset, both at L and at Γ three confined states are present. The contribution of the L states to the DOS is predominant due to the fact that the 2D effective mass at L, $m_L \simeq 0.26 m_0$, is much larger than $m_\Gamma = 0.034 m_0$ and also because of the fourfold degeneracy of the L valleys. As a realistic upper bound to the injected carrier densities $D_j$, we investigate the region $D_j \leq 5 \cdot 10^{18}\,\mathrm{cm}^{-3}$, which corresponds to $E_f \leq 556\,\mathrm{meV}$. For this injection range, only the first confined states $c\Gamma_1$ and $cL_1$ are occupied by carriers (see Fig. 4.3a). Moreover continuum states have energies higher than 644 meV. For this reason we find that if $D_j \leq 5 \cdot 10^{18}\,\mathrm{cm}^{-3}$, the

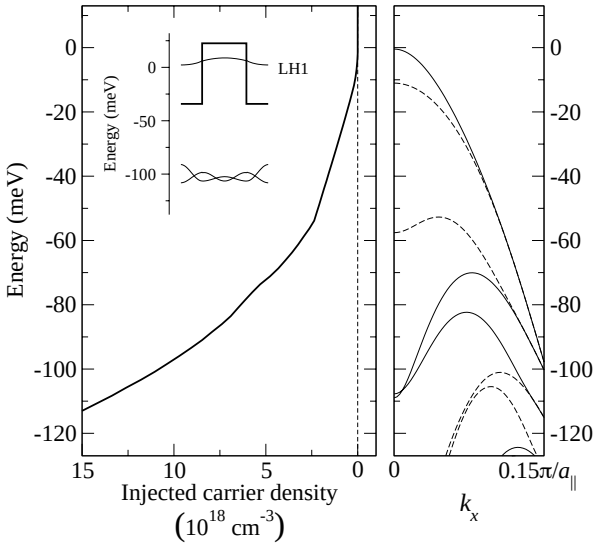


**Figure 4.5** – Right panel: Valence bands calculated for the MQW system A, as a function of $k_x$, at $k_y = 0$ and $k_z = 0$ (solid lines) or $k_z = \pi/a_\perp$ (dashed lines). Left panel: quasi-Fermi energy for holes as a function of the injected carrier density. In the left inset the LH band edge profile and the square modulus of the near-gap wavefunctions at Γ are also shown.

integrated DOS resulting from the electronic spectrum of the TB Hamiltonian is quite well reproduced by a simple 2D effective mass parabolic model of the L and Γ valleys where the dispersion along the growth axis ($z$) is assumed negligible (see Fig. 4.4, solid line).

The TB valence bands of system A and the corresponding integrated DOS are reported in Fig. 4.5. In the near gap region only one state is confined by the potential profile which originates from the light-hole bulk bands (see inset in Fig. 4.5). Heavy-hole states are lower in energy due to the band splitting caused by the tensile strain field in the Ge and $Si_{0.2}Ge_{0.8}$ layers. The interaction of the heavy-hole and light-hole bands at $\mathbf{k} \neq 0$ makes in this case the parabolic effective mass model a very crude approximation, especially for the lower energy band where a negative effective mass is obtained. Furthermore to evaluate the hole population, band dispersion along the $z$ direction must now be taken into account because of the shallower confinement of the hole states. For instance, comparing the band structure at $k_z = 0$ (solid lines) and $k_z = \pi/a_\perp$ (dashed lines) in the right panel of Fig. 4.5, we obtain for the $LH_1$ state an energy bandwidth along $k_z$ of about 10 meV and an even larger dispersion for the lower energy states. Finally, in the evaluation of the DOS and of the optical properties, also the anisotropy in the growth plane ($xy$) has been taken into account, sampling the Brillouin zone along eight nonequivalent directions in the $xy$ plane. In the low temperature limit, and for an injected carrier density $D_j \lesssim 5 \cdot 10^{18}\,\mathrm{cm}^{-3}$, only the first two valence states are filled. The second band (whose energy at the Γ point is about −110 meV) starts to be populated for densities $D_j \gtrsim 2.2 \cdot 10^{18}\,\mathrm{cm}^{-3}$, and because of its negative curvature, states with $\mathbf{k} \neq 0$ are filled first. Similar results hold also for system B.

The low temperature gain spectrum is evaluated as discussed in Sec. 2.2.2, according to the expressions (2.12), (2.13) and (2.14). For any given injected carrier density, the related Fermi levels are calculated so to satisfy the appropriate charge neutrality

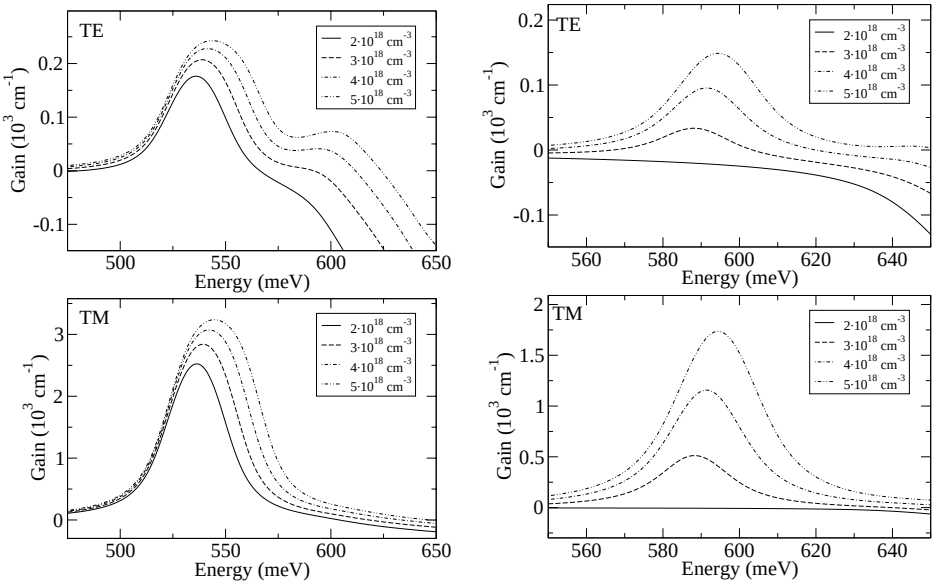


**(a)** Gain spectra for system A.

**(b)** Gain spectra for system B.

**Figure 4.6** – Gain spectra of systems A and B, evaluated at different injected carrier densities for TE (top panels) and TM (bottom panels) polarizations of the incident radiation.

equation. Notice also that only $k$-direct transitions are considered: therefore, positive contributions to the gain originate only from electron-hole pairs recombining in a neighbourhood of the Γ point. The leakages due to the presence of confined L states are accounted through their influence on the Fermi distribution function of the conduction band.

The evaluated TE and TM gain spectra of systems A and B, for the broadening parameter $\gamma = 10\,\text{meV}$ [139], are shown in Fig. 4.6 for different injected carrier densities. Notice that despite its indirect-gap structure, a positive gain is obtained also for system B, although a higher carrier density is required.

For both systems, the maximum gain is obtained with TM polarization. This is due to the symmetry of the involved states. To address this point we observe that the peak in the gain spectrum (at about 535–545 meV and 585–595 meV for system A and B, respectively) originates from the $c\Gamma_1 \rightarrow LH_1$ transition. The $c\Gamma_1$ state has prevalent $s$ character while, neglecting the strain coupling for the time being, the orbital character of the LH states at the Γ point writes:

$$\begin{aligned} \text{LH}_{J_z=1/2} &= -\frac{1}{\sqrt{6}}[(p_x^{\downarrow} + ip_y^{\downarrow}) - 2p_z^{\uparrow}], \\ \text{LH}_{J_z=-1/2} &= \frac{1}{\sqrt{6}}[(p_x^{\uparrow} - ip_y^{\uparrow}) + 2p_z^{\downarrow}], \end{aligned} \tag{4.1}$$

as discussed in Eqs. (1.23). Since the TE (TM) polarization couples the $s$–like conduction orbital only with the $p_{x,y}$ ($p_z$) valence orbitals, we expect a larger gain in the TM

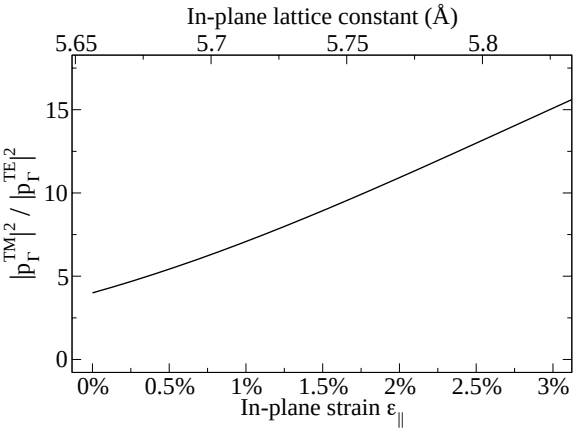


**Figure 4.7** – TM/TE ratio for the square modulus of the dipole matrix element for the LH→cΓ transition in bulk Ge. The dipole matrix element is evaluated at Γ as a function of the (001) in-plane tensile strain $\varepsilon_\parallel$. The value of the TM/TE ratio at $\varepsilon_\parallel = 0$ is four; it monotonically increases with $\varepsilon_\parallel$ because of the mixing of the valence bands caused by the strain field.

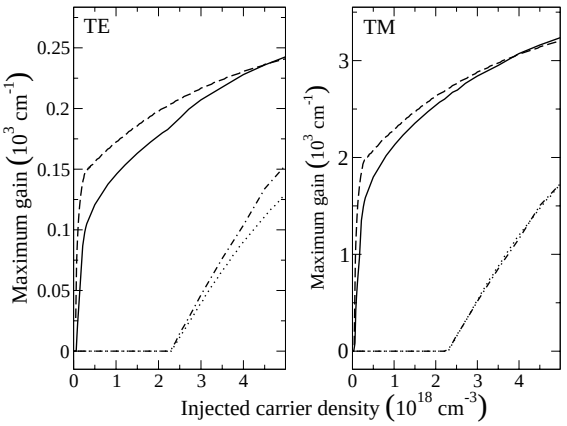


**Figure 4.8** – Maximum value of the TE (left panel) and TM (right panel) gain as a function of the injected carrier density. Solid and dashed-dotted lines have been calculated for the A and B system, respectively. Dashed and dotted lines are the respective values evaluated in the parabolic approximation (see text for details).

polarization. In particular, since gain is proportional to the square modulus of the matrix dipole element, a TM/TE ratio of the order of four is expected. However, for both systems A and B we find a much larger TM/TE ratio, of the order of 12–13. This large value is due to strain-induced mixing of the valence states, especially between the LH and split-off states which has not been considered above. Tensile strain induces an increase of the fractional $p_z$ character of LH states [140], thus increasing the TM/TE ratio. To support this argument we have plotted in Fig. 4.7 the ratio of the square moduli of the TM and TE dipole matrix elements between the bottom conduction and topmost valence states at the Γ point, calculated in bulk Ge as a function of the in-plane tensile strain. As expected, from Eq. (4.1) this ratio is four for relaxed Ge but increases with strain, in agreement with the results that we have obtained in the MQW systems.

In addition to the main peak of the TE gain spectrum of system A, we observe in Fig. 4.6a a second peak at about 610 meV whose intensity increases for increasing injected charge density. This feature is due to transitions from $c\Gamma_1$ to the (not confined) valence state below $LH_1$ (see inset of Fig. 4.5), which is active only for sufficiently large injected densities, i.e. when holes with $k_\parallel \neq 0$ start to populate the band below $LH_1$. Actually, the intensity of these transitions are of the same order of magnitude for

TE and TM polarizations, but since the $c\Gamma_1 \rightarrow LH_1$ transition in the TM polarization is much stronger, the related signal is only a small correction to the main TM peak and is not clearly resolved in the spectrum (see Fig. 4.6a, bottom panel).

Finally, in Fig. 4.8 we report the maximum value of the TE and TM gain spectrum of system A and B as a function of the injected carrier density. The threshold carrier density of system B at about $2.3 \cdot 10^{18}$ cm$^{-3}$ is associated with the filling of the L states below the $c\Gamma_1$ level (see also Fig. 4.3b). Conversely system A, having a direct gap, is characterized by positive gain already at small injected carrier densities. However it is worth to notice that for $D_j \simeq 5 \cdot 10^{18}$ cm$^{-3}$ the maximum gain for system B is only about one half of that obtained for system A. To evidence the role of the band structure effects on the gain spectra, we also show in Fig. 4.8 the maximum gain evaluated in a simple 2D parabolic model, where effective masses and band edges are taken from the TB results together with the $c\Gamma_1 \rightarrow LH_1$ dipole matrix elements, which are assumed to be $k$-independent.

Despite its simplicity, the parabolic model fits reasonably well the TB results, even if in the gain spectra obtained by means of this simplified model (not shown), the peak at about 610 meV reported in the top panel of Fig. 4.6a is not reproduced. This is not surprising considering that this feature is related to the transition to the valence band below $LH_1$. Furthermore, the main peak obtained in the parabolic approximation is redshifted of about 5 meV with respect to the TB spectra. This fact is to be attributed to the valence band dispersion along the $z$-direction, which has been neglected in the 2D effective mass model.

Thus, in conclusion, we have shown that in Ge/SiGe MQW structures the direct gap crossover requires higher strain fields with respect to bulk materials due to the large confinement energy associated to $\Gamma$ electrons. We have obtained large gain coefficients for realistic values of the injected carrier density, showing that this kind of systems could be good candidates as optically-active materials. We have also studied the TE and TM gain as a function of the tensile strain field, demonstrating that the applied strain increases the TM/TE ratio due to an increment of the fractional $p_z$ character of the topmost LH state. Finally, a critical comparison of the tight-binding results with a simple effective mass model has also been provided.

## 4.4 Small strain and doping

As shown in the previous Section, the large strain fields needed to obtain a direct-gap material shrink the band gap to about 550 meV, which is far below the above-mentioned telecom optical window. Moreover, we have to take into account that the technology for the epitaxial growth of group-IV structures containing Sn is not as well developed yet.

To overcome the above-mentioned difficulties, in 2007 Liu and coworkers [128] have theoretically proposed to engineer the electronic structure of [001] Ge thin layers grown on Si by the application of a small biaxial strain field (of the order of $\approx 0.25\%$, realizable with the thermal mismatch technique), in order to slightly reduce

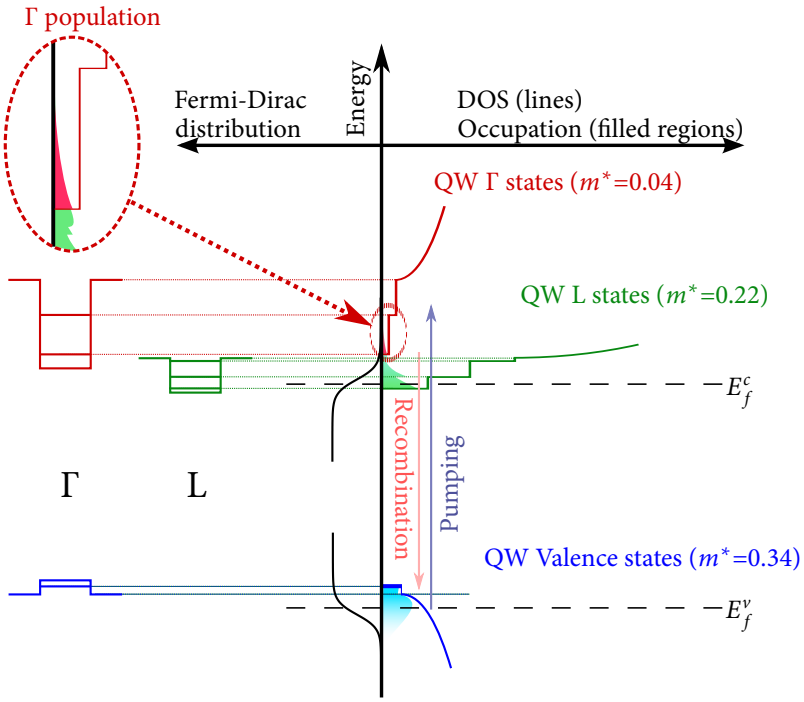


**Figure 4.9** – Schematic of density of states (DOS) and occupation (i.e., DOS times Fermi-Dirac distribution) of a Ge quantum well system. In the Figure, the 2D and continuum contributions to the DOS are evident. The quasi-Fermi energies for the conduction ($E_f^c$) and valence ($E_f^v$) bands are also shown. For clarity, the band profiles and the confined states at Γ and L are shown on the left. Under optical pumping, a strong inversion between conduction states at L and the valence band states at Γ builds up due to conduction electrons scattered from Γ to L bands. Eventually, electrons thermally excited to the Γ bands (in red) recombine radiatively (dipole allowed transitions) with holes filling the QW subbands. Since the hole occupation is close to unity, strong stimulated emission may set in.

the energy difference between the L and Γ conduction edges, and thereafter achieve population inversion across the direct gap by filling the lower-energy L states by means of $n$–type heavy doping. In this way, tuning the temperature, we can thermally excite some electrons in the Γ valley. A schematic graphical representation is provided in Fig. 4.9. Following this approach a significative enhancement of the signal related to radiative recombination across the direct gap has been reported by several groups in the last years, both in electroluminescence [141–143] and photoluminescence [126, 144–148] experiments with tensile-strained and/or heavily-doped Ge layers.

As an example, we show in Figs. 4.10a and 4.10b two sets of experimental PL spectra for different pump powers and temperatures performed on a Ge (100) $n^+p$ diode; the Figures are taken from Ref. [142]. In this Figures, it is evident how the PL signal due to direct-band transitions becomes more and more important (with respect to one due to indirect-band transitions) both when the pumping power or when the temperature are increased.

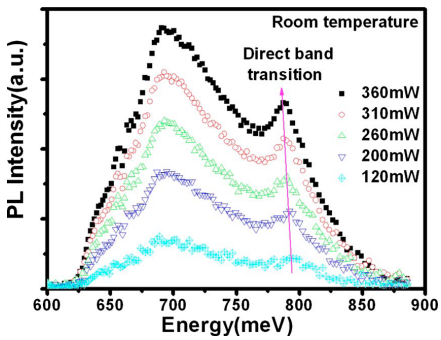


**(a)** The PL spectra of the Ge diode at room temperature. The contribution due to the direct band transition at the Γ point increases with increasing pump power.

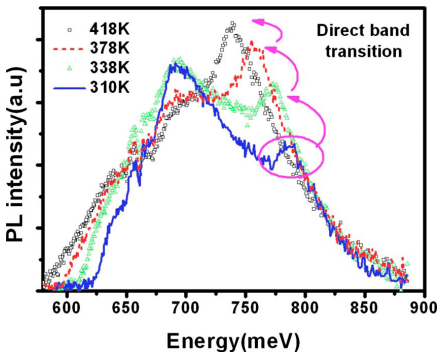


**(b)** Temperature dependent PL at the temperature of 310–415 K. Direct band gap transition enhancement is due to carrier distribution toward the high energy part as well as the decrease in the band gap difference between direct and indirect band gaps at high temperature.

**Figure 4.10** – Photoluminescence spectra of the Ge (100) $n^+p$ diode described in the text. The Figures are reproduced from Ref. [142].

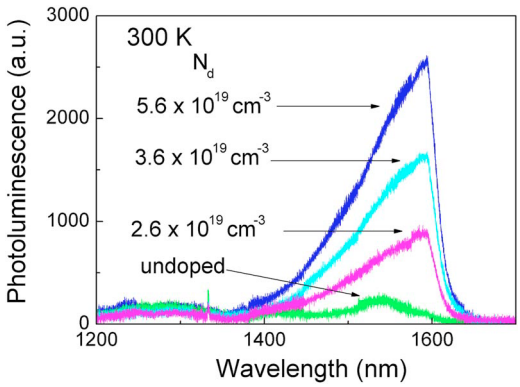


**Figure 4.11** – Room temperature photoluminescence spectra of phosphorus-doped bulk Ge obtained by the gas immersion laser doping process, compared to the photoluminescence of an undoped Ge sample. The active donor concentration is indicated in the graph. The detector has a cutoff at 1590 nm. The Figure is reproduced from Ref. [146].

As a second example, we report in Fig. 4.11 the room-temperature PL spectra of strongly $n$-doped bulk Ge as a function of the doping density, taken from Ref. [146]. In this Figure, a 20× increase of the PL signal associated to the direct-gap transitions is apparent for the largest doping density considered with respect to an undoped Ge sample, showing the effectiveness of the large doping technique in building a population inversion at Γ.

Note that the presence of a small strain has in fact some benefits (apart from the fact that it can be obtained in Sn-free structures). As a first point, it slightly reduces the gap energy at Γ, which gets closer to the C-band. Moreover, it splits the LH and HH valence states, and for tensile strains the top of the valence band has light-hole symmetry. Since the mass of the LH states is quite small ($m_{\mathrm{LH}} = 0.043m_0$), the optical gain increases faster with the injected carrier density due to the low density of states

associated with the light-hole band. Finally, since the electrons are thermally excited from the L to the Γ valley, even a small reduction of the Γ–L energy difference can lead to a large enhancement of the number of electrons at Γ, due to the exponential decay of the Fermi–Dirac distribution.

Nevertheless, the observation of robust optical gain in this kind of systems still remains elusive, even if the first evidence of (feeble) light amplification under optical pumping has been recently reported by Liu *et al.* [4], probably due to the large contribution to the absorption of the light by the free carriers: in such heavily-doped systems, free-carrier absorption (FCA) is the main loss mechanism and hence a fundamental limit to the performance of the devices [128,149].

In the effort of increasing the oscillator strengths adopting also here systems with lower dimensionality, one would be tempted to consider SiGe quantum wells with smaller strain fields than those discussed in Sec. 4.3, and $n$–dope the SiGe barriers. In this way, a filling of the remaining L states could in principle be obtained, similarly to what has been just discussed for "bulk" tensile Ge layers. Nevertheless, as we prove now by a quantitative argument, this approach can be ruled out, at least if the doping is limited to the barriers.

In fact, considering a direct gap in the range of the telecom window (i.e., a wavelength between 1520 and 1620 nm) one would require a strain of the order of 1 – 1.2%. Integrating the density of states (DOS) associated to the (four) L valleys, we get that the doping density required to push $E_f$ above the $c\Gamma_1$ level is already of the order of $2 \cdot 10^{19}$–$4 \cdot 10^{19}\,cm^{-3}$. For such high doping densities, the Hartree potential deeply affects the band edge profile (see Sec. 1.9). In fact, if one assumes that the doping electrons localize in the well and remain confined there, the resulting electrostatic energy at the well/barrier boundary is of the order of 1 eV. This value is much larger than the L band offset which is of about 130 meV for $Si_{0.2}Ge_{0.8}$ barriers (see e.g. Fig. 4.2). It follows, in analogy to what has also been discussed in Sec. 3.2, that one reaches a self-consistent solution where only a small portion of the doping charge is transferred into the well. Then, this small charge is not able to fill the L valleys.

Finally, it is worth to notice that as an alternative route towards a Ge-based quantum well laser, it has been recently proposed to $n$-dope the Ge active region of Ge/SiGeSn MQW systems [150]. This of course could heal the problem of the small charge transfer connected with the doping of the barriers, still exploiting lower strain fields, but it can introduce large impurity scattering contributions to the non-radiative relaxation times (in addition to the free carrier absorption) due to the presence of the doping ions within the well.

## 4.5 Simulating the photoluminescence

The physical nature of the population inversion process in the systems described in the previous Section is quite different from the one of "standard" III-V materials, due to the special non-equilibrium conditions at the direct gap (which is not the

fundamental energy gap). In the previous Section we have discussed how the interplay of strain and doping may result in a population inversion, and how in the last years many experiments of EL, PL, … have been performed in order to study the dependence of the direct-gap emission on temperature, doping, pumping power, etc.

A quantitative description of the competitiveness between the direct- and indirect-gap emission in Ge systems is then of the uttermost importance to gain further insight in the problem, and to predict and design new photonic devices based on Ge. With this aim, we have developed a general code for the treatment of PL in both bulk structures and MQWs, taking into consideration both direct and indirect transitions.

The code is still in an initial stage, but it is already capable of calculating the PL spectrum of optically-pumped bulk $Si_{1-x}Ge_x$ alloys under strain (focusing mainly on Ge-rich systems), both in undoped and doped systems. In the code, we take into account both the direct-gap transitions at Γ and the phonon-mediated transitions between the topmost valence states and the L valleys in the conduction band.

The model for the calculation of the state energies and the effective masses is the same described in Sec. 3.A for what concerns the conduction band. For the valence band, we use the following expressions for the HH, LH and SO edges measured from the average of the three bands [23]:

$$
\begin{aligned}
E_{\mathrm{HH}} &= \frac{\Delta_{so}}{3} - \frac{\delta E_{001}}{2}, \\
E_{\mathrm{LH}} &= -\frac{\Delta_{so}}{6} + \frac{\delta E_{001}}{4} + \frac{1}{2}\sqrt{\Delta_{so}^2 + \Delta_{so}\delta E_{001} + \frac{9}{4}\delta E_{001}^2}, \\
E_{\mathrm{SO}} &= -\frac{\Delta_{so}}{6} + \frac{\delta E_{001}}{4} - \frac{1}{2}\sqrt{\Delta_{so}^2 + \Delta_{so}\delta E_{001} + \frac{9}{4}\delta E_{001}^2},
\end{aligned}
$$

where $\Delta_{so}$ is the spin-orbit splitting and the quantity $\delta E_{001}$ is expressed in terms of the deformation potential $b_v$ and of the strain components as

$$
\delta E_{001} = 2b_v(\varepsilon_{zz} - \varepsilon_{xx}).
$$

The values of $b_v$ are $b_v^{\mathrm{Si}} = -2.1\,\mathrm{eV}$ [151] and $b_v^{\mathrm{Ge}} = -1.88\,\mathrm{eV}$ [125]; a linear interpolation scheme is adopted for $Si_{1-x}Ge_x$ alloys. For the effective masses in the valence band, we use the functional form suggested in Ref. [41] to fit the curve reported in [152] for the Luttinger parameters $\gamma_1$, $\gamma_2$ as a function of the Ge content $x$ of the alloy. Moreover, we make the approximation $\gamma_2 = \gamma_3$, that is we assume a cylindrical symmetry for the effective masses. The resulting fit functions are given by

$$
\begin{aligned}
\gamma_1 &= 4.4204 - 2.675\,39 \log\left(1 - 0.962\,19x^{1.35}\right) \\
\gamma_2 &= 0.276\,905 - 1.019\,21 \log\left(1 - 0.976\,85x^{1.35}\right)
\end{aligned}
$$

The (bulk) effective masses are then given by

$$
m_{\mathrm{HH}} = \frac{1}{\gamma_1 - 2\gamma_2}, \qquad m_{\mathrm{LH}} = \frac{1}{\gamma_1 + 2\gamma_2}, \qquad m_{\mathrm{SO}} = \frac{1}{\gamma_1}.
$$

Moreover, in the code we have also taken into account the bandgap shift as a function of the temperature, independently for the L and the Γ gaps. For the gap at Γ, we interpolate between the bandgap shifts of Si and Ge whose values in meV are given by [153]:

$$\Delta E_g^{\Gamma,\mathrm{Si}}(T) = -0.391\frac{T^2}{T+125},$$
$$\Delta E_g^{\Gamma,\mathrm{Ge}}(T) = -0.582\frac{T^2}{T+296},$$

where the temperature is expressed in K. For the bandgap at L, since no experimental data are present for Si, and we are concerned mainly with pure Ge or Ge-rich SiGe alloys, we use the formula for the bandgap shift of Ge [153]:

$$\Delta E_g^{\mathrm{L,Ge}}(T) = -0.48\frac{T^2}{T+235}.$$

The calculation of the recombination times is done as discussed in Sec. 2.3, with the assumption of parabolic bands and of a single quasi-Fermi level in the conduction band, both for the Γ and the L valleys. The quasi-Fermi levels in the conduction and valence bands are calculated using a bisection algorithm with the same technique of the code described in Sec. 3.A. We remind that the present model includes only three bands (HH, LH and SO) in the valence, while in the conduction band it takes into account one band at Γ and and one band at L (or more precisely four degenerate bands, one for each L valley).

To show some preliminary results, we report in Fig. 4.12 the temperature dependence of the total spontaneous recombination rate for a 0.5% tensile-strained Ge bulk with $1 \cdot 10^{18}\,\mathrm{cm}^{-3}$ $n-$doping and an optical pumping that induces a charge of $5 \cdot 10^{18}\,\mathrm{cm}^{-3}$.

At low temperature, since only the L conduction minimum is filled with electrons, the PL spectrum originates only from the indirect recombinations, as it is the case for instance for the spectrum at $T = 10$ K. We can recognize two contributions (the main peak and the shoulder at lower energy) which originate from the indirect transitions involving the HH and the LH valence states. We remind that in the calculation, the Ge bulk is tensile-strained, so that the HH and LH edges are not degenerate (the SO band plays only a minor role due to the fact that it is at much lower energy than the HH and LH bands). We remind moreover that at low temperature only the phonon emission channel is active. At higher temperatures, some of the electrons start to populate also the Γ valley due to the tail of the Fermi–Dirac distribution, so that also the direct-gap transitions contribute to the spectrum. Indeed, two new peaks appear at larger energy, whose magnitude increases with temperature. The two peaks originate from the direct transitions from the conduction Γ valley to the two HH and LH bands in the valence. In particular, the LH state is on top (at Γ), implying that the peak due to the LH-cΓ transition occurs at a lower transition energy. To understand the behavior of the relative magnitude of the direct and indirect contributions to

the spectra, we note that they both depend on the respective populations and on the magnitude of the matrix elements involved. In particular, if the populations are similar, the direct transitions are much more significant than the indirect ones. In our case, however, the Γ conduction valley has a much smaller population than the L valleys, and the two effects compensate. Increasing the temperature, the population in the Γ valleys increases and thus at large temperatures the direct contribution becomes the predominant one.

In Fig. 4.13 we instead show the dependence of the PL spectrum on the doping of the 0.5% tensile-strained Ge bulk. The spectra have been calculated assuming a temperature of 210 K, with an optical pumping that induces a charge of $5 \cdot 10^{18}\,\mathrm{cm}^{-3}$. Also in this case, we note that a large doping increases the direct contribution, due to the fact that for large doping densities the L valleys are filled and electrons can populate also the Γ valley. The overall qualitative structure of the spectrum does not change very much and the different features can be understood following the same considerations discussed above for Fig. 4.12.

Finally, in Fig. 4.14 we show the dependence of the total recombination rate on the strain of the Ge sample, calculated at $T = 210\,\mathrm{K}$, with $1 \cdot 10^{18}\,\mathrm{cm}^{-3}$ $n-$type doping and an optical pumping that induces a charge of $5 \cdot 10^{18}\,\mathrm{cm}^{-3}$. In this case, two main effects are visible. The first one is a global redshift of the spectrum for increasing tensile strain, due to the bandgap shrinking of tensile-strained Ge (see for instance Fig. 4.2). The second even more relevant effect is the splitting of the peaks originated from transitions involving the LH or HH bands. In fact, at zero strain the HH and LH states are degenerate at Γ, so that the onsets of the recombination spectra (both due to direct and indirect transitions) occur at the same energy for the transitions originating from the two bands. Indeed, at zero strain (black curve) we recognize only two peaks: the one at lower energy is due to the indirect transitions, while the narrower one at larger transition energies is due to the direct transitions. Increasing the tensile strain, we see that the direct contribution splits in two peaks, that can be assigned as discussed before to the LH-cΓ and HH-cΓ direct transitions. Analogously, a shoulder at low energy appears in the part of the spectrum originating from indirect transitions, also in this case due the different energies of the transitions involving HH or LH valence states.

To conclude this Section, we mention some further effects that we plan to include in the code. First of all, we are implementing the self-absorption correction to the spectrum. This effect is due to the fact that, when the light is emitted within the sample, it is typically reabsorbed by the material itself before reaching the surface and escaping from the sample. The PL spectrum is significantly altered by this effect, mainly because the direct-gap emission is much more affected by the self-absorption than the indirect-gap emission.

A second effect to be included is the recombination rate due to the localized donor levels; since we typically consider systems with very large doping density, this recombination channel may be relevant.

Then, the absorption due to the free carriers must also be included. In fact, in the samples that are typically considered, the density of free electrons is very large: these

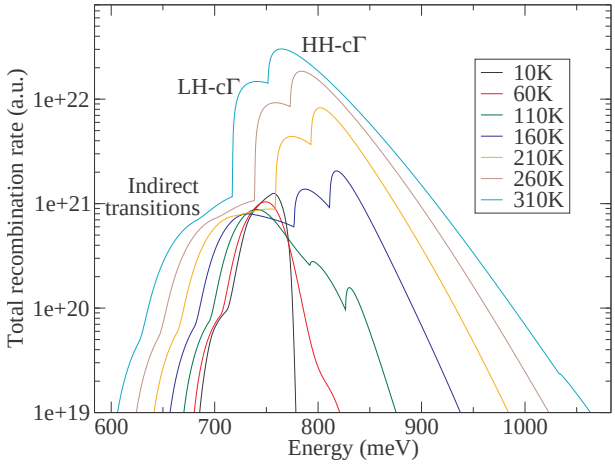


**Figure 4.12** – Temperature dependence of the total recombination rate for a 0.5% tensile-strained Ge bulk with $1 \cdot 10^{18}$ cm$^{-3}$ $n-$type doping and an optical pumping that induces a charge of $5 \cdot 10^{18}$ cm$^{-3}$.

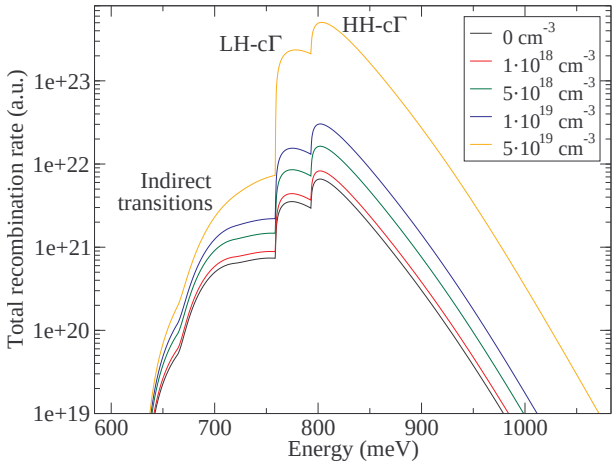


**Figure 4.13** – Doping dependence of the total recombination rate for a 0.5% tensile-strained Ge bulk under optical pumping that induces a charge of $5 \cdot 10^{18}$ cm$^{-3}$, at $T$ = 210 K.

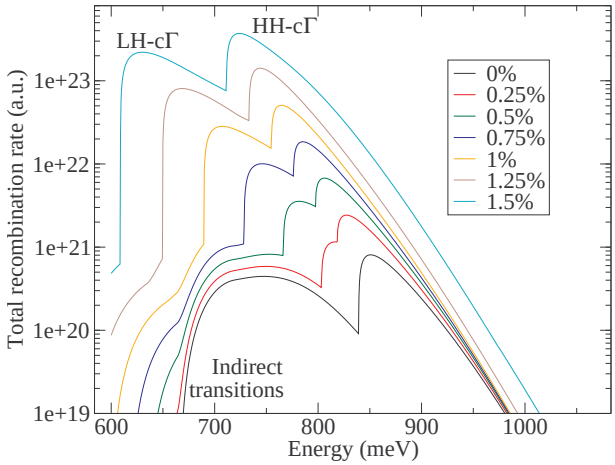


**Figure 4.14** – Strain dependence of the total recombination rate for a tensile-strained Ge bulk with $1 \cdot 10^{18}$ cm$^{-3}$ $n-$type doping and an optical pumping that induces a charge of $5 \cdot 10^{18}$ cm$^{-3}$, at $T$ = 210 K.

electrons can absorb the emitted light and then constitute a large loss mechanism. This must be taken into account especially if we are interested in obtaining a system with positive gain that can lead to laser action. We mention that formulae to fit the absorption due to free carriers are available in the literature (see for instance Ref. [128]).

Finally, the code has been developed with the idea of considering also quantum well systems, so that all data structures are ready to be generalized to this case. From a physical point of view, the generalization to such systems requires to analyze how all the calculated quantities change when we consider a two-dimensional system.

## 4.6 Annealing procedure to increase the tensile strain

The maximum strain that can presently be achieved with the thermal mismatch technique is not large enough to shift the lowest $LH_1$–$c\Gamma_1$ transition of Ge/SiGe MQW structures within the C-band. In Ref. [154] we investigated the possibility of increasing the (tensile) strain of Ge/SiGe MQW samples by means of a post-growth Rapid Thermal Annealing (RTA), and we interpreted the effects of this procedure on the direct-gap transitions. Indeed, the RTA allows to partially increase the tensile strain of the system. However, besides the redshift due to this strain increase, another effect had to be taken into account: in fact, if the annealing is performed after the heterostructure growth on the strained substrate, there can be a significant interdiffusion of Si atoms from the SiGe barriers in the Ge MQWs, which is detrimental for the device operation and moreover produces a blueshift of the bandgap. Actually, the results of the experiments can be interpreted only if interdiffusion is taken into account, and indeed the joint effect of the increased strain and of interdiffusion produces a net blueshift of the QW gap, as we discuss in this Section.

For what concerns the experimental part, we summarize here only the most relevant aspects and refer the reader to Ref. [154] for further details. The 10-period Ge/SiGe MQW heterostructures and 2 µm Ge-on-Si virtual substrate were grown using low-energy plasma-enhanced chemical vapor deposition [155].

X-Ray Diffraction (XRD) measurements give nominal barrier and QW widths of 8.8 nm and 17.6 nm, respectively. The $Si_{1-x}Ge_x$ barrier composition is determined as $x = 0.87$, whereas the QWs are of pure Ge ($x > 99\%$). In order to enhance the tensile-strain, a series of post-growth RTA samples was prepared between 650 °C and 850 °C in an inert-atmosphere oven. The sample chips were held at their maximum temperature for 30 s (5 s and 1 s for "flash-annealed" samples) and cooled at 28 °C/s (from 850 to 650 °C), limited by the thermal inertia of the oven.

Fig. 4.15 shows the transmission-spectrum (and first-derivative) of the as-prepared MQW sample, together with the first-derivative spectra of a series of annealed samples. The sharp features below 800 meV are due to the absorption edges of the bulk Ge-on-Si virtual substrate, in particular for the transitions at Γ between the light-hole valence band and the lowest conduction band (LH–cΓ), and from the

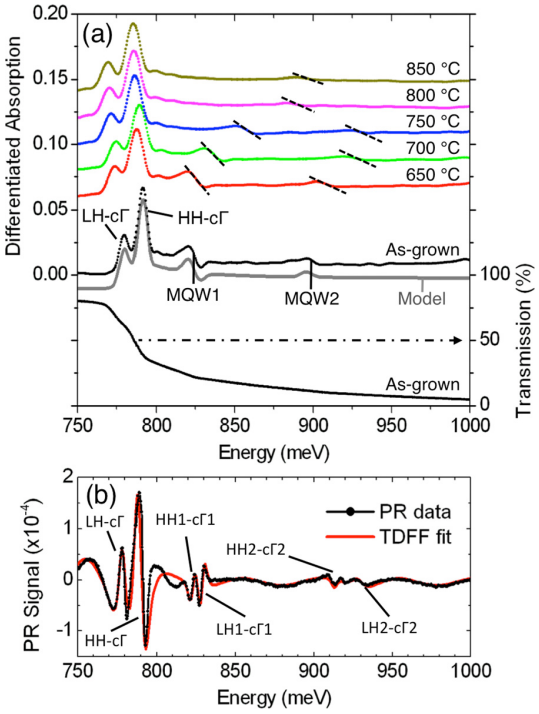


**Figure 4.15** – (a) Brewster-geometry transmission spectrum of the as-prepared sample, and first-derivative of transmission spectra of the as-prepared sample and of the annealed samples (annealing time of 30 s). The lineshape is fitted to a qualitative model to extract the MQW1 and MQW2 transition energies (see text). (b) Photoreflection spectrum of the as-prepared sample, clearly resolving individual light/heavy-hole transitions in MQW1 and MQW2. The PR-spectrum is fitted by a TDFF model to extract the LH/HH transition energies.

heavy-hole valence band to the conduction band (HH–cΓ). We remind here that for tensile strain fields, LH states are above HH states at Γ (see Figs. 1.15 and 1.16) and thus the LH-cΓ transition has a lower energy than the HH-cΓ transition. For moderate in-plane strain, the LH–HH splitting is proportional to the biaxial tensile-strain of the virtual substrate ($\varepsilon_{\parallel}$) and in particular it holds [156]

$$E_{\mathrm{LH}} - E_{\mathrm{HH}} = (6700 \pm 50)\,\mathrm{meV} \cdot \varepsilon_{\parallel}. \tag{4.2}$$

Without post- growth RTA, the VS biaxial tensile-strain (as deduced from transmission measurements) is 0.17%; this was independently verified using XRD rocking-curve measurements, which gave $\varepsilon_{\parallel} = 0.16 \pm 0.01\%$. The coherent growth of the Ge/SiGe MQWs was verified by XRD reciprocal space map measurements, i.e. they also have the same 0.17% tensile strain. Two quantum-confined direct-gap transitions can be resolved in the first-derivative spectra, and using the TB model described in Sec. 1.2, they can be attributed to the superposition of LH1/HH1–cΓ1 transitions, termed "MQW1", at $(824 \pm 1)$ meV, and to the superposition of LH2/HH2–cΓ2 transitions, termed "MQW2", at $(895 \pm 3)$ meV, with a dominant contribution from the LH transitions. Note that for this calculation for the as-grown samples, we assumed perfectly sharp interfaces. In fitting the experimental lineshape of the first-derivative spectra, MQW1 and MQW2 are reproduced by including an exciton feature in addition to the expected 2D band-to-band transition. For the only aim of the fit of the experimental data, this simple model uses *erf*-functions for the 2D band-to-band transitions and a Gaussian peak for the exciton feature.

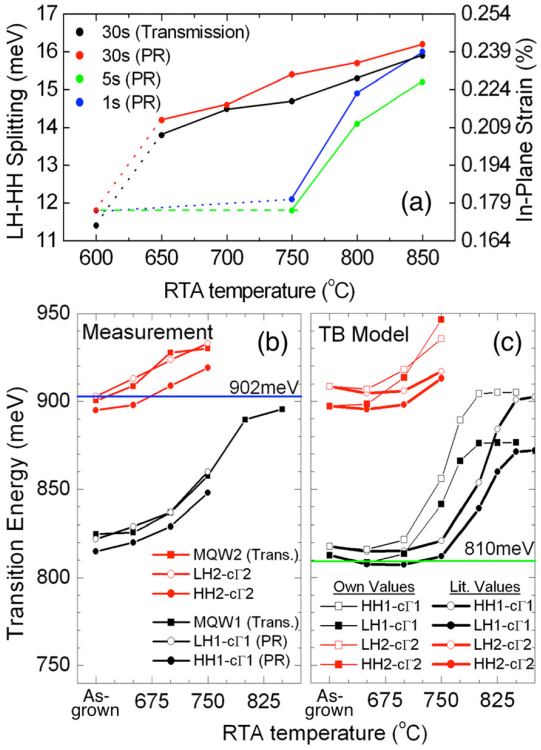


**Figure 4.16** – (a) LH–HH splitting from transmission and PR data, and the corresponding in-plane biaxial strain of the VS, as a function of the annealing time and temperature. (b) Transmission and PR determinations of MQW1 (LH1/HH1–cΓ1) and MQW2 (LH2/HH2–cΓ2) transition energies, as a function of the annealing temperature, with annealing time of 30 s. (c) TB calculations of the LH1/HH1–cΓ1 and LH2/HH2-cΓ2 transitions, taking the linear diffusion constants from both the literature and the XRD determination from the samples.

In Fig. 4.15b we show the photoreflectance (PR) spectrum of the as-prepared sample. In contrast to the transmission measurements, this technique is able to resolve also the LH–HH splitting of the quantum-confined MQW1 and MQW2 transitions (in addition to the bulk splitting of the virtual substrate). After accounting for the thin-film interference of the Ge-on-Si VS, the PR spectrum can be fitted using the third-derivative functional form model [157] including the contribution of excitons, and 3D and 2D band-to-band transitions (note that an exciton feature is needed to properly fit the MQW1 transition).

The transmission spectrum of the as-prepared sample gives the MQW1 transition at $(824 \pm 1)$ meV, and PR of the same sample resolves the HH1–cΓ1 transition at $(819 \pm 1)$ meV. This indicates that the strained Ge/SiGe MQWs have an exciton feature just 9–14 meV from the infrared telecommunication C-band (Erbium window: 810–792 meV). An exciton feature so close to the C-band is already of technological interest, because the absorption band can be fully shifted into the band using moderate Stark-effect tuning fields [158]. The possibility of redshifting this exciton feature further into the C-band motivated this study and in particular the investigation of the annealed samples.

As expected, RTA increases the strain of the MQWs, in particular from 0.17% to 0.24% as deduced from the LH–HH splitting using Eq. (4.2), see Fig. 4.16a, and redshifts the Ge-on-Si VS bulk absorption edges. However, both MQW1 and MQW2 transitions experience a blueshift, as shown in Fig. 4.16b, even for the lowest annealing temperature of 650 °C. In the annealed samples, MQW1 and MQW2 can be resolved

up to 750 °C, but after 800 °C only a single feature at 895 meV in transmission is observed. This is very close to the 902 meV direct gap of the strained $Si_{1-x}Ge_x$ ($x$ = 0.96) alloy given by the weighted stochiometric mix of QWs and barriers.

The net blueshift of MQW1 away from the C-band is explained by annealing-induced interdiffusion between the barriers and the QWs. We have used the numerical model for the evaluation of the interdiffusion process described in Sec. 1.11, starting with the as-prepared profile (assuming sharp interfaces, periodic boundary conditions, fixed nominal layer dimensions and barrier composition). For the annealed samples, alloy interdiffusion is calculated using two sets of temperature-dependent linear diffusion constant values: the first set is extrapolated from the literature [59], while the second set is obtained from the XRD measurements on the experimental samples, under the assumption of coherent growth of the MQWs without relaxation of the in-plane tensile strain. In particular, we assume a constant in-plane lattice parameter for each sample, deduced from the LH-HH splitting of the bulk virtual substrate.

The evaluated concentration profiles after the annealing and interdiffusion process are shown in Fig. 1.20. These profiles are then used to calculate the relevant interband electronic states by means of the TB code, which was suitably adapted to accept as input a generic concentration profile as described in Sec. 1.11. The calculated transition energies are shown in Fig. 4.16c. Comparing this panel with Fig. 4.16b, we can see that both the transition energies and the general trend of the blueshift of MQW1 and MQW2 are correctly reproduced.

The measured onset of interdiffusion (taken as the first net blueshift of the transitions) occurs at 650 °C when using our own XRD-determined diffusion constant, whereas the model based on literature values predicts 700 °C. The stronger-than-expected diffusion was experimentally verified by XRD analysis of the first superlattice (SL) satellite peak [159] and the SL signal reduction is found to be a factor of 5.5 times stronger than the existing literature values, equivalent to a 50 K temperature shift. It should be noted that reported values of the linear diffusion constant for Ge/SiGe MQWs can vary by 50 K (see Refs. [59, 160]). The model based on our own XRD-determined diffusion constant gives a better agreement, but still predicts a modest redshift of MQW1, which could however easily be offset by the natural variation of QW thickness in different chips cut from the same wafer. Note also that the TB calculations reported in Fig. 4.16c only include the difference between energy states at the Γ point of the BZ for MQW1, or at the BZ boundary along the growth direction for MQW2. Accounting for the $k_z$ band dispersion could bring the model and the experimental data into even better agreement.

In an effort to decouple the role of strain and interdiffusion, some chips were "flash-annealed" at their maximum temperature for just 1 s or 5 s. However, as shown in Fig. 4.16a, flash-annealing to below 800 °C does not increase the tensile strain, while annealing for even 1 s above 800 °C removes all traces of MQW features from the PR spectra.

The band structure calculations, using our XRD-determined diffusion constant, are used to estimate the annealing-induced transition broadening due to the band

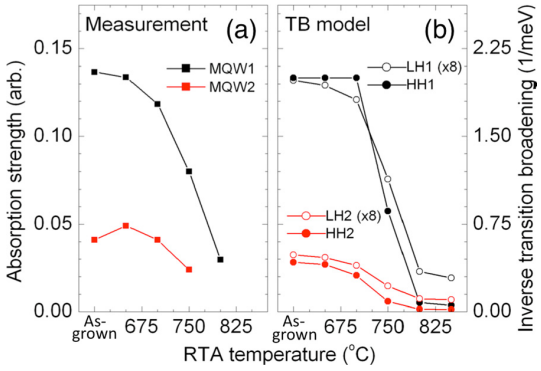


**Figure 4.17** – (a) Absorption strength of the MQW1 and MQW2 transitions, as determined from the transmission spectra. (b) The inverse transition broadening of the LH1/HH1-cΓ1 and LH2/HH2-cΓ2 transitions, as calculated from the TB model taking the linear diffusion constant from the XRD determination on the samples. For clarity, transitions involving LH states are scaled by a factor of eight.

dispersion along the growth direction. This dispersion is mainly due to the coupling of valence states confined in neighboring QWs and increases with the annealing temperature, since the height of the effective barrier is lowered for strongly interdiffused samples. Assuming a negligible dependence of the dipole matrix elements on $k_z$, the strength of the transmission features is expected to be inversely proportional to such broadening. This is clearly demonstrated in Fig. 4.17, where the measured MQW1 and MQW2 feature strength, and the calculated inverse of the band dispersion, differ only by a scaling factor.

In summary, quantum-confined direct-gap transitions have been clearly identified in 0.17–0.24% tensile-strained Ge/SiGe MQWs. The as-prepared MQWs have an exciton feature just 9–14 meV from the C-band edge. TB calculations are used to identify the different LH/HH transitions. RTA of the samples increases their strain, redshifting the VS absorption edges, but the quantum-confined transitions experience a net blueshift due to strong interdiffusion.

This study motivates a new investigation, where Ge/SiGe MQWs are grown directly onto 850 °C pre-annealed Ge virtual substrates, which could offer the strain needed for the LH1–cΓ1 transition to enter the C-band, eliminating the interdiffusion effects and the related blueshift.

## 4.7 Direct-gap $Si_n/Ge_m$ superlattices

In this Section, we discuss another possible strategy that could allow the realization of direct-gap group-IV light sources based on the exploitation of short-period Si/Ge superlattices [161]. In fact, intense research efforts during the Eighties and the Nineties have been devoted to the study of short period $Si_n/Ge_m$ superlattices as promising systems for band gap engineering, and in particular to address the physics of pseudodirect band gap systems (for a review see for instance Ref. [162]). As discussed below, also these kind of structures can display a direct gap, even if the physics that is at the basis of the direct gap is much different from the one of the systems that have been presented insofar. In fact, while in the previous Sections the direct gap was a mere consequence of the different deformation potentials of L and Γ valleys (so that a suitable strain — or a large enough doping — could fill of electrons

also the Γ valley and produce a population inversion), in the case of superlattices the direct gap is a consequence of the band folding and mixing due to the reduced symmetry, as we discuss below. A detailed discussion of folding effects in $Si_n/Ge_m$ SLs and the different respective space groups, which depend on the values of $n$ and $m$, can be found in the Appendix 4.A of this Chapter.

Structural properties of Si/Ge SLs have been theoretically investigated by means of first principle total energy [23,163,164] and valence force field [165] calculations and their electronic band structure has been addressed in the framework of pseudopotential [163,164,166–171], Kronig-Penney [172,173], and tight-binding (TB) [174–176] Hamiltonians. The accuracy of the theoretical results has often been limited by the indeterminacy affecting some relevant material parameters of the Si/Ge system, like the band offsets [23] or the deformation potentials. However, a quite general consensus was reached about the direct gap nature of $Si_n/Ge_m$ SLs grown along the [001] direction on Ge or Ge-rich substrates with period $n + m \geq 10$; for them non vanishing oscillator strengths (OS) of the band edge transitions were also predicted. In optimized Si/Ge SLs the estimated OS values were only one or two order of magnitude smaller than those measured in III-V direct gap semiconductors [170,171, 175,177].

On the experimental side, the impressive progresses in SiGe molecular epitaxy have made it possible the low-temperature growth of strain-symmetrized (ss) $Si_n/Ge_m$ SL samples on step-graded $Si_{1-x}Ge_x$ buffers with high crystalline quality, atomically sharp interfaces, very low defect density, large number of repetitions of the main period, and absence of strain relaxation (see Ref. [178] and references therein). A large amount of experimental data was thus collected through electro- and photoreflectance [172,179], photoluminescence [173,178,180–182], absorption [176,183,184], ellipsometry [185,186], electroluminescence [180], and photoconductivity [176] measurements.

From the above-mentioned results, it is well accepted that interband optical transitions in $Si_n/Ge_m$ strained SLs are to be interpreted in terms of direct transitions between zone-folded bands [187]. Of course these folded states are not merely equivalent to the bulk ones, since in the nanostructures their symmetry is modified by different perturbing potentials due to interfaces, inhomogeneous strain and confinement effects [171]. Under proper conditions, these symmetry modifications can guarantee a significant oscillator strength for the radiative transitions between conduction states folded at the Γ point and the topmost valence states.

To our knowledge, up to now no results have been reported on the possibility to reach positive optical gain in $Si_n/Ge_m$ SLs, in spite of the above-mentioned results and of the impressive efforts recently dedicated to the realization of laser action in Si/Ge based layers, as already discussed in the Introduction of this Chapter. We furthermore notice that PL results for short period $Si_n/Ge_m$ strained SLs [178,180,181] compare favorably with recent PL measurements [146] in tensile $n$-type Ge layers. In fact, as already discussed in Sec. 4.4, in Ref. [146] a room-temperature PL signal magnified by a factor of 20 in comparison with undoped germanium was obtained. On the other hand, in ss-$Si_6/Ge_4$ and $Si_9/Ge_6$ samples, low temperature PL peaks were found to

be enhanced by a factor of 150 and 90, respectively, when compared with the spectra of the corresponding $Si_{1-x}Ge_x$ equivalent alloys [178, 180, 181]. Moreover, room temperature strong electroluminescence in $Si_n/Ge_m$ systems due to band-to-band recombination was also demonstrated [180].

Motivated by the above considerations, we study in this Section the potential of $Si_n/Ge_m$ SLs as gain medium for optical amplification. Here, we assume coherently-grown and dislocation-free superlattices on fully relaxed substrates. The in-plane lattice constants of the Si and Ge layers are thus determined by the lattice constant of the buffer. The lattice spacing orthogonal to the interfaces is deduced from the macroscopic elasticity theory (see Sec. 1.3.2) which, as demonstrated by valence force field calculations (see Ref. [170] and references therein), can be safely applied also in this context where the single layers are only a few atoms thick. The equilibrium positions of the atoms in the Si and Ge layers are calculated accordingly. The Ge–Si bond lengths at the interfaces are set equal to the average of the Si–Si and Ge–Ge bond lengths in the corresponding strained layers [170,175].

In short-period superlattices, the atomistic details of the Si–Ge heterointerfaces can deeply affect the electronic and optical properties. It has been shown numerically that the presence of interface disorder or intermixing can increase the fundamental gap [174,188], modify the functional form of the absorption edge [174,188], reduce the oscillator strength of the pseudo-direct fundamental transition and, due to the breaking of the translation symmetry in the growth plane, produce allowed no-phonon transitions which involve folded states with $\Delta_{\|}$ symmetry [189]. On the other hand, due to the improvements of the growth processes, fabrication of quite ideal SLs was claimed [176,178]. In fact, X-ray diffraction spectra and Raman measurements demonstrated strong suppression of the Si–Ge interfacial vibrations [190]. For this reason in the present Section we discard disorder and intermixing effects and assume ideal sharp interfaces. As a consequence, appropriate periodic boundary conditions are applied along the growth direction and within each plane parallel to the interfaces.

For the description of the SLs electronic states and optical gain spectra, we adopt the $sp^3d^5s^*$ tight-binding Hamiltonian model with spin-orbit interaction described in Sec. 1.2. Here we use the self-energies and hopping integrals in the two-center approximation of Ref. [35] and Ref. [36] for Si and Ge, respectively. Scaling laws for the hopping parameters are taken from Refs. [16, 36]. For the valence band offset between the average of the valence-band edges in a strained $Si_{1-x}Ge_x$ and in a relaxed SiGe substrate, we adopt the formula of Eq. (1.37). Finally, optical properties are evaluated sampling the superlattice BZ so to fully take into account the strong non-parabolicities of the SL valence and conduction bands and the $k$-dependence of the optical matrix elements. The dipole allowed oscillator strengths for vertical transitions in the TB formalism and the low temperature material gain spectrum are calculated as described in Chap. 2. In particular, the quasi-Fermi levels are obtained from the injection carrier density and satisfy the appropriate charge neutrality condition, and the Lorentzian lineshape broadening $\gamma$ is set equal to 10 meV (see Ref. [180]). As refractive index $n_0$, we choose the static refractive index of the $Si_{1-x}Ge_x$ bulk alloy material with equivalent Ge concentration, calculated exploiting

**Table 4.1** – Superlattices investigated in the present paper. The buffers are made of pure Ge, or SiGe alloys with Ge content appropriate to obtain strain symmetrization (ss). Space groups, crystal system (OR=orthorhombic, T=tetragonal) and lattice kind (S=simple, BC=body centered) for each SL are reported. References of previous investigations are also shown.

| SL | Space group | System | Lattice | Refs. |
|---|---|---|---|---|
| $Si_2/Ge_{14}$ on Ge | $D^5_{2h}$ | OR | S | [177] |
| $Si_3/Ge_7$ on Ge | $D^9_{2d}$ | T | BC | [172] |
| ss-$Si_6/Ge_4$ | $D^{28}_{2h}$ | OR | BC | [173, 178, 191, 192] |
| ss-$Si_5/Ge_5$ | $D^9_{2d}$ | T | BC | [170, 175, 193] |
| ss-$Si_3/Ge_4$ | $D^{19}_{4h}$ | T | BC | [194] |

Eq. (1.35). Notice that only $k$-direct transitions are considered. We also stress that since no loss channels have been inserted in the model, the evaluated material gains have to be intended as an upper theoretical limit.

We limit our study to five short-period superlattices, which were chosen among a larger set of SL systems studied in the literature, selecting those that presented a direct gap with non-zero dipole moment for the lowest-energy transition. They are listed in Table 4.1 together with the corresponding space groups (for a discussion of the space groups, see Appendix 4.A of this Chapter). References of the main investigations of their electronic and optical properties are also reported.

Two of the studied SLs are grown on relaxed Ge substrates while the other three are ss-SLs grown on SiGe buffers. In all the investigated cases the Si layers are tensile strained due to the presence of germanium in the substrate while the Ge layers are relaxed (compressively strained) when grown on germanium (SiGe) buffers. We have thus (see also Sec. 1.3.6 and Fig. 4.18) that the minimum of the SLs conduction band edge profile occurs at the $\Delta_\perp$ minima in the Si layers while the topmost of the SLs valence band is at the $\Gamma$ point and lies in the Ge layers. It follows that the band gap alignment is of type II. This fact limits the thicknesses of the Si and Ge layers since, to achieve a robust oscillator strength for the direct gap recombination, the wavefunctions must have a significant overlap. As exemplificative cases, we report in Fig. 4.18 the band profiles evaluated for the ss-$Si_6/Ge_4$ SL, and for the $Si_3/Ge_7$ SL grown on a Ge relaxed buffer.

For what concerns the SL near-gap valence states, the energy difference of the heavy and light hole confined levels is determined by the interplay of the energy splitting of the HH and LH bands caused by the strain field, and the different confinement energies associated to the HH and LH quantum well profiles. For instance, in samples grown on Ge buffers, the HH and LH band edges in the Ge layer are degenerate and the height of the LH barrier in the Si layer is smaller than the HH one, due to the tensile strain. Therefore in ultrathin SL systems grown on Ge, since the large confinement energies associated to the small hole masses push both the HH and LH SL states close to the respective barrier energies, the topmost valence state can have light hole symmetry. This case is usually referred to as hole reversal.

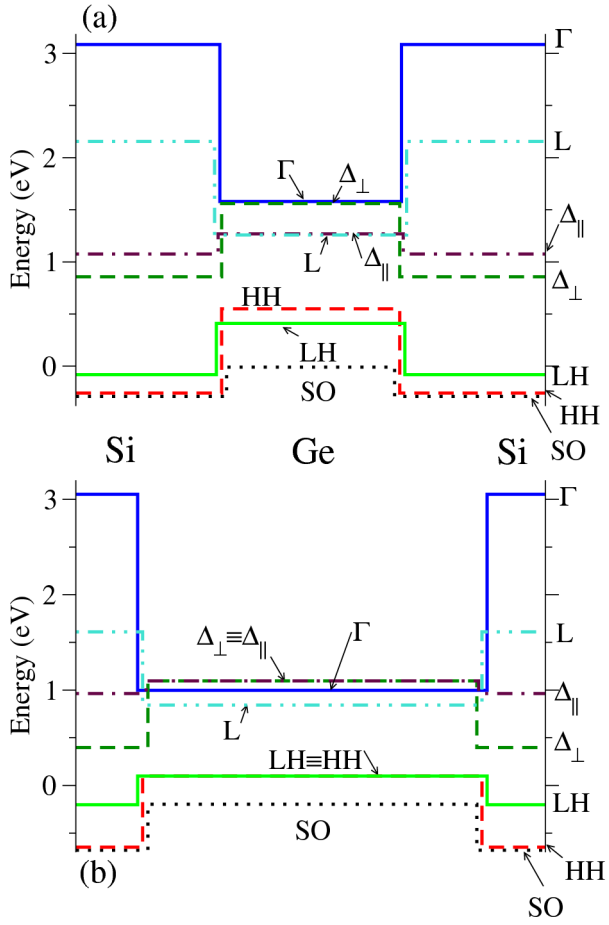


**Figure 4.18** – Band profiles of the ss-$Si_6/Ge_4$ SL grown on a $Si_{0.6}Ge_{0.4}$ relaxed substrate (top panel (a)) and of the $Si_3/Ge_7$ SL grown on a Ge relaxed substrate (bottom panel (b)). Note that the electronic degeneracies of the relaxed Ge layer in the $Si_3/Ge_7$ system are not present in the ss-$Si_6/Ge_4$ SL because of the strain field. The band gap alignments are of type II with electrons (holes) confined in the Si (Ge) regions. Here and in the following the zero of energy is set at the barycenter of the valence bands in the relaxed substrate.

On the other hand, when Si or Si-rich SiGe buffers are adopted, the topmost valence level usually has HH character because of the large HH–LH splitting in the Ge layers.

In short-period [001]-$Si_n/Ge_m$ SLs the L and Γ electrons are well above the bottom of the conduction band, since their light confinement masses push these states close to the energy of the respective barrier levels, i.e. the L and Γ band edges in the silicon layers (see Fig. 4.18). Thus one expects that the bottom conduction SL states originate from the $\Delta_\perp$ minima and are confined in the Si regions. Indeed, the tensile strain of the Si layers guarantees that the states resulting from the $\Delta_\parallel$ edges are at higher energies with respect to the $\Delta_\perp$ ones. Also confinements effects contribute to raise the energy of the SL $\Delta_\parallel$ states with respect to $\Delta_\perp$ ones since their confinement mass is lighter than the one associated to the $\Delta_\perp$ electrons. From the above considerations and since band folding occurs only along the growth direction, it follows that, to achieve a direct gap system, Ge-rich buffers must be adopted [163, 166, 168].

Another requirement to obtain direct gap systems was first put in evidence by Satpathy *et al.* [169] who demonstrated that for $Si_n/Ge_m$ SLs, upward dispersion of the lowest conduction band around the Γ point is obtained only for $n + m \geq 10$. This fact is a consequence of the position of the $\Delta_\perp$ minima in the $k$-space along the $\Gamma$–$X_\perp$ line.

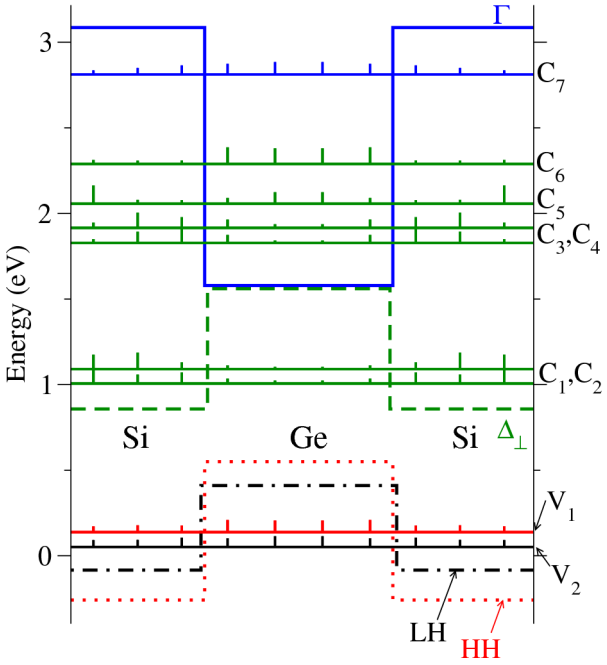


**Figure 4.19** – Square moduli (vertical bars) of the SL wavefunctions projected on each monolayer and related eigenvalues (horizontal lines), calculated at the Γ point for the valence and conduction near gap states of the ss-$Si_6/Ge_4$ SL. The HH, LH, $\Delta_\perp$, and Γ band edge profiles are also shown. The $C_1$–$C_6$ conduction states are $\Delta_\perp$ states folded into Γ; $C_7$ is the lowest genuine Γ state of the SL.

In SLs with shorter periods the $\Delta_\perp$ minima fold outside the Γ point. Therefore the conduction band at the zone center bends downward and the SL band gap remains indirect. Finally, also symmetry arguments have to be taken into account to select direct gap SLs with a dipole-allowed transition between the bottom conduction states and the topmost valence ones. In fact the SL space group is determined by the number of monoatomic layers in the Si and Ge regions [169,170,175]. In particular, if either $n$ or $m$ is even, there is a center of inversion. Either $n$ or $m$ must be odd for the existence of a fourfold axis perpendicular to the layers (tetragonal symmetry) since if this is not the case the projection on the growth plane of the Si–Ge bonds located at the interfaces of the Si and Ge regions are always oriented along the same direction (orthorombic symmetry) [170]. A complete symmetry analysis of $Si_n/Ge_m$ SLs and the indication of allowed dipole transitions for both TE and TM polarizations are reported in Refs. [169,170].

The near gap electronic levels in the conduction band at the Γ point of the SLs BZ can thus be classified as folded levels originating from the $\Delta_\perp$ states, or genuine Γ levels. As an example we show in Fig. 4.19 the near-gap wavefunctions for the ss-$Si_6/Ge_4$ system, calculated at the Γ point of the SL BZ. The $C_1$ (1006 meV) and $C_2$ (1091 meV) conduction levels originate from the folding of the two $k$-conjugate Γ–$X_\perp$ lines and the corresponding states extend mainly in the Si layers. We have verified that the amplitude of their wavefunctions are characterized by rapid oscillations with different phases, as it usually happens for couples of degenerate levels split by intervalley interaction [195]. Other couples of folded states are present at higher energies, above the $\Delta_\perp$ barrier level (see Fig. 4.19) and thus extend also in the Ge layers. The first genuine Γ state is $C_7$, about 1805 meV above $C_1$. Due to the light

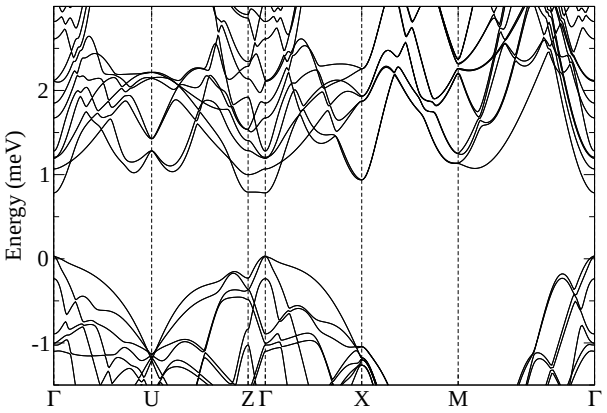


**Figure 4.20** – Electronic band structure of the $Si_2/Ge_{14}$ SL on Ge substrate. The high-symmetry points of the SL BZ are labeled according to Ref. [170].

confinement mass of electrons in this band, the $C_7$ energy is close to the Γ level of the bulk strained Si and it is only weakly confined in the Ge region. Also valence states $V_1$ and $V_2$ are weakly confined in the Ge layers and their character corresponds to the HH and LH bulk states, respectively. The poor confinement of the hole states is to be attributed to their masses which are lighter than the ones associated with $\Delta_\perp$ electrons. Accordingly, the hole miniband dispersion along the SL growth direction is expected to be significantly larger with respect to the bandwidth of the bottom conduction states.

After this brief discussion on the physics of the different states in Si/Ge SLs and of the main requirements that the SLs should satisfy in order to display a direct gap, we now present the results for the SLs listed in Table 4.1 concerning the optical matrix elements and the gain spectra in the low temperature limit, obtained for different injection levels and directions of the polarization vector. To this aim it is useful to briefly comment the electronic band structure of the SLs with reference to the case of the $Si_2/Ge_{14}$ SL grown on [001]-Ge buffer, reported in Fig. 4.20. We notice the direct fundamental gap at Γ. Direct fundamental gaps at the Γ point are obtained also for all the other investigated SLs (not shown). As discussed in the previous Section, the dispersion of the lowest conduction band along the Γ–Z line, corresponding to the growth direction, results to be much smaller with respect to the topmost valence band. The $Si_2/Ge_{14}$ crystal system is orthorhombic (see Table 4.1) and thus the two mutually orthogonal lines Γ–X and Γ–Y (Z–U and Z–T) within (at the boundary of) the SL BZ, which in real space correspond to two orthogonal directions in the growth plane, are not equivalent. The Γ–X and Γ–Y directions differ since the Γ–X line is orthogonal to the projection of the Si–Ge bonds on the interface plane, while the Γ–Y line is parallel. The same holds for the Z–U and Z–T directions, respectively. This fact is demonstrated in Fig. 4.21 where the band structures along the U–Γ–X and T–Γ–Y paths are compared.

To design direct-gap $Si_n/Ge_m$ SLs optimized for optical amplification, it is useful to understand the symmetry character of the SL states close to the bottom of the conduction band. These SL levels can be regarded as resulting from the superposition of bulk states with different $k_z$ vectors. It follows that the more effective is the SL

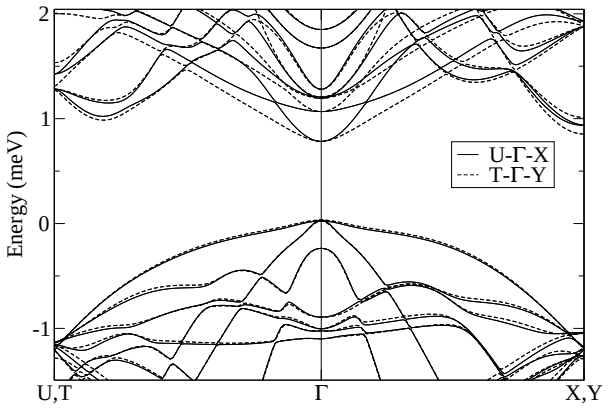


**Figure 4.21** – Comparison of the electronic band structure evaluated for the orthorhombic $Si_2/Ge_{14}$ SL on Ge substrate, along the non-equivalent U–Γ–X and T–Γ–Y paths.

**Table 4.2** – Optical matrix elements for the investigated SLs and for bulk Ge, evaluated at the Γ point for the transitions from the two topmost valence states $V_1$,$V_2$ to the lowest conduction level $C_1$. For orthorhombic SLs, the $\hat{x}$ ($\hat{y}$) in-plane direction is orthogonal (parallel) to the projection of the Si–Ge bonds on the interface planes. In the tetragonal SLs the in-plane projections of the Si–Ge bonds alternate between the $\hat{x}$ and $\hat{y}$ directions. $\hat{z}$ is along the growth axis. The dominant HH or LH character of the $V_1$ and $V_2$ states are also reported (see text). Units are chosen to set $|\langle \mathrm{HH}|p_x|c\Gamma_1\rangle|^2$ in bulk Ge equal to 100 as reference value.

| | $V_1$ | | | | $V_2$ | | | |
|---|---|---|---|---|---|---|---|---|
| system | $\lvert p_x\rvert^2$ | $\lvert p_y\rvert^2$ | $\lvert p_z\rvert^2$ | symmetry | $\lvert p_x\rvert^2$ | $\lvert p_y\rvert^2$ | $\lvert p_z\rvert^2$ | symmetry |
| bulk Ge | 100 | 100 | 0 | HH | 33.44 | 33.44 | 133.1 | LH |
| $Si_2/Ge_{14}$ on Ge | 4.422 | 0.483 | 3.408 | HH+LH | 0.524 | 8.920 | 3.151 | HH+LH |
| $Si_3/Ge_7$ on Ge | 0.305 | 0.305 | 2.438 | LH | 1.515 | 1.515 | 0.000 | HH |
| ss-$Si_6/Ge_4$ | 0.241 | 0.326 | 0.006 | HH | 0.041 | 0.739 | 0.152 | LH |
| ss-$Si_5/Ge_5$ | 0.438 | 0.438 | 0 | HH | 0.290 | 0.290 | 0.105 | LH |
| ss-$Si_3/Ge_4$ | 1.068 | 1.068 | 0 | HH | 0.634 | 0.634 | 0.739 | LH |

potential in mixing folded $\Delta_\perp$ states with genuine Γ ones, the larger is the oscillator strength (OS) associated with the radiative recombination across the fundamental direct gap. As discussed in the following, also the symmetry of the topmost valence state is relevant to determine the optical properties of the SLs. In fact, an important consequence of the hole reversal is the transfer of the OS from the TE (electric field perpendicular to the growth direction) to the TM (electric field parallel to the growth direction) polarization. The SL topmost valence level can also result from a strong hybridization of the heavy and light hole states. If this is the case, a significant OS for both the TE and TM modes is expected.

In Table 4.2 we report the square modulus of the optical matrix elements for the direct-gap transitions involving the two topmost valence states $V_1$,$V_2$ and the bottom conduction level $C_1$, calculated at Γ for two orthogonal TE polarizations and for the TM polarization. For comparison, we also report the optical matrix elements of the direct HH,LH→ $c\Gamma_1$ ($\Gamma_8^+ \rightarrow \Gamma_7^-$) transitions in bulk germanium, where a very modest biaxial compressive strain field has been applied along the [001] direction in order to separate the HH and LH contributions. Units are chosen so to obtain the

reference value 100 for the squared modulus of the TE component of the HH$\rightarrow c\Gamma_1$ transition in bulk Ge. In order to interpret the optical properties of $Si_n/Ge_m$ SLs, it is necessary to consider separately the tetragonal and orthorhombic structures. In fact, as mentioned before, if both $n$ and $m$ are even (orthorhombic symmetry) the projections of the Si–Ge bonds on the growth plane are aligned. As a consequence in-plane optical anisotropy in orthorhombic SLs can be evidenced for different TE polarizations. Indeed, as shown in Table 4.2, we obtain different optical matrix elements when the TE polarization vector $\hat{\mathbf{e}}$ is oriented perpendicular to the Si–Ge bonds ($\hat{x}$ direction) or along them ($\hat{y}$ direction). On the other hand, in the case of tetragonal SLs, the $\hat{x}$ and $\hat{y}$ components of the optical matrix element are equal because the Si–Ge bonds projections occur along both directions. The above results are also confirmed if we rotate the TE electric field by ±45 degrees with respect to the previous cases. In fact for both kind of symmetries the new directions are equivalent and accordingly we obtain equal optical matrix elements (not shown in Table 4.2).

In Table 4.2 we have indicated the dominant symmetry character of the $V_1$ and $V_2$ states. In the ss systems $V_1$ ($V_2$) has mainly HH (LH) character due to the presence of compressive strain in the Ge layers. On the other hand, hole reversal (LH on top) is obtained for the $Si_3/Ge_7$ SL grown on Ge. Finally, the topmost valence state in the $Si_2/Ge_{14}$ SL results from strong mixing of the HH and LH bulk states. The different behavior of the two latter SLs is to be attributed entirely to their geometrical differences since they have the same band edge profile. The HH or LH symmetry of the valence states accounts for the vanishing matrix optical elements along the $z$ axis reported in Table 4.2 and it is of help to interpret the relative strengths between parallel and orthogonal polarizations. The magnitude of the SL squared matrix elements given in Table 4.2 are one or two orders of magnitude smaller with respect to the direct transition in bulk Ge. The most robust OS for the $V_1 \rightarrow c\Gamma_1$ transition is obtained for the $Si_2/Ge_{14}$ SL with polarization vector in the growth plane. Robust OS is found also for the $Si_3/Ge_7$ system with polarization vector along the growth axis, since in this case the topmost valence state has LH symmetry.

Low temperature material gain spectra $g(\hbar\omega)$ evaluated for an injection level $n_{inj}$ equal to $7 \cdot 10^{18}$ cm$^{-3}$ in the TE mode with polarization vector along the $\hat{y}$ direction, and in the TM mode, are reported in Fig. 4.22a and Fig. 4.22b, respectively. The calculation of the gain spectra has been done as discussed in Sec. 2.2.2, according to the expressions (2.12), (2.13) and (2.14). For comparison, in Fig. 4.22 we also report $g(\hbar\omega)$ for bulk Ge, calculated at the same injection level and with the same transition broadening parameter. In this case the indirect L and Δ valleys of the conduction band have been intentionally neglected. Since the band structure of Ge in a neighborhood of the Γ point is similar to that of III-V compounds, the gain calculated for this "direct-gap" Ge system is comparable to that of a typical III-V direct bulk semiconductor. The magnitudes of the gain peaks in the studied SL systems are typically about one order of magnitude smaller than the value obtained for the the "direct-gap" Ge system. The largest gain value is found for the $Si_2/Ge_{14}$ SL in the TE polarization, and the positive portion of its gain spectrum consists of a single narrow peak with full width at half maximum of about 40 meV. For this

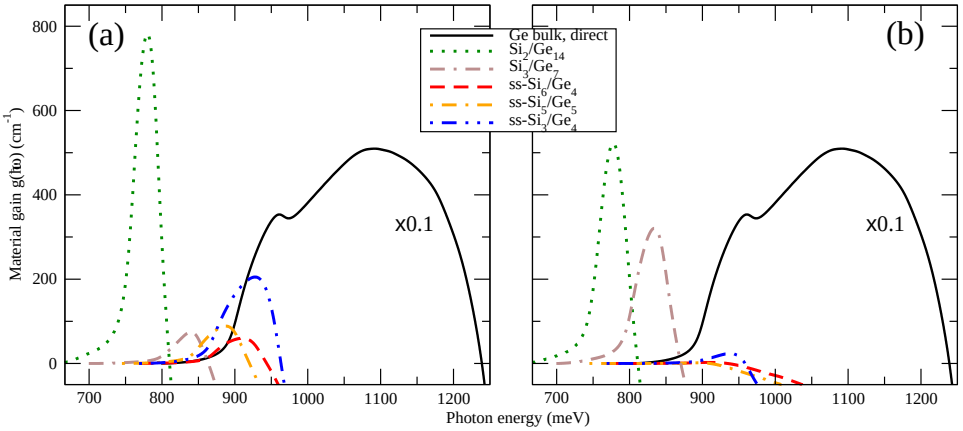


**Figure 4.22** – Material gain spectra, $g(\hbar\omega)$, of the investigated SL systems for the TE (panel (a)) and TM (panel (b)) mode, calculated for $n_{inj} = 7 \cdot 10^{18}$ cm$^{-3}$. In TE mode the polarization vector is set along the $\hat{y}$ direction (see text). For comparison, the gain spectra (scaled by a factor of ten) of an artificial (see text) Ge crystal with direct fundamental gap is also shown. For the latter system the two distinguishable features are related to the HH-LH energy separation of the active transitions with non vanishing $k$ vector.

system, in the TE mode we estimate a peak intensity of about 780 cm$^{-1}$, which is only a factor of 6 weaker than the Ge reference value. Robust gain is predicted also for TM polarization, due to the mixing of bulk HH and LH states in the almost degenerate V1 and V2 levels of the $Si_2/Ge_{14}$ SL (at this injection level, hole population extends in both the two topmost valence bands, their energy difference at Γ being 10 meV only). We stress that both in the TE and TM modes, the gain maximum is at about 780 meV, i.e. only 13 meV below the bottom of the erbium-window telecommunication band which is located at 793 meV (at this energy the TE gain is reduced to 533 cm$^{-1}$). Less pronounced but positive gain values are estimated also for the ss-$Si_3/Ge_4$ SL in the TE mode (205 cm$^{-1}$) and for the $Si_3/Ge_7$ SL grown on Ge buffer in the TM mode (322 cm$^{-1}$). The widths of the features shown in Fig. 4.22 are much narrower in SLs than in the "direct gap" Ge bulk system (note however that the inclusion of broadening effects associated to disorder in the SL could lead to the opposite result). We attribute this fact to the very different dispersions near the Γ point of the bottom conduction band in the SLs and in the bulk Ge system. In fact, in the investigated SLs there is negligible dispersion of the lowest conduction band along the growth direction (see e.g. Fig. 4.20); moreover along the in-plane directions the dispersion is governed by the transverse mass of the folded $\Delta_\perp$ electrons, which is about 10 times larger than the isotropic mass of the Γ electrons in Ge. For this reason the energy dispersion of the active transitions (positive gain contributions) are narrower in the SLs than in the considered Ge bulk system.

Gain spectra of the orthorhombic SL systems for TE incident radiation depend on the direction of the in-plane polarization vector, due to the optical anisotropy discussed above. This effect is demonstrated in Fig. 4.23 where the calculated TE

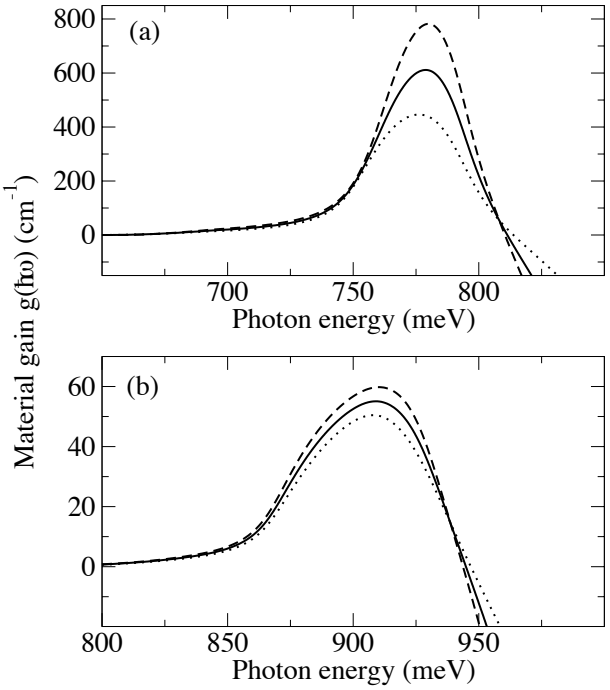


**Figure 4.23** – Material gain spectra $g(\hbar\omega)$ of the orthorhombic $Si_2/Ge_{14}$ (top panel (a)) and $Si_6/Ge_4$ (bottom panel (b)) SLs in the TE mode for $n_{inj} = 7 \cdot 10^{18}\,cm^{-3}$, evaluated for different directions of the polarization vector $\hat{\mathbf{e}}$ in the growth plane. Dashed (dotted) curve refers to $\hat{\mathbf{e}}$ parallel (perpendicular) to the direction of the Si–Ge bonds projected on the growth plane. The solid curve is obtained with $\hat{\mathbf{e}}$ lying in the growth plane at 45 degrees with respect to the in-plane projection of the Si–Ge bonds direction.

gain spectra of the orthorhombic $Si_2/Ge_{14}$ (top panel) and ss-$Si_6/Ge_4$ (bottom panel) SLs are shown for different directions of the in-plane polarization vector. We obtain larger gains when $\hat{\mathbf{e}}$ is along the projection of the Si–Ge bonds on the growth plane. It is for this in-plane direction of the oscillating field that the contribution to the optical matrix element arising from the mixed bonds is maximized. For the ss-$Si_6/Ge_4$ SL, the ratio between the maximum gain values obtained for $\hat{\mathbf{e}}$ parallel and orthogonal to the projection of the Si–Ge bonds on the growth plane is about 1.2 (see Fig. 4.23b). This value well agrees with the ratio of the corresponding square matrix elements for the $V_1 \rightarrow c\Gamma_1$ transition at the $\Gamma$ point reported in Table 4.2. In fact, for the considered injection value ($n_{inj} = 7 \cdot 10^{18}\,cm^{-3}$), the $V_2$ band edge is below the Fermi level and thus it plays no role. This is not true for the case of the $Si_2/Ge_{14}$ SL since the hole population extends also into the $V_2$ band whose edge is only 10 meV below the $V_1$ one.

Eventually, we address the dependence of the gain on the injected carrier density. Gain spectra for injection values $n_{inj}$ in the range $0.7 \cdot 10^{18}$–$7 \cdot 10^{18}\,cm^{-3}$ have been evaluated. In this regime, for all the investigated SLs the shape of the positive portion of $g(\hbar\omega)$ remains qualitatively stable, as reported in Fig. 4.24 where the gain of the $Si_2/Ge_{14}$ and $Si_3/Ge_7$ SLs for TE and TM polarizations are shown as examples. The peak value increases with $n_{inj}$ and its dependence from the injection level in the TE and TM modes is summarized in Fig. 4.25. Within the free carrier model of Eq. (2.12), we do not observe gain saturation in the investigated range of injection levels. In the TE mode, the $Si_2/Ge_{14}$ on Ge and the ss-$Si_3/Ge_4$ SLs reach the largest peak gain values, at about 800 and 200 $cm^{-1}$, respectively (see Fig. 4.25a). In the

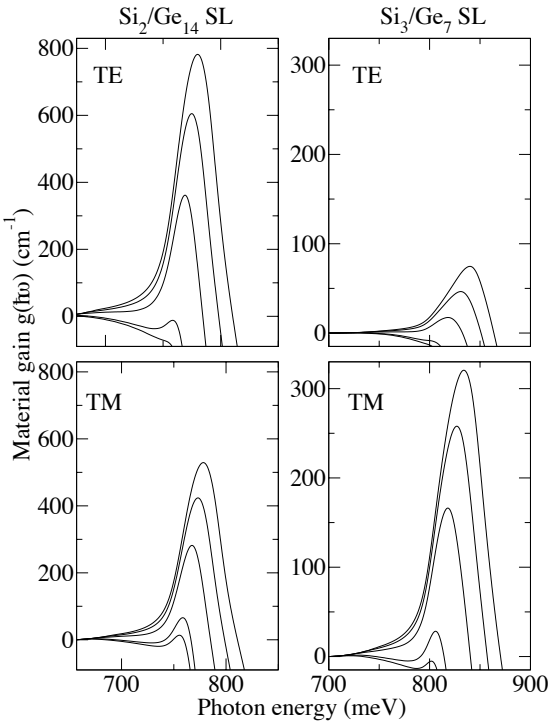


**Figure 4.24** – Material gain spectra $g(\hbar\omega)$ for the $Si_2/Ge_{14}$ (left plots) and the $Si_3/Ge_7$ (right plots) SLs, evaluated for injection levels $n_{inj}$ = 0.7, 1, 3, 5, and $7 \cdot 10^{18}$ cm$^{-3}$. Top and bottom panels refer to the TE and the TM mode, respectively. In the TE mode the polarization vector is along the $\hat{y}$ direction (see text). In each Figure the gain peak increases as $n_{inj}$ increases.

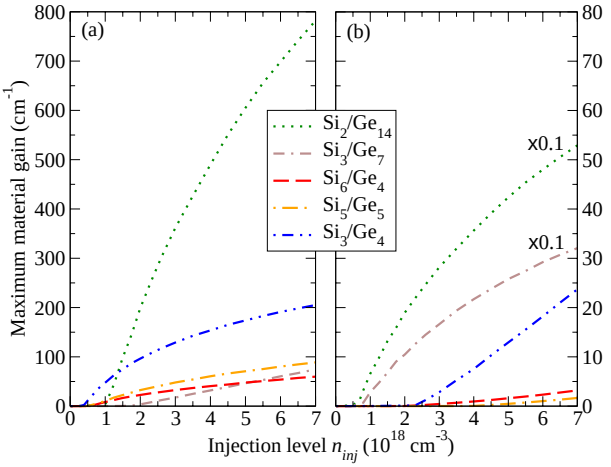


**Figure 4.25** – Maximum value of the TE (panel (a)) and TM (panel (b)) material gain spectrum as a function of the injected carrier density for the investigated SLs. In TE mode the polarization vector is along the $\hat{y}$ direction (see text). The gain of the $Si_2/Ge_{14}$ and $Si_3/Ge_7$ systems in the TM mode are scaled by 0.1. Note that the vertical scales of panels (a) and (b) are different.

TM mode, the largest values are observed for the $Si_2/Ge_{14}$ (~500 $cm^{-1}$) and for the ss-$Si_3/Ge_7$ (~300 $cm^{-1}$) systems. Note that different functional dependencies of the peak gain on $n_{inj}$ are obtained. Their interpretation is not immediate since a number of different factors are at work: among them the strong non-parabolicity of the bands, the $V_1$-$V_2$ energy separation, the HH-LH mixing and the $k$-dependence of the optical matrix elements. For instance we find a sublinear dependence behavior of the gain maximum in the TE mode (Fig. 4.25a), which is typical of quantum wells systems with direct gaps [64]. On the other hand, the ss-$Si_3/Ge_4$, ss-$Si_6/Ge_4$, and ss-$Si_5/Ge_5$ systems in the TM mode display a superlinear behavior of the peak values as function of $n_{inj}$ (see Fig. 4.25b). Since in the latter SLs the dominant character of the topmost valence level $V_1$ is HH, we attribute this superlinear behavior to the fact that the region in $k$ space where population inversion is achieved increases with $n_{inj}$, and on the same foot also the involved TM optical matrix elements becomes larger, due to the HH-LH mixing in the V1 states with $k \neq 0$.

In conclusion, we have provided a comparative investigation of some selected SiGe SLs which were indicated in the literature as possible direct gap materials. Their electronic band structure, optical matrix elements and material gain have been evaluated by means of a $sp^3d^5s^*$ tight-binding model. The role of buffer substrates, strain, band folding, charge injection level, SL symmetry due to the number of Si and Ge monolayers in the fundamental cell, has been analyzed in order to investigate the SL gain. Out of the studied samples we have obtained that the $Si_2Ge_{14}$ superlattice on [001] Ge buffer presents material gain which is only a factor 6 weaker than the gain of a typical direct gap material. Therefore these results indicate that well designed SiGe based SLs could be considered as suitable structures for light amplification in the infrared region, and call for further experimental investigations.

## 4.8 Conclusion of the Chapter

In conclusion, in this Chapter we have discussed critically different viable paths that could allow the realization of optically-active systems based on Si and Ge.

We have first shown the role of the strain in determining the relative position of the band edges in Ge bulk systems and Ge/SiGe heterostructures. We have shown that for large enough tensile strains, a direct-gap is obtained. In particular, we have calculated the gain spectra for strained Ge/SiGe MQWs, showing that this kind of system can provide very large gain coefficients. This large strain regime has however the disadvantage of shifting the direct-gap transition to about 500–600 meV, a region of the electromagnetic spectrum that is not interesting for long-range telecommunications. To circumvent this problem, we have discussed an approach recently presented in the literature, that adopts a modest tensile strain (shifting the transition energy within the C-band) and a large n-doping in order to fill the L valley and have some thermally-excited electrons in the Γ band. We have critically discussed whether this approach is suitable also in Ge/SiGe MQW systems, and how the physics behind this Γ population inversion mechanism can be investigated by means of electrolumi-

nescence and photoluminescence experiments. We have then presented a software that we are developing that calculates the photoluminescence spectra of Ge-based systems. This software can be used to interpret the experimental results and to predict and optimize the relevant parameters that can lead to light amplification in Ge. Subsequently, we have critically investigated the possible exploitation of thermal annealing procedures on Ge/SiGe MQW samples in order to increase the tensile strain and consequently redshift the lowest direct-gap transition within the C-band. We have shown how the competing interdiffusion mechanism produces however a net blueshift of the transition, and we have proposed a way to circumvent this problem. Finally, we have analyzed short-period superlattices as a different class of Si-based systems that can display a direct gap. We have discussed in detail the different physics that is at the origin of the direct gap. The gain spectra for different superlattices have been evaluated and we have identified five possible direct-gap candidates with positive gain coefficient.

## 4.A Appendix: Folding of the Brillouin zone and symmetries of SLs

We address in this Appendix the symmetry properties of $Si_n/Ge_m$ superlattices, their primitive cell in real space and the corresponding Brillouin zone in $k-$space. In the following, we denote with $z$ the growth direction [001], with $n$ the number of atomic monolayers of Si and with $m$ the number of atomic monolayers of Ge.

We start from the description of the symmetry properties of these lattices. Not all superlattices belong to the same symmetry group. The most important difference is if there exists a fourfold rotation symmetry around the $z$ axis, i.e. if the $x$ and $y$ directions are equivalent. In this case, the symmetry is called tetragonal. If instead this symmetry is not present, the symmetry is called orthorhombic. As we discuss below, the latter symmetry occurs only if both $n$ and $m$ are even. In this case, in fact, all mixed Si–Ge bonds are along the same direction, which is then different from the one rotated by $\pi/2$. In the case where at least one between $n$ and $m$ is odd, there exists instead a symmetry operation which leaves the system unchanged, consisting of a translation along $z$ plus a rotation of $\pi/2$ around $z$, and thus the symmetry becomes tetragonal. This can be better understood in Fig. 1.2, where the zincblende lattice together with first-neighbor bonds is shown: moving from one monolayer to the next one, the direction of the bonds between neighboring planes rotates of 90 degrees around $z$, so that an even number of Si and Ge monolayers (i.e., both $n$ and $m$ even) implies that the mixed Si–Ge bonds are always along the same direction.

Let us discuss independently all possible cases.

**$n$ and $m$ even** In this case, the cell is orthorhombic and the $x$ and $y$ directions are not equivalent. The effect on the band structure is shown for instance in Fig. 4.21 for a $Si_2Ge_{14}$ SL: the bands are different along two directions rotated of 90 degrees with respect to each other. Note that, in that Figure, the X and Y points are not along the [100] and [010] directions, but are instead defined as

$$X = \frac{\pi}{a}\left(\frac{1}{2}, \frac{1}{2}, 0\right), \qquad Y = \frac{\pi}{a}\left(-\frac{1}{2}, \frac{1}{2}, 0\right), \tag{4.3}$$

i.e. rotated of 45 degrees around $z$. In fact, in the case of $n$ and $m$ even, in the symmetry group there is also a glide symmetry whose glide vector[1] is on the $xy$ plane, at 45 degrees with respect to the axes, i.e. along one of the directions defined by the X and Y points of Eq. (4.3). That direction has higher symmetry and in particular there is a double degeneracy at the symmetry point X or Y that is located along the direction defined by the glide vector. Note that the glide plane is a plane orthogonal to $z$ at the center of a Si or Ge region (and since $n$ and $m$ are even, this plane does not contain any atom),

[1] A glide symmetry is the composition of the reflection about a plane followed by a translation $\mathbf{v}/2$ parallel to that plane. The glide vector $\mathbf{v}$ is twice the above-mentioned translation vector (in fact, applying twice the glide symmetry, we obtain a translation by the glide vector $\mathbf{v}$).

and the direction of the glide vector (towards the high symmetry point X or Y) depends on how we build the superlattice cell.

Moreover, we must consider the case $(n + m)/2$ even or odd. The final result is that, if $(n + m)/2$ is even, the unit cell is simple and the space group is $D^5_{2h}$, while if $(n + m)/2$ is odd, the unit cell is body-centered and the space group is $D^{28}_{2h}$ [170].

*n* **and** *m* **odd** Different is the case of $n$ and $m$ odd. In this case the symmetry is indeed tetragonal: we can in fact reflect the system about a plane at the center of a Si or Ge region (and since both $n$ and $m$ are odd, this plane contains Si or Ge atoms), and then rotate by 90 degrees around $z$. This is a symmetry of the superlattice and thus a fourfold rotational symmetry around $z$ exists.

Also in this case we must consider if $(n + m)/2$ is even or odd. The type of unit cell (simple of body-centered) is the same of the previous case, but the symmetry groups change (since here the group is tetragonal and not simply orthorhombic). If $(n+m)/2$ is even, the unit cell is simple and the space group is $D^5_{2d}$, while if $(n + m)/2$ is odd, the unit cell is body-centered and the space group is $D^9_{2d}$ [170].

*n* **even and** *m* **odd or viceversa** (i.e., $(n + m)$ odd). In this case, the unit cell has not a periodicity of $n + m$ but of $2(n + m)$: in fact, both the first and the last plane contain atoms of the same kind ("anions" or "cations") or, from another point of view, the atomic bonds between the last plane and the first one would not be correctly oriented along the vertices of a tetrahedron.

Doubling the cell, we recover a case similar to the one previously discussed with both $n$ and $m$ odd. The cell is thus always body-centered and tetragonal (the fourfold symmetry is given by a translation of $(n + m)$ monolayers in the $z$ direction followed by a rotation of 90 degrees around $z$). The space group is $D_{4h}$ (it is different from the previous case since we have now a lower number of symmetry operations) [170].

Note that the case $n = m = 1$ is special since it has more symmetries than all other cases and thus should be studied by itself. We do not address this special case here.

## Brillouin zones

Even if the unit cell is orthorhombic (i.e. the $x$ and $y$ directions are not equivalent), from a purely geometrical point of view the Brillouin zone is always tetragonal, since we are considering a biaxial strain with same strain components on the $xy$ plane. If we want to discuss only the shape of the Brillouin zone and the coordinates of its corners, we do not need to distinguish between the orthorhombic and the tetragonal cases. However, if we are concerned not only with the geometry of the lattice or of the Brillouin zone, but also with the the energy associated to a given $k$ point (or

with other similar properties of the crystal) we have to remember that the $x$ and $y$ directions are not equivalent, if both $n$ and $m$ are even.

We consider here only the case $n + m$ even: as we discussed in the previous section, if $n + m$ is odd the unit cell has actually to be doubled, and thus $2(n + m)$ is even and we can apply the same considerations that we make in the following.

In the following, we define as "layer" a couple of anion and cation planes; the number of layers within the supercell of a $Si_n/Ge_m$ SL is then given by $(n + m)/2$.

As we already mentioned before, we have two different possibilities, which generate different Brillouin zones, depending on the parity of $(n + m)/2$. We consider the two cases independently, after a short discussion of the standard FCC lattice.

**Standard FCC lattice**

Let us first consider the Brillouin zone of a FCC Bravais lattice. The real-space FCC lattice together with its primitive cell is shown in Fig. 1.1. This cell is the smallest possible and contains only one atom in the primitive cell (the one at the origin, for instance).

The lattice translation vectors $\tau_i$, $i = 1, 2, 3$ are given in the caption of Fig. 1.1. We want now to find the reciprocal-space translation vectors, i.e. the vectors $G_i$, $i = 1, 2, 3$ that satisfy

$$\tau_i \cdot G_j = 2\pi\delta_{ij}.$$

The simplest way to find them is to write the $\tau_i$ vectors in units of $a$ in the columns of a $3 \times 3$ matrix and to invert it; the columns of the inverted matrix are the components of the vectors $G_j$, in units of $2\pi/a$. We get

$$\tau = \begin{pmatrix} \frac{1}{2} & \frac{1}{2} & 0 \\ \frac{1}{2} & 0 & \frac{1}{2} \\ 0 & \frac{1}{2} & \frac{1}{2} \end{pmatrix} \Rightarrow G = \begin{pmatrix} 1 & 1 & -1 \\ 1 & -1 & 1 \\ -1 & 1 & 1 \end{pmatrix} \Rightarrow \begin{cases} \mathbf{G}_1 = \frac{2\pi}{a}(1, 1, -1) \\ \mathbf{G}_2 = \frac{2\pi}{a}(1, -1, 1) \\ \mathbf{G}_3 = \frac{2\pi}{a}(-1, 1, 1) \end{cases} . \tag{4.4}$$

These three vectors describe a BCC lattice, whose Brillouin zone (defined as the portion of space that is the nearest to a given lattice point than to any other) is shown in Fig. 1.3. Note that the boundaries of the BZ belong to planes that lie in the middle between two (reciprocal space) lattice points (this will be used later to calculate the coordinates of the vertices of the Brillouin zone).

**Superlattices with (n+m)/2 even**

In this case, we can obtain an "optimal" real-space unit cell (in the sense that it contains only $(n + m)/2$ layers in the supercell) using a tetragonal unit cell with one vector along $z$ (with length $a \cdot (n + m)/4$) and two vectors $\tau_1 = (\frac{1}{2}, \frac{1}{2}, 0)a$ and $\tau_2 = (\frac{1}{2}, -\frac{1}{2}, 0)a$ on the $xy$ plane. An example for the case $(n + m)/2 = 2$ is shown in Fig. 4.26. Since the real-space cell is a parallelepiped, also the reciprocal-space cell

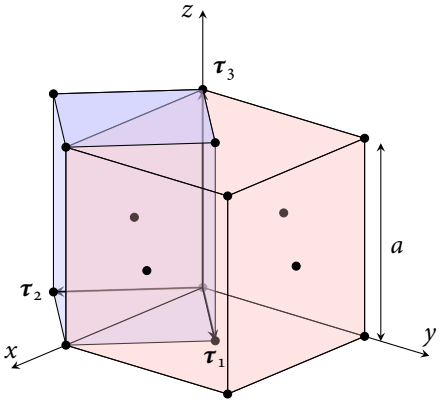


**Figure 4.26** – Real-space unit cell for the particular case $(n+m)/2 = 2$ (even). The points indicate the layers of the structure. The coordinates of the lattice translation vectors are

$$\tau_1 = \left(\frac{1}{2}, \frac{1}{2}, 0\right) a,$$
$$\tau_2 = \left(\frac{1}{2}, -\frac{1}{2}, 0\right) a,$$
$$\tau_3 = (0, 0, 1)\, a.$$

There are two atoms in the unit cell.

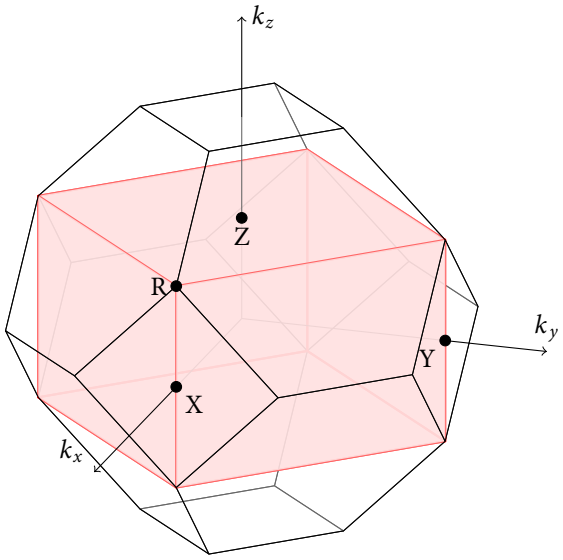


**Figure 4.27** – The Brillouin zone for a superlattice with $\frac{1}{2}(n+m) = 2$ (even) is shown in red. The Brillouin zone is a parallelepiped. The coordinates of some high-symmetry points are:

$$X = \frac{2\pi}{a}(1, 0, 0),$$
$$Y = \frac{2\pi}{a}(0, 1, 0),$$
$$Z = \frac{2\pi}{a}\left(0, 0, \frac{1}{2}\right),$$
$$R = \frac{2\pi}{a}\left(1, 0, \frac{1}{2}\right).$$

Note that these names are different from those used in Sec. 4.7.

is a parallelepiped, that can be obtained folding the BZ of the FCC lattice as shown in Fig. 4.27. Using the same method of Eq. (4.4), we get

$$\tau = \begin{pmatrix} \frac{1}{2} & \frac{1}{2} & 0 \\ \frac{1}{2} & -\frac{1}{2} & 0 \\ 0 & 0 & \frac{n+m}{4} \end{pmatrix} \Rightarrow G = \begin{pmatrix} 1 & 1 & 0 \\ 1 & -1 & 0 \\ 0 & 0 & \frac{4}{n+m} \end{pmatrix} \Rightarrow \begin{cases} \mathbf{G}_1 = \frac{2\pi}{a}(1, 1, 0) \\ \mathbf{G}_2 = \frac{2\pi}{a}(1, -1, 0) \\ \mathbf{G}_3 = \frac{2\pi}{a}\left(0, 0, \frac{4}{n+m}\right) \end{cases}.$$

### Superlattices with (n+m)/2 odd

In this case, we can obtain an "optimal" real-space unit cell (in the sense that it contains only $(n+m)/2$ atoms in the cell) using a face-centered unit cell similar to the case of a FCC lattice, but "stretched" along $z$, as shown for example for the case $(n+m)/2 = 3$ in Fig. 4.28. In this case, since the real-space cell is face-centered, the reciprocal-space cell is body-centered, as shown in Fig. 4.29. Using the same method

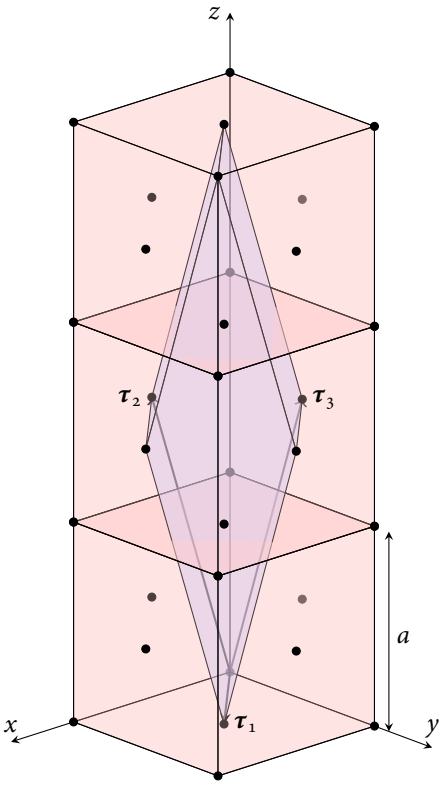


**Figure 4.28** – Real-space unit cell for the particular case $(n+m)/2 = 3$ (odd). The points indicate the layers of the structure. The coordinates of the lattice translation vectors are

$$\tau_1 = \left(\frac{1}{2}, \frac{1}{2}, 0\right) a,$$
$$\tau_2 = \left(\frac{1}{2}, 0, \frac{3}{2}\right) a,$$
$$\tau_3 = \left(0, \frac{1}{2}, \frac{3}{2}\right) a.$$

There are three atoms in the unit cell.

of Eq. (4.4), we get

$$\tau = \begin{pmatrix} \frac{1}{2} & \frac{1}{2} & 0 \\ \frac{1}{2} & 0 & \frac{n+m}{4} \\ 0 & \frac{1}{2} & \frac{n+m}{4} \end{pmatrix} \Rightarrow \begin{cases} \mathbf{G}_1 = \frac{2\pi}{a}(1, 1, -\frac{2}{n+m}) \\ \mathbf{G}_2 = \frac{2\pi}{a}(1, -1, \frac{2}{n+m}) \\ \mathbf{G}_3 = \frac{2\pi}{a}(-1, 1, \frac{2}{n+m}) \end{cases} . \tag{4.5}$$

## Final results

In the limit $\frac{n+m}{2} \to \infty$, both cases converge to the same BZ, i.e. a square in the $k_x k_y$ plane. In this limit, it is difficult to distinguish between the two cases $(n+m)/2$ even or odd.

The coordinates of the edges of the BZ reported in Figs. 1.3, 4.27 and 4.29 have been calculated as already said considering the intersections of the planes lying in the middle between two reciprocal lattice points. Calling **b** a reciprocal-space lattice vector, the plane orthogonal to **b** that goes through **b**/2 has equation

$$b_x k_x + b_y k_y + b_z k_z = \frac{\|\mathbf{b}\|^2}{2}. \tag{4.6}$$

Using this expression and knowing the coordinates of the reciprocal lattice vectors obtained previously, one can easily obtain the coordinates of the corners of the BZ also for the general cases.

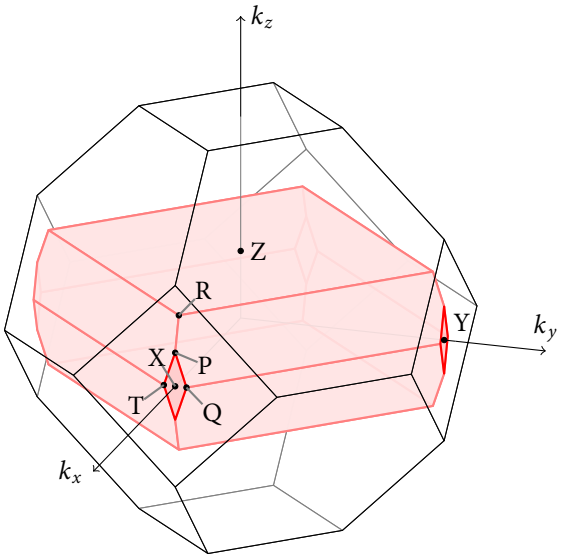


**Figure 4.29** – The Brillouin zone for a superlattice with $\frac{1}{2}(n+m) = 3$ (odd) is shown in red. The reciprocal lattice is body-centered and the Brillouin zone is a truncated octahedron (same topology of the usual Brillouin zone of a FCC direct lattice, but distorted). The coordinates of some high-symmetry points are (the names of the points are not standard):

$$X = \frac{2\pi}{a}(1,0,0), \quad Y = \frac{2\pi}{a}(0,1,0), \quad Z = \frac{2\pi}{a}\left(0,0,\frac{1}{3}\right),$$
$$P = \frac{2\pi}{a}\left(1,0,\frac{1}{6}\right), \quad Q = \frac{2\pi}{a}\left(1,\frac{1}{18},0\right), \quad R = \frac{2\pi}{a}\left(\frac{17}{18},0,\frac{1}{3}\right),$$
$$T = \frac{2\pi}{a}\left(1,-\frac{1}{18},0\right).$$

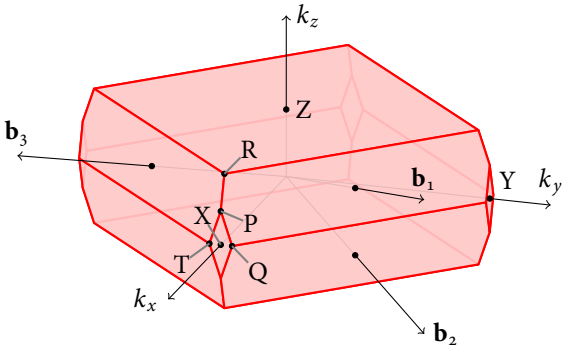


**Figure 4.30** – Brillouin zone for a superlattice with $\frac{1}{2}(n+m) = 3$ together with reciprocal lattice translation vectors. The coordinates of the vectors $\mathbf{b}_i$ are:

$$\mathbf{b}_1 = \frac{2\pi}{a}\left(1,1,\frac{1}{3}\right),$$
$$\mathbf{b}_2 = \frac{2\pi}{a}\left(1,1,-\frac{1}{3}\right),$$
$$\mathbf{b}_3 = \frac{2\pi}{a}\left(1,-1,\frac{1}{3}\right).$$

As an example, let us compute the coordinates of the points P, Q, R and T in the case $(n+m)/2$ odd (see Figs. 4.29 and 4.30 for the case $(n+m)/2 = 3$).

We choose as vectors $\mathbf{b}_i$ the vectors

$$\mathbf{b}_1 = \frac{2\pi}{a}\left(1, 1, \frac{2}{n+m}\right),$$
$$\mathbf{b}_2 = \frac{2\pi}{a}\left(1, 1, -\frac{2}{n+m}\right),$$
$$\mathbf{b}_3 = \frac{2\pi}{a}\left(1, -1, \frac{2}{n+m}\right).$$

which are linear combinations of the $\mathbf{G}_i$ reciprocal lattice translation vectors obtained in Eq. (4.5).

In Eq. (4.6), for simplicity, we define both $\mathbf{b}_i$ and the coordinates of a given $k-$space point $(k_x, k_y, k_z)$ in units of $2\pi/a$ (the equation remains the same). For all $\mathbf{b}_i$ vectors, we have

$$\frac{\|\mathbf{b}_i\|}{2} = \frac{(n+m)^2+2}{(n+m)^2}.$$

For the point Q, for instance, (see also Fig. 4.30) we study the intersection of the planes orthogonal to $\mathbf{b}_1$ and $\mathbf{b}_2$:

$$\begin{cases} k_x + k_y - \frac{2}{n+m}k_z = \frac{(n+m)^2+2}{(n+m)^2} \\ k_x + k_y + \frac{2}{n+m}k_z = \frac{(n+m)^2+2}{(n+m)^2} \end{cases}.$$

Summing and subtracting the two equations, we get $k_z = 0$ and $k_x + k_y = \frac{(n+m)^2+2}{(n+m)^2}$. Since, moreover, we know that all the points P, Q, T, X have $k_x = 1$ (it is the plane orthogonal to $\mathbf{b}_2 + \mathbf{b}_3$), we get

$$Q = \frac{2\pi}{a}\left(1, \frac{2}{(n+m)^2}, 0\right)$$

and similarly for point T one gets

$$T = \frac{2\pi}{a}\left(1, -\frac{2}{(n+m)^2}, 0\right).$$

With the same method one can obtain

$$R = \frac{2\pi}{a}\left(\frac{(n+m)^2-2}{(n+m)^2}, 0, \frac{2}{n+m}\right)$$

and

$$P = \frac{2\pi}{a}\left(1, 0, \frac{1}{n+m}\right).$$

# Appendices

# Appendix A

# Further addressed topics

In this Appendix, I briefly summarize other topics that I have addressed during my Ph.D., using methodologies similar to those discussed in the main part of the Thesis, or which also focus on SiGe systems, but that are not strictly related to the main topic concerning multilayer structures.

In particular, in Sec. A.1 the electronic states of SiGe rolled-up nanotubes are discussed, focusing in particular on the valley splitting at Γ and on the degeneracy lifting of the different valleys. The results of this work partially originate from a visiting period at the IFW Leibniz Institute in Dresden, directed by Prof. O. G. Schmidt. In Sec. A.2, visible-light emission from porous silicon is addressed, with a numerical study of the oscillator strength of the lowest-energy transition, and of the influence of porosity on the emission energy. Finally, in Sec. A.3 the effects of a vertical magnetic field on intersubband polaritons in MQW structures is discussed, with particular attention to systems composed of materials which display a large band non-parabolicity; this work has been done during an internship at the École Normale Supérieure in Paris, under the supervision of Prof. G. Bastard and Prof. R. Ferreira.

## A.1 SiGe rolled-up nanotubes

In the last years, significant research efforts have been oriented towards the exploitation of curvature effects to tailor the mechanical, electronic, transport and optical properties of different classes of nanostructures, as carbon nanotubes [196, 197], nanocorrugated thin films [198–203], and rolled-up nanotubes [204–208]. In particular rolled-up nanotubes, originating from the self-scrolling of a differentially stressed film when released from a substrate, have recently proven to be particularly promising for the design of new functional devices [207–214].

We briefly summarize in this Section the results presented in Ref. [215], where we have studied the electronic structure of Si/Ge rolled-up nanotubes in the whole conduction band, comparing it with the one of corresponding planar slab structures. As discussed in Ref. [215], the main features of the lowest conduction bands originate from the bulk band structure in terms of folding, strain and confinement effects. On this basis, the lifting of the degeneracy of the $\Delta$ valleys along the different directions in $k$-space has been explained. We have shown that the valley splitting (VS) interaction of the lowest conduction states is influenced by the curvature. This VS effect is due to the interface or the confining potential, that produce a coupling between states which are degenerate in the bulk. The study of the VS has a long-lasting story since the first measurements in Si inversion layers [216], followed by studies in quantum well and superlattice structures [195, 217–222] and, more recently, in other low-dimensional structures, as for instance quantum dots [223].

In Fig. A.1a a sketch of a typical $\mathrm{Si}_{N_{\mathrm{Si}}}/\mathrm{Ge}_{N_{\mathrm{Ge}}}$ rolled-up tube is reported. By choosing the unit cell of Fig. A.1b, we are assuming perfect periodic conditions not only for translations of integer multiples of $a_z$ along the $z$ axis, but also for rotations of integer multiples of $\theta_0 = 2\pi/N_\theta$ around the $z$ axis ($N_\theta$ gives the number of cells along $\theta$). To clarify how this structure is obtained, we show in Fig. A.1c the bulk unit cell of a Si or Ge crystal, from which the cell of Fig. A.1b can be obtained. The atomic positions are calculated minimizing the total elastic energy of the system exploiting the linear continuum elasticity theory (CET) for the curved geometry [224, 225], taking the relevant parameters (elastic constants and lattice constants) from Ref. [22].

Fig. A.2a shows the BZ of the (minimal) diamond-lattice primitive cell and its folding when we instead consider the conventional cell of Fig. A.1c. In the case of a planar slab with finite thickness in the $x$ direction (i.e., an "unrolled" tube), the corresponding BZ then further folds into the $yz$ plane, reducing to the dark rectangle of Fig. A.2b. Similar considerations also apply for the tube geometry, and the BZ in the $(k_\theta, k_z)$ space is again the rectangle sketched in Fig. A.2b. To illustrate the folding of the $\Delta$ states in the case of a finite slab or a tube with periodicity along $y \equiv \theta$ and along $z$ we show in Fig. A.2c the corresponding ellipsoids of constant energy. It is then apparent that the four $\Delta_\theta$ and $\Delta_z$ minima remain unfolded, while the two conjugated $\Delta_\rho$ valleys fold at $\Gamma$. Due to the different confinement masses and strains along the $z$ and $\theta$ direction, we expect for the lowest CB of the tube a structure similar to that schematically shown in Fig. A.2d; note the VS doublet at $\Gamma$ due to the interaction of the two $\Delta_\rho$ valleys (for a more detailed description we refer

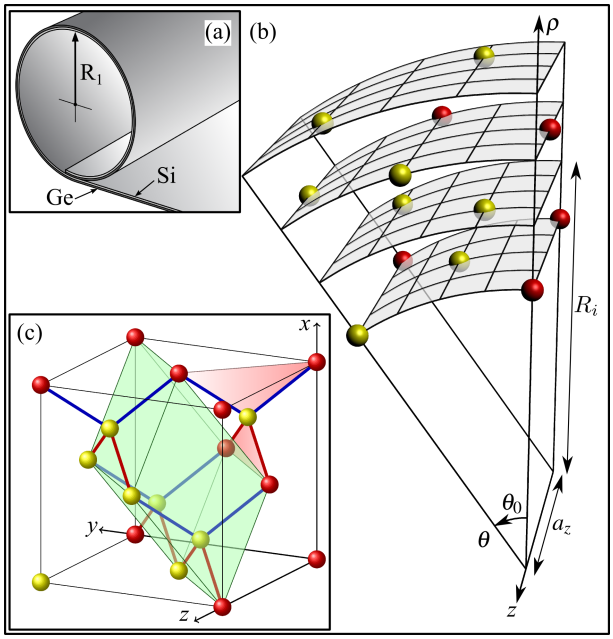


**Figure A.1** – (a): Sketch of a rolled-up Si–Ge tube; $R_1$ is the radius of the first shell of Si atoms. (b): Chosen unit cell for the tube with two atoms on each plane (yellow balls) evidencing the discrete rotational symmetry around the $z$ axis. Each red ball represents an atom that can be reached from the appropriate yellow ball on the same shell by means of discrete translations along (or discrete rotations around) $z$. (c): Conventional unit cell for a bulk diamond lattice (black cube) with eight atoms (yellow balls), from which the curved tube cell (panel b) originates. The green shaded region represents the primitive cell of the diamond lattice, containing only two atoms. Planes defined by couples of first-neighbor bonds are shaded in pink.

to Ref. [215]).

The quantitative evaluation of the tube band structure and of the valley splitting effect was performed by means of a TB model with $sp^3d^5s^*$ orbital basis set and first neighbors interactions, appropriately adapted to describe the discrete cylindrical symmetry. For the hopping and self energies in Si and Ge we adopted the TB parametrization of Niquet *et al.* [32]. For the dangling bonds at the innermost and outermost layers, which are passivated with hydrogen atoms, we used the TB parameters provided by Zheng *et al.* [226].

As an exemplificative case of the electronic band structure, in Fig. A.3 we show the conduction band structure of a tube with $N_{\mathrm{Si}} = 16$ and $N_{\mathrm{Ge}} = 9$, together with the band structure of a planar $\mathrm{Si_{16}/Ge_9}$ slab, obtained in the limit $R_1 \to \infty$. In both band structures, near-gap states are related to the three kinds of $\Delta$ valleys as schematized in Fig. A.2d.

Focusing then on the valley splitting (VS) of the lowest doublet at $\Gamma$, we report in panels a,b,c of Fig. A.4 the squared moduli of the wavefunctions calculated at the $\Gamma$ point, as a function of the radial coordinate, for three tubes with $N_{\mathrm{Si}} = 40$ and

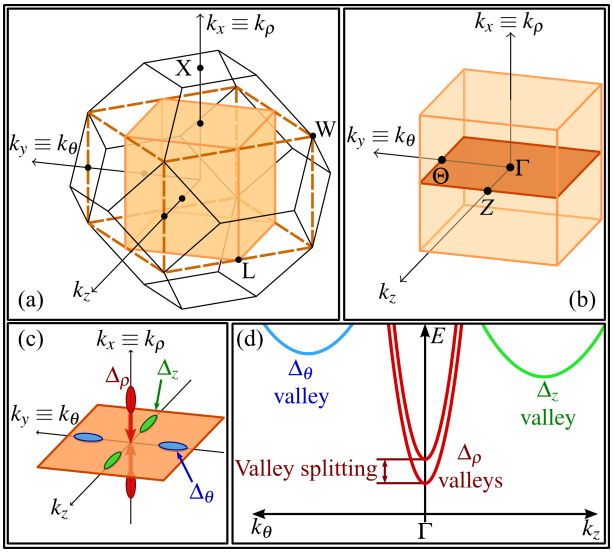


**Figure A.2** – (a): Brillouin zone (black lines) of the bulk diamond primitive cell. The shaded cube with vertices at the L points is the BZ corresponding to the conventional unit cell of Fig. A.1c. (b): Folding of the bulk BZ onto the two-dimensional BZ (dark orange rectangle) for the planar slab, or equivalently for the tube structure. (c): Ellipsoids of constant energy around the six Δ minima of the bulk Si (or Ge) crystal structure. The two conjugated $\Delta_\rho$ minima (red) fold into the Γ point of the 2D BZ of the tube. (d): Schematic of the CB electronic structure of a Si–Ge tube, adopting the same colors of panel c. The two conjugated $\Delta_\rho$ valleys fold into Γ and their degeneracy is resolved due to the VS interaction. The two conjugated $\Delta_\theta$ valleys remain unfolded and do not interact; the same holds for the $\Delta_z$ valleys.

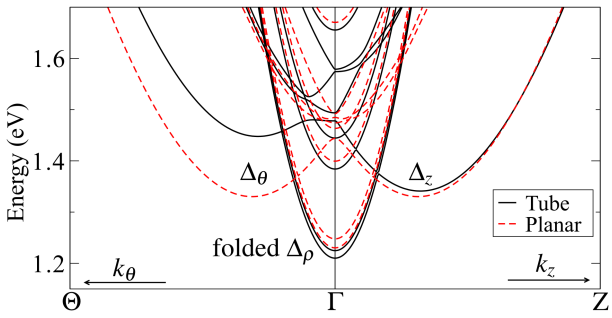


**Figure A.3** – Conduction band structure of a $Si_{16}/Ge_9$ tube (black solid lines) along the Θ – Γ–Z path. The internal radius of this tube is $R_1 = 49.1\,\text{nm}$. The band structure of a $Si_{16}/Ge_9$ planar slab ($R_1 \to \infty$) grown on a Si buffer is also reported with red dashed lines.

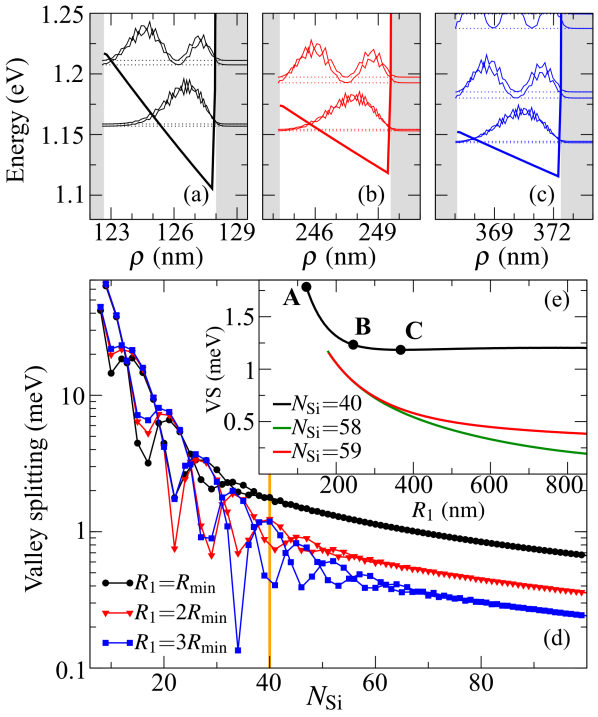


**Figure A.4** – (a), (b), (c): squared moduli of the wavefunctions, calculated at the Γ point, for tubes with $N_{Si} = 40$, and internal radius $R_1 = R_{min}$, $R_1 = 2R_{min}$, and $R_1 = 3R_{min}$ respectively. The corresponding values for $N_{Ge}$ are: 22, 85, 123. The triangular band profiles for the $\Delta_\rho$ valleys are also shown. The white central area represents the Si region; the left (inner side) is made of the H passivation layer; the Ge region in on the right side. (d): VS of the ground-state doublet at Γ as a function of $N_{Si}$. The value of $N_{Ge}$ is chosen in order to obtain the minimum internal radius of the tube $R_1 = R_{min}$ (black dots), or $R_1 = 2R_{min}$ (red triangles), or $R_1 = 3R_{min}$ (blue squares). The lines, connecting points with even or odd $N_{Si}$, are only a guide to the eye. The vertical orange line indicates the value of $N_{Si}$ for which panels a,b,c are calculated. (e): VS of the ground-state doublet at Γ as a function of the tube internal radius $R_1$, for three different values of $N_{Si}$. Each curve starts from the minimum attainable value for $R_1$. The black dots labeled A, B, C refer to the systems of panels a, b, c respectively.

different curvatures. Since the wavefunctions corresponding to the ground-state doublet are confined mainly in the Si region, it is interesting to plot the VS of the ground state doublet at Γ as a function of $N_{Si}$, for the minimum radius $R_1 = R_{min}$ that can be obtained by varying $N_{Ge}$ (black squares in Fig. A.4d). For comparison in Fig. A.4d we also show the VS data calculated for twice and three times of this radius (red and blue data points, respectively). From Fig. A.4d we deduce that damping of the VS oscillations can also be obtained for fixed value $N_{Si}$ but decreasing $R_1$ (vertical orange line in Fig. A.4d). Therefore, in Fig. A.4e we plot the VS as a function of the internal radius $R_1$, for three fixed values of $N_{Si}$. A detailed discussion of the behavior of the VS oscillations can be found in [215].

In conclusion, for the first time we have theoretically and numerically investigated the electronic band structure of Si/Ge rolled-up nanotubes, presenting the multivalley structure of the conduction band and the intervalley splitting of the tube levels at its bottom. Our results show that the Δ band-edge states are inequivalent. This degeneracy removal has been interpreted in terms of the confinement effects and of the action on the electronic spectrum of the non-biaxial strain fields induced by the tube curvature. We have thus shown that the curvature of the tube can be exploited to control the valley splitting magnitude.

## A.2 Porous silicon

The breakthrough of the discovery of room-temperature visible-light emission from porous silicon by Canham [227] has contributed to revive the interest in silicon for optoelectronic applications. Efforts have been focused in fabricating also other silicon nanostructures so to tailor their optical properties by means of quantum confinement (QC) effects. Among them we cite $Si/SiO_2$ superlattices [228], hydrogen-passivated silicon nanocrystals [229], and silicon nanowires [230]. Theoretical simulations show that whenever the charge carriers in these structures are confined in a region of 1–4 nm, at least in one direction, the obtained gap is located within the visible-light energy spectrum.

In order to understand the physics at the basis of this effect, and the role of the confinement effect in porous silicon, we have studied [231, 232] the emission energy and the oscillator strength of porous silicon with different porosity. Porous silicon is modeled by removing cylindrical holes from a bulk silicon crystal, as shown in Fig. A.5. Note that, for very large porosities, the system is in fact composed of individual nanowires (Fig. A.5f–h). The porosity $p$ is defined as the fraction of void within the porous silicon and it can easily be determined in experiments by weight measurement. Usually, the porosity of fabricated porous silicon may range from 4% for macroporous layers (where the pore size is larger than 50 nm), up to 95% for microporous layers (where the pore size is smaller than 2 nm). Theoretically, we

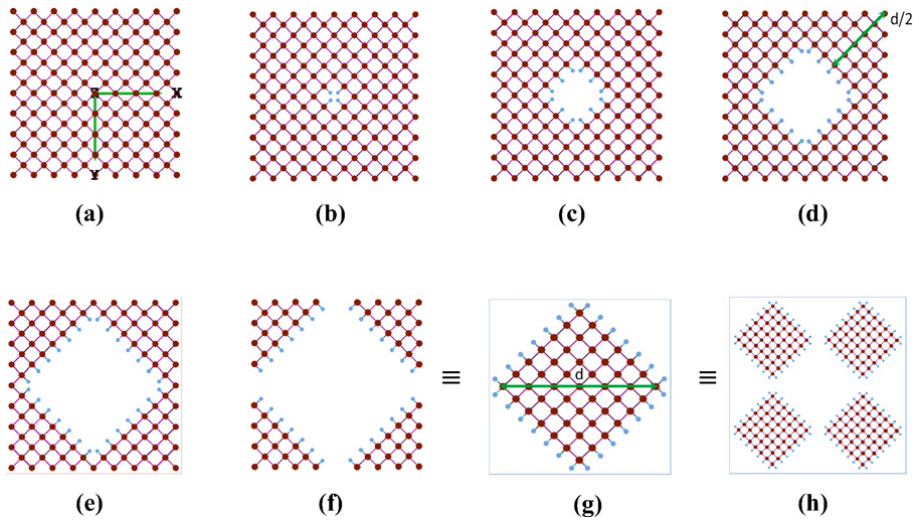


**Figure A.5** – Silicon supercell of size 4×4×1 unit cells with various porosities $p$: (a) $p = 0$ (bulk Si); (b) $p = 0.78\%$; (c) $p = 7\%$; (d) $p = 20\%$; (e) $p = 38\%$; and (f) $p = 62\%$. Cases (f)–(h) are equivalent and emphasize that, for large porosities, the system is in fact composed of Si nanowires. In particular, panel (h) shows four supercells to demonstrate the separation between the nanowires.The surface dangling bonds are passivated with hydrogen atoms (blue dots).

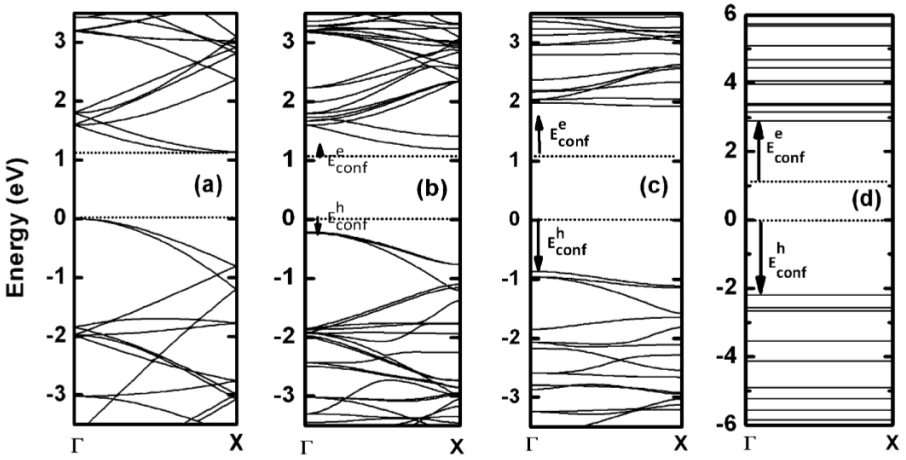


**Figure A.6** – Band structures along the Γ–X high-symmetry line of a fixed-size porous silicon sample of 2×2×1 unit cells but with different porosities: (a) $p = 0$ (bulk Si); (b) $p = 3\%$; (c) $p = 28\%$; (d) $p = 72\%$ (Si nanowire). The valence band edge of bulk Si is taken as energy reference. Confinement energies are also shown.

define the porosity as

$$p = \frac{N_{\mathrm{Si}}^{\mathrm{bulk}} - N_{\mathrm{Si}}}{N_{\mathrm{Si}}^{\mathrm{bulk}}},$$

where $N_{\mathrm{Si}}$ is the number of silicon atoms in the porous silicon sample and $N_{\mathrm{Si}}^{\mathrm{bulk}}$ is the number of silicon atoms supposed to be in a bulk silicon crystal with the same volume.

The band structures of systems with different size and porosity have been calculated, using a second-neighbor $sp^3$ tight-binding method including spin-orbit interaction, with the parametrization of Ref. [233]. An example of the band structures is reported in Fig. A.6.

We subsequently performed a critical study of the functional dependence of the bandgap energy as a function of porosity and interpore distance. The result is that the main parameter that controls the bandgap energy, and hence the emission frequency, is given by the interpore distance. This is due to confinement effects of the electrons and holes in the space between the pores, where the Si atoms are located. The fact that the emission frequency is controlled by confinement effects has been verified studying the power-law dependence of the bandgap energy vs. the interpore distance $d$, which has been verified to follow a low of the type

$$E_g = A + \frac{B}{d^C}$$

where $E_g$ is the gap energy, $d$ is the interpore distance defined in Fig. A.5, and $A$, $B$ and $C$ are constants.

Finally, the oscillator strength of the interband transitions at Γ of different samples of porous silicon has been evaluated with a method analogous to the one described

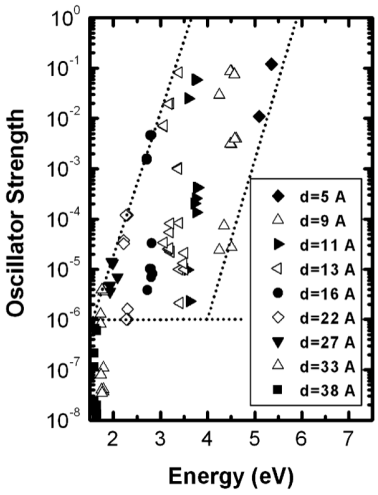


**Figure A.7** – TB results for the oscillator strength of the interband transitions at Γ versus the diameter $d$ of Si NWs in the range 5–38 Å. The results are presented in semi-log scale to display the exponential correlation. The dotted lines are guides to the eye.

in Sec. 2.2.1 (but generalized to the second-neighbor TB Hamiltonian); we show the results in Fig. A.7.

## A.3 Intersubband polaritons

During an internship at the École Normale Supérieure in Paris (France), under the supervision of Prof. G. Bastard and Prof. R. Ferreira I studied the effects of a vertical magnetic field on intersubband polaritons in MQW structures composed of materials which display a large band non-parabolicity. Since this work is not focused on Si/Ge-based systems, here only a brief introduction to the problem is given, referring the reader to Ref. [234] in which the results are published for all the details.

The idea of the polaritons was first proposed by Hopkins [235]. They are mixed quasiparticles which can be observed when there is a coupling between electronic and photonic states; they are the eigenstates of the system, which consist of a linear superposition of photonic and electronic excitations. The coupling is quantified by the Rabi frequency $\Omega_0$.

In particular, ISB polaritons are mixed states formed by the strong coupling of the light within a microcavity and the intersubband transitions of electrons confined in a semiconductor QW embedded in the cavity. Since the first experimental demonstration in 2003 [236] with a GaAs/AlGaAs MQW structure, intense research efforts have been devoted to the study of ISB polaritons. With this kind of polaritons the light–matter coupling can reach very large values [237, 238] becoming comparable to (or even larger than) the bare frequency of the cavity and of the ISB excitations. In this ultrastrong coupling regime, interesting quantum effects appear [239–242]. Moreover, since the coupling strength is proportional to the square root of the number of electrons, it can be controlled by electrical gating [243, 244]. Beside the observation of the strong coupling regime by means of reflectance spectroscopy as in the first experiments, and of photovoltaic measurements [245], also the electrical injection of cavity polaritons and their electroluminescence is being studied with considerable effort [246–249]. Moreover, the coupling of the ISB transition with a surface plasmon supported by a metal grating has been demonstrated [250]. In the effort of reaching larger light–matter couplings toward the ultrastrong coupling regime, other materials beside GaAs/AlGaAs have been considered, like for instance InAs/AlSb MQWs. Also the smaller effective mass of InAs with respect to GaAs ($m^*_{\mathrm{InAs}}/m^*_{\mathrm{GaAs}} = 0.39$) implies a stronger coupling [238].

At zero magnetic field, the polaritons can be simply and effectively described by a two-level problem [239], where the first level is the cavity mode with energy $E_{\mathrm{cav}}$, and the second level is the ISB transition with energy $E_{21}$ between the first (ground) and the second (excited) subband; the coupling is quantified by the Rabi frequency $\Omega_R$, where $2\hbar\Omega_R$ gives the splitting of the upper and lower polariton branches at the resonance $E_{\mathrm{cav}} = E_{21}$.

When a magnetic field $B$ is applied along the QW growth axis $\hat{z}$, neither the energies nor the strength of the ISB–cavity coupling are altered; thus, *a fortiori*, the two-level description of the polariton levels remains valid, if we still focus on transitions between the Landau levels belonging to different subbands. Actually, the aforementioned insensitivity to a vertical magnetic field is exact only for parabolic-band materials. It remains a very good approximation for GaAs-based heterostructures,

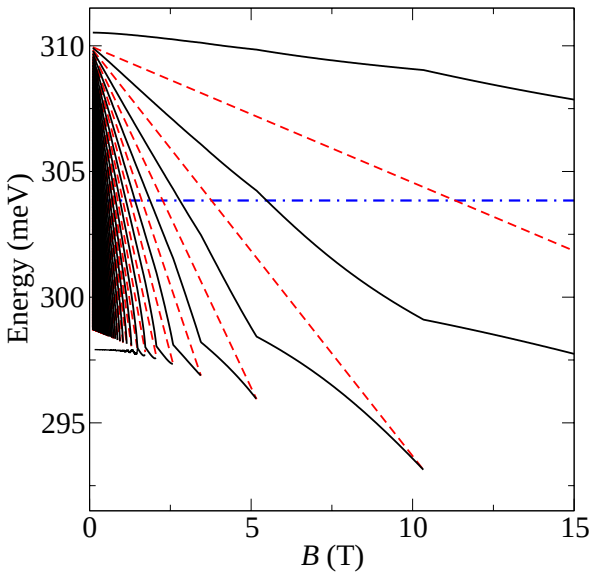


**Figure A.8** – Polariton branches at fixed in-plane vector $k_{\parallel}$ versus the magnetic field $B$ for a InAs/AlSb MQW structure embedded in a microcavity (black solid lines). Blue dotted–dashed line: bare cavity mode energy $E_{cav}$. Red dashed lines: ISB transition energies $\Delta E_j(B)$, plotted only in the $B$ range in which the corresponding Landau levels in the ground subband are not empty.

since GaAs shows very little non-parabolicity. On the contrary, in narrow-gap semiconductors like InAs or InSb, the band non-parabolicity effects cannot be disregarded in the calculation of the polaritonic states.

In Ref. [234], we show that for intersubband polaritons in narrow-gap semiconductors, with a significant non-parabolicity, the magnetic field plays a true role of an external control parameter that allows to tune the regime of light–matter interactions. It becomes then possible to tune the strength of the coupling of the light with the different non-degenerate intersubband levels. Our numerical results for a InAs/AlSb system identify three different regimes for the polariton coupling as a function of the intensity of the magnetic field. Just to show the final result, we report in Fig. A.8 the resulting magneto-polaritons (black lines) as a function of the magnetic field $B$, for fixed in-plane wavevector.

Our work has also allowed to design an optical parametric oscillator in the FIR spectral range. The structure is based on the existence of a mirror dispersion scheme for the magneto-polaritons, which ideally allows fulfilling phase-matching requirements for the pump and parametric waves.

# List of publications related to this Thesis

## Papers published in peer-reviewed journals

- M. De Seta, G. Capellini, Y. Busby, F. Evangelisti, M. Ortolani, M. Virgilio, G. Grosso, **G. Pizzi**, A. Nucara and S. Lupi, *Conduction band intersubband transitions in Ge/SiGe quantum wells*, Appl. Phys. Lett. **95**, 051918 (2009).

- **G. Pizzi**, M. Virgilio and G. Grosso, *Tight-binding calculation of optical gain in tensile strained [001]-Ge/SiGe quantum wells*, Nanotechnology **21**, 055202 (2010).

- Y. Busby, M. De Seta, G. Capellini, F. Evangelisti, M. Ortolani, M. Virgilio, G. Grosso, **G. Pizzi**, P. Calvani, S. Lupi, M. Nardone, G. Nicotra and C. Spinella, *Near- and far-infrared absorption and electronic structure of Ge-SiGe multiple quantum wells*, Phys. Rev. B **82**, 205317 (2010).

- N. Tit, Z. H. Yamani, **G. Pizzi** and M. Virgilio, *Comparison of confinement characters between porous silicon and silicon nanowires*, Phys. Lett. A **375**, 2422 (2011).

- **G. Pizzi**, F. Carosella, G. Bastard and R. Ferreira, *Magnetic field control of intersubband polaritons in narrow-gap semiconductors*, Phys. Rev. B **83**, 245318 (2011).

- L. Carroll, F. Imbert, H. Sigg, M. Süess, E. Müller, M. Virgilio, **G. Pizzi**, P. Rossbach, D. Chrastina and G. Isella, *Quantum-confined direct-gap transitions in tensile-strained Ge/SiGe multiple quantum wells*, Appl. Phys. Lett. **99**, 031907 (2011).

- M. Virgilio, **G. Pizzi** and G. Grosso, *Optical gain in short period Si/Ge superlattices on [001]-SiGe substrates*, J. Appl. Phys. **110**, 083105 (2011).

- M. Ortolani, D. Stehr, M. Wagner, M. Helm, **G. Pizzi**, M. Virgilio, G. Grosso, G. Capellini and M. D. Seta, *Long Intersubband Relaxation*

*Times in n-type Germanium Quantum Wells*, Appl. Phys. Lett. **99**, 201101 (2011).

### Submitted and accepted papers

- N. Tit, Z. H. Yamani, **G. Pizzi** and M. Virgilio, *Origins of visible-light emissions in porous silicon*, phys. stat. sol. (c) (Accepted).
- **G. Pizzi**, M. Virgilio, G. Grosso, S. Kiravittaya and O. G. Schmidt, *Curvature effects on valley splitting and degeneracy lifting: The case of Si/Ge rolled-up nanotubes*, Phys. Rev. B (Submitted).

## Conference proceedings

- M. Virgilio, **G. Pizzi**, G. Grosso, M. De Seta, G. Ciasca, Y. Busby, G. Capellini, F. Evangelisti, M. Ortolani, A. Nucara, P. Calvani, G. Nicotra, C. Spinella, *Intersubband absorption in n-type* [001] *Si/SiGe and Ge/SiGe MQWs*, in **Proceedings of The Tenth International Conference on Intersubband Transitions in Quantum Wells (ITQW2009)**, Montreal, Canada, September 6-11, 2009
- **G. Pizzi**, M. Virgilio, G. Grosso, *Optical Amplification in Tensile-Strained [001]-Ge/SiGe Multiple Quantum Wells: a Tight-Binding Model*, in **SiNEP-09, First International Workshop on Si based nano-electronics and -photonics, Book of Extended Abstracts**, NetBiblo (2009), ISBN: 978-84-9745-416-2
- Y. Busby, M. De Seta, G. Capellini, F. Evangelisti, M. Ortolani, M. Virgilio, G. Grosso, **G. Pizzi**, A. Nucara, S. Lupi, G. Nicotra, C. Spinella, *Terahertz intersubband transitions and band alignment in* n*-type Ge/SiGe Multi QWs*, in **The Second Transalpine Conference on Nanoscience and Nanotechnologies (Transalp'Nano2010)**, Como, Italy, June 3-5, 2010
- Y. Busby, M. De Seta, G. Capellini, F. Evangelisti, M. Ortolani, M. Virgilio, G. Grosso, **G. Pizzi**, A. Nucara, S. Lupi, *Intersubband transitions in the conduction band of Ge/SiGe MQWs*, in **Proceedings of the 2010 European Materials Research Society Meeting (EMRS2010)**, Strasbourg, France, June 7-11, 2010
- Y. Busby, G. Capellini, F. Evangelisti, M. Ortolani, M. Virgilio, G. Grosso, **G. Pizzi**, A. Nucara, S. Lupi, M. De Seta, *Terahertz intersubband transitions in the conduction band of Ge/SiGe multi quantum wells*, in **Infrared Millimeter and Terahertz Waves (IRMMW-THz), 2010 35th International Conference on**, Rome, Italy, September 5-10, 2010
- M. De Seta, Y. Busby, G. Capellini, F. Evangelisti, M. Ortolani, M. Virgilio, G. Grosso, **G. Pizzi**, A. Nucara, P. Calvani, *Intersubband transitions*

*in the conduction band of Ge/SiGe MQWs*, in **X International Conference on "Nanostructured Materials" (NANO2010)**, Rome, September 13-17, 2010

- **G. Pizzi**, M. Virgilio, G. Grosso, *$(Si)_n$ /$(Ge)_m$ superlattices for optoelectronic devices: a theoretical investigation*, in **Proceedings of the 96$^{th}$ annual meeting of the SIF (Italian Physical Society)**, Bologna, Italy, September 20-24, 2010

- **G. Pizzi**, F. Carosella, G. Bastard, R. Ferreira, *Magnetic field effects on intersubband polaritons in narrow gap semiconductors*, in **Proceedings of The 11$^{th}$ International Conference on Intersubband Transitions in Quantum Wells (ITQW2011)**, Badesi, Sardinia, Italy, September 11-16, 2011

- M. Virgilio, **G. Pizzi**, Y. Busby, M. De Seta, G. Capellini, M. Ortolani, S. Lupi, A. Nucara, P. Calvani, G. Grosso, F. Evangelisti, *Intersubband Transitions in Ge/SiGe Multi Quantum Wells on Si Substrate*, in **Proceedings of The 11$^{th}$ International Conference on Intersubband Transitions in Quantum Wells (ITQW2011)**, Badesi, Sardinia, Italy, September 11-16, 2011

## Participation at Schools and Conferences

- **SiNEP-09 (First International Workshop on Si based nano-electronics and -photonics)**, Vigo, Spain (Sep 20-23, 2009). In this Workshop I presented a poster titled *Optical amplification in tensile strained* [001]*-Ge/SiGe multiple quantum wells: a tight-binding model.*

- **CNR DMD 2009 National School on the Physics of Matter – "Physics of Spin in Materials"**, Chiavari (GE), Italy (Nov 2-9, 2009).

- **CMD23 (23$^{rd}$ General Conference of the Condensed Matter Division of the European Physical Society)**, Warsaw, Poland (Aug 30-Sep 3, 2010). In this Conference I presented a poster titled *Bound-to-bound conduction intersubband transitions in Ge/SiGe MQWs: experiment and modeling.*

- **CINECA 19$^{th}$ Summer School on Parallel Computation**, Casalecchio di Reno (BO), Italy (Sep 6-17, 2010).

- **96$^{th}$ annual meeting of the SIF (Italian Physical Society)**, Bologna, Italy (Sep 20-24, 2010). In this Conference I presented an oral contribution titled *$(Si)_n$/$(Ge)_m$ superlattices for optoelectronic devices: a theoretical investigation.*

- **6$^{th}$ Optoelectronics and Photonics Winter School: Physics and Applications of T-Rays**, Fai della Paganella, Trento, Italy (Feb 20-26, 2011). In this Winter School I presented an poster titled *Effects of the magnetic field on intersubband polaritons in narrow-gap materials.*

- **Polatom Conference on Cold Atoms, Semiconductor Polaritons and Nanoscience**, Chersonissos, Crete, Greece (May 2-6, 2011). In this conference I presented a poster titled *Magnetic field effects on intersubband polaritons in semiconductors with non-parabolic band dispersion*.
- **Ψ-k/CECAM/CCP9 Graduate School in Electronic-Structure Methods**, Oxford, UK (Jul 10-16, 2011).
- **ITQW 2011 (11$^{th}$ International Conference in Intersubband Transitions in Quantum Wells)**, Badesi, Sardinia, Italy (Sep 11-16, 2011). In this conference I presented an oral contribution titled *Magnetic field effect on intersubband polaritons in narrow gap semiconductors*.

## Internships and research collaborations during my Ph.D.

- **2010**: invited as Ph.D. student/guest scientist for one month at the **Leibniz-Institut für Festkörper- und Werkstoffforschung**, Dresden, Germany.

  During this period at the Institute for Integrative Nanosciences, directed by Prof. O. G. Schmidt, I studied the strain in Si/Ge "rolled-up" nano-and microtubes. The results are being published [215].

- **2010-2011**: internship of five months at the **École Normale Supérieure**, Paris, France.

  During this period I have studied the effects of a vertical magnetic field on the intersubband polaritons, under the supervision of Prof. G. Bastard and Prof. R. Ferreira. The results have been published in Ref. [234].

# Acknowledgements

It is a pleasure to thank here all the people who supported me during the last three years as a Ph.D. student, without whom all this work would not have been possible.

It is difficult to overstate my gratitude to my Ph.D. supervisor, Prof. Giuseppe Grosso, for his guidance and help throughout this Thesis, his expertise, his kindness, and his exquisite human qualities. He always provided encouragement, sound advice, good teaching, and he was always able to find the time to discuss with me.

I am really grateful to thank also Dr. Michele Virgilio, with whom I collaborated for most of the work presented in this Thesis: for the countless hours spent together coding, discussing Physics and performing calculations, even at distance.

I would like to acknowledge the support from Prof. Giuseppe La Rocca and Prof. Renato Colle. A special acknowledgment is also dedicated to the collaborators at University of Roma Tre, University of Roma La Sapienza, and NEST-CNR of Pisa: in particular, Prof. Florestano Evangelisti, Prof. Monica De Seta, Prof. Giovanni Capellini, Dr. Yan Busby, Dr. Michele Ortolani, Prof. Alessandro Tredicucci, Luca Masini, Dr. Alessandro Pitanti, Simone Zanotto.

I would then like to show my gratitude to the group of the Leibniz Institut-IFW Dresden, and in particular to prof. Oliver G. Schmidt and Dr. Suwit Kiravittaya, and to the group of École Normale Supérieure of Paris, in particular to prof. Gérald Bastard, Dr. Robson Ferreira and Dr. Francesca Carosella, for their hospitality during my periods abroad.

It is a pleasure to acknowledge also all the people that I have met during these periods abroad, and all friends and colleagues in Pisa and in Pordenone, whose list would be way too long to be written here. But to everyone of them goes my gratitude, because they all directly and indirectly helped me through these years.

And of course a special thank goes to Marcella, not only for her patience and for having encouraged me constantly; but for her love and for the very special person she is.

Lastly, and most importantly, I wish to thank my parents, Adele and Giuseppe, and my sister Antonella, for their love and unconditional support.

# Bibliography


[1] P. Cheben, R. Soref, D. Lockwood and G. Reed, *Silicon Photonics*, Adv. Opt. Tech. **2008**, Article ID 510937 (2008).

[2] L. Pavesi, *Silicon-Based Light Sources for Silicon Integrated Circuits*, Adv. Opt. Tech. **2008**, Article ID 416926 (2008).

[3] D. Paul, *Silicon photonics: a bright future?*, Electron. Lett. **45**, 582 (2009).

[4] J. Liu, X. Sun, R. Camacho-Aguilera, L. C. Kimerling and J. Michel, *Ge-on-Si laser operating at room temperature*, Opt. Lett. **35**, 679 (2010).

[5] K. Takai, C. Kaneta, Y. Uehara and Y. Kadooka, *Development of Problem Solving Environment for Large Scale Electronic Structure Calculations Based on Tight Binding Method*, J. Conv. Inform. Technol. **5**, 195 (2010).

[6] http://www.nanohub.org.

[7] http://wwww.nextnano.de.

[8] J. Sée, P. Dollfus and S. Galdin, *Comparison between a $sp^3d^5$ tight-binding and an effective-mass description of silicon quantum dots*, Phys. Rev. B **66**, 193307 (2002).

[9] A. Zunger, *On the Farsightedness (hyperopia) of the Standard k·p Model*, phys. stat. sol. (a) **190**, 467 (2002).

[10] N. H. Quang, N. T. Truc and Y.-M. Niquet, *Tight-binding versus effective mass approximation calculation of electronic structures of semiconductor nanocrystals and nanowires*, Comp. Mat. Sci. **44**, 21 (2008).

[11] H. Mera, M. Persson, Y. Niquet and M. Bescond, *Effective mass versus tight-binding: Where is the discord?*, in *Computational Electronics (IWCE), 2010 14th International Workshop on* (2010).

[12] R. W. G. Wyckoff, *Crystal Structures*, vol. 1, Interscience Publishers, 2nd ed. (1963).

[13] P.-O. Löwdin, *On the Non-Orthogonality Problem Connected with the Use of Atomic Wave Functions in the Theory of Molecules and Crystals*, J. Chem. Phys. **18**, 365 (1950).

[14] J. C. Slater and G. F. Koster, *Simplified LCAO Method for the Periodic Potential Problem*, Phys. Rev. **94**, 1498 (1954).

[15] P. Vogl, H. P. Hjalmarson and J. D. Dow, *A Semi-empirical tight-binding theory of the electronic structure of semiconductors*, J. Phys. Chem. Sol. **44**, 365 (1983).

[16] J.-M. Jancu, R. Scholz, F. Beltram and F. Bassani, *Empirical $spds^*$ tight-binding calculation for cubic semiconductors: General method and material parameters*, Phys. Rev. B **57**, 6493 (1998).

[17] M. E. Rose, *Relativistic Electron Theory*, Wiley (1961).

[18] J. D. Jackson, *Classical Electrodynamics*, Wiley, third ed. (1998).

[19] F. Bassani and G. Pastori Parravicini, *Electronic States and Optical Transitions in Solids*, Pergamon Press, Moscow (1975).

[20] J. M. Luttinger and W. Kohn, *Motion of Electrons and Holes in Perturbed Periodic Fields*, Phys. Rev. **97**, 869 (1955).

[21] R. J. Elliott, *Spin-Orbit Coupling in Band Theory — Character Tables for Some "Double" Space Groups*, Phys. Rev. **96**, 280 (1954).

[22] O. Madelung (Editor), *Semiconductors: Group IV Elements and III-V Compounds*, Springer, New York (1991).

[23] C. G. Van de Walle and R. M. Martin, *Theoretical calculations of heterojunction discontinuities in the Si/Ge system*, Phys. Rev. B **34**, 5621 (1986).

[24] P. N. Keating, *Effect of Invariance Requirements on the Elastic Strain Energy of Crystals with Application to the Diamond Structure*, Phys. Rev. **145**, 637 (1966).

[25] P. N. Keating, *Relationship between the Macroscopic and Microscopic Theory of Crystal Elasticity. I. Primitive Crystals*, Phys. Rev. **152**, 774 (1966).

[26] P. N. Keating, *Relationship between the Macroscopic and Microscopic Theory of Crystal Elasticity. II. Nonprimitive Crystals*, Phys. Rev. **169**, 758 (1968).

[27] A. B. Anderson, *Valence-Force-Field Potentials for Diamondlike Crystals*, Phys. Rev. B **8**, 3824 (1973).

[28] P. C. Chou and N. J. Pagano, *Elasticity: Tensor, dyadic, and engineering approaches*, Dover Publications (1992).

[29] W. A. Harrison, *Electronic structure and the properties of solids: The physics of the chemical bond*, Freeman and Company, San Francisco (1980).

[30] S. Y. Ren, J. D. Dow and D. J. Wolford, *Pressure dependence of deep levels in GaAs*, Phys. Rev. B **25**, 7661 (1982).

[31] T. B. Boykin, G. Klimeck, R. C. Bowen and F. Oyafuso, *Diagonal parameter shifts due to nearest-neighbor displacements in empirical tight-binding theory*, Phys. Rev. B **66**, 125207 (2002).

[32] Y. M. Niquet, D. Rideau, C. Tavernier, H. Jaouen and X. Blase, *Onsite matrix elements of the tight-binding Hamiltonian of a strained crystal: Application to silicon, germanium, and their alloys*, Phys. Rev. B **79**, 245201 (2009).

[33] Y. M. Niquet, C. Delerue, G. Allan and M. Lannoo, *Method for tight-binding parametrization: Application to silicon nanostructures*, Phys. Rev. B **62**, 5109 (2000).

[34] T. B. Boykin, G. Klimeck and F. Oyafuso, *Valence band effective-mass expressions in the $sp^3d^5s^*$ empirical tight-binding model applied to a Si and Ge parametrization*, Phys. Rev. B **69**, 115201 (2004).

[35] F. Sacconi, A. Di Carlo, P. Lugli, M. Stadele and J.-M. Jancu, *Full band approach to tunneling in MOS structures*, IEEE Trans. Electron Devices **51**, 741 (2004).

[36] J.-M. Jancu and P. Voisin, *Tetragonal and trigonal deformations in zinc-blende semiconductors: A tight-binding point of view*, Phys. Rev. B **76**, 115202 (2007).

[37] T. B. Boykin, M. Luisier, M. Salmani-Jelodar and G. Klimeck, *Strain-induced, off-diagonal, same-atom parameters in empirical tight-binding theory suitable for [110] uniaxial strain applied to a silicon parametrization*, Phys. Rev. B **81**, 125202 (2010).

[38] N. J. Ekins-Daukes, K. Kawaguchi and J. Zhang, *Strain-Balanced Criteria for Multiple Quantum Well Structures and Its Signature in X-ray Rocking Curves*, Cryst. Growth Des. **2**, 287 (2002).

[39] J. Matthews and A. Blakeslee, *Defects in epitaxial multilayers: III. Preparation of almost perfect multilayers*, J. Cryst. Growth **32**, 265 (1976).

[40] J. P. Dismukes, L. Ekstrom and R. J. Paff, *Lattice Parameter and Density in Germanium-Silicon Alloys*, J. Phys. Chem. **68**, 3021 (1964).

[41] M. M. Rieger and P. Vogl, *Electronic-band parameters in strained $Si_{1-x}Ge_x$ alloys on $Si_{1-y}Ge_y$ substrates*, Phys. Rev. B **48**, 14276 (1993).

[42] D. Paul, *The progress towards terahertz quantum cascade lasers on silicon substrates*, Laser Photonics Rev. **4**, 610 (2010).

[43] R. Scholz, J.-M. Jancu, F. Beltram and F. Bassani, *Calculation of Electronic States in Semiconductor Heterostructures with an Empirical spds* Tight-Binding Model*, phys. stat. sol. (b) **217**, 449 (2000).

[44] J. Weber and M. I. Alonso, *Near-band-gap photoluminescence of Si-Ge alloys*, Phys. Rev. B **40**, 5683 (1989).

[45] L. Colombo, R. Resta and S. Baroni, *Valence-band offsets at strained Si/Ge interfaces*, Phys. Rev. B **44**, 5572 (1991).

[46] G. P. Schwartz, M. S. Hybertsen, J. Bevk, R. G. Nuzzo, J. P. Mannaerts and G. J. Gualtieri, *Core-level photoemission measurements of valence-band offsets in highly strained heterojunctions: Si-Ge system*, Phys. Rev. B **39**, 1235 (1989).

[47] E. Yu, E. Croke, T. McGill and R. Miles, *Measurement of the valence-band offset in strained Si/Ge-(100) heterojunctions by x-ray photoelectron spectroscopy*, Appl. Phys. Lett. **56**, 569 (1990).

[48] E. O. Kane, *Band structure of indium antimonide*, J. Phys. Chem. Solids **1**, 249 (1957).

[49] G. Bastard, *Wave mechanics applied to semiconductor heterostructures*, Les éditions de physique, Les Ulis (1990).

[50] M. El kurdi, G. Fishman, S. Sauvage and P. Boucaud, *Comparison between 6-band and 14-band k·p formalisms in SiGe/Si heterostructures*, Phys. Rev. B **68**, 165333 (2003).

[51] S. Richard, F. Aniel and G. Fishman, *Energy-band structure of Ge, Si, and GaAs: A thirty-band k·p method*, Phys. Rev. B **70**, 235204 (2004).

[52] S. Richard, F. Aniel and G. Fishman, *Band diagrams of Si and Ge quantum wells via the 30-band k·p method*, Phys. Rev. B **72**, 245316 (2005).

[53] M. G. Burt, *The justification for applying the effective-mass approximation to microstructures*, J. Phys.: Cond. Matt. **4**, 6651 (1992).

[54] G. Lehmann and M. Taut, *On the Numerical Calculation of the Density of States and Related Properties*, phys. stat. sol. (b) **54**, 469 (1972).

[55] F. Stern and W. E. Howard, *Properties of Semiconductor Surface Inversion Layers in the Electric Quantum Limit*, Phys. Rev. **163**, 816 (1967).

[56] K. Driscoll and R. Paiella, *Design of n-type silicon-based quantum cascade lasers for terahertz light emission*, J. Appl. Phys. **102**, 093103 (2007).

[57] P. Harrison, *Quantum Wells, Wires and Dots*, Wiley, 2nd ed. (2005).

[58] C. Jacoboni and L. Reggiani, *The Monte Carlo method for the solution of charge transport in semiconductors with applications to covalent materials*, Rev. Mod. Phys. **55**, 645 (1983).

[59] N. Ozguven and P. C. McIntyre, *Silicon-germanium interdiffusion in high-germanium-content epitaxial heterostructures*, Appl. Phys. Lett. **92**, 181907 (2008).

[60] M. Meduňa, O. Caha, M. Keplinger, J. Stangl, G. Bauer, G. Mussler and D. Grützmacher, *Interdiffusion in Ge rich SiGe/Ge multilayers studied by in situ diffraction*, phys. stat. sol. (a) **206**, 1775 (2009).

[61] G. Grosso and G. Pastori Parravicini, *Solid State Physics*, Academic Press (2000).

[62] S.-Y. Ren and W. A. Harrison, *Semiconductor properties based upon universal tight-binding parameters*, Phys. Rev. B **23**, 762 (1981).

[63] F. Trani, G. Cantele, D. Ninno and G. Iadonisi, *Tight-binding calculation of the optical absorption cross section of spherical and ellipsoidal silicon nanocrystals*, Phys. Rev. B **72**, 075423 (2005).

[64] W. W. Chow and S. W. Koch, *Semiconductor-Laser Fundamentals*, Springer (1999).

[65] H. Bebb and E. Williams, *Photoluminescence I: Theory*, in *Transport and Optical Phenomena*, edited by R. Willardson and A. C. Beer, *Semiconductors and Semimetals*, vol. 8, chap. 4, pp. 181–320, Elsevier (1972).

[66] S. Zollner, S. Gopalan and M. Cardona, *Intervalley deformation potentials and scattering rates in zinc blende semiconductors*, Appl. Phys. Lett. **54**, 614 (1989).

[67] C. Jacoboni, F. Nava, C. Canali and G. Ottaviani, *Electron drift velocity and diffusivity in germanium*, Phys. Rev. B **24**, 1014 (1981).

[68] M. Fischetti, *Monte Carlo simulation of transport in technologically significant semiconductors of the diamond and zinc-blende structures. I. Homogeneous transport*, IEEE Trans. Electron Devices **38**, 634 (1991).

[69] H. Haug and S. W. Koch, *Quantum Theory of Optical and Electronic Properties of Semiconductors*, World Scientific Publishing Company, fourth ed. (2004).

[70] D. P. Davé and H. F. Taylor, *Thomas-Kuhn sum rule for quantum mechanical systems with a spatially varying effective mass*, Phys. Lett. A **184**, 301 (1994).

[71] Y. Fu and M. Willander, *Optical absorption coefficients of semiconductor quantum-well infrared detectors*, J. Appl. Phys. **77**, 4648 (1995).

[72] F. M. Peeters, A. Matulis, M. Helm, T. Fromherz and W. Hilber, *Oscillator strength and sum rule for intersubband transitions in a superlattice*, Phys. Rev. B **48**, 12008 (1993).

[73] M. Helm, *The Basic Physics of Intersubband Transitions*, in *Intersubband Transitions in Quantum Wells, Physics and Device Applications I*, edited by H. C. Liu and F. Capasso, *Semiconductors and Semimetals*, vol. 62, chap. 1, pp. 1–99, Academic Press (2000).

[74] S. K. Chun and K. L. Wang, *Oscillator strength for intersubband transitions in strained n−type $Si_xGe_{1-x}$ quantum wells*, Phys. Rev. B **46**, 7682 (1992).

[75] J. Faist, F. Capasso, D. L. Sivco, C. Sirtori, A. L. Hutchinson and A. Y. Cho, *Quantum Cascade Laser*, Science **264**, 553 (1994).

[76] R. Köhler, A. Tredicucci, F. Beltram, H. E. Beere, E. H. Linfield, A. G. Davies, D. A. Ritchie, R. C. Iotti and F. Rossi, *Terahertz semiconductor-heterostructure laser*, Nature **417**, 156 (2002).

[77] A. Tredicucci and R. Köhler, *Terahertz Quantum Cascade Lasers*, in *Intersubband Transitions in Quantum Structures*, edited by R. Paiella, pp. 45–105, McGraw-Hill (2006).

[78] J. R. Gao, J. N. Hovenier, Z. Q. Yang, J. J. A. Baselmans, A. Baryshev, M. Hajenius, T. M. Klapwijk, A. J. L. Adam, T. O. Klaassen, B. S. Williams, S. Kumar, Q. Hu and J. L. Reno, *Terahertz heterodyne receiver based on a quantum cascade laser and a superconducting bolometer*, Appl. Phys. Lett. **86**, 244104 (2005).

[79] H.-W. Hübers, S. Pavlov, A. Semenov, R. Köhler, L. Mahler, A. Tredicucci, H. Beere, D. Ritchie and E. Linfield, *Terahertz quantum cascade laser as local oscillator in a heterodyne receiver*, Opt. Express **13**, 5890 (2005).

[80] A. Lee, B. Williams, S. Kumar, Q. Hu and J. Reno, *Real-time imaging using a 4.3-THz quantum cascade laser and a 320×240 microbolometer focal-plane array*, IEEE Photon. Techn. Lett. **18**, 1415 (2006).

[81] H.-W. Hübers, S. G. Pavlov, H. Richter, A. D. Semenov, L. Mahler, A. Tredicucci, H. E. Beere and D. A. Ritchie, *High-resolution gas phase spectroscopy with a distributed feedback terahertz quantum cascade laser*, Appl. Phys. Lett. **89**, 061115 (2006).

[82] M. Tonouchi, *Cutting-edge terahertz technology*, Nat. Photonics **1**, 97 (2007).

[83] G. Scalari, C. Walther, M. Fischer, R. Terazzi, H. Beere, D. Ritchie and J. Faist, *THz and sub-THz quantum cascade lasers*, Laser Photonics Rev. **3**, 45 (2009).

[84] S. Kumar, Q. Hu and J. L. Reno, *186 K operation of terahertz quantum-cascade lasers based on a diagonal design*, Appl. Phys. Lett. **94**, 131105 (2009).

[85] C. W. I. Chan, S. Fathololoumi, E. Dupont, Z. R. Wasilewski, S. R. Laframboise, D. Ban, Q. Hu and H. C. Liu, *A terahertz quantum cascade laser operating up to 193K*, in *Proceedings of the 11$^{th}$ ITQW conference, Badesi, Sardinia, Italy* (2011).

[86] A. Wade, G. Fedorov, D. Smirnov, S. Kumar, B. S. Williams, Q. Hu and J. L. Reno, *Magnetic-field-assisted terahertz quantum cascade laser operating up to 225 K*, Nat. Photonics **3**, 41 (2009).

[87] M. Belkin, Q. J. Wang, C. Pflugl, A. Belyanin, S. Khanna, A. Davies, E. Linfield and F. Capasso, *High-Temperature Operation of Terahertz Quantum Cascade Laser Sources*, IEEE J. Sel. Topics Quantum Electron. **15**, 952 (2009).

[88] L. Ajili, G. Scalari, N. Hoyler, M. Giovannini and J. Faist, *InGaAs–AlInAs/InP terahertz quantum cascade laser*, Appl. Phys. Lett. **87**, 141107 (2005).

[89] D. J. Paul, *Si/SiGe heterostructures: from material and physics to devices and circuits*, Semicond. Sci. Tech. **19**, R75 (2004).

[90] G. Dehlinger, L. Diehl, U. Gennser, H. Sigg, J. Faist, K. Ensslin, D. Grützmacher and E. Müller, *Intersubband Electroluminescence from Silicon-Based Quantum Cascade Structures*, Science **290**, 2277 (2000).

[91] S. A. Lynch, R. Bates, D. J. Paul, D. J. Norris, A. G. Cullis, Z. Ikonic, R. W. Kelsall, P. Harrison, D. D. Arnone and C. R. Pidgeon, *Intersubband electroluminescence from Si/SiGe cascade emitters at terahertz frequencies*, Appl. Phys. Lett. **81**, 1543 (2002).

[92] H. von Känel, M. Kummer, G. Isella, E. Muller and T. Hackbarth, *Very high hole mobilities in modulation-doped Ge quantum wells grown by low-energy plasma enhanced chemical vapor deposition*, Appl. Phys. Lett. **80**, 2922 (2002).

[93] M. De Seta, G. Capellini, Y. Busby, F. Evangelisti, M. Ortolani, M. Virgilio, G. Grosso, G. Pizzi, A. Nucara and S. Lupi, *Conduction band intersubband transitions in Ge/SiGe quantum wells*, Appl. Phys. Lett. **95**, 051918 (2009).

[94] Y. Busby, M. De Seta, G. Capellini, F. Evangelisti, M. Ortolani, M. Virgilio, G. Grosso, G. Pizzi, P. Calvani, S. Lupi, M. Nardone, G. Nicotra and C. Spinella, *Near- and far-infrared absorption and electronic structure of Ge-SiGe multiple quantum wells*, Phys. Rev. B **82**, 205317 (2010).

[95] V. A. Shah, A. Dobbie, M. Myronov, D. J. F. Fulgoni, L. J. Nash and D. R. Leadley, *Reverse graded relaxed buffers for high Ge content SiGe virtual substrates*, Appl. Phys. Lett. **93**, 192103 (2008).

[96] G. Capellini, M. De Seta, Y. Busby, M. Pea, F. Evangelisti, G. Nicotra, C. Spinella, M. Nardone and C. Ferrari, *Strain relaxation in high Ge content SiGe layers deposited on Si*, J. Appl. Phys. **107**, 063504 (2010).

[97] G. Ciasca, M. D. Seta, G. Capellini, F. Evangelisti, M. Ortolani, M. Virgilio, G. Grosso, A. Nucara and P. Calvani, *Terahertz intersubband absorption and conduction band alignment in n-type Si/SiGe multiple quantum wells*, Phys. Rev. B **79**, 085302 (2009).

[98] E. R. Brown and S. J. Eglash, *Calculation of the intersubband absorption strength in ellipsoidal-valley quantum wells*, Phys. Rev. B **41**, 7559 (1990).

[99] V. V. Afanas'ev, A. Stesmans, L. Souriau, R. Loo and M. Meuris, *Valence band energy in confined $Si_{1-x}Ge_x$ (0.28<x<0.93) layers*, Appl. Phys. Lett. **94**, 172106 (2009).

[100] S. V. Kondratenko, A. S. Nikolenko, O. V. Vakulenko, M. Y. Valakh, V. O. Yukhymchuk, A. V. Dvurechenskii and A. I. Nikiforov, *Band offsets and photocurrent spectroscopy of Si/Ge heterostructures with quantum dots*, Nanotechnology **19**, 145703 (2008).

[101] P. Murzyn, C. R. Pidgeon, J.-P. R. Wells, I. V. Bradley, Z. Ikonic, R. W. Kelsall, P. Harrison, S. A. Lynch, D. J. Paul, D. D. Arnone, D. J. Robbins, D. Norris and A. G. Cullis, *Picosecond intersubband dynamics in p-Si/SiGe quantum-well emitter structures*, Appl. Phys. Lett. **80**, 1456 (2002).

[102] R. W. Kelsall, Z. Ikonic, P. Murzyn, C. R. Pidgeon, P. J. Phillips, D. Carder, P. Harrison, S. A. Lynch, P. Townsend, D. J. Paul, S. L. Liew, D. J. Norris and A. G. Cullis, *Intersubband lifetimes in p-Si/SiGe terahertz quantum cascade heterostructures*, Phys. Rev. B **71**, 115326 (2005).

[103] P. Rauter, T. Fromherz, G. Bauer, N. Q. Vinh, B. N. Murdin, J. P. Phillips, C. R. Pidgeon, L. Diehl, G. Dehlinger and D. Grützmacher, *Direct monitoring of the excited state population in biased SiGe valence band quantum wells by femtosecond resolved photocurrent experiments*, Appl. Phys. Lett. **89**, 211111 (2006).

[104] P. Rauter, T. Fromherz, N. Q. Vinh, B. N. Murdin, G. Mussler, D. Grützmacher and G. Bauer, *Continuous Voltage Tunability of Intersubband Relaxation Times in Coupled SiGe Quantum Well Structures Using Ultrafast Spectroscopy*, Phys. Rev. Lett. **102**, 147401 (2009).

[105] M. Ortolani, D. Stehr, M. Wagner, M. Helm, G. Pizzi, M. Virgilio, G. Grosso, G. Capellini and M. D. Seta, *Long Intersubband Relaxation Times in n-type Germanium Quantum Wells*, Appl. Phys. Lett. **99**, 201101 (2011).

[106] D. Stehr, S. Winnerl, M. Helm, T. Dekorsy, T. Roch and G. Strasser, *Pump-probe spectroscopy of interminiband relaxation and electron cooling in doped superlattices*, Appl. Phys. Lett. **88**, 151108 (2006).

[107] B. N. Murdin, G. M. H. Knippels, A. F. G. van der Meer, C. R. Pidgeon, C. J. G. M. Langerak, M. Helm, W. Heiss, K. Unterrainer, E. Gornik, K. K. Geerinck, N. J. Hovenier and W. T. Wenckebach, *Excite-probe determination of the intersubband lifetime in wide GaAs/AlGaAs quantum wells using a far-infrared free-electron laser*, Semicond. Sci. Tech. **9**, 1554 (1994).

[108] G. Scalari, L. Ajili, J. Faist, H. Beere, E. Linfield, D. Ritchie and G. Davies, *Far-infrared ($\lambda \simeq 87\mu m$) bound-to-continuum quantum-cascade lasers operating up to 90 K*, Appl. Phys. Lett. **82**, 3165 (2003).

[109] A. Valavanis, Z. Ikonić and R. W. Kelsall, *Intersubband carrier scattering in n - and p-Si/SiGe quantum wells with diffuse interfaces*, Phys. Rev. B **77**, 075312 (2008).

[110] T. Unuma, M. Yoshita, T. Noda, H. Sakaki and H. Akiyama, *Intersubband absorption linewidth in GaAs quantum wells due to scattering by interface roughness, phonons, alloy disorder, and impurities*, J. Appl. Phys. **93**, 1586 (2003).

[111] A. Valavanis, T. V. Dinh, L. J. M. Lever, Z. Ikonić and R. W. Kelsall, *Material configurations for n-type silicon-based terahertz quantum cascade lasers*, Phys. Rev. B **83**, 195321 (2011).

[112] F. Schäffler, *High-mobility Si and Ge structures*, Semicond. Sci. Tech. **12**, 1515 (1997).

[113] C. G. Van de Walle, *Band lineups and deformation potentials in the model-solid theory*, Phys. Rev. B **39**, 1871 (1989).

[114] O. Gunnarsson and B. I. Lundqvist, *Exchange and correlation in atoms, molecules, and solids by the spin-density-functional formalism*, Phys. Rev. B **13**, 4274 (1976).

[115] M. Franz, K. Pressel, A. Barz, P. Dold and K. W. Benz, *Shallow donors in Ge-rich GeSi bulk crystals*, Appl. Phys. Lett. **74**, 2708 (1999).

[116] R. Krüssmann, H. Vollmer and R. Labusch, *The Activation Energy of Phosphorus Donors in Silicon-Rich Silicon-Germanium Alloys*, Phys. Stat. Sol. (b) **118**, 275 (1983).

[117] B. Zheng, J. Michel, F. Y. G. Ren, L. C. Kimerling, D. C. Jacobson and J. M. Poate, *Room-temperature sharp line electroluminescence at $\lambda$=1.54 $\mu$m from an erbium-doped, silicon light-emitting diode*, Appl. Phys. Lett. **64**, 2842 (1994).

[118] N. Koshida, *Device Applications of Silicon Nanocrystals and Nanostructures*, Springer (2009).

[119] X. Sun, A. Zadok, M. J. Shearn, K. A. Diest, A. Ghaffari, H. A. Atwater, A. Scherer and A. Yariv, *Electrically pumped hybrid evanescent Si/InGaAsP lasers*, Opt. Lett. **34**, 1345 (2009).

[120] K.-i. Takakura, N. Hiroi, T. Suemasu, S. F. Chichibu and F. Hasegawa, *Investigation of direct and indirect band gaps of [100]-oriented nearly strain-free β-$FeSi_2$ films grown by molecular-beam epitaxy*, Appl. Phys. Lett. **80**, 556 (2002).

[121] N. Koshida and H. Koyama, *Visible electroluminescence from porous silicon*, Appl. Phys. Lett. **60**, 347 (1992).

[122] Y.-H. Kuo, Y. K. Lee, Y. Ge, S. Ren, J. E. Roth, T. I. Kamins, D. A. B. Miller and J. S. Harris, *Strong quantum-confined Stark effect in germanium quantum-well structures on silicon*, Nature **437**, 1334 (2005).

[123] M. Bonfanti, E. Grilli, M. Guzzi, M. Virgilio, G. Grosso, D. Chrastina, G. Isella, H. von Kanel and A. Neels, *Optical transitions in Ge/SiGe multiple quantum wells with Ge-rich barriers*, Phys. Rev. B **78**, 041407 (2008).

[124] Y.-H. Kuo, Y. K. Lee, Y. Ge, S. Ren, J. E. Roth, T. I. Kamins, D. A. B. Miller and J. S. Harris, Jr., *Quantum-Confined Stark Effect in Ge/SiGe Quantum Wells on Si for Optical Modulators*, IEEE J. Sel. Topics Quantum Electron. **12**, 1503 (2006).

[125] J. Liu, D. D. Cannon, K. Wada, Y. Ishikawa, D. T. Danielson, S. Jongthammanurak, J. Michel and L. C. Kimerling, *Deformation potential constants of biaxially tensile stressed $Ge$ epitaxial films on $Si(100)$*, Phys. Rev. B **70**, 155309 (2004).

[126] M. El Kurdi, H. Bertin, E. Martincic, M. de Kersauson, G. Fishman, S. Sauvage, A. Bosseboeuf and P. Boucaud, *Control of direct band gap emission of bulk germanium by mechanical tensile strain*, Appl. Phys. Lett. **96**, 041909 (2010).

[127] J. Liu, D. D. Cannon, K. Wada, Y. Ishikawa, S. Jongthammanurak, D. T. Danielson, J. Michel and L. C. Kimerling, *Tensile strained Ge p-i-n photodetectors on Si platform for C and L band telecommunications*, Appl. Phys. Lett. **87**, 011110 (2005).

[128] J. Liu, X. Sun, D. Pan, X. Wang, L. C. Kimerling, T. L. Koch and J. Michel, *Tensile-strained, n-type Ge as a gain medium formonolithic laser integration on Si*, Opt. Express **15**, 11272 (2007).

[129] J. Menendez and J. Kouvetakis, *Type-I $Ge/Ge_{1-x-y}Si_xSn_y$ strained-layer heterostructures with a direct Ge bandgap*, Appl. Phys. Lett. **85**, 1175 (2004).

[130] Y.-Y. Fang, J. Tolle, R. Roucka, A. V. G. Chizmeshya, J. Kouvetakis, V. R. D'Costa and J. Menéndez, *Perfectly tetragonal, tensile-strained Ge on $Ge_{1-y}Sn_y$ buffered Si(100)*, Appl. Phys. Lett. **90**, 061915 (2007).

[131] S. Takeuchi, A. Sakai, O. Nakatsuka, M. Ogawa and S. Zaima, *Tensile strained Ge layers on strain-relaxed $Ge_{1-x}Sn_x$/virtual Ge substrates*, Thin Solid Films **517**, 159 (2008).

[132] R. A. Soref and C. H. Perry, *Predicted band gap of the new semiconductor SiGeSn*, J. Appl. Phys. **69**, 539 (1991).

[133] P. Moontragoon, Z. Ikonic and P. Harrison, *Band structure calculations of Si–Ge–Sn alloys: achieving direct band gap materials*, Semicond. Sci. Tech. **22**, 742 (2007).

[134] M. Bauer, C. Ritter, P. A. Crozier, J. Ren, J. Menendez, G. Wolf and J. Kouvetakis, *Synthesis of ternary SiGeSn semiconductors on Si(100) via $Sn_xGe_{1-x}$ buffer layers*, Appl. Phys. Lett. **83**, 2163 (2003).

[135] P. Aella, C. Cook, J. Tolle, S. Zollner, A. V. G. Chizmeshya and J. Kouvetakis, *Optical and structural properties of $Si_xSn_yGe_{1-x-y}$ alloys*, Appl. Phys. Lett. **84**, 888 (2004).

[136] J. Tolle, R. Roucka, A. V. G. Chizmeshya, J. Kouvetakis, V. R. D'Costa and J. Menendez, *Compliant tin-based buffers for the growth of defect-free strained heterostructures on silicon*, Appl. Phys. Lett. **88**, 252112 (2006).

[137] V. R. D'Costa, Y.-Y. Fang, J. Tolle, J. Kouvetakis and J. Menendez, *Tunable Optical Gap at a Fixed Lattice Constant in Group-IV Semiconductor Alloys*, Phys. Rev. Lett. **102**, 107403 (2009).

[138] G. Pizzi, M. Virgilio and G. Grosso, *Tight-binding calculation of optical gain in tensile strained [001]-Ge/SiGe quantum wells*, Nanotechnology **21**, 055202 (2010).

[139] S.-W. Chang and S. L. Chuang, *Theory of Optical Gain of Ge-$Si_xGe_ySn_{1-x-y}$ Quantum-Well Lasers*, IEEE J. Quantum Elect. **43**, 249 (2007).

[140] G. Jones and E. O'Reilly, *Improved performance of long-wavelength strained bulk-like semiconductor lasers*, IEEE J. Quantum Elect. **29**, 1344 (1993).

[141] S.-L. Cheng, J. Lu, G. Shambat, H.-Y. Yu, K. Saraswat, J. Vuckovic and Y. Nishi, *Room temperature 1.6 $\mu$m electroluminescence from Ge light emitting diode on Si substrate*, Opt. Express **17**, 10019 (2009).

[142] T.-H. Cheng, C.-Y. Ko, C.-Y. Chen, K.-L. Peng, G.-L. Luo, C. W. Liu and H.-H. Tseng, *Competitiveness between direct and indirect radiative transitions of Ge*, Appl. Phys. Lett. **96**, 091105 (2010).

[143] M. de Kersauson, R. Jakomin, M. El Kurdi, G. Beaudoin, N. Zerounian, F. Aniel, S. Sauvage, I. Sagnes and P. Boucaud, *Direct and indirect band gap room temperature electroluminescence of Ge diodes*, J. Appl. Phys. **108**, 023105 (2010).

[144] T.-H. Cheng, K.-L. Peng, C.-Y. Ko, C.-Y. Chen, H.-S. Lan, Y.-R. Wu, C. W. Liu and H.-H. Tseng, *Strain-enhanced photoluminescence from Ge direct transition*, Appl. Phys. Lett. **96**, 211108 (2010).

[145] Y. Chen, C. Li, Z. Zhou, H. Lai, S. Chen, W. Ding, B. Cheng and Y. Yu, *Room temperature photoluminescence of tensile-strained Ge/$Si_{0.13}Ge_{0.87}$ quantum wells grown on silicon-based germanium virtual substrate*, Appl. Phys. Lett. **94**, 141902 (2009).

[146] M. El Kurdi, T. Kociniewski, T.-P. Ngo, J. Boulmer, D. Debarre, P. Boucaud, J. F. Damlencourt, O. Kermarrec and D. Bensahel, *Enhanced photoluminescence of heavily n-doped germanium*, Appl. Phys. Lett. **94**, 191107 (2009).

[147] C. Li, Y. Chen, Z. Zhou, H. Lai and S. Chen, *Enhanced photoluminescence of strained Ge with a delta-doping SiGe layer on silicon and silicon-on-insulator*, Appl. Phys. Lett. **95**, 251102 (2009).

[148] X. Sun, J. Liu, L. C. Kimerling and J. Michel, *Direct gap photoluminescence of n-type tensile-strained Ge-on-Si*, Appl. Phys. Lett. **95**, 011911 (2009).

[149] X. Sun, J. Liu, L. Kimerling and J. Michel, *Toward a Germanium Laser for Integrated Silicon Photonics*, IEEE J. Sel. Topics Quantum Electron. **16**, 124 (2010).

[150] G.-E. Chang, S.-W. Chang and S. L. Chuang, *Theory for n-type doped, tensile-strained Ge–$Si_xGe_ySn_{1-x-y}$ quantum-well lasers at telecom wavelength*, Opt. Express **17**, 11246 (2009).

[151] L. D. Laude, F. H. Pollak and M. Cardona, *Effects of Uniaxial Stress on the Indirect Exciton Spectrum of Silicon*, Phys. Rev. B **3**, 2623 (1971).

[152] T. Fromherz, E. Koppensteiner, M. Helm, G. Bauer, J. F. Nützel and G. Abstreiter, *Hole energy levels and intersubband absorption in modulation-doped Si/$Si_{1-x}Ge_x$ multiple quantum wells*, Phys. Rev. B **50**, 15073 (1994).

[153] http://www.ioffe.ru/SVA/NSM/Semicond.

[154] L. Carroll, F. Imbert, H. Sigg, M. Süess, E. Müller, M. Virgilio, G. Pizzi, P. Rossbach, D. Chrastina and G. Isella, *Quantum-confined direct-gap transitions in tensile-strained Ge/SiGe multiple quantum wells*, Appl. Phys. Lett. **99**, 031907 (2011).

[155] G. Isella, D. Chrastina, B. Rössner, T. Hackbarth, H. J. Herzog, U. König and H. von Känel, *Low-energy plasma-enhanced chemical vapor deposition for strained Si and Ge heterostructures and devices*, Solid State Electron. **48**, 1317 (2004).

[156] Y. Ishikawa, K. Wada, J. Liu, D. D. Cannon, H.-C. Luan, J. Michel and L. C. Kimerling, *Strain-induced enhancement of near-infrared absorption in Ge epitaxial layers grown on Si substrate*, J. Appl. Phys. **98**, 013501 (2005).

[157] H. Shen, P. Parayanthal, F. H. Pollak, M. Tomkiewicz, T. J. Drummond and J. N. Schulman, *Photoreflectance study of GaAs/AlAs superlattices: Fit to electromodulation theory*, Appl. Phys. Lett. **48**, 653 (1986).

[158] D. J. Paul, *8-band $k \cdot p$ modeling of the quantum confined Stark effect in Ge quantum wells on Si substrates*, Phys. Rev. B **77**, 155323 (2008).

[159] J.-M. Baribeau, *X-ray scattering analysis of interface roughness and diffusion*, J. Vac. Sci. Technol. B **16**, 1568 (1998).

[160] X.-C. Liu and D. R. Leadley, *Silicon–germanium interdiffusion in strained Ge/SiGe multiple quantum well structures*, J. Phys. D: Appl. Phys. **43**, 505303 (2010).

[161] M. Virgilio, G. Pizzi and G. Grosso, *Optical gain in short period Si/Ge superlattices on [001]-SiGe substrates*, J. Appl. Phys. **110**, 083105 (2011).

[162] F. Cerdeira, *Optical properties*, in *Germanium Silicon: Physics and Materials*, edited by R. Hull and J. C. Bean, *Semiconductors and Semimetals*, vol. 56, chap. 5, pp. 226–292, Academic Press, San Diego (1999).

[163] S. Froyen, D. M. Wood and A. Zunger, *Structural and electronic properties of epitaxial thin-layer $Si_nGe_n$ superlattices*, Phys. Rev. B **37**, 6893 (1988).

[164] S. Ciraci, A. Baratoff and I. P. Batra, *Zone-folded direct band gaps and energetics in strained $(Si)_4/(Ge)_4$ superlattices*, Phys. Rev. B **41**, 6069 (1990).

[165] J. Zi, K. Zhang and X. Xie, *Theoretical study of structures and growth of strained Si/Ge superlattices*, Appl. Phys. Lett. **57**, 165 (1990).

[166] M. S. Hybertsen and M. Schlüter, *Theory of optical transitions in Si/Ge(001) strained-layer superlattices*, Phys. Rev. B **36**, 9683 (1987).

[167] K. B. Wong, M. Jaros, I. Morrison and J. P. Hagon, *Electronic Structure and Optical Properties of Si-Ge Superlattices*, Phys. Rev. Lett. **60**, 2221 (1988).

[168] M. A. Gell, *Effect of buffer-layer composition on new optical transitions in Si/Ge short-period superlattices*, Phys. Rev. B **38**, 7535 (1988).

[169] S. Satpathy, R. M. Martin and C. G. Van de Walle, *Electronic properties of the (100) (Si)/(Ge) strained-layer superlattices*, Phys. Rev. B **38**, 13237 (1988).

[170] U. Schmid, N. E. Christensen, M. Alouani and M. Cardona, *Electronic and optical properties of strained Ge/Si superlattices*, Phys. Rev. B **43**, 14597 (1991).

[171] R. J. Turton and M. Jaros, *Linear and nonlinear optical properties of direct gap Si-Ge superlattices*, Optoelectronics IEEE Proceedings J. **138**, 323 (1991).

[172] T. P. Pearsall, J. M. Vandenberg, R. Hull and J. M. Bonar, *Structure and optical properties of strained Ge-Si superlattices grown on (001) Ge*, Phys. Rev. Lett. **63**, 2104 (1989).

[173] R. Zachai, K. Eberl, G. Abstreiter, E. Kasper and H. Kibbel, *Photoluminescence in short-period Si/Ge strained-layer superlattices*, Phys. Rev. Lett. **64**, 1055 (1990).

[174] I. A. Papadogonas, A. N. Andriotis and E. N. Economou, *Optical properties of $Si_mGe_n$ superlattices: A CPA treatment of the interface diffusion*, Phys. Rev. B **55**, 10760 (1997).

[175] C. Tserbak, H. M. Polatoglou and G. Theodorou, *Unified approach to the electronic structure of strained Si/Ge superlattices*, Phys. Rev. B **47**, 7104 (1993).

[176] T. P. Pearsall, L. Colace, A. DiVergilio, W. Jäger, D. Stenkamp, G. Theodorou, H. Presting, E. Kasper and K. Thonke, *Spectroscopy of band-to-band optical transitions in Si-Ge alloys and superlattices*, Phys. Rev. B **57**, 9128 (1998).

[177] M. Gell, *Direct-gap Si/Ge superlattices*, Phys. Rev. B **40**, 1966 (1989).

[178] U. Menczigar, G. Abstreiter, J. Olajos, H. Grimmeiss, H. Kibbel, H. Presting and E. Kasper, *Enhanced band-gap luminescence in strain-symmetrized $(Si)_m/(Ge)_n$ superlattices*, Phys. Rev. B **47**, 4099 (1993).

[179] P. A. M. Rodrigues, M. A. Araújo Silva, F. Cerdeira and J. C. Bean, *Confinement and zone folding in the $E_1$-like optical transitions of Ge/Si quantum wells and superlattices*, Phys. Rev. B **48**, 18024 (1993).

[180] J. Olajos, J. Engvall, H. G. Grimmeiss, U. Menczigar, M. Gail, G. Abstreiter, H. Kibbel, E. Kasper and H. Presting, *Photo- and electroluminescence in short-period Si/Ge superlattice structures*, Semicond. Sci. Tech. **9**, 2011 (1994).

[181] H. Presting, H. Kibbel, M. Jaros, R. M. Turton, U. Menczigar, G. Abstreiter and H. G. Grimmeiss, *Ultrathin $Si_mGe_n$ strained layer superlattices — a step towards Si optoelectronics*, Semicond. Sci. Tech. **7**, 1127 (1992).

[182] S. Ghosh, J. Weber and H. Presting, *Photoluminescence processes in $Si_mGe_n$ superlattices*, Phys. Rev. B **61**, 15625 (2000).

[183] T. P. Pearsall, *Differential optical absorption spectroscopy in Ge-Si superlattices*, Appl. Phys. Lett. **60**, 1712 (1992).

[184] T. P. Pearsall, H. Polatoglou, H. Presting and E. Kasper, *Optical absorption spectroscopy of Si-Ge alloys and superlattices*, Phys. Rev. B **54**, 1545 (1996).

[185] U. Schmid, J. Humlíček, F. Luke, M. Cardona, H. Presting, H. Kibbel, E. Kasper, K. Eberl, W. Wegscheider and G. Abstreiter, *Optical transitions in strained Ge/Si superlattices*, Phys. Rev. B **45**, 6793 (1992).

[186] Y. D. Kim, M. V. Klein, J.-M. Baribeau, S. H. Hwang, K. W. Whang and E. Yoon, *Spectroscopic ellipsometry study on $E_2$ peak splitting of Si–Ge short period superlattices*, J. Appl. Phys. **81**, 7952 (1997).

[187] U. Gnutzmann and K. Clausecker, *Theory of direct optical transitions in an optical indirect semiconductor with a superlattice structure*, Appl. Phys. A **3**, 9 (1974).

[188] G. Theodorou and C. Tserbak, *Interface intermixing influence on the electronic and optical properties of Si/Ge strained-layer superlattices*, Phys. Rev. B **51**, 4723 (1995).

[189] R. J. Turton and M. Jaros, *Effects of interfacial ordering on the optical properties of Si-Ge superlattices*, Semicond. Sci. Tech. **8**, 2003 (1993).

[190] C. Sheng, T.-C. Zhou, Q. Cai, Dawei-Gong, M.-R. Yu, X.-J. Zhang and X. Wang, *Suppression of Si-Ge interfacial vibration mode in the Raman spectrum of a $Si_6Ge_4$ superlattices*, Phys. Rev. B **53**, 10771 (1996).

[191] E. Kasper, H. Kibbel, H. Jorke, H. Brugger, E. Friess and G. Abstreiter, *Symmetrically strained Si/Ge superlattices on Si substrates*, Phys. Rev. B **38**, 3599 (1988).

[192] U. Schmid, F. Luke, N. E. Christensen, M. Alouani, M. Cardona, E. Kasper, H. Kibbel and H. Presting, *Interband transitions in strain-symmetrized $Ge_4Si_6$ superlattices*, Phys. Rev. Lett. **65**, 1933 (1990).

[193] H. M. Polatoglou, G. Theodorou and C. Tserbak, *Optical absorption of pseudomorphic Si/Ge superlattices*, Phys. Rev. B **49**, 8132 (1994).

[194] C. Tserbak, H. M. Polatoglou and G. Theodorou, *$(Si)_3/(Ge)_4$ Superlattices: Direct-Gap Semiconductors?*, Europhys. Lett. **18**, 451 (1992).

[195] M. Virgilio and G. Grosso, *Valley splitting and optical intersubband transitions at parallel and normal incidence in [001]-Ge/SiGe quantum wells*, Phys. Rev. B **79**, 165310 (2009).

[196] O. Gülseren, T. Yildirim and S. Ciraci, *Systematic ab initio study of curvature effects in carbon nanotubes*, Phys. Rev. B **65**, 153405 (2002).

[197] S. B. Fagan, L. B. da Silva and R. Mota, *Ab initio Study of Radial Deformation Plus Vacancy on Carbon Nanotubes: Energetics and Electronic Properties*, Nano Lett. **3**, 289 (2003).

[198] V. M. Osadchii and V. Y. Prinz, *Quantum confinement in nanocorrugated semiconductor films*, Phys. Rev. B **72**, 033313 (2005).

[199] Y. Mei, S. Kiravittaya, M. Benyoucef, D. J. Thurmer, T. Zander, C. Deneke, F. Cavallo, A. Rastelli and O. G. Schmidt, *Optical Properties of a Wrinkled Nanomembrane with Embedded Quantum Well*, Nano Lett. **7**, 1676 (2007).

[200] S. Ono and H. Shima, *Tuning the electrical resistivity of semiconductor thin films by nanoscale corrugation*, Phys. Rev. B **79**, 235407 (2009).

[201] Y. Mei, S. Kiravittaya, S. Harazim and O. G. Schmidt, *Principles and applications of micro and nanoscale wrinkles*, Mat. Sci. Eng. R: Reports **70**, 209 (2010).

[202] C. Ortix, S. Kiravittaya, O. G. Schmidt and J. van den Brink, *Curvature-induced geometric potential in strain-driven nanostructures*, Phys. Rev. B **84**, 045438 (2011).

[203] P. Cendula, S. Kiravittaya, I. Mönch, J. Schumann and O. G. Schmidt, *Directional Roll-up of Nanomembranes Mediated by Wrinkling*, Nano Lett. **11**, 236 (2011).

[204] O. G. Schmidt and K. Eberl, *Nanotechnology: Thin solid films roll up into nanotubes*, Nature **410**, 168 (2001).

[205] S. V. Golod, V. Y. Prinz, V. I. Mashanov and A. K. Gutakovsky, *Fabrication of conducting GeSi/Si micro- and nanotubes and helical microcoils*, Semicond. Sci. Tech. **16**, 181 (2001).

[206] J. Zang, M. Huang and F. Liu, *Mechanism for Nanotube Formation from Self-Bending Nanofilms Driven by Atomic-Scale Surface-Stress Imbalance*, Phys. Rev. Lett. **98**, 146102 (2007).

[207] X. Li, *Strain induced semiconductor nanotubes: from formation process to device applications*, J. Phys. D: Appl. Phys. **41**, 193001 (2008).

[208] M. Huang, F. Cavallo, F. Liu and M. G. Lagally, *Nanomechanical architecture of semiconductor nanomembranes*, Nanoscale **3**, 96 (2011).

[209] C. C. Bof Bufon, J. D. Cojal González, D. J. Thurmer, D. Grimm, M. Bauer and O. G. Schmidt, *Self-Assembled Ultra-Compact Energy Storage Elements Based on Hybrid Nanomembranes*, Nano Lett. **10**, 2506 (2010).

[210] K. Dietrich, C. Strelow, C. Schliehe, C. Heyn, A. Stemmann, S. Schwaiger, S. Mendach, A. Mews, H. Weller, D. Heitmann and T. Kipp, *Optical Modes Excited by Evanescent-Wave-Coupled PbS Nanocrystals in Semiconductor Microtube Bottle Resonators*, Nano Lett. **10**, 627 (2010).

[211] E. J. Smith, S. Schulze, S. Kiravittaya, Y. Mei, S. Sanchez and O. G. Schmidt, *Lab-in-a-Tube: Detection of Individual Mouse Cells for Analysis in Flexible Split-Wall Microtube Resonator Sensors*, Nano Lett. (2010), doi: 10.1021/nl1036148.

[212] S. Sanchez, A. N. Ananth, V. M. Fomin, M. Viehrig and O. G. Schmidt, *Superfast Motion of Catalytic Microjet Engines at Physiological Temperature*, J. Am. Chem. Soc. (2011), doi: 10.1021/ja205012j.

[213] Z. Tian, V. Veerasubramanian, P. Bianucci, S. Mukherjee, Z. Mi, A. G. Kirk and D. V. Plant, *Single rolled-up InGaAs/GaAs quantum dot microtubes integrated with silicon-on-insulator waveguides*, Opt. Express **19**, 12164 (2011).

[214] C. C. Bof Bufon, J. D. Arias Espinoza, D. J. Thurmer, M. Bauer, C. Deneke, U. Zschieschang, H. Klauk and O. G. Schmidt, *Hybrid Organic/Inorganic Molecular Heterojunctions Based on Strained Nanomembranes*, Nano Lett. (2011), doi: 10.1021/nl201773d.

[215] G. Pizzi, M. Virgilio, G. Grosso, S. Kiravittaya and O. G. Schmidt, *Curvature effects on valley splitting and degeneracy lifting: The case of Si/Ge rolled-up nanotubes*, Phys. Rev. B (Submitted).

[216] A. B. Fowler, F. F. Fang, W. E. Howard and P. J. Stiles, *Magneto-Oscillatory Conductance in Silicon Surfaces*, Phys. Rev. Lett. **16**, 901 (1966).

[217] D. Z.-Y. Ting and Y.-C. Chang, *L-valley-derived states in (001) GaSb/AlSb quantum wells and superlattices*, Phys. Rev. B **38**, 3414 (1988).

[218] G. Grosso, G. Pastori Parravicini and C. Piermarocchi, *Valley splitting in triangular Si(001) quantum wells*, Phys. Rev. B **54**, 16393 (1996).

[219] T. B. Boykin, G. Klimeck, M. A. Eriksson, M. Friesen, S. N. Coppersmith, P. von Allmen, F. Oyafuso and S. Lee, *Valley splitting in strained silicon quantum wells*, Appl. Phys. Lett. **84**, 115 (2004).

[220] M. A. Wilde, M. Rhode, C. Heyn, D. Heitmann, D. Grundler, U. Zeitler, F. Schäffler and R. J. Haug, *Direct measurements of the spin and valley splittings in the magnetization of a Si/SiGe quantum well in tilted magnetic fields*, Phys. Rev. B **72**, 165429 (2005).

[221] A. Valavanis, Z. Ikonić and R. W. Kelsall, *Intervalley splitting and intersubband transitions in n -type Si/SiGe quantum wells: Pseudopotential vs. effective mass calculation*, Phys. Rev. B **75**, 205332 (2007).

[222] M. Virgilio and G. Grosso, *Optical transitions between valley split subbands in biased Si quantum wells*, Phys. Rev. B **75**, 235428 (2007).

[223] S. Srinivasan, G. Klimeck and L. P. Rokhinson, *Valley splitting in Si quantum dots embedded in SiGe*, Appl. Phys. Lett. **93**, 112102 (2008).

[224] M. Grundmann, *Nanoscroll formation from strained layer heterostructures*, Appl. Phys. Lett. **83**, 2444 (2003).

[225] A. Malachias, C. Deneke, B. Krause, C. Mocuta, S. Kiravittaya, T. H. Metzger and O. G. Schmidt, *Direct strain and elastic energy evaluation in rolled-up semiconductor tubes by x-ray microdiffraction*, Phys. Rev. B **79**, 035301 (2009).

[226] Y. Zheng, C. Rivas, R. Lake, K. Alam, T. Boykin and G. Klimeck, *Electronic properties of silicon nanowires*, IEEE Trans. Electron Devices **52**, 1097 (2005).

[227] L. T. Canham, *Silicon quantum wire array fabrication by electrochemical and chemical dissolution of wafers*, Appl. Phys. Lett. **57**, 1046 (1990).

[228] D. J. Lockwood, Z. H. Lu and J.-M. Baribeau, *Quantum Confined Luminescence in Si/$SiO_2$ Superlattices*, Phys. Rev. Lett. **76**, 539 (1996).

[229] M. Nayfeh, *Highly nonlinear photoluminescence threshold in porous silicon*, Appl. Phys. Lett. **75**, 4112 (1999).

[230] B. Tian, X. Zheng, T. J. Kempa, Y. Fang, N. Yu, G. Yu, J. Huang and C. M. Lieber, *Coaxial silicon nanowires as solar cells and nanoelectronic power sources*, Nature **449**, 885 (2007).

[231] N. Tit, Z. H. Yamani, G. Pizzi and M. Virgilio, *Comparison of confinement characters between porous silicon and silicon nanowires*, Phys. Lett. A **375**, 2422 (2011).

[232] N. Tit, Z. H. Yamani, G. Pizzi and M. Virgilio, *Origins of visible-light emissions in porous silicon*, phys. stat. sol. (c) (Accepted).

[233] G. Grosso and C. Piermarocchi, *Tight-binding model and interactions scaling laws for silicon and germanium*, Phys. Rev. B **51**, 16772 (1995).

[234] G. Pizzi, F. Carosella, G. Bastard and R. Ferreira, *Magnetic field control of intersubband polaritons in narrow-gap semiconductors*, Phys. Rev. B **83**, 245318 (2011).

[235] J. J. Hopfield, *Theory of the Contribution of Excitons to the Complex Dielectric Constant of Crystals*, Phys. Rev. **112**, 1555 (1958).

[236] D. Dini, R. Köhler, A. Tredicucci, G. Biasiol and L. Sorba, *Microcavity Polariton Splitting of Intersubband Transitions*, Phys. Rev. Lett. **90**, 116401 (2003).

[237] E. Dupont, J. A. Gupta and H. C. Liu, *Giant vacuum-field Rabi splitting of intersubband transitions in multiple quantum wells*, Phys. Rev. B **75**, 205325 (2007).

[238] A. A. Anappara, D. Barate, A. Tredicucci, J. Devenson, R. Teissier and A. Baranov, *Giant intersubband polariton splitting in InAs/AlSb microcavities*, Solid State Commun. **142**, 311 (2007).

[239] C. Ciuti, G. Bastard and I. Carusotto, *Quantum vacuum properties of the intersubband cavity polariton field*, Phys. Rev. B **72**, 115303 (2005).

[240] S. De Liberato, C. Ciuti and I. Carusotto, *Quantum Vacuum Radiation Spectra from a Semiconductor Microcavity with a Time-Modulated Vacuum Rabi Frequency*, Phys. Rev. Lett. **98**, 103602 (2007).

[241] S. De Liberato, D. Gerace, I. Carusotto and C. Ciuti, *Extracavity quantum vacuum radiation from a single qubit*, Phys. Rev. A **80**, 053810 (2009).

[242] P. Nataf and C. Ciuti, *Vacuum Degeneracy of a Circuit QED System in the Ultrastrong Coupling Regime*, Phys. Rev. Lett. **104**, 023601 (2010).

[243] A. A. Anappara, A. Tredicucci, G. Biasiol and L. Sorba, *Electrical control of polariton coupling in intersubband microcavities*, Appl. Phys. Lett. **87**, 051105 (2005).

[244] G. Günter, A. A. Anappara, J. Hees, A. Sell, G. Biasiol, L. Sorba, S. De Liberato, C. Ciuti, A. Tredicucci, A. Leitenstorfer and R. Huber, *Sub-cycle switch-on of ultrastrong light-matter interaction*, Nature **458**, 178 (2009).

[245] L. Sapienza, A. Vasanelli, C. Ciuti, C. Manquest, C. Sirtori, R. Colombelli and U. Gennser, *Photovoltaic probe of cavity polaritons in a quantum cascade structure*, Appl. Phys. Lett. **90**, 201101 (2007).

[246] R. Colombelli, C. Ciuti, Y. Chassagneux and C. Sirtori, *Quantum cascade intersubband polariton light emitters*, Semicond. Sci. Tech. **20**, 985 (2005).

[247] L. Sapienza, A. Vasanelli, R. Colombelli, C. Ciuti, Y. Chassagneux, C. Manquest, U. Gennser and C. Sirtori, *Electrically Injected Cavity Polaritons*, Phys. Rev. Lett. **100**, 136806 (2008).

[248] Y. Todorov, P. Jouy, A. Vasanelli, L. Sapienza, R. Colombelli, U. Gennser and C. Sirtori, *Stark-tunable electroluminescence from cavity polariton states*, Appl. Phys. Lett. **93**, 171105 (2008).

[249] P. Jouy, A. Vasanelli, Y. Todorov, L. Sapienza, R. Colombelli, U. Gennser and C. Sirtori, *Intersubband electroluminescent devices operating in the strong-coupling regime*, Phys. Rev. B **82**, 045322 (2010).

[250] S. Zanotto, G. Biasiol, R. Degl'Innocenti, L. Sorba and A. Tredicucci, *Intersubband polaritons in a one-dimensional surface plasmon photonic crystal*, Appl. Phys. Lett. **97**, 231123 (2010).

# List of Figures

# List of Tables